MODELLING AND OBSERVATIONS OF THE ATMOSPHERIC BOUNDARY LAYER OF THE ARCTIC MARGINAL ICE ZONE

A thesis submitted to the School of Environmental Sciences
of the University of East Anglia in partial fulfilment
of the requirements for the degree of Doctor of Philosophy

RHIANNON DAVIES
100017072

JUNE 2017

Rhiannon Davies

100017072

ABSTRACT

The Arctic is undergoing big changes, there has been a reduction in sea ice extent and an increase in the amount of thinner, newer ice. This changing surface causes challenges to numerical weather prediction and climate simulation, due to the very interconnected nature of the surface and atmosphere in the Arctic.

Changes to the surface may impact on the air temperature, the surface fluxes of heat and moisture and the microphysics of clouds amongst others. These areas could also, in turn, change the surface. The Marginal Ice Zone (MIZ) is the area of the sea ice which is between the open water and solid ice, and is characterised by a complex and constantly changing ice surface.

The impact of thinning ice in the MIZ was investigated using a series of idealised modelling experiments, and it was found that thinner sea ice in the MIZ would increase the surface temperature and fluxes of heat. In turn this causes the clouds, which form over the open water, to form closer to the ice edge. The clouds were found to be thinner for the experiments with thinner ice, which resulted in them allowing more shortwave radiation to reach the surface. This result implies that thinning sea ice would act to further thin sea ice. Using observations from the Aerosol-Clouds Coupling And Climate Interactions in the Arctic (ACCACIA) campaign, two sets of model sensitivity studies were undertaken to test which boundary layer parametrisation schemes would perform better.

It was discovered that the boundary layer in the model is more sensitive to the surface representation rather than the choice of boundary layer scheme. These results point to the need for more work, both observations and modelling, on the sea ice and its impact on the atmosphere in order to better predict the changes the Arctic and the planet will undergo with a changing climate.

ACKNOWLEDGEMENTS

I have to start with my supervisors without whom this project would not exist. They have met with me, prodded me when I needed it and found the time to read my work which has made it much better. So my thanks go to Prof Ian Renfrew, the late Roland von Glasow, Dr John King and Prof Ian Brooks. A special mention goes to Dr Manoj Joshi who was able to step in when Roland so sadly left us and has helped me get through my final year of the PhD.

I need to thank all the people who were involved on the ACCACIA field campaign, the pilots and the crew of the FAAM aircraft, the other scientists and students. The data was essential to the thesis (obviously) and they were fun people to spend several weeks in the north of Sweden with. Also essential to the thesis were UEA hpc, who have helped me to install, debug and run my model on GRACE, and to all the poor helpdesk people who fielded my confused emails when things weren't working with my model, the ECMWF data or anything else!

My family didn't blink when I announced I was going to do a PhD, and I hope I've made them proud. I need to thank my parents for helping me move to Norwich (including driving the van with my furniture) and not questioning me too often about when I was going to get a real job. I need to thank all those who have encouraged me, my grandparents, my Grandmother who improved my ability to explain science to people who have absolutely no clue about what I do, my Tadcu who hasn't seemed too jealous of my travels and my Nan, who just doesn't seem to let much stop her! And thanks too to Mr Thorn, who always did want me to get a first.

Many people in Norwich need thanking. Nick and Andy who showed me that you don't need to be a complete geek to get a PhD. Honza who provided beer and toasties at happy hour. Karin who instilled a belief in lunch breaks and not working late (and taught me about Dutch toast-sprinkles). Celine for being slightly scary. Tahmeena, Louise and Ruth who have been friends and supports over cups of tea and cake. Umberto for being good for a chat. Rich for the tea breaks, help with making nice plots and listening while I thought out loud. Osgur for being up for beers. Luke and

Kat for board games and watching Eurovision. Dave, for more tea breaks and good discussions. Lauren who was so lovely to have in the office even for a short time. And George who kept the office lively in the summer. Also anyone else who has been there for a moan, a beer, a board game night or a cup of tea during my time doing the PhD.

The most important person who needs thanking is Chris, who started by teaching me about the weather and helping me set up WRF, and has become my best friend and biggest support through all the trials and tribulations of doing my PhD. I think he is the best person in the world. Reader, I married him.

CONTENTS

LIST OF FIGURES

LIST OF TABLES

LISTS OF SYMBOLS AND ACRONYMS

Table 1: Variables, names, units and value (if standard) - Greek

Symbol	Name	Units	Value
α	Albedo		0-1
α_H, α_M	Non dimensional stability functions for QNSE-EDMF		
γ	Environmental lapse rate	$\mathrm{K\,m^{-1}}$	
γ_C	Correction term for non-local eddies		
γ_d	Dry adiabatic lapse rate	$\mathrm{K\,m^{-1}}$	
ϵ	Eddy Dissipation		
θ	Potential Temperature	K	
θ_e	Equivalent potential temperature	K	
κ_C	Eddy diffusivity coefficient		
λ	Slope of particle size distribution		
μ	Shape parameter of particle size distribution		
ψ_H	Stability Correction for heat		
ψ_M	Stability Correction for moisture		
ρ	Air density	$\mathrm{kg\,m^{-3}}$	

Table 2: Variables, names, units and value (if standard)

Symbol	Name	Units	Value
Alt	Altitude	m	
BL_h	Boundary Layer Height	m	
C_{DN10}	10 meter neutral drag coefficient		
$C_{1,2,3,f,N}$	Various constants for QNSE-EDMF		
C_H	Exchange Coefficient	W m^{-2} K^{-1}	
D	Particle diameter	m	
f	Coriolis Parameter	rad s^{-2}	
Fr_*	Velocity based Froude Number		
g	Acceleration due to gravity	m s^{-2}	9.8
GHF	Ground Heat Flux	W m^{-2}	
h	Height of inversion layer	m	
H	Heat capacity for surface skin temperature		
I_t	Ice Thickness	m	
IWP	Cloud Ice Water Path	kg m^{-2}	
k	von Karman Constant		0.4
k_e	Kinetic Energy	kg m^2 s^{-2}	
K_H	Vertical Diffusivity coefficient		
K_M	Vertical Eddy Viscosity		
l	Length Scale	m	
l_B	Blackadar Scale	m	
l_m	Master eddy mixing length scale	m	
l_N	Length Scale limitation due to stable stratification		
l_k	The turbulence Macroscale used in K- $epsilon$ modelling	m	
L	Monin-Obukhov Length Scale	m	
Lat	Latitude	deg N	
L_v	Latent heat of vaporisation	K	
LHF	Latent heat flux	W m^{-2}	
Lon	Longitude	deg E	
LWP	Cloud Liquid water path	kg m^{-2}	
$LW \uparrow (\downarrow)$	Long-wave radiation upwards (downwards)	W m^{-2}	
M	Moisture Flux	kg m^{-2} s^{-1}	
M_{avail}	Moisture availability		0-1
M_{ij}	The Tranilient Matrix for ACM2		
N^{-2}	Brunt-Väisälä Frequency	s^2	
N_0	Intercept of particle size distribution		
P	Air Pressure	hPa	
P_s	Production of TKE by shear		
P_b	Production of TKE by buoyancy		
q	Specific Humidity	g kg^{-1}	

Table 3: Variables, names, units and value (if standard)

Symbol	Name	Units	Value
Q	Generic mixing ratio	$\mathrm{g\,kg^{-1}}$	
Q_t	Diabatic processes		
Q_{IW}	Cloud ice mixing ratio	$\mathrm{g\,kg^{-1}}$	
Q_{LW}	Cloud liquid water mixing ratio	$\mathrm{g\,kg^{-1}}$	
Q_{TW}	Total water mixing ratio	$\mathrm{g\,kg^{-1}}$	
Q_V	Cloud Vapour mixing ratio	$\mathrm{g\,kg^{-1}}$	
Q_{flx}	Moisture flux	$\mathrm{kg\,m^{-2}\,s}$	
R	Specific Gas Constant for Dry Air	$\mathrm{J\,kg^{-1}\,K^{-1}}$	
R_{water}	Specific Gas Constant for water	$\mathrm{J\,kg^{-1}\,K^{-1}}$	
RH	Relative Humidity		%
RH_i	Relative Humidity with respect to ice		%
Ri_b	Bulk Richardson Number		
Ri_{crit}	Critical Richardson Number		
Ri_g	Local Gradient Richardson Number		
S_d	Snow depth	m	
S_k	Empirical constant in MYJ scheme		
SHF	Sensible Heat Flux	$\mathrm{W\,m^{-2}}$	
$SW \uparrow (\downarrow)$	Short wave radiation up (down)	$\mathrm{W\,m^{-2}}$	
T	Air Temperature	K	
T_{dew}	Dewpoint temperature	K	
T_{sfc}	Surface temperature	K	
T_r	SW Radiation transmitted beyond the surface $\mathrm{W\,m^{-2}}$		
TKE	Turbulent kinetic energy	m^2/s^2	
u_*	Friction velocity		
u	eastward wind component	$\mathrm{m\,s^{-1}}$	
$\mathbf{U}$	Windspeed	$\mathrm{m\,s^{-1}}$	
v	Northwards wind component	$\mathrm{m\,s^{-1}}$	
$\mathbf{v}$	3D wind vector		
$\mathbf{V}$	Horizontal wind vector		
V_{Nx}	Number weighted terminal particle fall speed for a species x	$\mathrm{m\,s^{-1}}$	
V_{qx}	Mass weighted terminal particle fall speed for a species x	$\mathrm{m\,s^{-1}}$	
w	Vertical wind component	$\mathrm{m\,s^{-1}}$	
w_m	Convective Velocity Scale	$\mathrm{m\,s^{-1}}$	
W_d	Wind Direction	°N	
z_0	Roughness length	m	
z_{0h}	Thermal roughness length	m	
$z_{1/2}$	Half model layer between surface and z_1		
z_1	Lowest model level		
z_{eff}	Effective roughness length	m	
z_{mix}	Model level at the top of the mixing layer		

Table 4: Acronyms A - L

2D-S	Two-Dimensional Stereoscopic Probe
ACCACIA	Aerosol-Cloud Coupling And Climate Interactions in the Arctic
ACM2	Asymmetric Convective Model v.2
AIDJEX	Arctic Ice Dynamics Joint Experiment
AOE	Arctic Ocean Experiment
ARCMIP	Arctic Regional Climate Model Intercomparison project
ARCPAC	Aerosol, Radiation and Cloud Processes affecting Arctic Climate
ARW	Advanced Research WRF
ASCOS	Arctic Summer Cloud Ocean Study
BASE	Beaufort Arctic Storms Experiment
BASIS	Baltic Air-Sea-Ice Study
BL	Boundary Layer
CAO	Cold Air Outbreak
CCN	Cloud Condensation Nuclei
CDP	Cloud Droplet Probe
CIBL	Convective Internal Boundary Layer
COAMPS	Coupled Ocean/Atmosphere Mesoscale Prediction System
ECMWF	European Centre for Medium-range Weather Forecasting
ERA-interim	ECMWF ReAnalysis - Interim
EUMETSAT	European Organisation for the Exploitation of Meteorological Satellites
FIRE-ACE	First ISCCP Regional Experiment - Arctic Cloud Experiment
GABLS	GEWEX Atmospheric Boundary Layer Study
GEWEX	Global Energy and Water Cycle Experiment
IGBP	International Geosphere-Biosphere Programme
IN	Ice Nuclei
ISCCP	International Satellite Cloud Climatology Project
FAA	Federal Aviation Administration
FAAM	Facility for Airborne Atmospheric Measurements
FYI	First Year Ice
LEADEX	Arctic Leads Experiment
LSM	Land Surface Model

Table 5: Acronyms M - Z

M-PACE	Mixed-Phase Arctic Cloud Experiment
MASIN	Meteorological Airborne Science INstrumentation
MetUM	Met Office Unified Model
MIZ	Marginal Ice Zone
MIZEX	MIZ Experiment
MM5	Mesoscale Model v.5
MODIS	Moderate Resolution Imaging Spectroradiometer
MYI	Multi Year Ice
MYJ	Mellor-Yamada-Janjic
NCEP	National Centre for Environmental Prediction
NOAA	National Oceanic and Atmospheric Aviation
NWP	Numerical Weather Prediction
OSI-SAF	Ocean and Sea Ice Satellite Applications Facility
OSTIA	Operational Sea Surface Temperature and Sea Ice Analysis
PBL	Planetary Boundary Layer
PWRF	Polar WRF
QNSE- EDMF	Quasi-Normal Scale Elimination - Energy Density Mass Flux
RANS	Reynolds-Averaged Navier Stokes equations
SHEBA	Surface Heat Budget of the Arctic
SSTs	Sea Surface Temperatures
STABLE	Spring Time Atmospheric Boundary Layer Experiment
WMO	World Metererorological Organisation
WRF	The Weather Research and Forecasting model
YSU	Yonsei University

1

INTRODUCTION

1.1 THE RAPIDLY CHANGING ARCTIC

The world is warming up. The planet is now 0.78°C warmer than in the period 1850-1900 (Pachauri *et al.*, 2014). Perhaps the most obvious visible impact of this warming is the reduction in sea ice cover in the Arctic. Multi-year ice (MYI) is declining rapidly, with a 17.3% reduction in area in the last ten years (Comiso, 2012). The sea ice is getting thinner, with a decrease in mean winter thickness from 3.64m in 1980 to 1.89m in 2008 (Kwok & Rothrock, 2009). There is also an ongoing shift in the Arctic sea ice cover from MYI to seasonal ice, which does not persist in the summer (Perovich & Polashenski, 2012). This loss of sea ice leaves the Arctic increasingly vulnerable to change. This is due to interactions between increased temperatures, sea ice and snow cover. The enhanced warming of the Arctic due to these interactions is termed Arctic amplification (Serreze & Francis, 2006).

For those who call the Arctic home, this is greatly concerning, with the indigenous Saami and Inuit expressing concern over the impact of sea ice loss on their livelihoods (Larsen *et al.*, 2014). Polar bears rely on the thick ice for their hunting and are showing increased fasting which has been attributed to large scale changes in sea ice composition (Cherry *et al.*, 2008). In fact in the western Hudson Bay, polar bear populations could struggle to continue beyond 2050 (Castro de la Guardia *et al.*, 2013).

However an increase in the length of ice free periods benefits shipping with shorter Northern routes safer for longer periods of time. Also resources such as oil and minerals which were previously inaccessible will become available (Larsen *et al.*, 2014). Changes in marine traffic may well bring jobs and new infrastructure to the Arctic, but could also have a negative impact through increases in pollution.

It is therefore of utmost importance that we are able to predict both the short term weather of the Arctic for those who live and work there, and that we are able to make predictions about the future state of the Arctic with increasing global temperatures.

1.2 THE MARGINAL ICE ZONE AND ITS COMPLEX SYSTEM

The area where the sea ice and open ocean meet is known as the Marginal Ice Zone (MIZ) and is defined by the World Meteorological Organisation (WMO) as,“the part of the sea ice which is affected by the waves penetrating into the ice”. The stress of the ocean swell on the ice gives rise to features like leads, which are gaps or cracks in the sea ice, and the action of the wind on the surface can cause the ice floes to raft on each other.

During the autumn ice is formed at the MIZ, new ice includes frazil ice, grease ice, slush and shuga which are all composed of ice crystals which are loosely frozen together. At the beginning of freezing frazil ice forms, these are fine bits of ice, suspended in the water, which then coagulate into grease ice, forming a layer on the surface. The grease ice is dark but matt, meaning the surface reflects less light and will absorb more heat from the sun. If heavy snowfall has occurred snow clumps can float on the sea surface as slush. The slush and grease ice can coagulate forming shuga which is defined as an accumulation of white lumps floating on the sea surface.

As the freezing continues the grease ice, which is comprised of separate flakes, becomes a thin, elastic crust of ice known as nilas. Nilas can flex with the waves, is thin (up to 10 cm) and becomes whiter the thicker it is with dark nilas being up to 5 cm thick and light nilas being whiter and over 5 cm thick.

Ice which is transitioning from nilas to first year ice is known as young ice. As it freezes the sea ice becomes thicker, less elastic and lighter coloured. Grey young ice (less than 15 cm thick) will raft under pressure, that is the sheets of ice will crack and

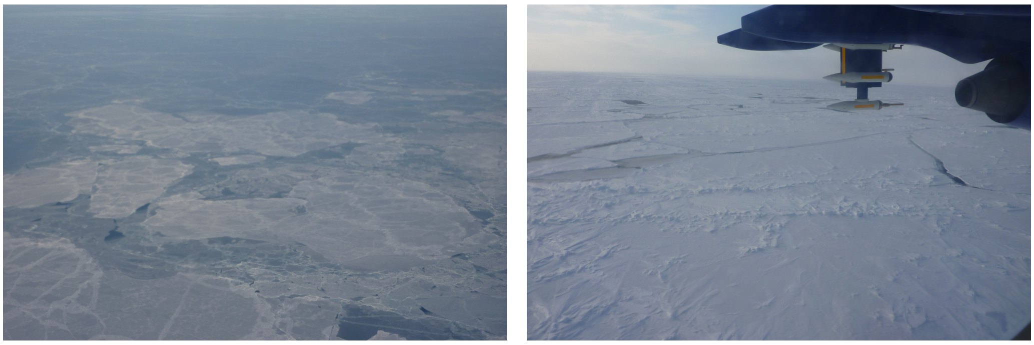

(a) Thin, dark young sea ice which is overlapping (rafting).

(b) Larger, thicker white floes with small leads.

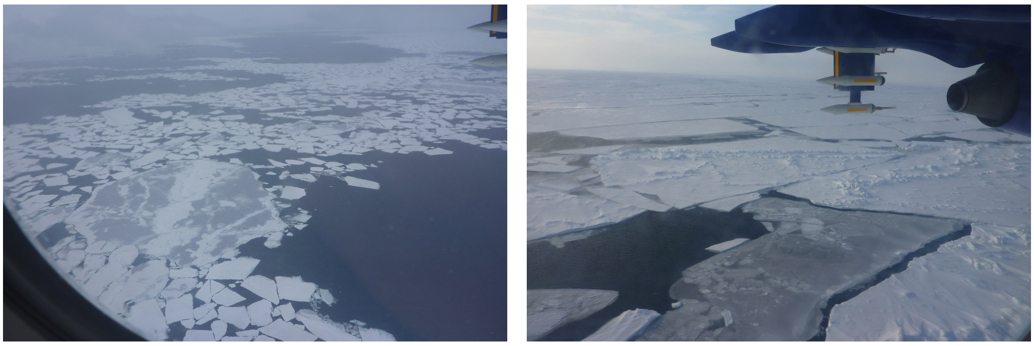

(c) Small floes, moving freely with large amounts of open water.

(d) Floes with open leads and darker ice within the leads.

Figure 1.1: Various states of sea ice in the MIZ seen during the ACCACIA campaign. Photos taken by the author.

then overlap as in Fig. 1.1a, while grey-white ice (15 to 30 cm thick) is more likely to ridge, i.e. form elevated banks, when placed under pressure.

Ice which has not had more than one winter's growth is known as first year ice (FYI), this is the continuation of freezing from the young ice. FYI is between 30 cm and 2 m thick. The thicker the ice is the more likely it is to last through the summer melt, becoming old ice. Sea ice which has survived many seasons is known as multi year ice (MYI) and can be 3 m thick or more.

The sea ice does not stay as one solid covering of ice. The action of wind and waves causes the sea ice to crack and forms ridges or raft on top of other ice. Openings which form within the ice are termed leads, and look like cracks as seen in Figs. 1.1b and 1.1d. Any chunk of sea ice can be termed a floe, the smaller floes can float with large amounts of open water around them in a formation known as open ice (Fig. 1.1c), or if there is less open water, close ice.

Due to the warming climate more of the sea ice cover is made up of thin first year ice now than in the past (Nghiem *et al.*, 2007; Comiso, 2012). The fraction of total ice extent made up of MYI in March has decreased from around 75% in the mid-1980s to 45% in 2011, while the proportion of the oldest ice (+5 years) has declined from 50% of the MYI to 10% (Maslanik *et al.*, 2011).

The sea ice surface in the MIZ is very complex, formed of many different types of sea ice, these move under the influence of the wind and waves, but also influence the atmosphere above. The linking between atmosphere and surface is very important and comprises many processes, which are discussed below.

1.3 ATMOSPHERIC BOUNDARY LAYER

Defining exactly what the boundary layer is in an atmospheric context can be difficult, one good definition can be found in Garrat (1992), " the atmospheric boundary layer can be defined as the layer of air which is directly above the Earth's surface in which the effects of the surface (heating, cooling, friction) are felt directly on time scales less than a day, and in which significant fluxes of momentum, heat, or matter are carried by turbulent motions on a scale of the order of the depth of the boundary layer, or less." The boundary layer (BL) plays an important role in many fields, such as air pollution, agricultural meteorology, aeronautics, hydrology, mesoscale meteorology, weather forecasting and climate. For pollution and air quality it is the ability of the BL to transport and disperse pollutants which is important, while for aircraft safety features such as low clouds, high wind events and high turbulence can be of particular interest. Agricultural interest stems from the processes such as evaporation and frost formation which occur in the BL, as well as the surface energy balance. In numerical weather prediction (NWP) and climate simulations the atmospheric models depend on a realistic representation of the processes occurring in the BL. The BL affects both the dynamics, by friction causing the loss of kinetic energy, and thermodynamics of the atmosphere by heating and cooling. The BL is also affected by both the dynamics and thermodynamics of the wider atmosphere, making it a very important component of NWP and climate simulations.

The BL can have different vertical potential temperature structures depending on external forcing. Idealised BL profiles are shown in Fig. 1.2, a is taken to be typical of a profile over solid ice where the potential temperature gradient may always be positive (warmer at higher altitudes) as the surface is colder than the air above, the BL

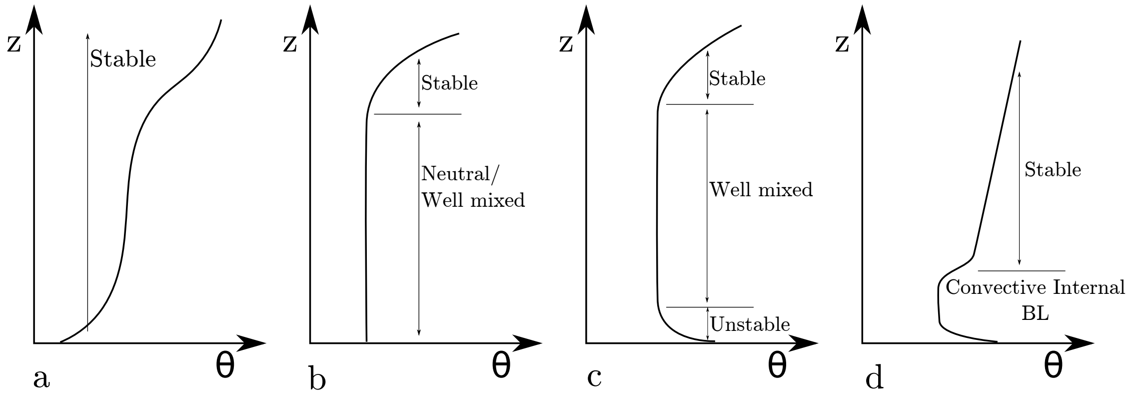

Figure 1.2: Different BL structures. a. shows a stable BL ,b a neutral or well mixed BL ,c shows a typical convective BL ,d shows a convective internal BL. The horizontal line marking the change to stable is the start of the capping inversion.

is known as stable, as any vertical motion of air will be impeded by the stratification. Figure 1.2.b shows a neutral layer, where strong winds have mixed the stable BL so the surface is the same potential temperature as the air. Over the open water, a convective BL is seen as in Fig.1.2.c, now the surface is warmer than the atmosphere so the gradient is negative and thus unstable, any air which rises can continue unimpeded until the stable layer which is known as a capping inversion. An unstable boundary layer could also form over the solid ice, if the air advected over is sufficiently cold meaning the surface is warmer than the air above. The height of the boundary layer is defined here as the start of the capping inversion. Over the MIZ a convective internal BL (CIBL) may be seen, this is where the very bottom of the stable atmosphere is warming and forms a convective BL, this decouples the stable atmosphere above from the surface below. An internal BL is associated with the horizontal advection of air across a discontinuity in the surface such as a change in roughness, temperature, humidity or surface flux (Garratt, 1990; Chechin *et al.*, 2013). The CIBL could grow upwards by entrainment, mixing downwards, of the air above the capping inversion and become a standard convective BL or even totally well mixed. As air travels from the sea ice to the open water, the change in surface forcing can lead to a dramatic deepening of the BL (Renfrew & Moore, 1999).

The BL is a turbulent place, full of swirling, whirling air. These swirls are known as eddies, and can exist in many sizes, from microscopic to almost the whole height of the BL, and larger eddies will cause smaller eddies in a form of turbulent cascade. The mixing caused by the turbulence increases the transport of heat, moisture and cloud condensation nuclei upwards (Anderson & Neff, 2008). This upwards transport

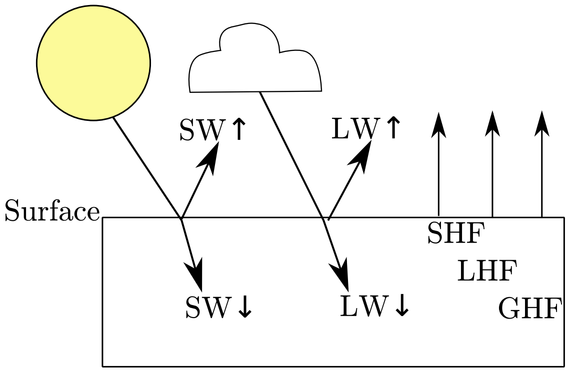

Figure 1.3: Simple schematic of the surface energy budget, the SW radiation originates from the sun, while the LW from clouds, the atmosphere and the surface. The arrows are not representative of magnitude.

means that by coupling the atmosphere to the surface, the BL allows sea ice anomalies to influence the entire atmospheric column (Rinke *et al.*, 2006).

1.4 SURFACE FLUXES AND THE SURFACE ENERGY BALANCE

The turbulence in the BL transfers heat, moisture and other quantities, this transfer is known as a flux. The eddies can move warm, moist air from the surface to the atmosphere, or move warm, moist air from the atmosphere downwards to the surface (Wallace & Hobbs, 2005a). In the MIZ where there are areas of open water the fluxes of sensible and latent heat and moisture between the atmosphere and ocean can be large when compared to that over the ice. The sum of the heat fluxes make up the surface energy budget. As energy cannot be created or destroyed, the energy from the sun which reaches the surface must be either absorbed or transferred. A schematic diagram is shown in Fig. 1.3. The energy from the sun is short wave radiation, $SW\downarrow$ with the arrow indicating its direction. The surface reflects some of the energy back up, denoted $SW\uparrow$, with the amount dependent on the albedo (α), the reflectivity of the surface ($\alpha = SW\uparrow/SW\downarrow$). The atmosphere and clouds emit long wave radiation downwards to the surface $LW\downarrow$, the surface also emits long wave radiation upwards, $LW\uparrow$. Turbulent heat fluxes of sensible and latent heat are represented by SHF and LHF (positive upwards), while a heat flux through the ground or sea ice can be termed the ground heat flux (GHF). A change in temperature of the surface can then be represented using the surface energy balance, where c is the heat capacity of the ground,

$$c\Delta T = SW\downarrow - SW\uparrow + LW\downarrow - LW\uparrow - SHF - LHF - GHF. \tag{1.1}$$

As leads are a source of heat, they are important for the surface heat budget of the whole Arctic; during most of the year sensible and latent heat fluxes from leads can be up to two orders of magnitude greater than fluxes from the surrounding ice pack, and these are one of the biggest terms in the heat budget (Andreas *et al.*, 1979). The increased fluxes in the MIZ can also have an impact on great distances away, for example via the intensification of polar lows (Bracegirdle & Gray, 2009).

Field observations have confirmed that heat fluxes are sensitive to lead width and wind speed, with wider leads and higher wind speeds giving higher heat fluxes. Fluxes of sensible heat have been found to be 30 Wm^{-2} from a narrow lead and 170 Wm^{-2} downwind of a wider lead (Ruffieux *et al.*, 1995; Persson *et al.*, 1997). Observed latent and sensible heat is also up to two orders of magnitude larger over leads than solid sea ice, as the sea ice shields the atmosphere from the warmer surface (Pinto *et al.*, 2003). Fluxes over the MIZ can be high, the Spring Time Atmospheric Boundary Layer Experiment (STABLE) campaign investigated fluxes from leads with varying ice cover. They observed sensible fluxes as high as 180 Wm^{-2} and found that the fluxes are sensitive to the newly forming ice cover in the leads (Tetzlaff *et al.*, 2015).

The transfer of moisture from the surface to atmosphere is also important, in Renfrew & Moore (1999) the air downwind of the ice edge had high heat fluxes of 500 W m^{-2} for SHF and 100 W m^{-2} for LHF. The LHF is related to the flux of moisture by multiplying the moisture flux by the latent heat of vaporisation. This leads to a dramatic deepening of the BL, which rises by about 950 m over a 380 km cross section. The moisture flux allows clouds to form off ice.

1.5 ARCTIC CLOUDS

The fluxes of heat and moisture over the MIZ are important for cloud formation, under ideal conditions clouds forming above a lead may extend hundreds of kilometres downstream (Gultepe *et al.*, 2003). Clouds are an important component of the radiative energy budget of the Arctic as they reflect short wave and emit long wave radiation (Sedlar *et al.*, 2011). This means that they can act to cool or warm the surface, Intrieri *et al.* (2002) found that clouds act to warm the Arctic surface for most of the year, with a short period of cooling in the middle of summer. However the impact of clouds on the surface depends not just on the amount of clouds but also on their properties: cloud base height, the amount and phase of the cloud water and content of ice water. Liquid clouds dominate both the long and short wave radiative impacts on the surface. Due to the presence of temperature inversions in the BL, Arctic clouds are often warmer than the surface (Shupe & Intriei, 2003) meaning they act to warm the surface. The longwave warming is often dominant in the Arctic due to the surface albedo being high, meaning that much of the incident shortwave radiation is reflected away from the surface.

The onset of the sea ice melt in the spring is controlled by clouds and albedo (Persson, 2012). However cloud cover may also act to shade the surface from incoming solar radiation so in a situation with a reduced ice extent cloud cover could act to cool the surface (Serreze & Francis, 2006). This complexity means that clouds are a major source of uncertainty in the Arctic. They are however so important for the BL that they may have a bigger impact on the BL than the surface as radiative cooling at the top of the clouds helps to drive turbulence in the boundary layer below, through buoyancy flux (Curry *et al.*, 1988; Zuidema *et al.*, 2005).

The phase of the water in clouds is important, with liquid having a bigger radiative impact than ice (Shupe & Intriei, 2003), however most clouds in the Arctic are mixed phase (ice and supercooled liquid water). Mixed-phase clouds occur frequently all year round in the Arctic and they often persist for many days at a time (Morrison *et al.*, 2012). These clouds are so frequently seen in the Arctic in part due to their persistence. They can persist under a variety of conditions including weak synoptic scale forcing and large scale subsidence (they do not require synoptic scale upwards motions that are associated with cyclones and fronts) (Pinto, 1998; Zuidema *et al.*, 2005) The persistence of these mixed-phase clouds is surprising, considering the mixture of supercooled liquid water and ice is unstable, one would expect all the water to freeze into ice very quickly. The Wegner-Bergeron-Findeisen (WBF) mechanism describes the growth of ice by vapour deposition at the expense of liquid (Wallace & Hobbs, 2005b) and why one would expect them to rapidly become fully glaciated.

There is a complex web of interactions which makes it difficult to find out why and how these mixed phase clouds persist. Turbulence and cloud scale upwards motion seem critical in maintaining mixed phase clouds under weak synoptic scale forcing (Shupe *et al.*, 2008). For example, supercooled liquid water leads to strong cloud top radiative cooling (exceeding 60 K per day at cloud top) (Pinto, 1998). The cooling at the top leads to decreased static stability, as the cold air will sink downwards, and thus buoyant production of turbulent updrafts is reduced, along with the growth of cloud droplets by condensation (Solomon *et al.*, 2011). In the Arctic there is often a moisture inversion above the cloud due to the advection of moist air. This means turbulent entrainment of air from above the cloud actually moistens the cloud layer and helps to sustain it even when it is near-continually losing mass by ice precipitation (Solomon *et al.*, 2011) Consequently a cloud which is de-coupled from the surface can maintain itself through these processes.

Clouds which are coupled to the surface can sustain themselves by feedbacks which involve the surface. Supercooled liquid water can induce surface LW warming and atmospheric cooling, decreasing stability and increasing fluxes of heat and moisture. The magnitude of these fluxes depends on surface type, as open water will provide more moisture than solid ice (Zuidema *et al.*, 2005). Atmospheric aerosol (minute particles) can also influence the persistence of Arctic mixed phase clouds by affecting cloud microphysical characteristics, by making ice more likely to form. Ice formation in the temperatures of a mixed phase cloud (-40 to 0°C) involves a subset of aerosol particles with heterogeneous ice-nucleating (IN) properties (Wallace & Hobbs, 2005b). There are far fewer IN than cloud condensation nuclei (CCN, like IN but for liquid) The concentration of ice particles and hence IN is important for mixed phase clouds as it impacts the WBF process, making it easier to form ice at warmer temperatures (Pinto, 1998; H. *et al.*, 1999). Changes in the CCN can also change the radiative impact of clouds. Increased aerosol associated with transport from mid-latitudes increases cloud droplet concentration and thus LW emissivity of thin clouds. The subsequent increase in $LW\downarrow$ can result in surface warming (Wang *et al.*, 2001), which could increase turbulent fluxes and provide a greater source of moisture. This could increase the cloud fraction, which may in turn warm the surface (Curry *et al.*, 1996). Clouds are very important for the Arctic, but with so many processes involved their impact on the surface under the conditions of decreasing amounts of sea ice is still uncertain.

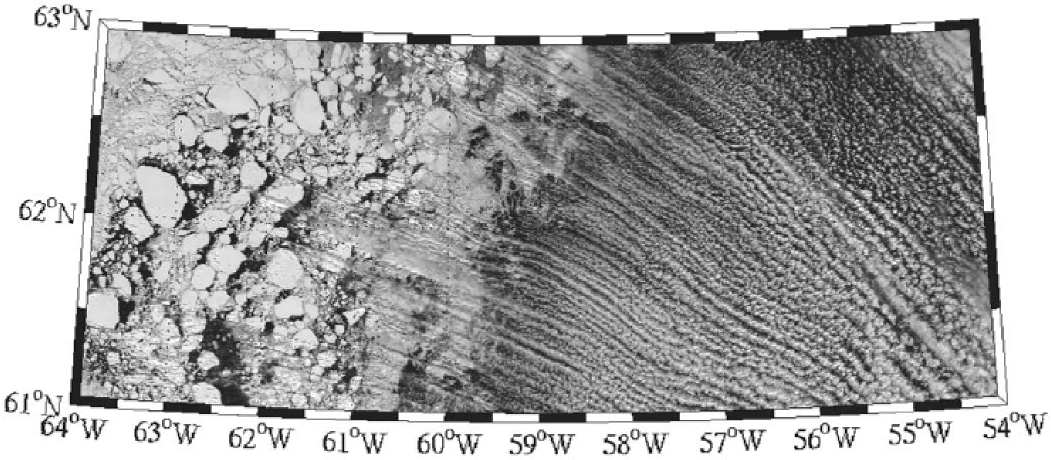

Figure 1.4: MODIS image of cloud streets from 12 April 2002, shows the organisation of convection into roll clouds over and downstream of the MIZ of the Labrador Sea, from Liu *et al.* (2006).

1.6 COLD AIR OUTBREAKS

The interaction between surface, boundary layer and clouds is particularly important during a cold air outbreak (CAO), which is when cold, dry air flows equator-ward from the Arctic. As the CAO travels south, the surface beneath changes substantially from the solid MYI to the more complex MIZ and finally becomes open ocean. When the cold, dry air meets the warm, moist open water within the MIZ the surface changes the atmosphere as heat and moisture and momentum can all be transferred upwards between the surface to the atmosphere (Liu *et al.*, 2006). The transfer of heat and moisture upwards causes the formation of mesoscale shallow convection, which is convection that is 1 to 2 km deep and has a horizontal length scale of between one to a few tens of kilometres (Atkinson & Zhang, 1996). The mesoscale shallow convection is important for the occurrence of Arctic stratocumulus clouds and the transport of the heat, moisture and momentum between the BL into the free atmosphere. One form the clouds take is distinctive bands, or cloud streets, forming over and downwind of the MIZ, often parallel to the wind direction, as can be seen in Fig. 1.4. The sea ice surface in the MIZ is important for the formation of these clouds off the ice edge, along with the high sensible and latent heat fluxes (Gryschka *et al.*, 2008).

The transfer of heat from ocean to atmosphere can trigger convective activity, which may impact the formation of polar mesoscale cyclones otherwise known as

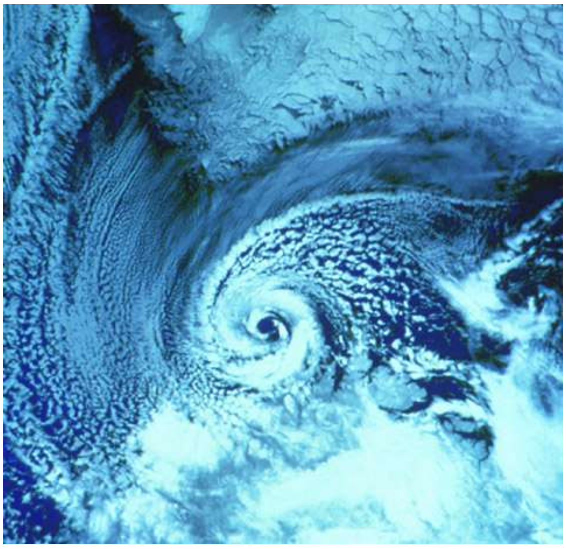

Figure 1.5: A NOAA-9 polar orbiter satellite image (visible band) of a polar low over the Barents Sea on 27 February 1987. The southern tip of Svalbard is visible at the top of the image. Public Domain, https://commons.wikimedia.org/w/index.php?curid=848445

a polar low as seen in Fig.1.5, (Moore *et al.*, 1996). Polar lows small, short lived low pressure systems occurring at high latitudes. Polar lows are difficult to forecast, which is a problem as a particularly active low can cause damage and even loss of life if they impact coastal communities (Rasmussen & Turner, 2003). Strong surface temperature gradients associated with the change in sea ice cover, along with low level shear caused by winds can cause a baroclinic zone to form, this is where the temperature and pressure gradients are not parallel to each other, and the resulting instability can cause polar lows to form (Rasmussen & Turner, 2003). Strong fluxes of heat from the ocean to the atmosphere which can occur during these lows cool the surface and cause ice to form, as the ice rejects the salt when it freezes, this creates brine which then increases the salinity and thus the density of the water, triggering overturning which can impact ocean deep convection (Renfrew & Moore, 1999).

Changes in ice cover in the MIZ can strongly influence local temperature conditions, by removing the insulation between surface and atmosphere, this is particularly important for CAOs, as larger areas of open water may lead to deeper BLs and thicker cloud layers, impacting the surface energy balance (Tetzlaff *et al.*, 2014). The turbulent heat fluxes off the sea ice edge during CAOs are the major contributor to the surface energy balance, with stronger CAOs (larger difference between air and ocean temperatures) having bigger fluxes (Papritz *et al.*, 2015).

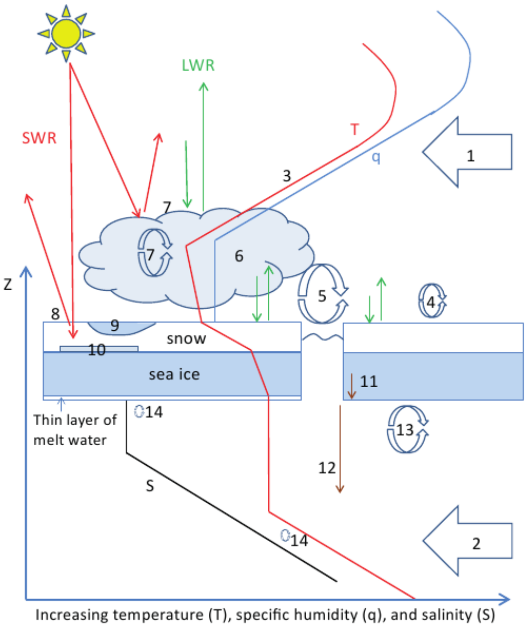

Figure 1.6: A schematic of processes in the MIZ, from Vihma *et al.* (2014). The vertical profiles of temperature T, specific humidity q and salinity S are shown along with processes which are numbered as follows. 1 - Advection of heat and moisture to the Arctic. 2 - Oceanic advection of heat and salt to the Arctic. 3 - Generation of temperature and humidity inversions. 4 - Turbulence in the stable boundary layer. 5 - Convection over leads. 6 - Cloud microphysics. 7 - Cloud, radiation and turbulence interactions. 8 - Reflection and penetration of solar radiation in snow/ice. 9 - Surface melt. 10 - Formation of superimposed ice and snow ice. 11 - Gravity drainage of salt in sea ice. 12 - Brine formation. 13 - Turbulent exchange of momentum, heat and salt during ice growth. 14 - Double diffusive convection.

1.7 FEEDBACKS

The processes occurring around the MIZ do not happen in isolation, each element impacts on the others in a variety of ways. A schematic of the processes is in Fig. 1.6. The advection of air is represented by process 1, the heat and moisture fluxes which form the clouds are represented by processes 4 and 5. Then as the clouds form, they interact with the radiative energy balance (processes 6, 7, 8). If the surface begins to melt then there is a freshening of the water below, while during freezing more salt is added and turbulent exchange of momentum, heat and salt takes place in the ocean (13, 14). The interactions between processes are termed feedbacks, with a positive feedback being one where a change in one quantity acts to increase another process or quantity, and enhance the original change and a negative feedback being the opposite.

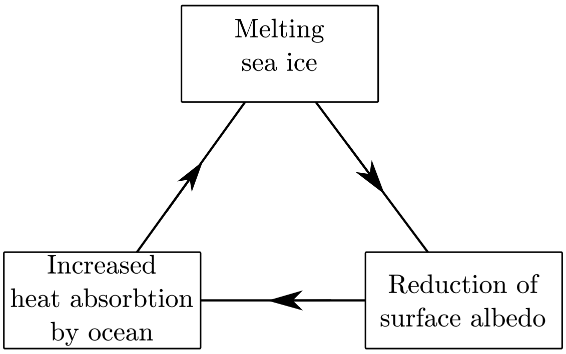

Figure 1.7: The ice albedo feedback, after (Serreze & Francis, 2006). This shows a positive feedback loop.

One important feedback mechanism is the ice-albedo feedback which is shown schematically in Fig. 1.7. As the sea ice is warmed and melted, the albedo is lowered by the presence of melt ponds on the ice and open water in leads. The reduction in albedo means that more solar radiation can be absorbed. The areas of warmer water can then act on the sea ice, further increasing melting. In areas with leads this is enhanced by the increased surface area of ice at the lead edge which is exposed to the warmer water. Increased sea surface temperatures are particularly problematic in the polar night, where there is no incoming solar radiation. The heat capacity of the water means that the ambient air temperature is warmer in areas where there is more open water. Higher temperatures in the winter can delay the onset of freezing, which also further reduces the sea ice cover for the next year. The feedback loop is then complete, as this extra reduction in sea ice now enhances the melting and decreases the albedo.

The clouds, being such an important component of the energy balance also impact on the surface, which in turn impacts the clouds. Figure 1.8 shows the processes included in the cloud-radiation feedback. If the sea ice melt is enhanced, then this will increase the heat and moisture fluxes from the surface to the atmosphere, increasing the atmosphere temperature and humidity. The enhanced fluxes also bring CCN upwards, increasing cloud optical depth and cloud fraction. The cloud then may warm or cool the surface, further enhancing sea ice melting or acting to slow melting. More information on this fascinating yet complex area of feedbacks can be found in Vihma *et al.* (2014) and Curry *et al.* (1996).

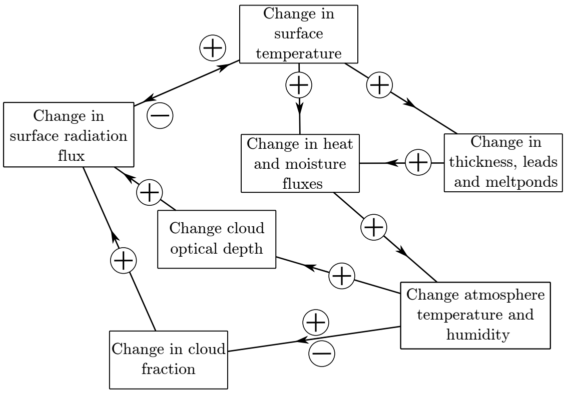

Figure 1.8: The cloud-radiation feedback, after (Curry *et al.*, 1996). The plus and minus symbols indicate the possible change caused in the next part of the system. Where both are shown either the impact is unknown, or could be in both directions depending on the initial change in surface temperature.

1.8 THESIS PLAN

The complexity and interconnectedness of the processes occurring in and over the MIZ means it is difficult to accurately simulate this area in Numerical Weather Prediction (NWP) or in climate simulations. As many of these processes are small scale (less than a kilometre) then to include them in a model the process needs to be parametrised. In the past global climate or NWP forecasts have not paid enough attention to the problem of parametrisation in the Arctic, but the situation is improving, driven by our need to understand what will happen in the Arctic with climate change (Vihma *et al.*, 2014). Indeed prediction of cloud is thought to be the biggest source of error in climate forecasts, due to the difficulty in understanding the numerous processes (Stocker *et al.*, 2013).

The Arctic is an area of utmost importance, which is changing rapidly as the climate changes. The number of interlinking processes makes the MIZ a challenge to numerical weather prediction models, and the inaccessibility means there is a lack of observations. This thesis aims to examine the MIZ and the processes which occur in the atmosphere using a combination of modelling and observations. Firstly in Chapter 2 the weather research and forecasting model (WRF) which will be used in this thesis is introduced and the important parametrisation schemes are discussed in detail. Then in Chapter 3, the question of what happens over the MIZ if the sea ice becomes thinner will be addressed using a series of idealised experiments using WRF, with the aim of recommending whether sea ice thickness needs to be included in weather and climate models. Observations are the subject of Chapter 4, where a brief history of Arctic field campaigns is given, providing context to the Aerosol-Cloud Coupling Climate Interactions in the Arctic (ACCACIA) field campaign. Then two cases are selected and will be discussed in depth. This provides background to the following chapters. The case studies are discussed in Chapters 5 and 6, where simulations with the WRF model are compared to observations. In Chapter 5 four different BL parametrisations are tested against both cases, to establish if there is a best parametrisation for use in the Arctic. Then following this, Chapter 6 investigates whether the representation of sea ice in the model is a bigger influence on the prediction of the BL than the choice of BL parametrisation scheme. Finally in Chapter 7 the whole thesis is summarised and recommendations as to future work are made.

2

MODEL DESCRIPTION

The Weather Research and Forecasting (WRF) model is a mesoscale model designed to be used for both research and weather prediction (Skamarock & Klemp, 2008). WRF is a fully compressible, non-hydrostatic model using a terrain following, dry hydrostatic-pressure vertical coordinate and Arakawa C-grid staggering for the horizontal coordinates. The time-split integration is performed using a 2nd or 3rd order Runge-Kutta scheme with a smaller time step for acoustic and gravity-wave modes. The Advanced Research WRF (ARW) dynamics solver integrates the compressible, non-hydrostatic Euler equations which have been cast into flux form. The prognostic equations solve for velocity components u and v in Cartesian coordinates, vertical velocity w along with perturbations in θ, geopotential and pressure.

Users of, and contributors to WRF include the National Center for Atmospheric Research (NCAR), the National Oceanic and Atmospheric Aviation (NOAA), the Naval Research Laboratory and the Federal Aviation Administration (FAA). A polar version of WRF (Polar WRF, hereafter PWRF) is developed and maintained by the Polar Meteorology Group at Ohio State University. PWRF includes modifications to the surface energy balance and heat transfer over sea ice, the ability to specify sea ice thickness and to specify snow on sea ice. Some developments, such as the ability to use fractional sea ice, were first made in PWRF before being implemented in the standard WRF release. The development and testing of PWRF is documented in Hines & Bromwich (2008), Bromwich *et al.* (2009), Bromwich *et al.* (2013) and Hines *et al.* (2015) among others. PWRF has also been used in sensitivity studies such as Tastula *et al.* (2012), Kilpeläinen *et al.* (2012) and Valkonen *et al.* (2014). This work uses PWRF version 3.5.1.

To use PWRF, data is needed to both act as initial conditions and to provide the boundary conditions. For the atmosphere ERA-interim data is used, following Bromwich *et al.* (2013). Produced by the European Centre for Medium-Range Weather Forecasts (ECMWF), ERA-interim is a global atmospheric reanalysis product (Dee *et al.*, 2011). The spatial resolution of the data set is approximately 80 km (T255 spectral) on 60 vertical levels from the surface up to 0.1 hPa, data is provided at six hourly temporal resolution and can be interpolated onto a number of different grids, with the 0.25° × 0.25° resolution being used here.

While ERA-interim can provide sea surface temperatures (SSTs) and sea ice fraction, a higher resolution product was required for these simulations. The Operational Sea Surface Temperature and Sea Ice Analysis (OSTIA) dataset is provided by the Met Office and produces daily fields of SST and sea ice at a 1/20° resolution. The OSTIA dataset can be accessed at marine.copernicus.eu. Sea ice fraction is from the European Organisation for the Exploitation of Meteorological Satellites (EUMETSAT) Ocean and Sea Ice Satellite Applications Facility (OSI-SAF), while SSTs are derived from both satellite observations and in-situ data from drifting buoys. OSTIA is used in all forecast models at the Met Office and at the ECMWF.

WRF (and by extension PWRF) has a modular approach to model physics parametrisations. As this work includes sensitivity studies including the surface and boundary layer representation, as well as an analysis of clouds produced by the model, a brief discussion of these various physics options are detailed below. The model set up and boundary conditions used will be discussed in Chapter 3 for the idealised work in Chapters 5 and 6.

2.1 BOUNDARY LAYER PARAMETRISATION

The atmospheric boundary layer is a place where turbulence is of great importance. The flow of air is not smooth over the surface, but chaotic, with interactions on many different scales between the air closer to the surface and the air higher up.

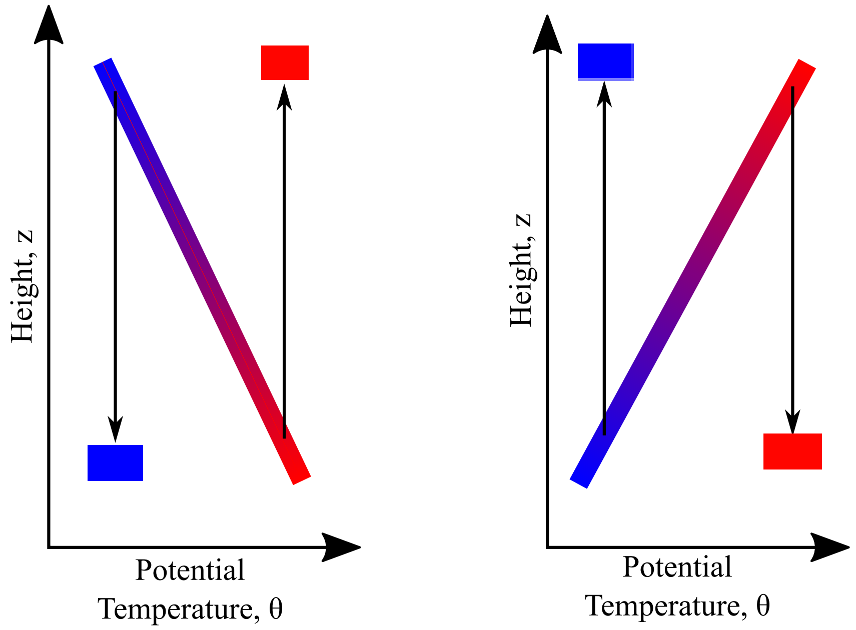

Figure 2.1: Schematic showing the mixing of air in an unstable (left) and stable (right) boundary layer, the warmer air (red colours) is mixed to an area with colder air (blue colours) and vice versa. Diagram after Wallace & Hobbs (2005a).

The turbulence is important for the exchange of heat, moisture and momentum between the surface and atmosphere. Momentum is transferred as the turbulence over surface the causes the air to slow down, losing momentum. Exchange of heat and moisture is achieved by mixing and swirling of the air, what is known as an eddy. A schematic is shown in Fig. 2.1, the vertical motions of the air move the warm air, represented by the red colour, to areas of colder air, represented by the blue colour. The change in potential temperature varies with the turbulent fluctuations of the air. Modelling turbulence is very difficult, the first problem is that turbulence occurs on a scale smaller than the horizontal grid spacing used in numerical weather prediction models, which typically have a grid spacing larger than 1 km. A turbulent eddy could be as large as the model grid spacing, but will spawn smaller eddies, which in turn will create smaller eddies and so on, in a cascade. The size of these eddies is below that of the model grid spacing, meaning that the effect of turbulence needs to be parametrised in the model. That is, the model needs to take into account the effects of turbulence, but without actually computing turbulence directly. The second issue is that attempting to find the equations for turbulence more unknowns are added to the equations, leading to a system which is under described.

In fact, describing turbulence mathematically results in a system of equations with more unknowns than equations. The change in potential temperature (θ) over time (t) seen in Fig. 2.1 can be written as,

$$\frac{\partial \overline{\theta}}{\partial t} = -\frac{\partial \overline{w'\theta'}}{\partial z} + ... \tag{2.1}$$

where the over line denotes an average, and the $\overline{w'\theta'}$ is the covariance of the turbulent contributions of vertical wind and potential temperature. To forecast how the mean potential temperature will change over time, an expression for the heat flux $\overline{w'\theta'}$ needs to be derived. Finding this expression yields another non-linear term,

$$\frac{\partial \overline{w'\theta'}}{\partial z} = -\frac{\partial \overline{w'w'\theta'}}{\partial z} + ... \tag{2.2}$$

The $\overline{w'w'\theta'}$ is the turbulent flux of turbulent heat flux. Each attempt to further describe the turbulence yields another non-linear term, which in turn needs describing and so on. This is known as the turbulence closure problem (Stensrud, 2007).

A boundary layer parametrisation scheme must provide the model with the tendencies (how a variable is changing) of heat and moisture which cannot be modelled directly and to do this the turbulence closure problem must be dealt with. A BL scheme can be categorised by how many of the non-linear terms are retained, if just eqn. 2.1 is used then the closure is first order, if both 2.1 and 2.2 are used then the closure is second order and so on. A half order closure is also possible by using the higher order closure for some terms and not others. A scheme is also classified as local or non-local, a local scheme is one where the flux at a particular location is only dependent on the gradient of the variable (temperature or moisture) at that location, which assumes that only small size eddies exist. A non-local closure is one where the flux at a location depends on transport by a range of eddy sizes, from tiny to eddies which span the whole of the boundary layer.

Four parametrisation schemes are described below, the MYJ which is a non-local 1.5 order scheme where the equations are closed using TKE, the YSU a first order non-local scheme which uses gradient transfer theory, the QNSE-EDMF which is a 1.5 order non-local scheme with a spectral closure and finally the ACM2 which is a combined local and non-local scheme which uses a transilient matrix to describe turbulence on many scales. These schemes will be looked at in more depth below.

2.1.1 MYJ SCHEME

The Mellor-Yamada-Janjic (MYJ) scheme is a 1.5 order Turbulent Kinetic Energy (TKE) scheme (Janjic, 1994), based on the level 2.5 scheme found in Mellor & Yamada (1982). That is the equations are found for one 2nd order moment. Here the turbulence equations are closed using the TKE equation, which means the fluxes are assumed proportional to the TKE. The production of TKE by shear (P_s) and buoyancy (P_b) along with eddy dissipation (ϵ) can be described using,

$$\frac{d}{dt}\left(\frac{(2k_e)^2}{2}\right)-\frac{\partial}{\partial z}\left[l_m 2k_e S_k \frac{\partial}{\partial z}\left(\frac{(2k_e)^2}{2}\right)\right]=P_s+P_b+\epsilon, \tag{2.3}$$

where k_e is the kinetic energy ($k_e = \frac{1}{2}mv^2$, m being mass and v velocity), l_m the master eddy mixing length and S_k is an empirical constant. The master length, l_m is the average distance an eddy travels before it exchanges momentum with the surrounding eddies. In the MYJ scheme this is given as,

$$l_m = l_0\frac{kz}{kz+l_0}, \tag{2.4}$$

where k is the von Karman constant and l_0 is,

$$l_0 = 0.23\frac{\int_0^z (2k_e)|z|dz}{\int_0^z (2k_e)dz}. \tag{2.5}$$

On the RHS of Eq.(2.3)the production of TKE by shear (P_s), buoyancy (P_b) and eddy dissipation (ϵ) are determined from,

$$P_s = -(\overline{u'v'})\frac{\partial u}{\partial z} - (\overline{u'w'})\frac{\partial v}{\partial z} \tag{2.6}$$

$$P_b = \beta_1 g(\overline{u'\theta_v'}) \tag{2.7}$$

$$\epsilon = \frac{(2k_e)^3}{B_1 l_m}. \tag{2.8}$$

Where β_1 and B_1 are constants. If the MYJ scheme is used, the model defines the height of the BL as where $2k_e$ falls below 0.001 kgm^{2}s^{-2}.

2.1.2 YSU SCHEME

The Yonsei University (YSU) parametrisation scheme is a first order, non-local scheme (Hong *et al.*, 2006). The YSU scheme assumes that is the mixing is proportional to a specified profile, denoted K (this is known as a K-profile approach, gradient-transfer theory or eddy-diffusivity theory). The degree of mixing over time is proportional to the second derivative of a heat or momentum variable (C) with respect to height,

$$\frac{\partial C}{\partial t} = \kappa_c \frac{\partial^2 C}{\partial z^2}, \tag{2.9}$$

where κ_C is the eddy diffusivity coefficient. In the YSU scheme this approach is modified with the inclusion of a correction term for non-local eddies (γ_C) and entrainment flux, $-\overline{(w'c')_h}\left(\frac{z}{h}\right)^3$ where h denotes the inversion layer, such that,

$$\frac{\partial C}{\partial t} = \left[\kappa_C \left(\frac{\partial C}{\partial z} - \gamma_C\right) - \overline{(w'c')_h}\left(\frac{z}{h}\right)^3\right]. \tag{2.10}$$

The entrainment flux term means that this scheme has an explicit treatment of BL top entrainment, unlike the other schemes discussed here.

For this scheme to diagnose the height of the BL, the bulk Richardson number,

$$Ri_b = \frac{\frac{g}{\theta}\frac{\partial\overline{\theta}}{\partial z}}{\left[\left(\frac{\partial\overline{u}}{\partial z}\right)^2 + \left(\frac{\partial\overline{v}}{\partial z}\right)^2\right]}, \tag{2.11}$$

is used. The BL height is defined as the first point (from surface upwards) which exceeds a threshold value in Ri_b. Initially this was set to 0, however it was found to produce too little vertical mixing in a stable BL, the critical Ri_b was then increased to 0.25 over land (Hong & Kim, 2008).

2.1.3 QNSE-EDMF

The Quasi-Normal Scale Elimination-Eddy-Diffusivity Mass Flux (QNSE-EDMF) is a non-local 1.5 order closure, which takes a spectral approach to formulate a $k_e - \epsilon$ model (Sukoriansky *et al.*, 2005). The physics behind the QNSE scheme is very similar to that of the MYJ scheme, however it has been developed to better parametrise stable boundary layers. As a stable boundary layer reduces the vertical mixing, leading to the development of spatial anisotropy. With increasing strength of stratification, the near surface layer may become de-coupled from the overlaying atmospheric circulation, essentially shielding this circulation from the surface fluxes. The QNSE scheme uses a spectral closure, which has an advantage over standard Reynolds-Averaged Navier-Stokes equations based models (RANS, such as the YSU) due to retaining more comprehensive physics. The spectral closure developed for the QNSE scheme maps the velocity field onto a quasi-Gaussian field whose modes are governed by the Langevin equation (Sukoriansky *et al.*, 2003). The parameters for this mapping are calculated using a systematic process of successive averaging over small shells of velocity and temperature modes that yields equations for increasingly larger-scale modes. In this procedure the combined contribution of turbulence and internal waves is accounted for and the spatial anisotropy is explicitally resolved. When this averaging process is extended to the largest scales available in the system (the turbulence macroscale) the spectral closure yields a new RANS model, which has been implemented as the $k_e - \epsilon$ closure. In an unstable situation the QNSE uses the equations of the MYJ scheme. Here k_e represents TKE and ϵ the dissipation rate. In non-neutral stratification the $k_e - \epsilon$ equations in 1D, single column formation are,

$$\begin{aligned} \frac{Dk_e}{Dt} &= K_M\left[\left(\frac{\partial u}{\partial z}\right)^2 + \left(\frac{\partial v}{\partial z}\right)^2\right] - \frac{g}{\theta_0}K_H\frac{\partial\theta}{\partial z} \\ &\quad -\epsilon + \frac{\partial}{\partial z}\left(K_M\frac{\partial K}{\partial z}\right), \qquad (2.12) \\ \frac{D\epsilon}{Dt} &= \frac{\epsilon}{k_e}\left\{C_1K_M\left[\left(\frac{\partial u}{\partial z}\right)^2 + \left(\frac{\partial v}{\partial z}\right)^2\right] - C_3\frac{g}{\theta_0}K_H\frac{\partial\theta}{\partial z}\right\} \\ &\quad - C_2\frac{\epsilon^2}{k_e} + \frac{\partial}{\partial z}\left(K_\epsilon\frac{\partial\epsilon}{\partial z}\right) \qquad (2.13) \end{aligned}$$

The terms to the right hand side of Eqn. 2.12 represent shear production, buoyant destruction, dissipation and vertical turbulent transport of TKE, while the terms on the right hand of Eqn. 2.13 are shear and buoyancy forcing, destruction and vertical turbulent transport of ϵ. The vertical eddy viscosity and diffusivity coefficients (K_M and K_H) are replaced with ν_z and κ_z from the spectral model. In the neutral case the expression for vertical viscosity is,

$$\nu_n = C_\mu\frac{k_e^2}{\epsilon} \qquad (2.14)$$

where $C_\mu \approx 0.09$. Using Eqn. 2.14 K_M and K_H can be represented as,

$$K_M = \alpha_M C_\mu \frac{k_e^2}{\epsilon} \tag{2.15}$$

$$K_H = \alpha_H C_\mu \frac{k_e^2}{\epsilon}, \tag{2.16}$$

where

$$\alpha_M = \frac{1+8Ri_g^2}{1+2.3Ri_g+35Ri_g^2}, \tag{2.17}$$

$$\alpha_H = \frac{1.4-0.01Ri_g+1.29Ri_g^2}{1+2.344Ri_g+19.8Ri_g^2} \tag{2.18}$$

are the non-dimensional stability functions from QNSE theory, and Ri_g is the local gradient Richardson number.

The length scale l is given, in the $TKE-l$ format by,

$$\frac{1}{l} = \frac{1}{l_B} + \frac{1}{l_N} \tag{2.19}$$

where

$$l_B = \frac{\kappa z}{1+\frac{\kappa z}{\lambda}} \quad l_N = c_N, \quad c_N = 0.75 \quad \lambda = \frac{Bu_*}{f}, B = 0.0063. \tag{2.20}$$

l_B is the Blackadar scale, l_N is the length scale limitation due to stable stratification. Returning to Eqn. 2.13, C_1 can be described using the friction velocity-based Froude number $Fr_* = u_*/NL$ (N is the Brunt-Väisälä frequency),

$$C_1 = C_1^0 + C_f Ro_*^{-1} - C_N Fr_*^{-1}, \tag{2.21}$$

where $Ro = u_*/|f|l_k$, with f the Coriolis parameter and $l_k = 0.16K^{3/2}/\epsilon$ is the turbulence macroscale used in $K-\epsilon$ modelling. C_N = 0.55, C_f = 111, C_1^0 = -1.44 are empirical constants. The coefficient C_2 is 1.92 and the value of C_3 is set at 1 when stratification is non-neutral.

The BL height is defined as when the doubled kinetic energy, $2k_e$ falls below 0.0101 $\mathrm{m^2s^{-2}}$.

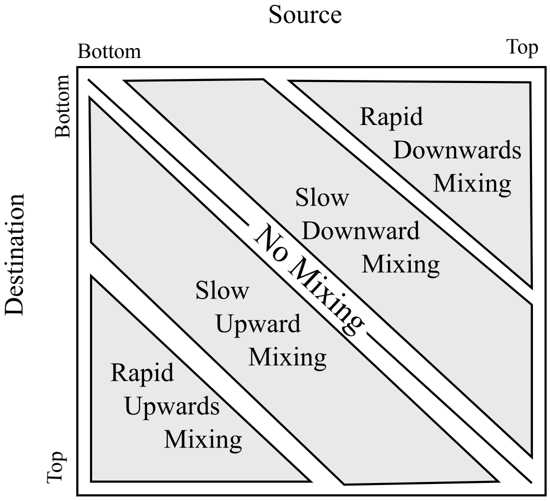

Figure 2.2: A schematic showing the arrangement of terms in a transilient matrix and their physical meaning, from Stull (2012).

2.1.4 ACM2

The Asymmetric Convective Model v.2 (ACM2) (Pleim, 2007) is a combined local and non-local closure which has been designed for more convective situations. As a standard eddy-diffusion approach assumes that all the turbulence is subgrid-scale the combination of this with a non-local scheme means that turbulence which is both subgrid- and supergrid-scale can be represented. The ACM2 uses a transilient matrix M that defines the maximum flux between any pair of model levels even if they are not adjacent,

$$\frac{\partial \theta_i}{\partial t} = \sum_j M_{ij} \theta_j, \tag{2.22}$$

where θ is again potential temperature and i, j are two layers. A transilient matrix can describe many sorts of mixing, as shown in the schematic in Fig.2.2. The rows and columns must sum to 1, as there is no loss of energy, so if the only terms are on the leading diagonal then there is no mixing. Terms in the corners denote movement from the very top to very bottom or vice versa, which is rapid and caused by large eddies, whereas terms closer to the leading diagonal represent the action of smaller eddies. The interactions between the layers are represented in the schematic in Fig. 2.3, transport by eddies from the surface up to even the highest level of the boundary layer is allowed, as well as a gradual down-ward transport due to subsidence. The eddy diffusion between the layers is also described. For a mass mixing ratio C in layer

i the ACM2 governing equation in discrete form is,

$$\frac{\partial C_i}{\partial t} = Mu_2 C_1 - Md_{2i} C_i + Md_{2i+1} C_{i+1} \frac{\Delta z_{i+1}}{\Delta z_i} + \frac{1}{\Delta z_i} \left[\frac{K_{i+\frac{1}{2}} (C_{i+1} - C_i)}{\Delta z_{i+\frac{1}{2}}} + \frac{K_{i-\frac{1}{2}} (C_i - C_{i-1})}{\Delta z_{i-\frac{1}{2}}} \right] \tag{2.23}$$

where Mu_2 and Md_2 are the upward and downward convective mixing rate respectively, z is height above ground and K is eddy diffusivity. The terms in eqn. 2.23 which contain Mu_2 and Md_2 represent the non-local mixing, while the terms in square brackets represent the local mixing caused by eddy diffusivity.

For stable conditions the BL height is diagnosed using,

$$h = Ri_{crit} \frac{\overline{\theta_v} u(h)^2}{g \left[\theta_v(h) - \theta_v(z_1) \right]}, \tag{2.24}$$

where θ_v is the virtual potential temperature, with the overline indicating the average between the surface and height h and z_1 is the lowest model level.

For unstable conditions, to begin with the top of the mixing layer (z_{mix}) is found as where θ_v becomes equal to θ_s,

$$\theta_s = \theta_v(z_1) + b \frac{\left(\overline{w'\theta_v'} \right)_o}{w_m} \tag{2.25}$$

where b = 8.5 and w_m is the convective velocity scale. Then the bulk Richardson number is defined for the entrainment layer above z_{mix} such that,

$$Ri_b = \frac{g \left[\theta(h) - \theta_s \right] (h - z_{mix})}{\overline{\theta}_v \left[u(h) - u(z_{mix}) \right]^2}, \tag{2.26}$$

where U is the windspeed. The top of the BL is then diagnosed as the height where $Ri_b = Ri_{crit} = 0.25$.

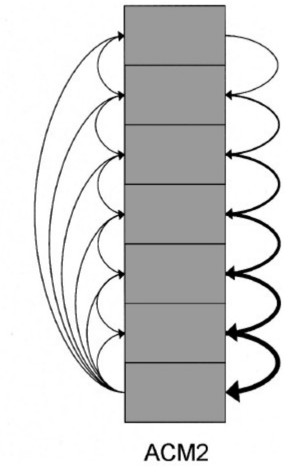

Figure 2.3: Schematic showing the possible interactions between the different layers in the ACM2 BL parametrisation scheme, from Pleim (2007).

2.2 COMPARISON OF SCHEMES

Each of these schemes was initially tested in the paper which introduced them. For the YSU a case study of a frontal tornado outbreak was performed in Hong *et al.* (2006), and the YSU was found to improve a systematic cold bias above 850 hPa found with the previous MRF scheme. The YSU was found to be better at producing convective inhibition, which helps to improve forecasting of precipitation ahead of a front. The YSU is also found to improve characteristics such as a double line of intense convection seen in the case study, due to the BL being less diluted by entrainment which leaves more fuel for severe convection when triggered by the front.

The MYJ was tested in Janjic (1994) against a case where heavy precipitation had been forecast incorrectly and another with a successfully simulated tropical storm. The MYJ was found to reduce the heavy spurious precipitation in the first case, and perform well in the case of the tropical storm.

As the QNSE was developed for stable Arctic boundary layers, it is tested initially against data from the SHEBA (Surface HEat Budget of the Arctic) and Beaufort Arctic Storms Experiment (BASE) campaigns. For the BASE simulation, the observations had a stably stratified BL which extended all the way to the surface. Using WRF in single-column formulation, Sukoriansky *et al.* (2005) found the QNSE was very good for the case of moderate stratification. In the case of the SHEBA data, the QNSE performs well producing vertical profiles which are in agreement with the observations.

The ACM2 was tested initially in an LES and then against a Global Energy and Water Cycle Experiment (GEWEX) Atmospheric Boundary Layer Study (GABLS) test case (Pleim, 2007). In both of these tests the ACM2 performed well, simulating realistic BL heights, temperature profiles and surface heat fluxes. The ability to simulate the profiles so well is attributed to the ACM2 being a solution to the problem of modelling both the small (subgrid) and large scale turbulent transport within convective boundary layers.

Many sensitivity studies have been carried out with varying combinations of these BL schemes using both WRF and PWRF, a discussion of these is included in Chapter 5.

2.3 SURFACE PHYSICS

Surface physics or surface exchange parametrisations are needed to provide the sub-grid scale fluxes of heat, moisture and momentum to the BL scheme. They provide the only physical boundary for atmospheric models. In WRF the surface physics is either controlled by the Land Surface Model (LSM) over land and ice or the surface layer scheme over water. There can be no mixed land and water grid points. Over fractional ice both schemes are used and the results averaged together with the fraction of sea ice as a weighting, otherwise known as a mosaic method (Vihma, 1995). For the LSM surface variations in moisture, albedo, snow cover and land-use need to be taken into account.

A LSM needs to provide four things to the atmospheric model, the surface sensible and latent heat fluxes and the upward long- and short-wave radiation. While the surface physics scheme needs to calculate the sensible and latent heat fluxes over water, as well as the surface stress and provide the LSM with the friction velocities and exchange coefficients. The surface layer scheme needs to work with the chosen BL scheme, with some such as the QNSE having their own dedicated surface physics. The YSU and ACM2 both use the MM5 similarity surface physics, while the MYJ uses the Eta surface layer. The QNSE surface physics is a modification of the Eta scheme, so will be discussed with the Eta scheme. As the surface physics schemes are linked to a BL scheme in WRF, this means that the surface layer schemes are not explicitly

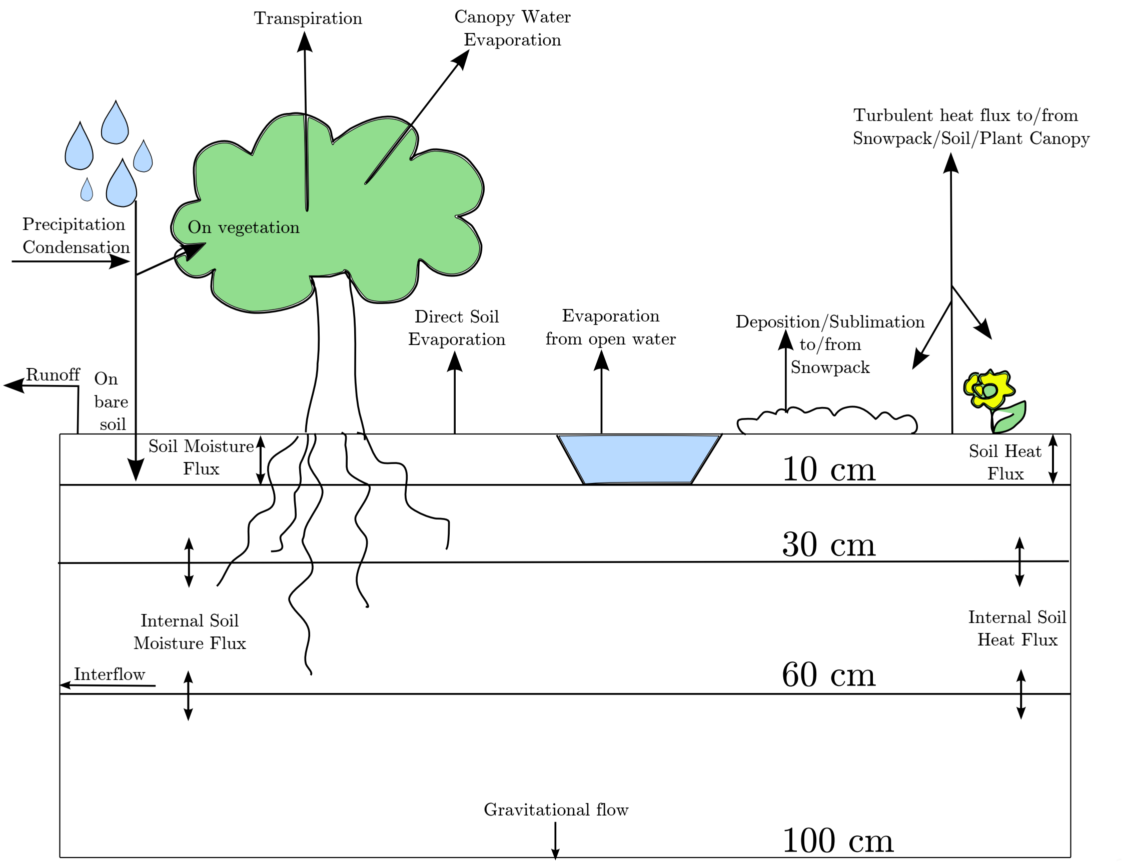

Figure 2.4: The interactions within the Noah LSM.

tested in this thesis.

2.3.1 LAND SURFACE MODEL

The Noah LSM has been used in NCEP Eta, MM5 and WRF models. The schematic in Fig. 2.4 shows the interactions which are represented within the Noah LSM. These processes include changes in soil moisture, soil temperature, liquid, transpiration from vegetation and canopy resistance (Chen *et al.*, 1996, 1997; Chen & Dudhia, 2001; Ek *et al.*, 2003). The land-use data comes from the MODIS IGBP 21-category data.

The Noah LSM is enhanced by Polar WRF, primarily these modifications improve the representation of heat transfer through snow and ice along with the ability to specify a variable sea ice thickness and snow depth on sea ice (Hines *et al.*, 2015).

2.3.2 SURFACE LAYER SCHEMES

ETA SURFACE LAYER

The Eta surface layer scheme (J., 1990; Janjic, 1994) is based on Monin-Obukhov similarity theory. The scheme includes parametrisations of the viscous sublayer. Over water surfaces the viscous sublayer is parametrised explicitly following Janjic (1994). Over land, the effects of the viscous sublayer are taken into account through variable roughness heights for temperature and humidity as proposed by Zilitinkevich (1995). The Beljaars correction is applied in order to avoid singularities in the case of unstable surface layer and vanishing wind speed (Beljaars, 1995). The surface fluxes are then computed by an iterative method.

The sensible heat flux is given by,

$$SHF = \frac{P(1)}{(RT(1))} c_p C_H \left(\theta(1) - \theta(z_0)\right) \tag{2.27}$$

where P is pressure, R is the gas constant c_p is the specific heat capacity for air, and z_0 is the roughness length.

The exchange coefficient C_H, is the maximum of $0.001 \times 1/z_{1/2}$ (where $z_{1/2}$ is half way between the first and second layers) and

$$C_H = \frac{u_* \kappa}{\left(\psi_H\left(\frac{z_{eff}}{L}\right) - \psi_H\left(\frac{z_{0h}}{L}\right) - \ln\left(\frac{z_{eff}}{z_{0h}}\right)\right)}. \tag{2.28}$$

Where z_{eff} is the effective roughness length, z_{0h} is the thermal roughness length and κ is the von Karman constant (0.4).

The exchange coefficient uses the stability correction of Paulson (1970) for unstable conditions,

$$\psi_H(x) = -2\ln\left[\frac{1+x^2}{2}\right], \tag{2.29}$$

$$x = (1-15\zeta)^{1/4} \tag{2.30}$$

$$\zeta = \frac{z_{eff}}{L} \tag{2.31}$$

For stable conditions, the formulation of Holtslag & Bruin (1988) is used,

$$\psi_H = 0.7\zeta + 0.75\zeta\,(6 - 0.35\zeta)\exp\left(-0.35\zeta\right). \tag{2.32}$$

The friction velocity u_* and also C_H are calculated iteratively with u_* using the Beljaars correction (Beljaars, 1995).

Latent heat flux is given by,

$$LHF = L_v \frac{P(1)}{(RT(1))} C_H \left(Q(1) - Q(z_0)\right) M_{avail} \tag{2.33}$$

where M_{avail} is the surface moisture availability (between 0 and 1) and L_v is the latent heat of vaporisation.

For the QNSE the stability functions are changed, following Sukoriansky *et al.* (2005) ψ_H is the largest between the value given by Eqn. (2.29) and,

$$\psi_H(\zeta) = 2\zeta + 10.3\zeta^2 + 130\zeta^3. \tag{2.34}$$

MM5 SURFACE LAYER

Both the YSU and the ACM2 boundary layer scheme work with the MM5 surface layer scheme. This scheme uses stability functions from Paulson (1970),Dyer & Hicks (1970), and Webb (1970) to compute surface exchange coefficients for heat, moisture, and momentum. A convective velocity following Beljaars (1995) is used to enhance surface fluxes of heat and moisture. No thermal roughness length parametrisations is included in the current version of this scheme. A Charnock relation relates roughness length to friction velocity over water. There are four stability regimes following Zhang & Anthes (1982).

The sensible heat flux is calculated using,

$$SHF = C_H(\theta_s - \theta(1)). \tag{2.35}$$

Where the subscript s implies a surface value.

Here the exchange coefficient is given by,

$$C_H = \frac{c_p \frac{P}{R\theta_v} u_* z_{0h}}{\theta(1) - \theta_s} \tag{2.36}$$

where u_* is the friction velocity and z_{0h} the thermal roughness length from similarity theory.

The friction velocity is described by,

$$u_* = \frac{1}{2}\frac{\kappa \mathbf{U}}{\ln\left(\frac{z}{z_0} - \psi_M\left(\frac{z}{L}\right)\right)} \tag{2.37}$$

where the stability correction for momentum ψ_M is dependent on the stability regime.

The stability regime is determined by the bulk Richardson number Ri_b (Zhang & Anthes, 1982),

$$Ri_b = \frac{g}{\theta}\frac{(\theta(z) - \theta_s)z}{W_s^2} \tag{2.38}$$

$$Ri_b = \begin{cases} \geq 0.2 & \text{Nighttime stable} \\ 0.0 < Ri_b < 0.2 & \text{Damped Mechanical Turbulence} \\ = 0 & \text{Forced Convection} \\ < 0 & \text{Free Convection} \end{cases} \tag{2.39}$$

The stability correction is thus

$$\psi_M = \begin{cases} -10\ln\left(\frac{z}{z_0}\right) \text{ Minimum = -10} & \text{Nighttime stable} \\ \frac{-5Ri_b \ln\left(\frac{z}{z_0}\right)}{1.1 - 5Ri_b} & \text{Damped Mechanical Turbulence} \\ 0 & \text{Forced Convection} \\ 2\ln\left(\frac{1}{2}(1+x)\right) + \ln\left(\frac{1}{2}(1+x^2)\right) - 2\tan^{-1}(x) + 2\tan^{-1}(1) & \text{Free Convection} \end{cases} \tag{2.40}$$

where $x = \left(1 - 16\frac{z}{L}\right)^{1/4}$.

The thermal roughness length is given by,

$$z_{0h} = \frac{(\theta - \theta_s)}{\ln\left(\frac{z}{z_0}\right) - \psi_H + C_{ZIL}\sqrt{\frac{u_* z_L}{visc}}}. \tag{2.41}$$

where ψ_H is the stability correction for heat, $C_{ZIL} = 10^{(\frac{-0.4 z_L}{0.07})}$ and $visc = (1.32 + 0.009(T - 273.15))10^{-5}$. ψ_H is equal to ψ_M except for the case of free convection where,

$$\psi_H = 2\ln\left(\frac{1}{2}(1-y)\right), \tag{2.42}$$

$y = \left(1 - 16\frac{z}{L}\right)^{1/2}$ where L is the Monin-Obhukov length scale.

The latent heat flux is related to the moisture flux QFX by $LHF = L_v QFX$ where

$$QFX = C_M(Q_{vs} - Q_v(1)). \tag{2.43}$$

Here C_M is the exchange coefficient for moisture given by,

$$C_M = \frac{\theta_v M_{avail} u_* \kappa}{\ln\left(\frac{(\kappa u_* z)}{x_{ka}} + \frac{z}{0.01}\right) - \psi_H} \tag{2.44}$$

where $x_{ka} = 2.4 \times 10^{-5}$.

2.4 CLOUD MICROPHYSICS

Cloud microphysics schemes parametrise the processes that occur within clouds, such as the formation of cloud droplets, freezing into ice and snow, melting and precipitation. A microphysics scheme provides the atmosphere with tendencies of moisture and heat, the surface with rainfall and snow and is important for the radiation scheme. This thesis uses the Morrison 2005 microphysics schemes, which is a 2-moment 5-class bulk microphysics scheme which predicts the mixing ratios and number concentrations of cloud droplets, cloud ice, snow, rain and graupel (Morrison *et al.*, 2005, 2009). The schematic in Fig.2.5 shows the different processes which are described in the microphysics scheme and how they relate to the different hydrometeors.

The cloud and precipitation particle size distributions are represented by gamma functions,

$$N(D) = N_0 D^{\mu} e^{-\lambda D}, \tag{2.45}$$

where D is the particle diameter and N_0, λ and μ are the intercept, slope and shape parameters of the size distribution, respectively. The parameters N_0 and λ are derived from the predicted number concentration N and mixing ratio Q and the specified μ for each species.

$$\lambda = \left[\frac{cN\Gamma(\mu + d + 1)}{Q\Gamma(\mu + 1)}\right]^{\frac{1}{d}} \tag{2.46}$$

$$N_0 = \frac{N\lambda^{\mu+1}}{\Gamma(\mu + 1).} \tag{2.47}$$

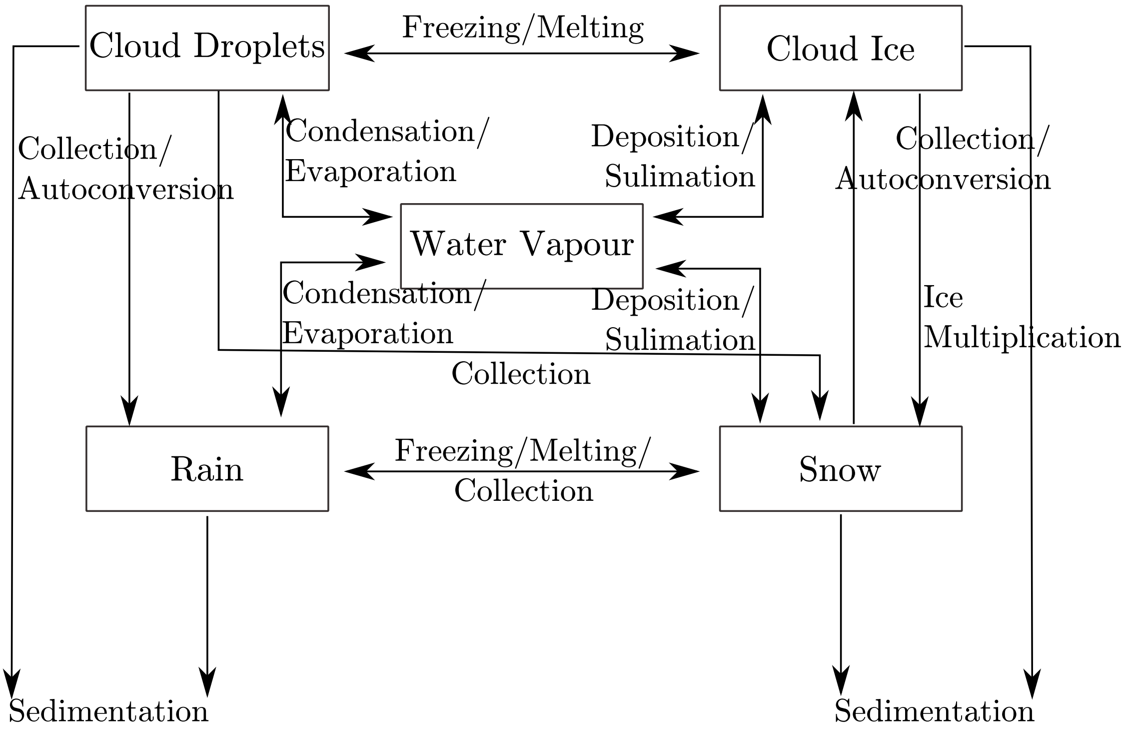

Figure 2.5: Schematic showing the interractions in the cloud microphysics scheme. After Morrison *et al.* (2005).

Where Γ is the Euler gamma funon, c and d are the assumed power-law mass-diameter relationship of the hydrometeors for each species where $m = cD^d$. For the precipitation species (rain, snow and graupel) along with cloud ice, $\mu = 0$ means the size distributions for these species are exponential functions.

The change in mixing ratio Q and number concentration N over time are given by,

$$\begin{aligned}\frac{\partial Q}{\partial t} = & -\nabla.(\mathbf{v}Q) + \frac{\partial}{\partial z}\left(V_{qx}\right) + \nabla_D Q + \left(\frac{\partial Q}{\partial t}\right)_{\text{PRO}} \\ & \left(\frac{\partial Q}{\partial t}\right)_{\text{COND/DEP}} + \left(\frac{\partial Q}{\partial t}\right)_{\text{AUTO}} + \left(\frac{\partial Q}{\partial t}\right)_{\text{COAG}} \\ & \left(\frac{\partial Q}{\partial t}\right)_{\text{MLT/FRZ}} + \left(\frac{\partial Q}{\partial t}\right)_{\text{MULT}}.\end{aligned} \tag{2.48}$$

$$\begin{aligned}\frac{\partial N}{\partial t} = & -\nabla.(\mathbf{v}N) + \frac{\partial}{\partial z}\left(V_{Nx}\right) + \nabla_D N + \left(\frac{\partial N}{\partial t}\right)_{\text{PRO}} \\ & \left(\frac{\partial N}{\partial t}\right)_{\text{EVAP/SUB}} + \left(\frac{\partial N}{\partial t}\right)_{\text{AUTO}} + \left(\frac{\partial N}{\partial t}\right)_{\text{SELF}} \\ & \left(\frac{\partial N}{\partial t}\right)_{\text{COAG}} + \left(\frac{\partial N}{\partial t}\right)_{\text{MLT/FRZ}} + \left(\frac{\partial N}{\partial t}\right)_{\text{MULT}}.\end{aligned} \tag{2.49}$$

Where **v** is the 3D wind vector, $V_N x$ and $V_q x$ denote the number and mass weighted terminal particle fall speed for each species. The ∇_D is a turbulent diffusion operator. The first three terms on the RHS of Eqns.2.48 and 2.49 are advection, sedimentation and turbulent diffusion and the remainder of the terms are the microphysical processes. The last six terms in Eqn. 2.48 are primary production (ice nucleation or droplet activation), condensation/deposition (evaporation/sublimation), autoconversion (parametrised transfer of mass and number concentration from the cloud ice and droplet classes to snow and rain due to coalescence and diffusional growth), collection between hydrometeor species, melting/freezing and ice multiplication (transfer of mass from the snow class to ice). The last seven terms in Eqn. 2.49 are primary production, evaporation/sublimation, auto-conversion, self-collection, collection between hydrometeor species, melting/freezing and ice multiplication.

The Morrison 2005 microphysics scheme was chosen following Bromwich *et al.* (2009) where the scheme was also used in their PWRF sensitivity test. The Morrison 2005 scheme was chosen due to being developed and tested for the Arctic (Morrison *et al.*, 2008), tests in the MM5 model (Morrison & Pinto, 2005, 2006) show the scheme simulates the cloud persistence and microphysical characteristics of Arctic mixed phase clouds reasonably.

2.5 MODEL INTERACTIONS

As in the real world, the various parts of the complex system of interactions which occur between the surface, atmosphere, clouds and radiation must also be accounted for in the model. The interactions have to be simplified somewhat, so schemes for particular areas can be called one after the other, rather than continually interacting as in the real world. The diagram in Fig.2.6 shows the interactions between the parametrisation schemes in the smallest grid (3 km) which is used in this thesis. When the model is stepping forward, firstly the radiation schemes are called with short-wave radiation first and long-wave second. The radiation scheme uses the cloud cover and microphysical properties from the previous step (or the initialising data) to calculate the radiative forcing, which is passed to the LSM. The surface driver is then called, which runs the surface layer scheme and the LSM in turn. The surface layer

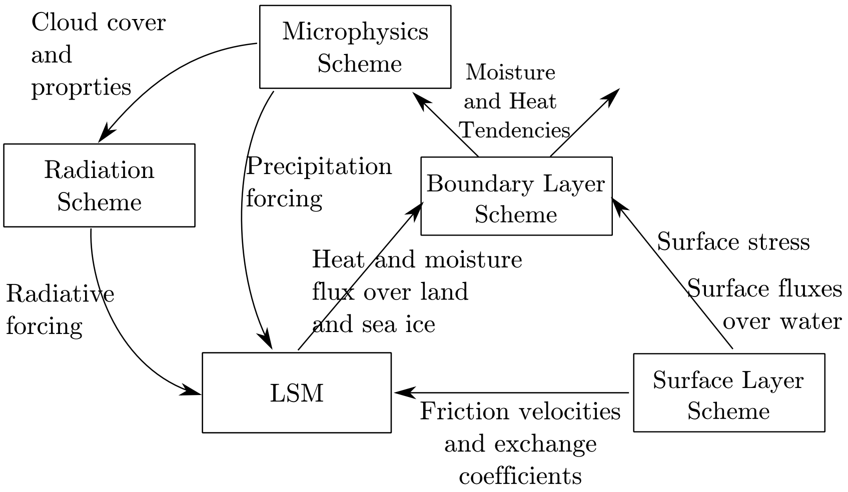

Figure 2.6: The interactions between some of the physics schemes in WRF.

provides the friction velocities and exchange coefficients to the LSM and the surface stress and fluxes over water to the BL scheme. The LSM uses the radiative forcing, friction veclocity and exchange coefficients from the surface layer and precipitation from the microphysics of the previous step. Using these, the LSM calculates the fluxes of heat and moisture over the land and sea ice. After the LSM, the BL driver is called. The BL driver takes the fluxes from both the surface layer scheme and the LSM, and calculates the fluxes over fractional sea ice using the mosaic method (Vihma, 1995). Once this is done, the BL scheme is called, and takes the fluxes and surface stress and calculates the TKE (if it is a TKE based scheme), moisture and heat tendencies. The tendencies are passed on to the cumulus scheme (if used, not included in diagram) and the microphysics scheme. The cumulus scheme is used for larger grid spacing, where sub-grid scale clouds will not be resolved by the microphysics scheme. The cumulus scheme takes moisture and momentum tendencies and returns these after calculation for the microphysics scheme. Called last, the microphysics scheme takes the tendencies of heat and moisture and calculates the mass and number concentrations of cloud variables (liquid, ice, rain, graupel etc), the precipitation calculated here is important for the LSM, and the cloud cover and properties is taken by the radiation scheme in the next step.

3

THE IMPACT OF THINNER ICE ON ATMOSPHERIC BOUNDARY LAYER.

3.1 INTRODUCTION

A cold air outbreak (CAO), when dry and cold air flows equator-wards from the sea ice, over the MIZ, and onto the open ocean causes the transfer of large amounts of heat, moisture and momentum between the ocean and atmosphere (Liu *et al.*, 2006). CAOs often form mesoscale shallow convection, which is important both for the occurrence of Arctic stratocumulus clouds, and for the transport of the heat, moisture and momentum into the free atmosphere (Atkinson & Zhang, 1996). Surface heat fluxes can trigger convective activity which may impact the formation of polar mesoscale cyclones (Moore *et al.*, 1996). A baroclinic zone forms at the ice edge due to surface temperature gradients, and this along with low level shear over the MIZ are important for the formation of Polar mesoscale cyclones and polar lows (Rasmussen & Turner, 2003). The ocean can also be affected by cold air above, the strong heat fluxes cool the surface and cause ice to form, which increases the salinity and thus the density of the water, triggering overturning which can impact ocean deep convection (Renfrew & Moore, 1999).

Sea ice plays an important role at high latitudes. It acts to insulate the atmosphere from the ocean and, due to its high albedo, sea ice is important for the surface energy balance. The atmosphere, sea ice and ocean are linked by a complex series of forcings and feedbacks. Known to be particularly important is the ice-albedo feedback, where the melting of sea ice reduces the surface albedo, which in turn increases the absorption of heat by the ocean which then leads to more melting (Serreze & Francis, 2006). The ice-albedo feedback is also shown in Fig 1.7, which emphasises the loop nature of the feedback. Linked to the ice albedo-feedback is the cloud-radiation feedback, an increase in lead fraction and reduction in albedo would cause an increase in sensible heat flux and moisture flux leading to more clouds. Which could in turn warm the surface and accelerate melt during the winter by long wave warming of the surface, further increasing the lead fraction (Curry *et al.*, 1996). A schematic of the cloud feedback is shown in Fig 1.8, however clouds could also shade and cause shortwave cooling in the summer (Serreze & Francis, 2006).

Due to changes in climate there are greater amounts of thin first year ice than in the past (Nghiem *et al.*, 2007; Comiso, 2012). The fraction of total ice extent made up of multi-year ice in March has decreased from around 75% in the mid-1980s to 45% in 2011, while the proportion of the oldest ice (+ 5 years) has declined from 50% of the multi-year ice to 10% (Maslanik *et al.*, 2011).

First year ice is thinner than multi year ice, with the thickness being less than 1.2 m for first year ice, compared to up to 3 m thick multi-year ice (JCOMM, 2014). Due to the ice being thinner, first year ice is optically clearer; and thus shows the dark sea surface, so it has a lower albedo than multi-year ice. First year ice is also less insulating than multi-year ice, as it allows more heat to diffuse through from the warmer sea surface below. The shift from multi-year to first year ice will increase the total solar heat input into the ice cover, enhancing summer ice melting and increasing the amount of shortwave radiation absorbed by the ocean (Perovich & Polashenski, 2012). At present most numerical weather prediction (NWP) models assume a thicker multi-year ice than is observed, which could cause errors in forecasting at high latitudes. Therefore the inclusion of a realistic ice thickness may be important, and become increasingly important.

Many studies highlight uncertainties in the representation of sea ice as an important error source Vihma *et al.* (2014) has a good review of this. For example, Rinke *et al.* (2006) finds that variables such as air temperature, turbulent heat fluxes, cloud cover and precipitation are dependent on sea ice conditions. Changes in sea ice concentration lead to changes in heat fluxes, increasing the surface temperature. Biases in surface temperature can be caused by having an incorrect ice cover. Comparing a simulation with 100% sea ice cover to one with fractional sea ice (observations from SHEBA) Bromwich *et al.* (2009) found up to +14.3 K differences in surface temperature and +100 Wm^{-2} sensible heat flux over an area with high open water fraction. Using a 60 member ensemble, Screen *et al.* (2014) show that in proximity to areas of sea ice loss there is a statistically significant near surface warming with a 2 K increase in surface temperature where there is a 50% reduction in sea ice concentration, due to the increase in surface heat fluxes. Therefore having a realistic sea ice extent in NWP models is essential for many other variables.

Including different types of sea ice or snow on sea ice is also important. Modelling of off ice airflow done by Pinto *et al.* (2003) shows a warm bias during the day which is attributed to neglecting the impact of frost flowers (which are formed on new ice by freezing from the vapour phase and increase the albedo of the newly forming ice) and the uncertainty in the treatment of solar absorption by new ice. Snow cover is important for the albedo, as the albedo of sea ice which is covered in snow is the same for both multiyear ice and newer ice. However once melt begins the albedo of newer ice will change faster than that of older ice, meaning that newer ice generally has a lower albedo (Perovich & Polashenski, 2012). The albedo is often represented simplistically in models, in Birch *et al.* (2009) two versions of the Met Office Unified Model (MetUM) along with the Coupled Ocean/Atmosphere Mesoscale Prediction System (COAMPS) model are compared with observations from the Arctic Ocean Experiment (AOE). The MetUM uses a simple relationship of surface temperature to calculate surface albedo. The albedo of thicker ice is seen to be underestimated which causes a positive bias in surface temperature and upwelling shortwave radiation. They recommend that in future versions of the NWP UM that the albedo is controlled by the amount of snow, ice and liquid water present at the surface. However due to a lack of high quality complete datasets of radiation, snow and ice properties it remains difficult to test parametrisations of snow and ice albedo (Vihma *et al.*, 2014).

During cold air outbreaks, the presence of leads and open water in the sea ice is important for boundary-layer height and the formation of clouds, through the increase in surface flux (Liu *et al.*, 2006; Gryschka *et al.*, 2008). Turbulent heat fluxes from leads in winter is one of the largest terms in the Arctic heat budget

(Andreas *et al.*, 1979). The inclusion of subgrid scale leads is therefore particularly important. The First International Satellite Cloud Climatology Project (ISCCP) Regional Experiment - Arctic Cloud Experiment (FIRE-ACE) observed the atmosphere of the marginal ice zone (MIZ) of the Beaufort Sea and found that a lead of 3 km width generated sensible and latent heat fluxes of 56 $\mathrm{Wm^{-2}}$ and 14 $\mathrm{Wm^{-2}}$ respectively compared to -20 $\mathrm{Wm^{-2}}$ and -13 $\mathrm{Wm^{-2}}$ respectively over the surrounding sea ice. They saw that clouds tended to form over the leads and polynyas or downwind as cold air flows from north to south (Gultepe *et al.*, 2003). A comparison between a model and observations from SHEBA show that models have problems with capturing the turbulent heat fluxes in the MIZ properly, the heat flux deficit was 50% larger than estimated from observations (Pinto *et al.*, 2003). In the polar version of the MM5 model, surface fluxes were sensitive to sea ice representation but not to the choice of atmospheric boundary layer parametrisation scheme (Valkonen *et al.*, 2008). Comparing the six ARCMIP regional scale models to SHEBA data, Tjernström *et al.* (2005) found that errors in the models are generally larger below 1km, which points to problems with representing boundary layer clouds.

The inclusion of accurate sea ice in models is therefore important for many variables such as surface temperature, heat fluxes and cloud cover. Many models now include a representation of fractional sea ice as standard, due to the sensitivity of these variables to the presence of open water. However with sea ice cover becoming thinner with the changing climate, and new sea ice products being made available, such as Cryosat II which now provides seasonal ice thickness datasets to the scientific community (CPOM, 2015) it is now imperative that the impact of decreasing sea ice thickness on the BL of the MIZ and further downstream is investigated. This will help inform the community of the importance of including sea ice thickness in NWP and climate simulations of high latitudes. In version 3.5, Polar WRF includes the ability to specify a variable sea ice thickness. With this new ability, idealised modelling experiments can be performed to examine the impact of reducing the ice thickness of the MIZ on the surface temperature, fluxes, boundary layer structure and transition and any downstream effects. This chapter will first discuss the set-up of these experiments, before examining the results for each area in turn, before making recommendations about the inclusion of sea ice thickness in NWP and climate simulations.

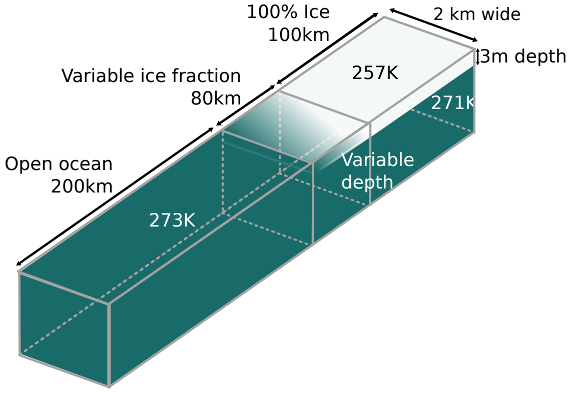

Figure 3.1: A schematic diagram of the quasi-two dimensional idealised domain (2 km wide). The sea ice fraction is linearly decreasing across the MIZ from 100% to 10%. The temperatures of the ice, water and water under sea ice are specified. The thickness of the ice in the MIZ is varied for the experiments.

3.2 EXPERIMENTAL SETUP

These experiments use the Weather Research and Forecast (WRF) model 3.5.1 with polar modifications PWRF) to the sea ice parts of the land surface model. PWRF 3.5.1 introduced the ability to specify the thickness of the sea ice and the depth of snow on sea ice (Hines *et al.*, 2015). For an in-depth description of WRF see chapter 2. The idealised sea breeze case gives a quasi-2D domain, consisting of a long strip of land/water two grid points (2 km) wide and a full height atmosphere. A horizontal grid resolution of 1 km is set, along with an integration time step of 3 s. The idealised cases allow full control over the surface and atmosphere initial conditions. A schematic of the domain is in Fig. 3.1, the domain and its results will be referred to from north to south, starting with the solid sea ice. The northern end of the domain is a 100 km long, 3m thick area of solid sea ice, representing MYI cover. The long upstream fetch ensures the atmosphere is fully equilibrated with the surface. The surface temperature of the MYI ice is set to 257 K initially, as this is the minimum temperature observed for Case 1 in Chapter 4 and the temperature of the water under the sea ice set to 271 K which is approximately the freezing point of sea water. The MYI is then followed by an 80 km section of fractional sea ice, as a MIZ. The fraction of the sea ice varies linearly between 100% and 10 %. The minimum was chosen to be 10% as below this the low sea ice fraction caused the albedo to become too low so defaulting to a higher value, which caused a spike in the albedo, with a knock on effect to the heat fluxes. Previous experiments such as Liu *et al.* (2006),Gryschka *et al.*

(2008), Vihma *et al.* (2005) and Dare & Atkinson (1999) have examined the impact of features such as leads and sea ice distribution on the formation of clouds over the MIZ, so here the impact of the sea ice distribution is not examined. Instead the impact of changing the sea ice thickness in the MIZ is studied. South of the MIZ is a 200 km stretch of open ocean, the surface temperature here is set to 273 K, the maximum temperature observed in Case 1 in Chapter 4. The length of the open ocean was selected to be sufficiently long to capture convection beginning off ice. As thinner sea ice would be optically transparent and have a lower albedo, a 5 cm layer of snow is prescribed upon the sea ice, to allow the effect of changes in albedo to be neglected, so only the thickness causes changes. WRF provides a mixed albedo over areas of mixed sea ice and water,

$$\alpha = fraction \times \alpha_{ice} + (1 - fraction) \times \alpha_{water}. \tag{3.1}$$

The atmosphere for the idealised case comprises of 75 levels, with 25 in the lowest 1 km, the model top is 50 hPa. The atmosphere is initialised with a profile of Q, θ and windspeed and direction, the sounding is shown in Fig.3.2, the basic values of θ and q were taken from ERA-interim at 82 °N 24.5 E at 00 UTC on the 31 March 2013, the date of Case 2 in Chapter 4 and then modified to dry out the lowest part of the atmosphere. The profile is chosen to be typical of a CAO. The profile was dried out to avoid the whole domain being filled with cloud. The wind direction is only from the north, in keeping with the 2D north-south alignment of the domain. The wind speed is given as an ideal logarithmic wind profile. The θ profile for the lowest 500 m is shown to the right in Fig 3.2, and highlights the neutral lowest layer and initial boundary layer height of 163 m. The surface temperature is 253 K over the ice, making the profile stable. In order to neglect the effects of a diurnal cycle, the sun's hour angle is held fixed, so the model is constantly insolated. This was done to isolate only the effect of changing ice thickness.

The model physics are set up as follows in Table 3.1, other than the surface layer and boundary-layer physics, the physics options are taken from Hines & Bromwich (2008) with the microphysics scheme updated from the WRF single moment scheme to the more advanced Morrison 2005 microphysics (Morrison *et al.*, 2005) scheme as in Bromwich *et al.* (2009). The option for a cumulus parametrisation is turned

Table 3.1: The control physics set up for WRF experiments

mp_physics	Microphysics	10	Morrison double moment scheme
ra_lw_physics	Long Wave	4	RRTMG
ra_sw_physics	Short Wave	4	RRTMG
sf_sfclay_physics	Surface Layer	4	QNSE-EDMF Surface
sf_surface_physics	Land Surface Model	2	Noah LSM
bl_pbl_physics	BL Scheme	4	QNSE-EDMF

off due to the convection-resolving spatial resolution of the model. The boundary layer scheme and corresponding surface layer scheme are chosen to be the QNSE-EDMF, which has been specifically developed for stably stratified turbulence over sea ice (Sukoriansky *et al.*, 2005). Some studies have also shown the QNSE-EDMF has promise in the Arctic (Kilpeläinen *et al.*, 2012; Mayer *et al.*, 2012). The surface layer and BL physics schemes are discussed in more detail in Chapter 2.

The thickness experiments use 5 different ice thickness values in the MIZ , as can be seen in Fig. 3.3. The thickness values broadly correspond to various types of sea ice in the real world, as outlined in the WMO sea ice nomenclature document (JCOMM, 2014). The control run has 3 m thick ice, this was chosen as 3 m is the current default ice thickness used in WRF and it corresponds to the thickness of the solid Multi Year ice (MYI) used in these experiments, so the control only has the effect of the fractional MIZ on the atmosphere. Next 1 m was chosen as it corresponds to typical first year ice thickness. The thinner experiments represent newer ice, being thin first year ice (0.5 m), grey-white young ice (0.25 m) and young ice (0.1 m). However the ice here is covered in snow and thus is white. The thinnest experiment represents the transition stage between nilas and first year ice. Experiments are named ITx where IT stands for ice thickness and the $x$is the value of ice thickness in m.

For each experiment, the model is run for 9 hours with a low time output resolution, which allows the model to 'spin up' and reach a quasi-steady state. As the wind speed is 10 m s^{-1} 9 hours means the air from the northernmost end of the domain has travelled 324 km, well beyond the end of the MIZ. The quasi-steady state was assessed by comparing cross sections over the whole time of the run, and when there ceased to be any substantial change between the half hourly snapshots, the model was deemed to have reached a quasi-steady state. A restart run is then begun, with the model now run for an hour with one minute output. The high time output allows turbulent fields to be averaged and give a broad snapshot of the

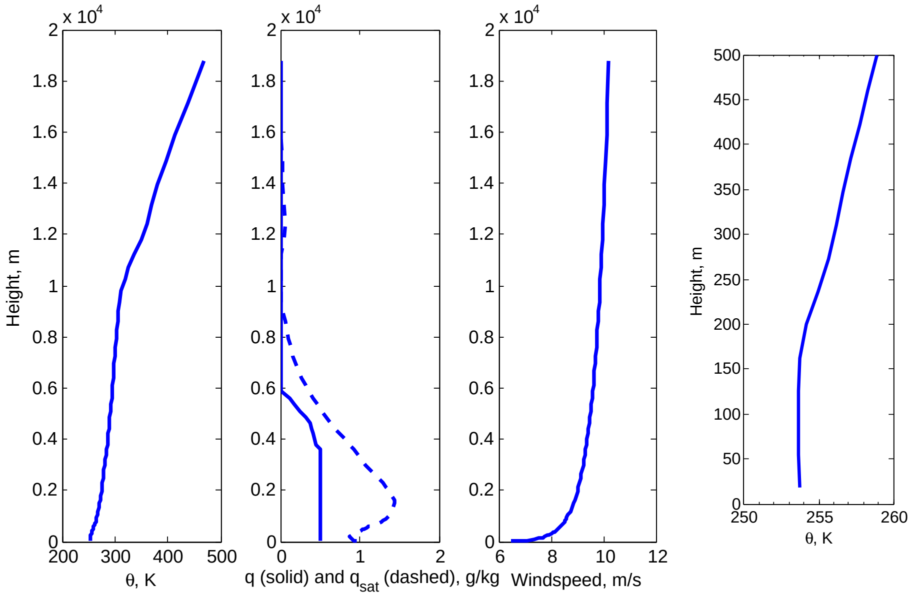

Figure 3.2: The initial profile provided to the model. The potential temperature and q were both taken from ERA-i and any features such as high clouds were removed. The windspeed is an ideal logarithmic wind profile. The profile of θ for the lowest 500 m is shown on the right.

average behaviour, rather than instantaneous values which may miss details due to the turbulent nature of some of the phenomena being examined, such as the convection.

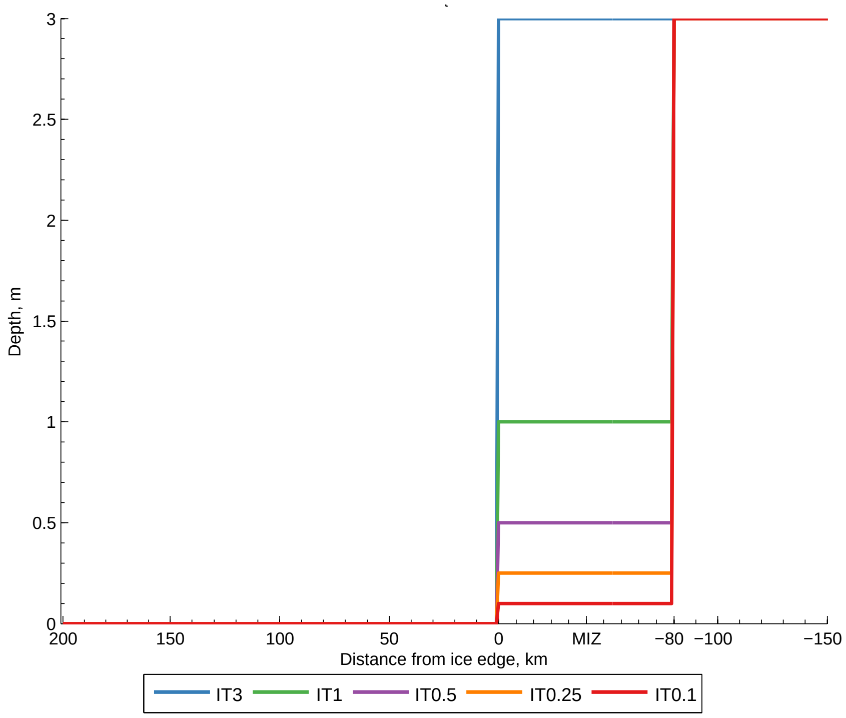

Figure 3.3: The ice thickness in the MIZ (0 to -80km) is varied for the five experiments. The ice thickness has a step change between the pack ice and the MIZ, and is the same for the whole MIZ.

3.3 RESULTS

3.3.1 SURFACE

The most immediate impact of changing the ice thickness is at the surface. Note that the surface temperature (T_{sfc}) in PWRF is calculated for a fractional sea ice area in the same way as α in Eq. (3.1), as a weighted average between the open water temperature and the ice surface temperature. The T_{sfc} over the ice is calculated using

$$H\frac{\partial T_{sfc}}{\partial t} = \epsilon\left[LW\downarrow - \sigma T_{sfc}^4\right] + (1-\alpha)SW\downarrow - T_r - SHF - LHF + GHF + Q_t. \tag{3.2}$$

Where H is the heat capacity of relevance to the skin temperature, σ is the Stefan-Boltzmann constant, T_r is the SW radiation transmitted beyond the surface, and Q_t represents other diabatic processes such as phase change and heat flux by precipitation (Hines *et al.*, 2015).

The T_{sfc} increases linearly across the MIZ (Fig. 3.4), due to the averaging including a linear change in sea ice fraction as the weighting. The effect of thinner ice on T_{sfc}

can only be seen in the MIZ, most clearly as a sudden jump in surface temperature at the start of the MIZ. The largest differences are recorded at the start of the MIZ, with a +2.9 K difference here for IT0.1 compared to IT3. At the start of the MIZ the change in ice thickness is much more important as the ice fraction is high, meaning a change in surface temperature is caused mostly by the decrease in sea ice thickness and the corresponding increase in amount of heat which is diffused through the ice (GHF). The first line of Table 3.2 shows the maximum difference from IT3 for each experiment, which shows that thinner ice means a warmer surface temperature. The magnitude of the T_{sfc} differences increase as the ice thickness decreases, this is especially noticeable between IT0.5 and and IT0.25, which shows a non-linear relationship between sea ice thickness and T_{sfc}. There is a 3 K difference between the temperature at the end of the MIZ and the temperature of the open water, showing the impact of even low concentrations of sea ice on the surface temperature in the model. Over open water the values of T_{sfc} all converge at 273 K, the value given for open water temperature in the initialisation. While the surface temperature of the ice is able to vary, the surface temperature of the sea is held fixed in this idealised model.

The ground heat flux through the ice (GHF, upwards positive) is shown in Fig. 3.5 and forms part of the calculation for T_{sfc}. GHF is calculated in the model by solving the equation for the diffusion of heat through the sea ice and snow using the temperature given for under the sea ice, and the thickness of the sea ice and snow, and a thermal conductivity which is moderated by the snow cover and condition, when there is no snow cover the thermal conductivity has a value of 2.2 W/mK. See Chapter 2 for more information.

For the control run IT3, the ground heat flux in Fig. 3.5 over the MIZ only changes due to the presence of the fractional sea ice, as there can be no ground heat flux through the open water, the values decrease across the MIZ as there is more open water (again the value is weighted by ice fraction). Just as for the T_{sfc} in Fig. 3.4, as soon as the surface changes from the MYI to the MIZ there is a sudden jump in GHF which is particularly obvious for IT0.1, with a +56.3 Wm^{-2} increase in GHF. The second line of Table 3.2 shows that for GHF the reduction in ice thickness leads to an increase in flux, with there being a point between IT0.5 and IT0.25 where the surface becomes more sensitive to the reduction in ice thickness. This increase in GHF is what is causing the changes in T_{sfc} seen in Fig. 3.4. Note the GHF plot does

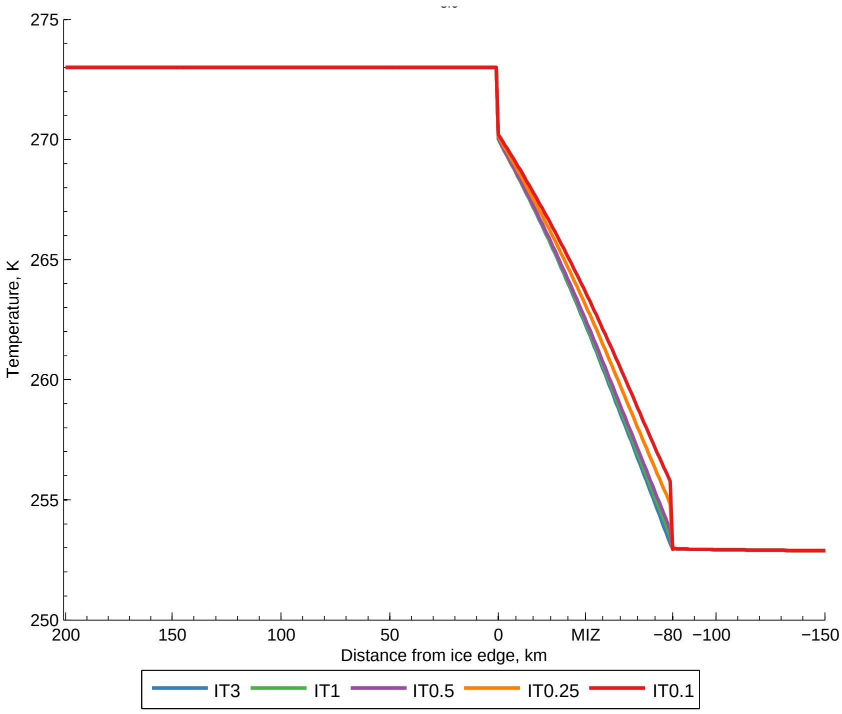

Figure 3.4: The surface temperature (T_{sfc}) in K, averaged over one hour.The airflow is travelling N-S (right to left).

show an odd negative value caused by a point with exactly 10% sea ice concentration, which creates a problem with the snow cover, leading to a spurious GHF value.

Table 3.2: Table showing maximum T_{sfc} (in K to the nearest 0.1K) and ground heat flux GHF (in W/m^2) differences from IT3

	IT1	IT0.5	IT0.25	IT0.1
T_{sfc} maximum difference from IT3	+0.3	+0.5	+1.6	+2.9
GHF maximum difference over MIZ	+3.9	+7.9	+32.0	+56.3

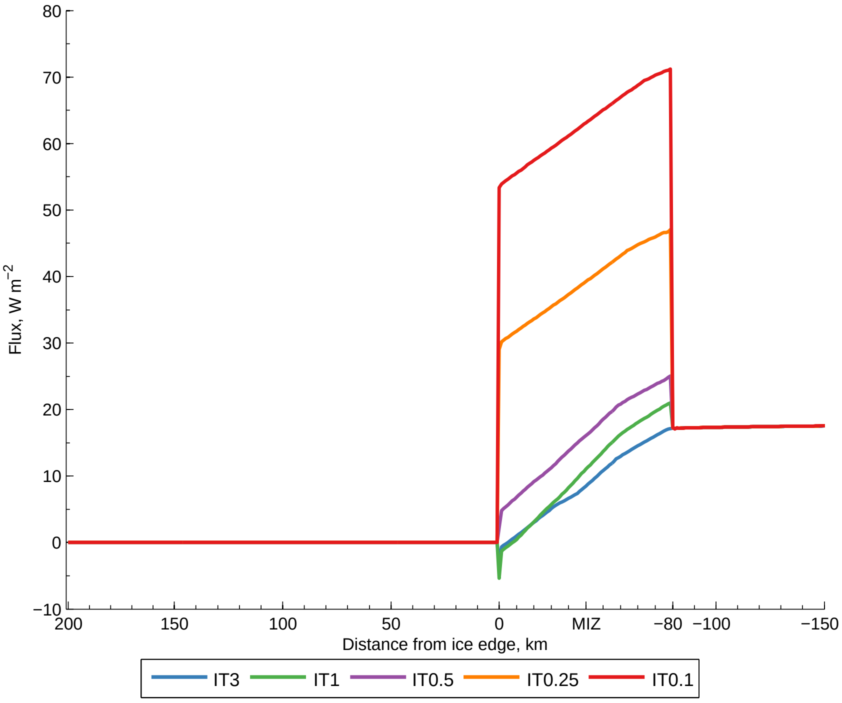

Figure 3.5: The ground heat flux, GH in Wm^{-2}. The negative spike in GHF for IT1 is linked to the sea ice concentration in the final sea ice point being 10% as this causes problems for the snow cover. The airflow is travelling N-S (right to left).

3.3.2 FLUXES

The thinner ice might be expected to allow an increase in surface heat flux into the atmosphere, as it is less insulated from the ocean. This means that with a larger GHF, sensible heat flux (SHF) and latent heat flux (LHF) would also increase as the surface is warmed, and the difference in temperature between the surface and the atmosphere increases.

The SHF in Fig. 3.6 shows the effect of thinner ice, as soon as the ice becomes thinner over the MIZ, there is an increase in SHF. The increase in SHF is coincident with the increase in T_{sfc} in Fig. 3.4. The maximum difference is between the control and IT0.1 with IT0.1 being 45.5 Wm^{-2} higher.

LHF also shows the same features as SHF (Fig. 3.7), with a maximum difference of +16.3 Wm^{-2} between IT0.1 and IT3 over the MIZ. At about 150 km downstream from the ice edge, SHF and LHF become less smooth and show an oscillation, which coincides with the onset of convection in the model, as discussed later in section 3.3.4. The exchange coefficient reflects the up and down-drafts shown in w-wind, with an oscillation, which causes the oscillations in the fluxes. An interesting feature

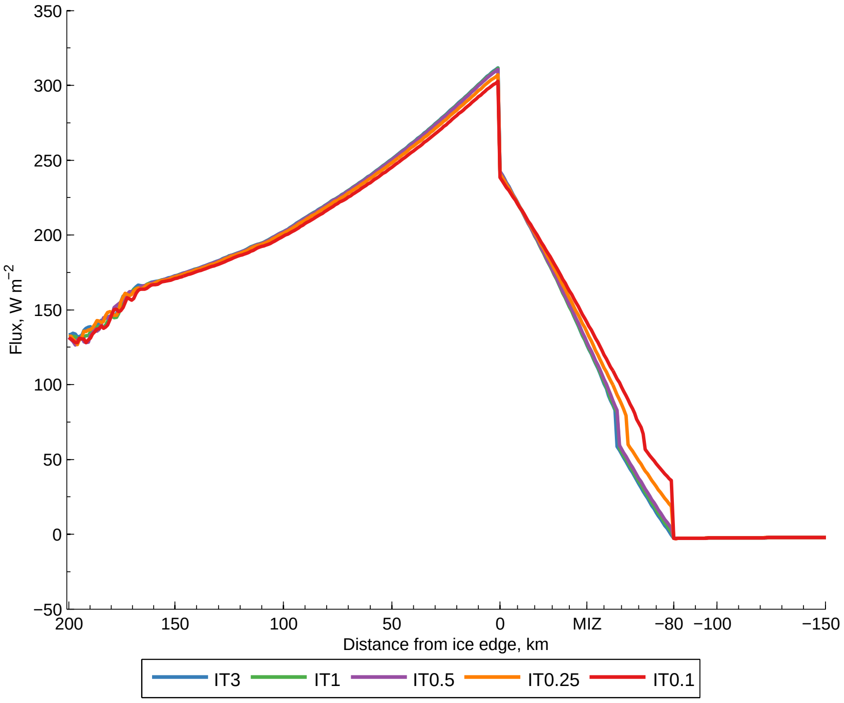

Figure 3.6: Surface sensible heat flux (SHF) in Wm^{-2}. The airflow is travelling N-S and thus the plot should be read right to left.

in Fig. 3.6 is that all the experiments show a sudden increase in the SHF over the MIZ, and this occurs in different places for the different ice thickness experiments and is discussed in more detail below.

Over the MIZ both LHF and SHF fluxes are larger for thinner ice, whereas over the open water the SHF and LHF fluxes are largest for the thickest experiments. Once over open water, the SHF and LHF differences are negative when compared to the control for all experiments. This follows from the method of calculating the fluxes detailed below in 3.3.2 and discussed in more detail in Ch. 2, where the difference between the surface and atmosphere is what drives the flux. As the atmosphere is warmed by the increased fluxes, so the difference between the surface and atmosphere decreases, leading to a reduction in fluxes downstream (Fig. 3.8). The difference between surface and air temperature is shown in Fig. 3.8 and reaches a maximum at the edge of the MIZ, and then decreases across the open water. When looking at both the MIZ and the open water (termed ALL) the effect of thinner ice is decreased. Table 3.3 shows the bias between the average values for SHF and LHF for the different experiments. IT0.1 has 2.1 Wm^{-2} higher SHF and 1.3 Wm^{-2} higher LHF than the control, these are equivalent to a + 1.1 % and + 1.5% change from

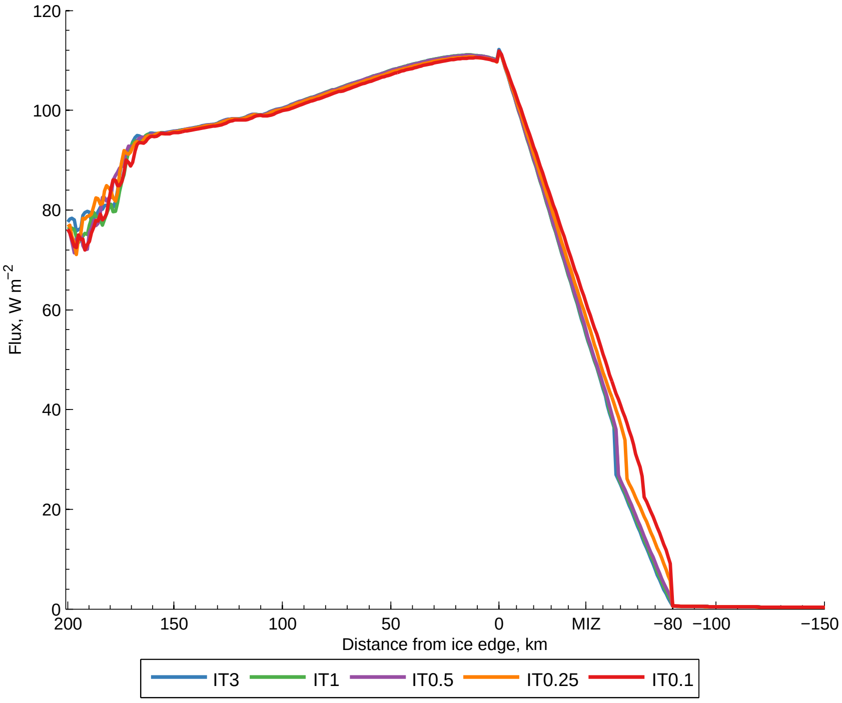

Figure 3.7: Latent heat flux (*LHF*) for the five different thickness experiments, Wm^{-2}.

IT3 respectively, implying that the changes in ice thickness impact *LHF* and *SHF* significantly locally over the MIZ, but have little impact further downstream.

It is thought that the MIZ is a significant source of moisture for the Arctic (Gultepe *et al.*, 2003; Liu *et al.*, 2006). The moisture flux M (not shown) increases sharply across the MIZ, from 0 kg/(m^{2}s) over the MYI to a maximum of 4.4 $\times 10^{-5}$ kg/(m^{2}s) at the end of the MIZ.These values seem sensible according to Boisvert *et al.* (2012), who compared satellite derived moisture flux data for Arctic polynas, which are areas of open water within sea ice areas, to observations taken during field campaigns and find mean maximum moisture fluxes of up to 4.9 $\times 10^{-5}$ kg/(m^{2}s). As *LHF* is calculated using M ($LH = L_v \times M$, where $L_v = 2.5\times 10^{-6}$ J/kg is the latent heat of vapourisation), the two curves have the same shape so only the *LH* plot is shown.

Table 3.3: Table showing the difference (experiment - control) in average *SHF* and *LHF* over both the MIZ and the open water (ALL) along with the percentage difference from the control.

	IT1	IT0.5	IT0.25	IT0.1
SHF difference in average over ALL (Wm^{-2})	-0.2	+0.1	+1.5	+2.1
% difference from IT3	0.1	0.05	0.8	1.1
LHF difference in average over ALL (Wm^{-2})	-0.1	+0.1	+0.8	+1.3
% difference from IT3	0.1	0.1	0.9	1.5

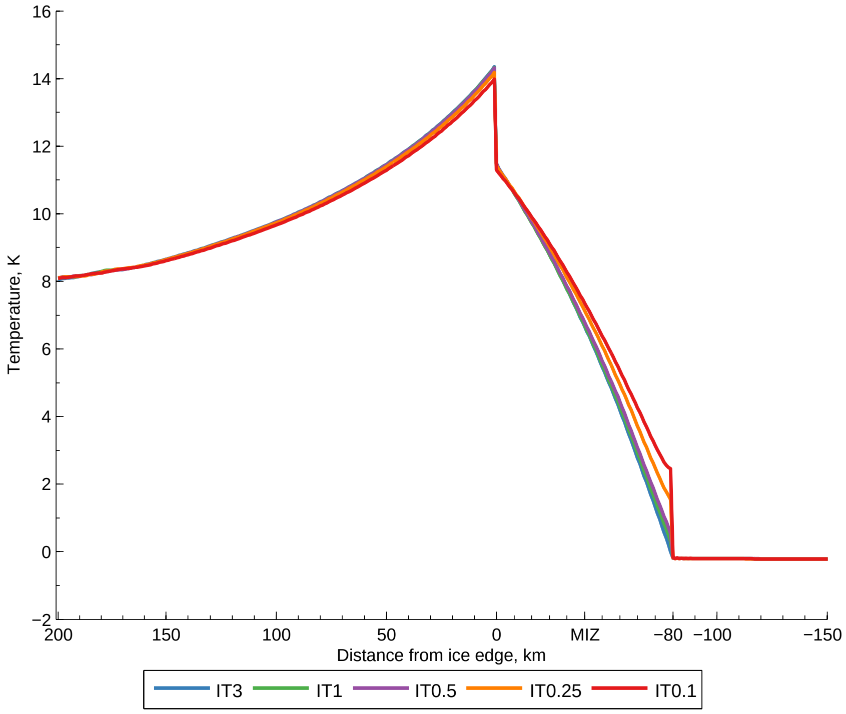

Figure 3.8: Difference between surface and lowest level atmosphere temperature ($T_{sfc} - T(1)$), K.

THE JUMP IN THE FLUXES

A prominent feature in the plots of LHF and SHF in Figs. 3.7 and 3.6 is a jump occurring over the MIZ. This jump is not realistic and thus must be some aspect of the model physics. The jump doesn't occur in the same place (i.e. with the same ice fraction) for each experiment, as can be seen in Fig. 3.9 which shows the ice fraction against thickness. There is a non-linear relationship between ice thickness and the location of the start of the jump. Thus the change in ice thickness by itself does not cause the change in location of the jump, but rather it must affect some other variables which impact on the flux jump instead.

The fluxes for mixed ice-water areas are calculated twice, once for water (in the surface layer scheme) and once for ice (the Land Surface Model, LSM). The surface layer scheme provides the surface exchange coefficient for ice surfaces (C_{Hice}) to the LSM. After the fluxes have been calculated they are then blended along with the exchange coefficients for the areas of fractional sea ice, using a mosaic method (Vihma, 1995). Therefore the surface exchange coefficient and surface temperatures that the model provides as the output are not actually what is used to calculate the fluxes over the MIZ.

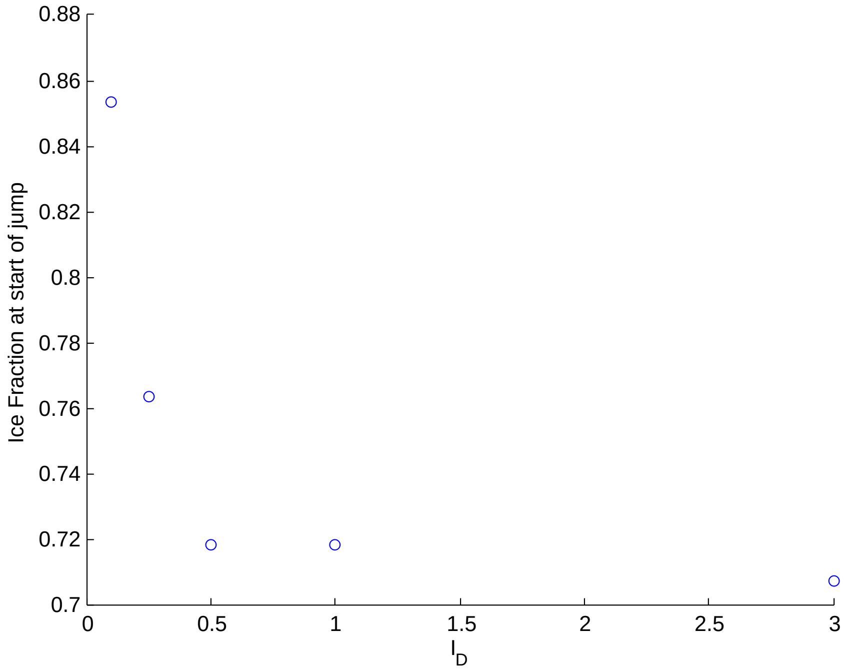

Figure 3.9: The ice thickness (m) and the corresponding ice fraction (0-1) of the location of the start of the jump in the fluxes.

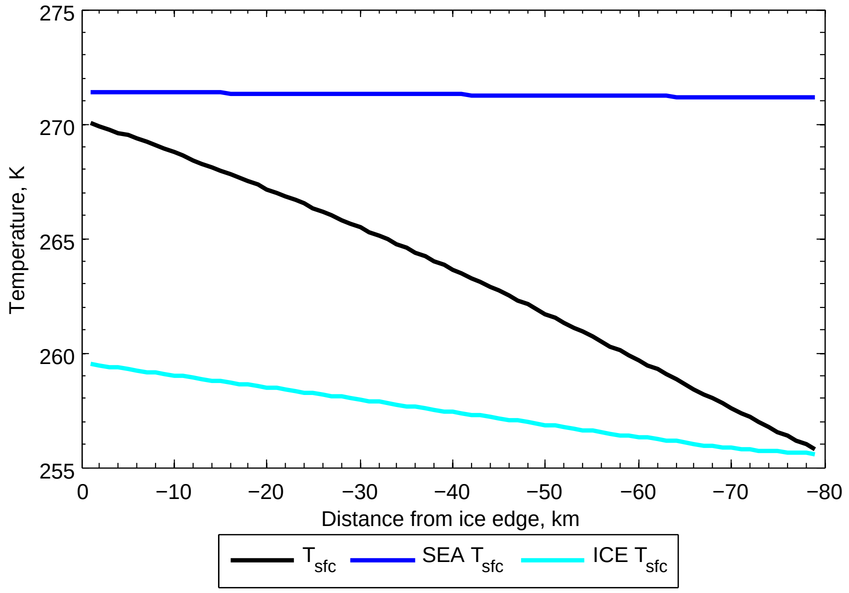

Figure 3.10: The blended T_{sfc} (black) along with the split T_{sfc} for both sea (dark blue) and ice (light blue) over the MIZ, for IT0.1 (K).

Firstly the model splits the T_{sfc} into an ice and water T_{sfc}, as shown in Fig. 3.10. (Here IT0.1 has been re-run with edited code so these separated variables are output). It can be seen that the T_{sfc} for the sea is set at 271.2 K, while the ice T_{sfc} varies between 256.6 and 259.5 K.

Once the T_{sfc} has been split, the model then calculates the exchange coefficients

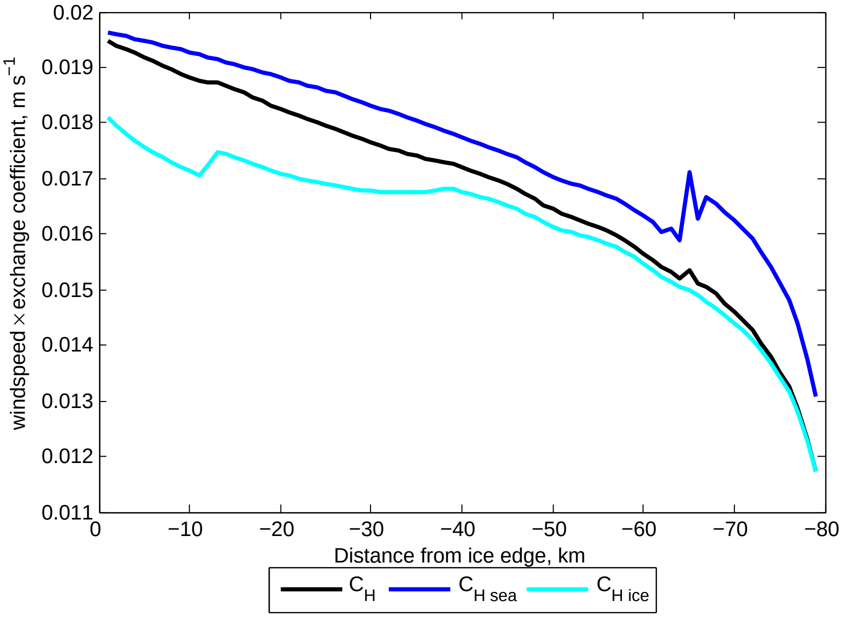

Figure 3.11: The blended exchange coefficient, CH (black) along with the split CH for both sea (dark blue) and ice (light blue) over the MIZ for IT0.1, all values in m s^{-1}.

$\mathbf{U}.C_{Hice}$ and $\mathbf{U}.C_{Hsea}$ in the surface layer scheme. These are given in units of m s^{-1} and are technically a conductance as they have been multiplied by windspeed, $\mathbf{U}$. The calculation of C_H is complicated, involving Monin-Obhukov similarity theory along with corrections for the different atmospheric stabilities and an iteration using the Beljaars correction for friction velocity (Beljaars, 1995). The resulting split values for $\mathbf{U}.C_H$ are shown along with the standard model output which is a blend of the two values in Fig. 3.11. The values for $\mathbf{U}.C_{Hsea}$ are higher than those for $\mathbf{U}.C_{Hice}$ and show a small spike at about the location of the jump in the fluxes.

After finding the $\mathbf{U}.C_H$ for both sea and ice the model then solves for SHF. Over ice the model calls the LSM which solves,

$$SH = -\frac{C_{Hice}c_pP_{sfc}}{R\theta_v(1)}(\theta(1) - (ICET_{sfc})) \tag{3.3}$$

where c_p is the specific heat capacity for air, P_{sfc} is the pressure at the surface, R is the gas constant. The $\theta_v(1)$ and $\theta(1)$ are virtual potential temperature and potential temperature at the lowest model level and $ICET_{sfc}$ is the ice part of the surface temperature.

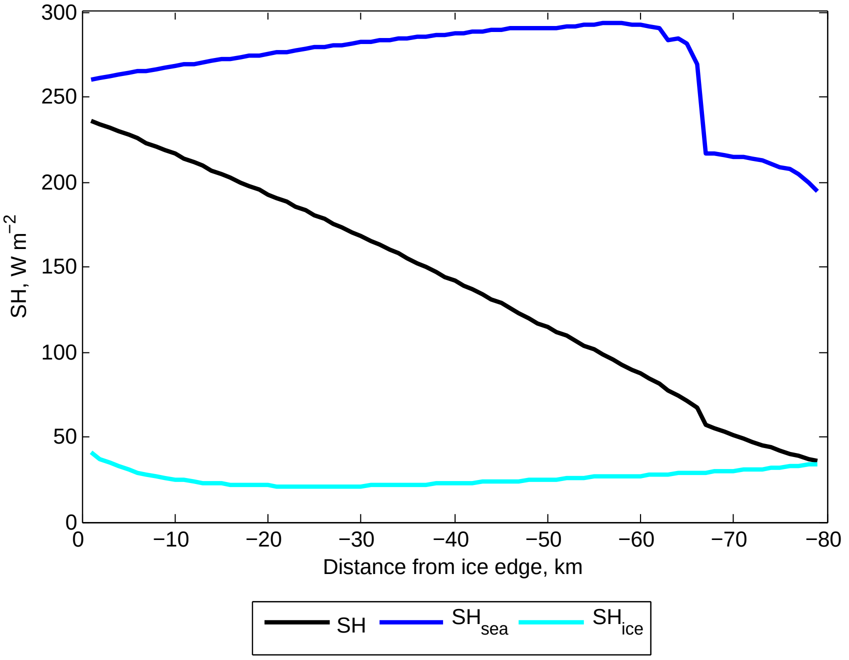

Figure 3.12: The blended SHF (black) along with the split SHF for both sea (dark blue) and ice (light blue) over the MIZ for IT0.1, all values in Wm^{-2}.

Over open water, the surface layer scheme is called and it uses,

$$SH = -\frac{C_{Hsea} c_p P_{sfc}}{RT(1)} (\theta(1) - \theta(z_0)) \tag{3.4}$$

where z_0 is the roughness length. The split SHF can be seen in Fig. 3.12. It is immediately obvious that the jump in the blended fluxes (black) is related to a much larger jump in SH_{sea} (blue) . The blended value is reduced due to the much lower flux over the ice. The start of the jump is exactly coincident with the start of the small oscillation in C_{Hsea} seen in Fig. 3.11. Interestingly though, the values of C_{Hsea} are actually reduced after the oscillation, while the values of SHF are increased and then begin to decrease while CH_{sea} increases. Implying that it isn't just the exchange coefficient which has a problem, but possibly also the difference $(\theta(1) - \theta(z_0))$ (not shown). Once again there is a jump in the values here, at the same point as the other plots. This jump is passed on from $\theta(z_0)$. The calculation for $\theta(z_0)$ includes a weighting which is also dependent on the exchange coefficient.

The flux between surface and atmosphere is related to the stability of the atmosphere above, a more stable atmosphere would inhibit fluxes, while an unstable convective boundary layer would increase fluxes. The parametrisations for surface fluxes are often derived for a neutral atmosphere and then require correcting for the different stability possibilities. The stability correction functions are often denoted ψ and based on Monin-Obhukov similarity theory (Stensrud, 2007). In the QNSE-EDMF scheme, the stability functions values are initially calculated and stored in a look-up table. Then using an index calculated using the Monin-Obhukov length scale, the value of the stability correction is interpolated from the look-up table. For sensible heat the stability correction part of the calculation for C_H is termed $SIMH$. See Ch. 2 for more information about the stability corrections. As the boundary layer is changing rapidly across the MIZ, the stability functions could change value suddenly, as the atmosphere changes from unstable to stable. To test if the stability function is changing too fast due to the fast change in sea ice fraction, an additional version of IT0.1 with a 160km long MIZ was run. The longer MIZ was also to check if the transition could be slowed down and avoid the jump, or if the jump was actually caused by interference from waves set off at the ice edge.

The over sea component for SHF over the MIZ for IT0.1_longMIZ has a jump at almost exactly the same place near the start of the MIZ (figure not shown), which implies that the jump is not something that is caused by waves from the end of the MIZ interfering with the BL over the MIZ. Looking at Fig. 3.13 which shows the stability correction $SIMH$ over the sea, it can be seen there is a dramatic jump in the value of the function. This jump coincides with that in C_{Hsea} and then SHF. It can be concluded that the rapidly changing atmospheric stability over the MIZ, causes there to be a very sudden change in the stability correction $SIMH$, which may be caused by the lookup table being too coarse. The change in stability correction then affects the exchange coefficient and then the fluxes. The flux values themselves are not unreasonable, and if the MIZ were to include features such as leads, a sudden jump in fluxes would be expected. The jump in the fluxes can therefore be thought of as a feature of the model's code which has come to light due to the idealised and thus unrealistic surface of linearly changing sea ice fraction.

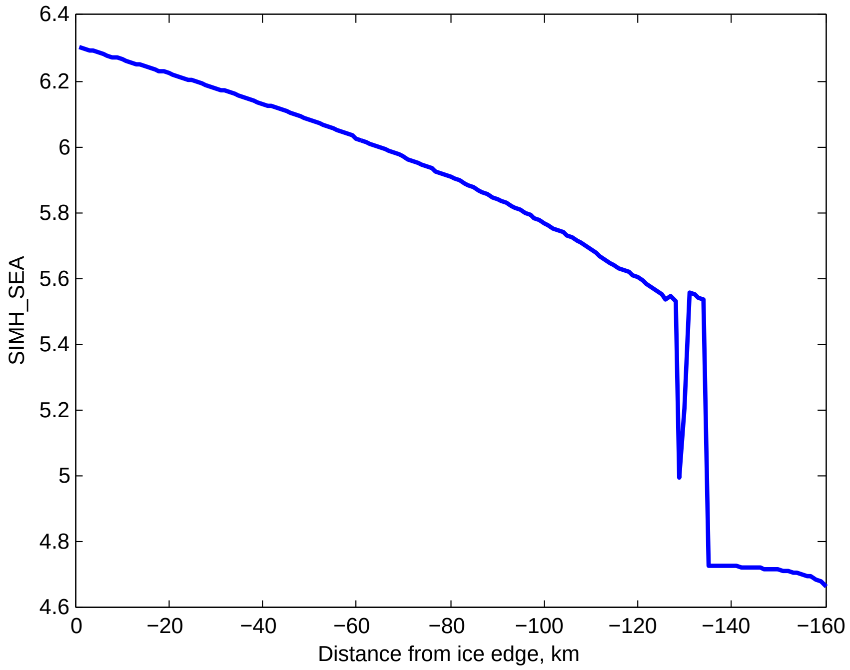

Figure 3.13: Values of $SIMH$, the stability correction for heat flux, over the 160km long MIZ in the extra experiment IT0.1_longMIZ.

3.3.3 BOUNDARY LAYER

As the boundary layer passes over the MIZ, it is modified by the surface below and transitions from a stable BL over the MYI to a convective BL over the open water (Liu *et al.*, 2006; Gryschka *et al.*, 2008). The changes made to the ice thickness and the subsequent increase in fluxes of heat and moisture would be expected to impact this BL transition and is investigated here.

Profiles of potential temperature θ, over the MIZ are shown in Fig. 3.14 along with the BL height indicated by a dot. The BL height is defined as the height of the inversion which is given by,

$$h_{inv} = \max\left(\frac{\partial^2\theta}{\partial z^2}\right). \tag{3.5}$$

As the model has discrete layers, the dots lie on top of one another, so not all dots are visible. Most immediately apparent is that all the profiles show a warming and destabilising of the mixed layer, the bottom of the column is at 18 m and this warms by up to 5.9 K over the MIZ for IT0.1 due to the atmosphere responding to SHF (Fig. 3.6) convergence and warming continuously as it passes over the MIZ. The profile also changes from statically stable at the start of the MIZ (-80 km) to absolutely unstable at the end of the MIZ. The thinner experiments have a warmer mixed layer across the whole MIZ with the maximum temperature difference between IT0.1 and IT3 being 0.6 K from -60 to -20 km from the ice edge. As for the surface fluxes there is a non-linear relationship between the mixed layer temperature and surface thickness. The thicker experiments, IT3, IT1 and IT0.5 all have maximum mixed layer temperature which are very close together, with at most a 0.1 K difference between them. This again implies that the the atmosphere becomes increasingly sensitive as the ice becomes thinner.

The other most obvious feature in Fig. 3.14 is the BL height. Starting near 163 m for all the experiments, the inversion height then increases fastest for experiments IT0.25 and IT0.1, so that by the middle of the MIZ (-40 km) the inversion is about 37 m higher for those experiments. The other profiles then catch up, with the final profile at 0 km having only IT0.1 with a higher inversion (468 m compared to 430 m). As the model has discrete levels the BL heights fall on one of these vertical levels, which is why the dots are all on top of one another.

While Fig.3.14 shows that the thinner experiments have warmer mixed layers, in order to see the rate of the increase in the lowest level θ Fig. 3.15 shows this across the whole MIZ. It can be seen in Fig. 3.15 that for most of the MIZ the thinnest experiments have slightly (0.1 K) warmer lowest layers than the control. The atmosphere for IT0.1 and IT0.25 changes much faster upon reaching the MIZ (0.2 K/km and 0.15 K/km respectively) when compared to IT3 which changes by less than 0.1 K km^{-1} over the first few km. The difference in speed of change is due to the more sudden change in ice thickness and the attendant increase in surface temperature for the thinner experiments. The rate of change of θ remains the fastest for IT0.1, while IT0.25 joins the other experiments, then by -55 km from the ice edge the thicker experiments IT3, IT1 and IT0.5 begin to change at the same rate as IT0.1 and IT0.25 (0.08 K km^{-1}). This location is where there the differences between the fluxes in SHF are reduced, as shown in Fig 3.6. As the surface is warmer and SHF and LHF larger at the very start of the MIZ for the thinner ice experiments, so the lowest level of the atmosphere is warmed first and fastest. This then results in a more unstable BL and a higher capping inversion for the thinner experiments. The spread in temperatures in the mixed layer is largest across the middle of the MIZ, from -60 to -20 km from the ice edge. As the fluxes begin to be larger for the thinner experiments by the end of the MIZ and over the open water, so the BL becomes warmer. Eventually further down stream all the experiments converge to one BL height and temperature, driven by the temperature of the open water, which is the same for all experiments.

The specific humidity q also changes over the MIZ, in response to both the changing moisture flux and the increasing boundary layer height. In Fig. 3.16 the values for q for the five different experiments are shown, along with the BL height marked as a dot. It can be seen that values for q increase across the MIZ, with the increase being largest in IT0.1 at 0.34 g kg^{-1} compared to 0.32 g kg^{-1} for IT3. The 0 and -20 km plots show a reduction in q above 250 m and 300 m respectively when compared to lower down in the BL, implying that the top of the boundary layer is being dried out by the entrainment of dry air from above the BL. In Fig. 3.17 the values of Turbulence Kinetic Energy, TKE are shown for each experiment across the MIZ. The TKE is indeed non-zero across the top of the BL, which is again marked as a dot, which confirms that there is entrainment of dry air down from above the BL, which is reducing the values of q in the top of the BL.

The TKE is not only implying the existence of entrainment, there are differences in the lowest part of the boundary layer as well. Across the MIZ the TKE increases in the BL for all experiments, with the thinner experiments having a higher TKE value. Indeed at -70 km from the ice edge, TKE is highest for IT0.1 at 0.16 m^2 s^{-2} compared to 0.1 m^2 s^{-2} for IT3, the TKE also extend up to over 300 m for both IT0.1 and IT0.25 which is 25 m higher than for IT3. The TKE also increases faster for IT0.1, at -60 km from the ice edge, the maximum TKE for IT0.1 has increased to 0.21 m^2 s^{-2} (+0.05) compared to 0.14 m^2 s^{-2} (+0.04) for IT3. This follows from the θ plots, as the BL is more unstable for the thinner experiments at the start of the MIZ there is higher TKE. Eventually as the thicker experiments become more unstable later in the MIZ the TKE values become closer so that by the ice edge there is only a 0.01 m^2 s^{-2} difference between the experiments. Higher TKE values within the BL would enhance the turbulent transport of heat and moisture upwards into the atmosphere. The increased tubulent mixing would also act to increase the availability of CCN and IN to the atmosphere, changing the microphysical properties of the clouds above.

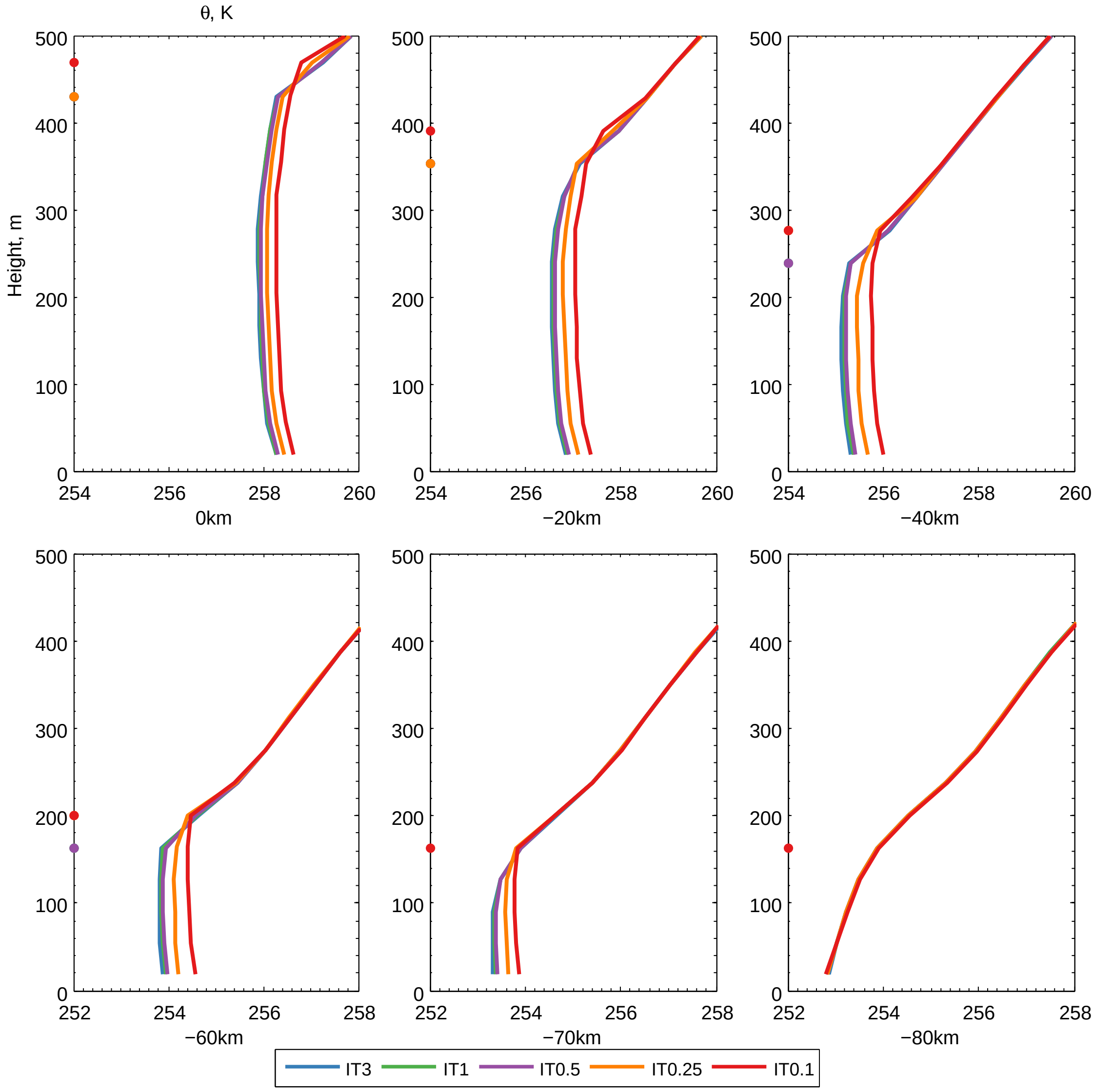

Figure 3.14: Profiles of θ over the MIZ, the start of the MIZ is at the bottom right at -80km and the end of the MIZ is in the top left at 0km. Note the change in x axis between the two rows. The BL height as defined by eqn. 3.5 is shown as a dot on the y axis in the colour of the experiment. Due to the discrete levels used within the model, the dots fall on top of one another, so not all the dots are visible.

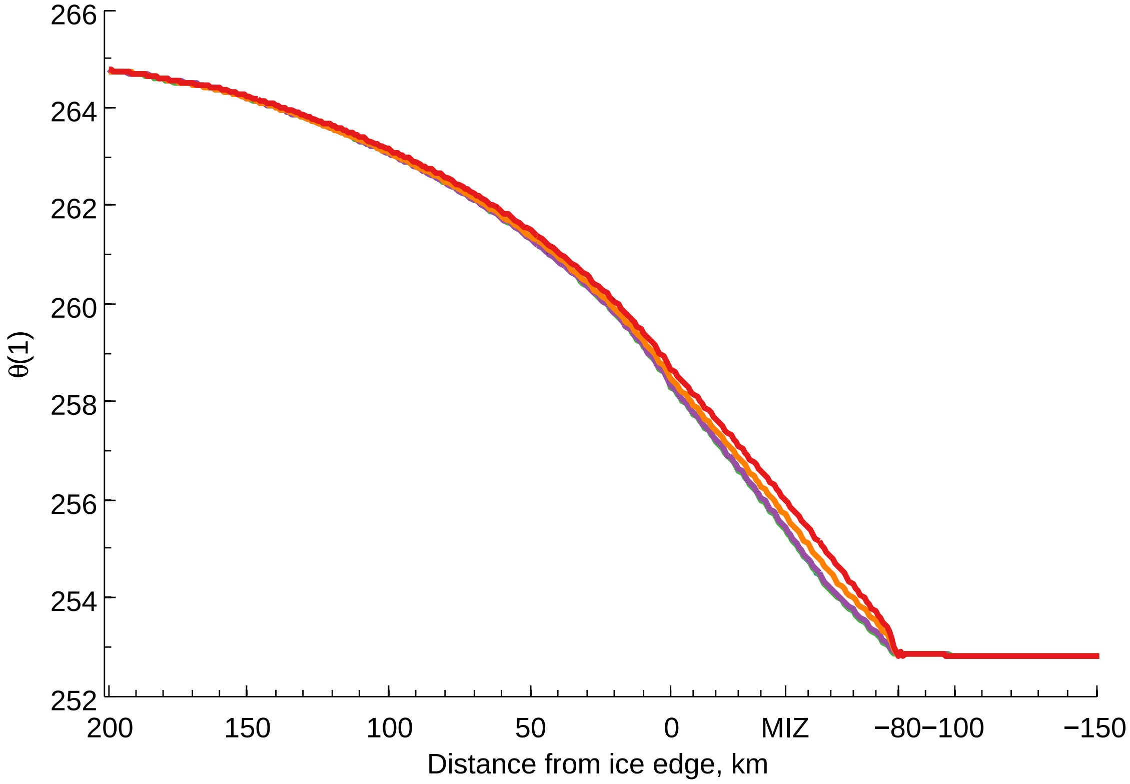

Figure 3.15: Lowest level (20 m) θ

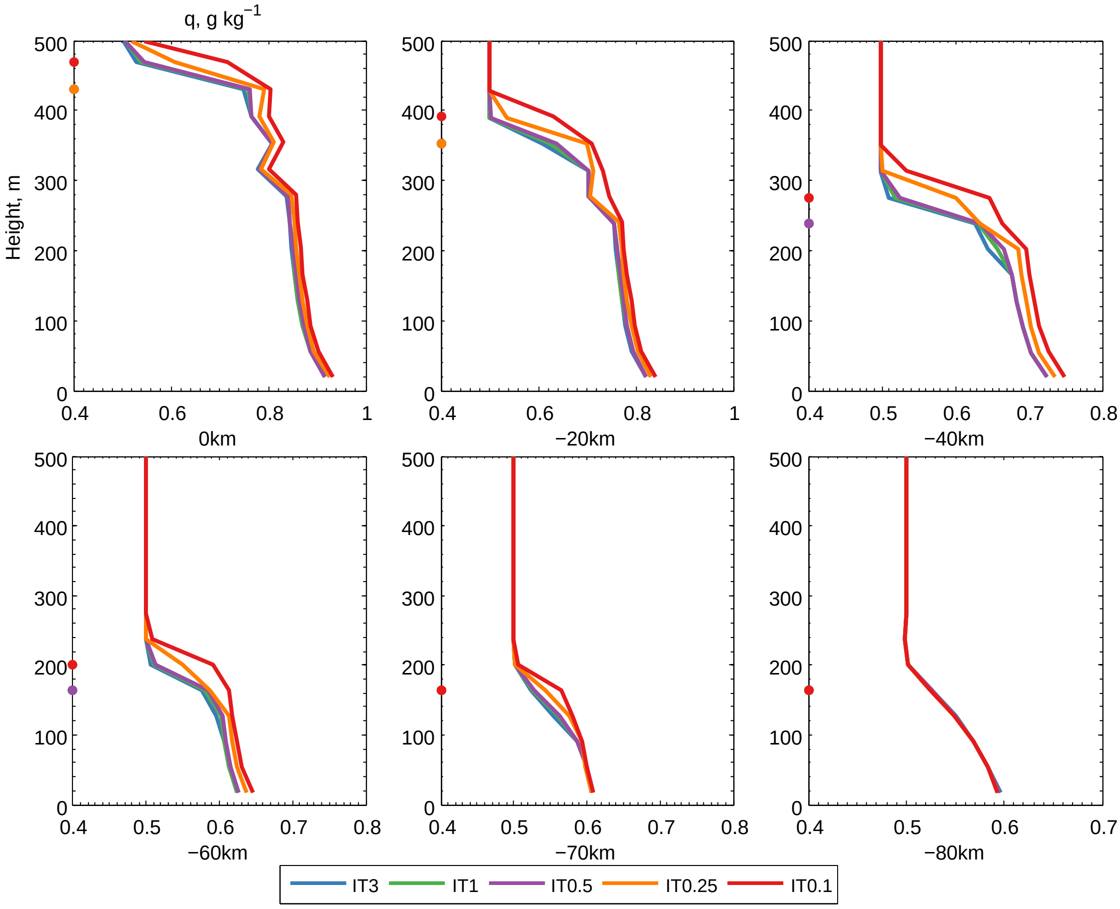

Figure 3.16: Profiles of q (g kg^{-1}) over the MIZ, the start of the MIZ is at the bottom right at -80km and the end of the MIZ is in the top left at 0km. Note the change in x axis between the plots. The BL height as defined by eqn. 3.5 is shown as a dot on the y axis in the colour of the experiment.

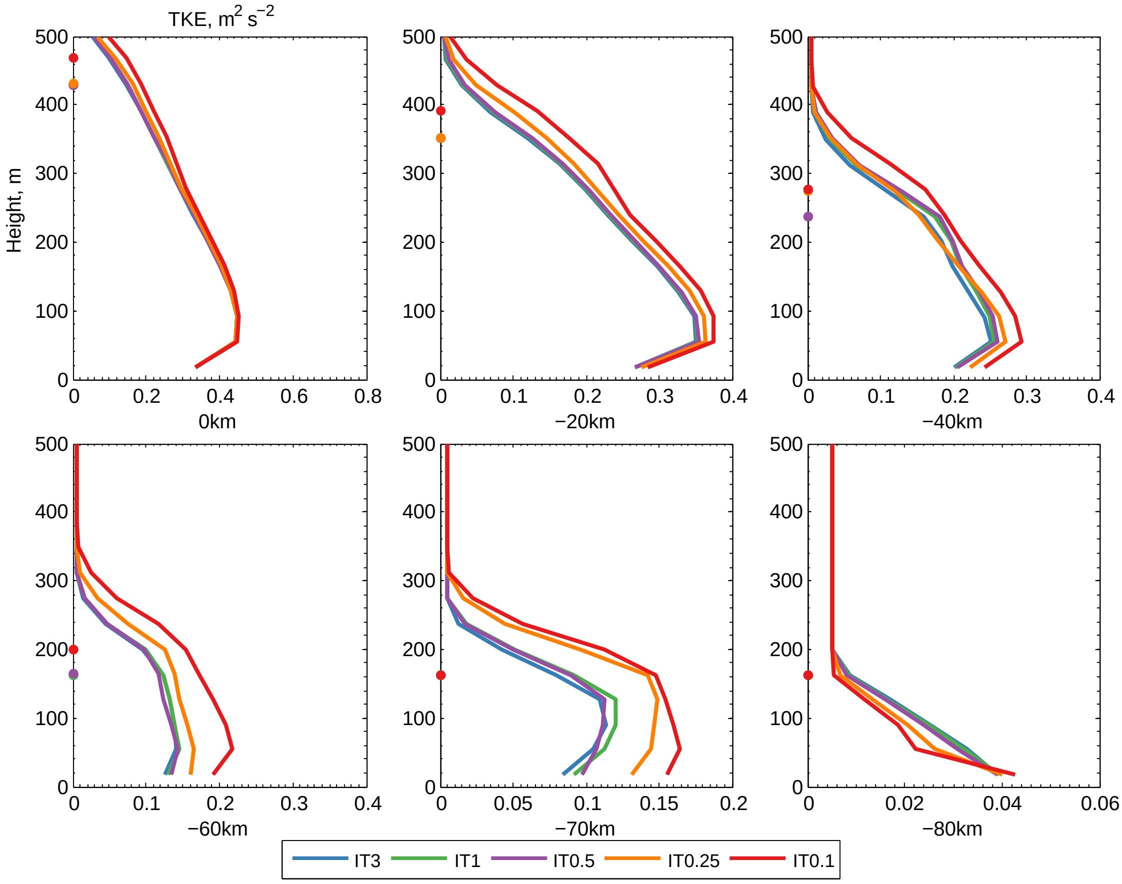

Figure 3.17: Profiles of TKE ($m^2\ s^{-2}$) over the MIZ, the start of the MIZ is at the bottom right at -80km and the end of the MIZ is in the top left at 0km. Note the change in x axis between the plots. There is a minimum value set at 0.005 $m^2\ s^{-2}$. The BL height as defined by eqn. 3.5 is shown as a dot on the y axis in the colour of the experiment.

ATTRIBUTING BL HEATING.

It would be instructive to investigate whether the heating of the boundary layer is primarily driven by flux convergence. As WRF only outputs fluxes in the surface layer and land surface model, they are only 2D fields. There is no option to output fluxes at model levels. Thus a direct calculation of flux convergence by looking at the gradient of a vertical flux profile is not possible. In order to then establish the source of heating for the BL a thermodynamic approach is used. Following Zeng *et al.* (2014) the change in heat of a parcel of air can be written as,

$$\frac{\partial T}{\partial t} = -\mathbf{V}.\nabla T + w\left(\gamma_d - \gamma\right) + Q_t, \tag{3.6}$$

where $\mathbf{V}$ is the horizontal wind vector with w the vertical component, γ_d and γ are the dry adiabatic lapse rate and the environmental lapse rate respectively and Q_t is the diabatic heating term which represents, among other things, heating by flux convergence, radiation and condensation processes. The Q_t is taken to mainly represent the heating by flux convergence (Zeng *et al.*, 2015). This assumption can be made as over the whole MIZ the solar forcing is identical due to the lack of clouds. While there is some water vapour present over the MIZ, the phase change (from liquid to vapour) would act to cool the BL, so any positive value of Q_t implies that the heating by fluxes is larger than the latent heat used by the phase change.

The first term on the RHS represents advection (ADV), so the advection of cold air would cool the boundary layer and vice versa. The second term represents heating by convection (CONV) and implies that under a stable atmosphere where $\left(\gamma_d - \gamma\right) < 0$ ascending motion would induce cooling while under unstable conditions $\left(\gamma_d - \gamma\right) > 0$ ascending motion would induce heating of the lowest layer of the atmosphere. Thus eqn. 3.6 can be re-written as,

$$\frac{\partial T}{\partial t} = \mathrm{ADV} + \mathrm{CONV} + Q_t. \tag{3.7}$$

The ADV, CONV and change in heat terms are easy to calculate with WRF output, however the Q_t must be calculated as the residual of the other terms. Following Zeng *et al.* (2014) the lowest model level is used to calculate boundary layer heating. Here the lowest model level is $\approx$ 18 m and as the minimum BL height is 163.1 m this is

11% of the BL height, which is sufficiently low for surface fluxes to be considered. In Zeng *et al.* (2014) the lowest model level used is $\approx$ 30 m.

The three terms for IT3 are shown in Fig. 3.18. As the other experiments are qualitatively similar, only IT3 is shown. The values show the average heating or cooling of the BL in K hr^{-1}. It can be seen that over the MYI there is no heating or cooling of the boundary layer. The ADV term then acts to cool the boundary layer, as there is a constant source of cold air being advected from the north of the domain. The magnitude of the cooling is reduced as the air travels over the domain, as the air being advected is warmer. The CONV term acts to cool over the MIZ, while the atmosphere here is absolutely unstable there is also a downwards motion of the air as seen in the w-wind plot (Fig. 3.24). The subsidence is caused by the acceleration of the air over the MIZ, which is due to a reduction in the friction felt by the lowest level of the atmosphere due to the presence of a viscous sublayer forming at the surface. Thus the boundary layer is cooled by the movement of colder air from aloft. Over the open water CONV becomes positive, as now there is both absolutely unstable air and vertical motion. Once the atmosphere establishes convective cells after 150 km off the ice edge, the CONV term becomes the largest contributor to the BL heating, with the strong updrafts causing heating, it also acts to strongly cool in the downdrafts, however the heating outweighs the cooling, so the boundary layer continues to warm. The diabatic heating term Q_t is the sole source of BL heating over the MIZ, as the BL is warming here despite the subsidence and advection of cold air. The magnitude of this diabatic heating reduces over the open water, which is what happens to SHF and LHF in Figs. 3.6 and 3.7. It can, therefore, be said that the heating of the BL over the MIZ is mostly due to flux convergence.

Comparing the Q_t and CONV terms for the variations in ice thickness shows the impact of the ice thickness on the BL heating terms. For CONV Fig. 3.19 shows that initially IT0.1 has the largest cooling (-1.1 K hr^{-1} for IT0.1 compared to -0.6 K hr^{-1} for IT3). As the vertical motion is very small for all the experiments (Fig. 3.24) the magnitude of the cooling is dominated by the lapse rate term. As the surface temperature for IT0.1 is warmest (Fig. 3.4) the lapse rate is thus the most unstable, implying that subsidence would bring down air that is comparatively cooler compared to the other experiments. By the end of the MIZ the other experiments show the larger cooling (-1.3 K hr^{-1} for IT3 compared to -1.2 K hr^{-1} for IT0.1),

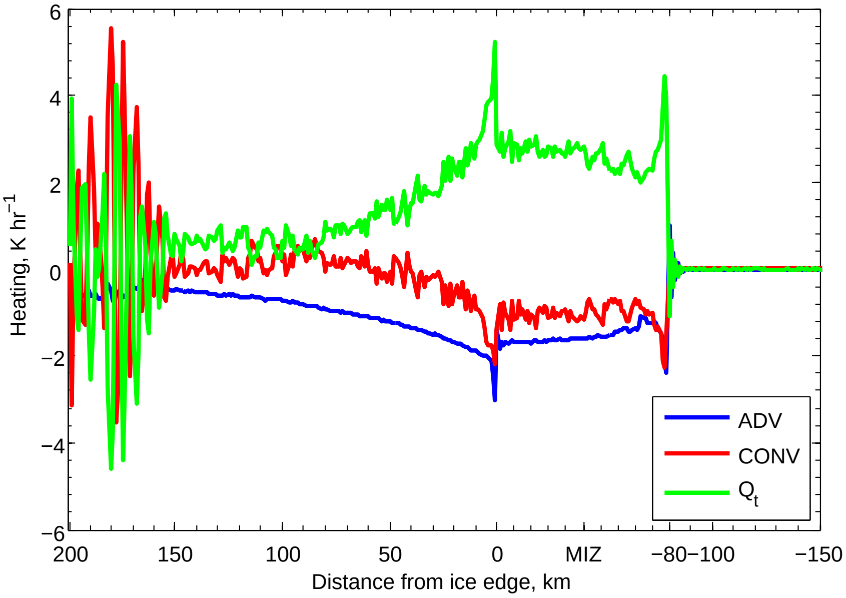

Figure 3.18: The average contributions to BL heating by advection (ADV), convection (CONV) and diabatic processes (Q_t) in K hr^{-1} for IT3.

corresponding to the BL being more well mixed and thus less unstable (though still absolutely unstable) for IT3. Over the open water at 50 km away from the ice edge, the convection becomes a source of heat for all the experiments, though most notably IT0.5 shows the largest positive contribution at the start of the convective heating (+0.14 K hr^{-1} for IT0.5 compared to -0.04 K hr^{-1} for IT3), as the vertical winds become positive for IT0.5 first. These vertical winds in IT0.5 lead to the mean contribution between 50 and 100 km off ice being largest for IT0.5 at +0.26 K hr^{-1} compared to +0.17 K hr^{-1} for IT0.1. The magnitude of the lapse rate term is reduced for IT0.1 due to the warming of the atmosphere which has occurred over the MIZ, which reduces the magnitude of any warming by convection. Finally, after 150 km off ice, all the experiments show larger contributions to the BL heating. The average heating by convection between 150 and 200 km off ice is shown in Table 3.4, which shows that the heating by convection is largest for IT0.25, with +0.81 K hr^{-1} compared to +0.66 K hr^{-1} for IT3.

The Q_t in Fig. 3.20 shows that initially the heating by the fluxes is largest for IT0.1 (+2.57 K hr^{-1} for IT0.1 compared to 1.4 K hr^{-1} for IT3), indeed the fluxes here are largest in Figs. 3.6 and 3.7. As in the SHF and LHF plots, by the end of the MIZ the heating by the fluxes is largest for the thicker experiments. Over the whole MIZ the average heating is shown in Table 3.4 showing that the contribution to the heating by

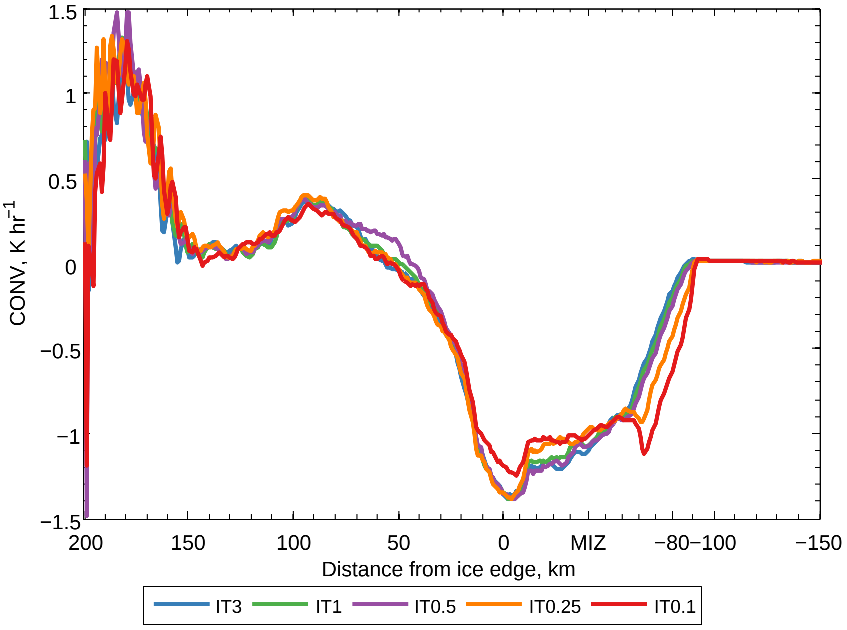

Figure 3.19: The average contributions to BL heating by convection (CONV) in K hr^{-1} for all the experiments, a 3 km smoothing has been applied.

Table 3.4: The mean contribution to the BL heating by CONV and Q_t for certain parts of the MIZ.

	IT3	IT1	IT0.5	IT0.25	IT0.1
Mean CONV 50 - 100 km off ice (K hr^{-1})	+0.21	+0.23	+0.26	+0.22	+0.17
Mean CONV 150 - 200 km off ice (K hr^{-1})	+0.66	+0.75	+0.78	+0.81	+0.68
Mean Q_t MIZ (K hr^{-1})	+2.45	+2.44	+2.49	+2.53	+2.62

the fluxes is largest for IT0.1, with +2.62 K hr^{-1} compared to + 2.45 K hr^{-1} for IT3. The higher heating for thinner ice matches that seen in SHF and LHF, where over the MIZ the thinnest experiments have the highest values (Figs. 3.6 and 3.7). The heating by the fluxes reduces from the maximum at the ice edge to near +0.5 K hr^{-1} at 100 km away from the ice edge, in Figs. 3.6 and 3.7 it can also be seen that the surface fluxes reduce over the open water. After 150 km from the ice edge, the diabatic processes act to slightly cool the boundary layer. The fluxes here are reduced, but still positive in Figs. 3.6 and 3.7. The cooling could therefore be caused by other diabatic processes such as evaporation of water as the water vapour mixing ratio is highest here (figure not shown), the precipitation from the clouds or the shading of the surface by the clouds that have formed (discussed below). However as the heating here is dominated by the convection, there is still a heating of the BL.

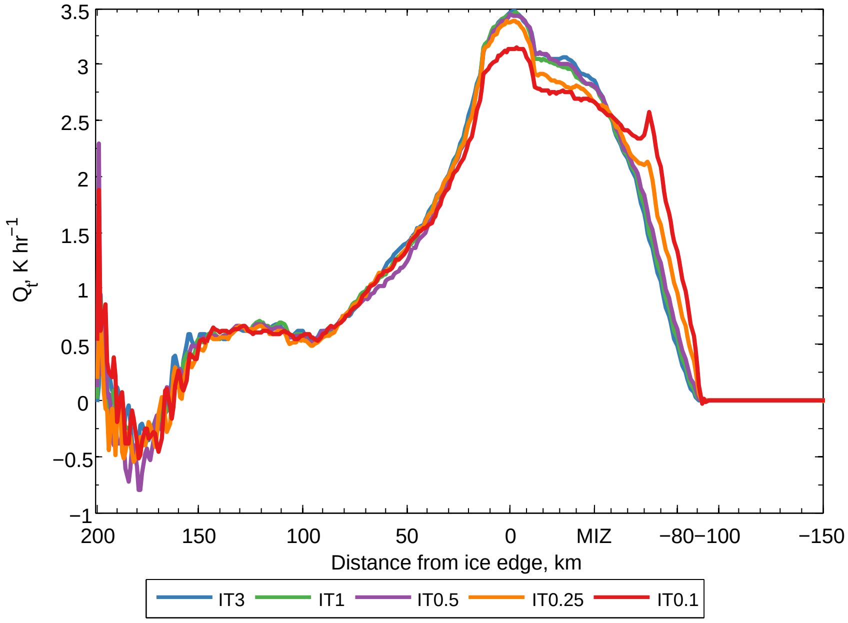

Figure 3.20: The average contributions to BL heating by diabatic processes (Q_t) in K hr^{-1} for all the experiments.

Overall the surface acts to warm the BL, over the MIZ the warming is predominantly due to the diabatic heating processes, which has been assumed to be mostly flux convergence. The thinner ice experiments show a larger contribution from the fluxes over the MIZ. This heating then acts to reduce the magnitude of the lapse rate term in CONV, which in turn inhibits the heating by convection which occurs further downstream, with IT0.1 having the lowest contribution between 50 and 100 km off ice, and the second lowest contribution at 150 - 200 km off ice. At the southernmost end of the domain the heating is predominantly driven by convection.

3.3.4 CLOUDS

The increase in heat and moisture flux into the boundary layer, and the attendant increase in boundary layer height for the thinner experiments may impact the presence of clouds in the model. The liquid water path (LWP) is a measure of the weight of liquid water in the atmosphere above a unit surface and is given in units of kg m^{-2} . The LWP is calculated by numerically integrating,

$$LWP = \int_0^{z_{max}} \rho Q_{LW} dz, \tag{3.8}$$

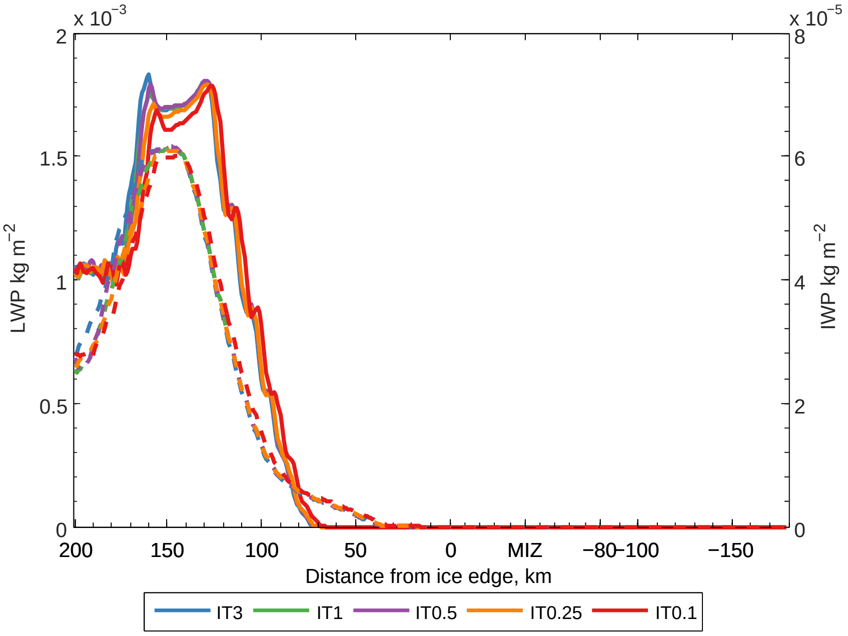

Figure 3.21: Cloud liquid water path LWP (solid) and cloud ice water path IWP (dashed), kg m^{-2}. Note the difference in order on the two y axis.

where Q_{LW} is the liquid water mixing ratio (g kg^{-1}) and is shown in Fig. 3.21 as the solid line. The LWP starts to increase around 70 km off the ice edge, with the increase starting 4 km earlier for IT0.1. Once the cloud starts to form, the LWP increases at the same rate for all experiments, with IT0.1 being consistently 4 km ahead of the other experiments. Between 70 and 120 km off the ice edge, the LWP exhibits a periodicity, reaching local maximum every 9-11 km. The periodicity matches that of the convective plumes shown in w-wind (Fig. 3.24) as alternating bands of up- and down-drafts between 70 and 120 km.

The first maximum in LWP occurs around 126 km off the ice edge with IT0.1 having the lowest maximum value here at 1.75 $\times 10^{-3}$ kg m^{-2} compared to 1.80 $\times 10^{-3}$ kg m^{-2} for IT1. Then a second maximum occurs around 160 km off ice edge. This maximum shows a much higher spread between the different experiments, with the IT3 having the highest value for LWP at 1.83 $\times 10^{-3}$ kg m^{-2} compared to 1.68 $\times 10^{-3}$ kg m^{-2}. After the second maximum, the amount of liquid present in the cloud decreases to around 1.0 $\times 10^{-3} kgm^{-2}$ and oscillates around this point. These oscillations coincide with the strong up- and down-drafts seen in Fig. 3.24 after 150 km. The minima at about 130 km off ice corresponds to a local maximum in snow water path SWP (analogous to LWP) in Fig 3.22, implying that the reduction in cloud liquid is due to the process of collection and freezing and falling out as snow. This

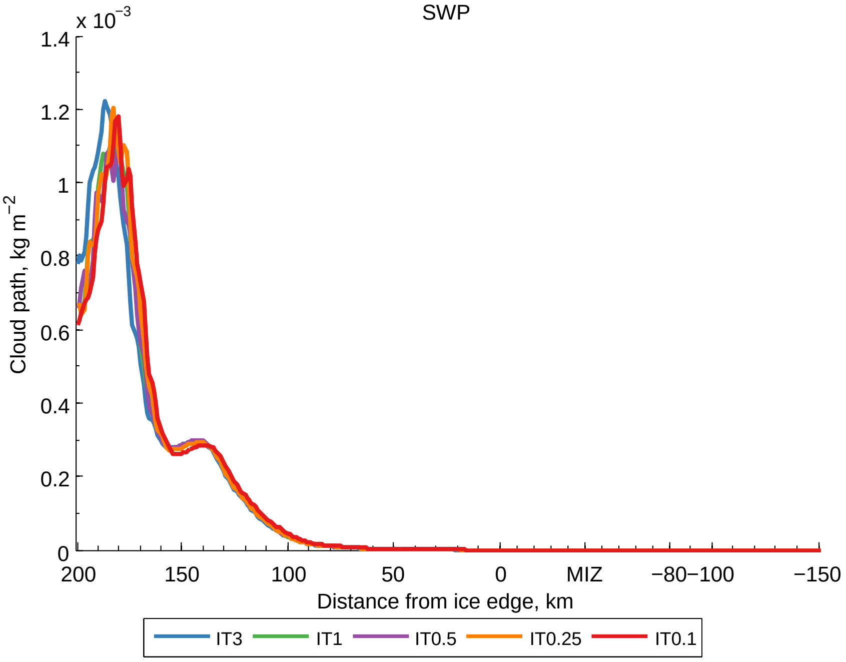

Figure 3.22: Cloud snow water path SWP kg m^{-2}.

precipitation of snow could be causing the Q_t term above to become negative, due to the subsequent melting of the snow closer to the surface. The formation of snow starts earlier in IT0.1, as the formation of cloud ice and liquid starts sooner. As it has lost more liquid by forming snow and precipitating it out, this explains why it has the lowest maximum value. The loss of both ice and liquid to snow causes the reduction in both IWP and LWP after 150 km off ice. The loss of both ice and water implies the snow forming by collection and ice melt. These values are at the low end, so are rather tenuous clouds, with observations of clouds in the Arctic being above 50 $\times 10^{-3}$ kg m^{-2} (Shupe *et al.*, 2013) or between 0 and 50 $\times 10^{-3}$ kg m^{-2} (Sedlar *et al.*, 2011). The air temperature T cross-section in Fig. 3.23 shows that all the experiments have a warmer BL than IT3, with thinner ice producing a warmer BL over the MIZ, as seen above. All the experiments also have a cooler band at the top of the BL, where there is stronger turbulence caused by the stronger convection, which is causing cold air to be entrained down from above the BL. The colder air aloft is what allows IT0.1 to create ice faster, as below 263.15 K ice may grow by contact freezing irrespective of droplet radius, and by immersion freezing if the droplet radius is greater than 10 μm (Morrison *et al.*, 2005). The intense red colours in the plots for IT1 and IT0.5 are coincident with the formation of snow, and imply there is a release of latent heat by liquid freezing which is starting earlier for IT1 and IT0.5 compared to IT3. This latent heat release would increase Q_t higher up in the BL, rather than at the surface. There is not as much freezing in IT0.25 and IT0.1 as in IT1 and IT0.5, as there is less liquid in these clouds.

The cross-sections of cloud liquid water mixing ratio Q_L are shown in Fig. 3.25, with the uppermost plot being for IT3 and the rest of the plots show the difference from IT3. The cloud base and height do not change between the different experiments, but the distribution of the liquid is changed, with there being higher concentrations at the top of the clouds. The diagonal lines seen around 100 km off the ice edge, correspond to wave motions seen in the w-wind plots in Fig. 3.24.

Another key feature of Arctic clouds is the presence of both ice and water, making the clouds mixed phase. The Morrison 2-moment cloud microphysics scheme used here, includes cloud ice (Morrison *et al.*, 2005). The ice water path (IWP) which is analogous to the LWP is shown in Fig. 3.21 as the dashed lines. The IWP starts to increase closer to the sea ice edge than the LWP, beginning at about 30 km from the ice edge, with IT0.1 once again starting first. Possibly as the thinnest experiment produces moisture earlier while the atmosphere is colder, thus producing ice earlier. Between 30 and 90 km off the ice edge, the IWP increases slowly, then between 90 and 130 km there is a much faster increase in IWP due to conversion from liquid to ice, and a maximum is reached between 130 and 150 km off the ice edge. The maximum in IWP corresponds to the local minima in the LWP at this location, indicating that the increase in liquid available causes an increase in ice content and a subsequent decrease in liquid content. Again IT0.1 has the lowest maximum value at 5.9×10^{-5} kg m^{-2} compared to 6.1×10^{-5} kg m^{-2} for IT1. It seems that the thinnest experiment produces the lowest maximum values, but starts to produce cloud closer to the ice edge and also loses its cloud fastest. The cross-section plots for ice water mixing ratio Q_{IW} are shown in Fig. 3.26. The earlier production of Q_{IW} for IT0.1 is immediately obvious. As is the reduction in Q_{IW} after 150 km from the ice edge.

The presence of clouds impacts the surface radiation balance. The clouds shade the surface, reducing $SW\downarrow$ arriving at the surface. Clouds also emit $LW\downarrow$ which warms the surface. The $SW\downarrow$ (not shown) closely follows the curves for LWP and IWP, but with the opposite shape. As the cloud starts to form, more $SW\downarrow$ is blocked from reaching the surface, and thus the values are reduced. The minimum is coincident with the maximum for LWP . The $LW\downarrow$ (not shown) also follows the

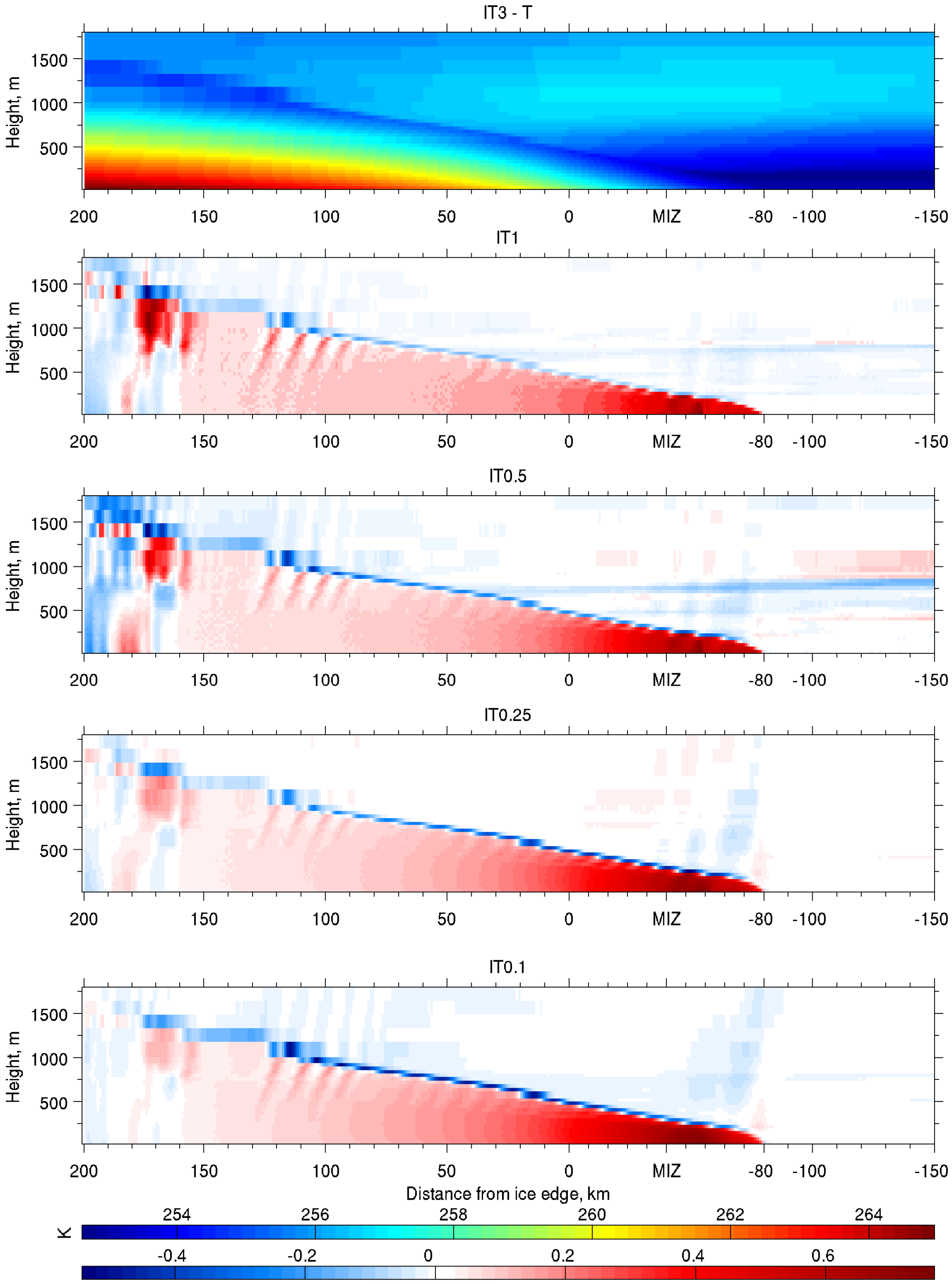

Figure 3.23: Air Temperature (T), K below 2000 m over the whole domain. The top plot shows IT3 and the others show the difference from IT3 for their respective experiment.

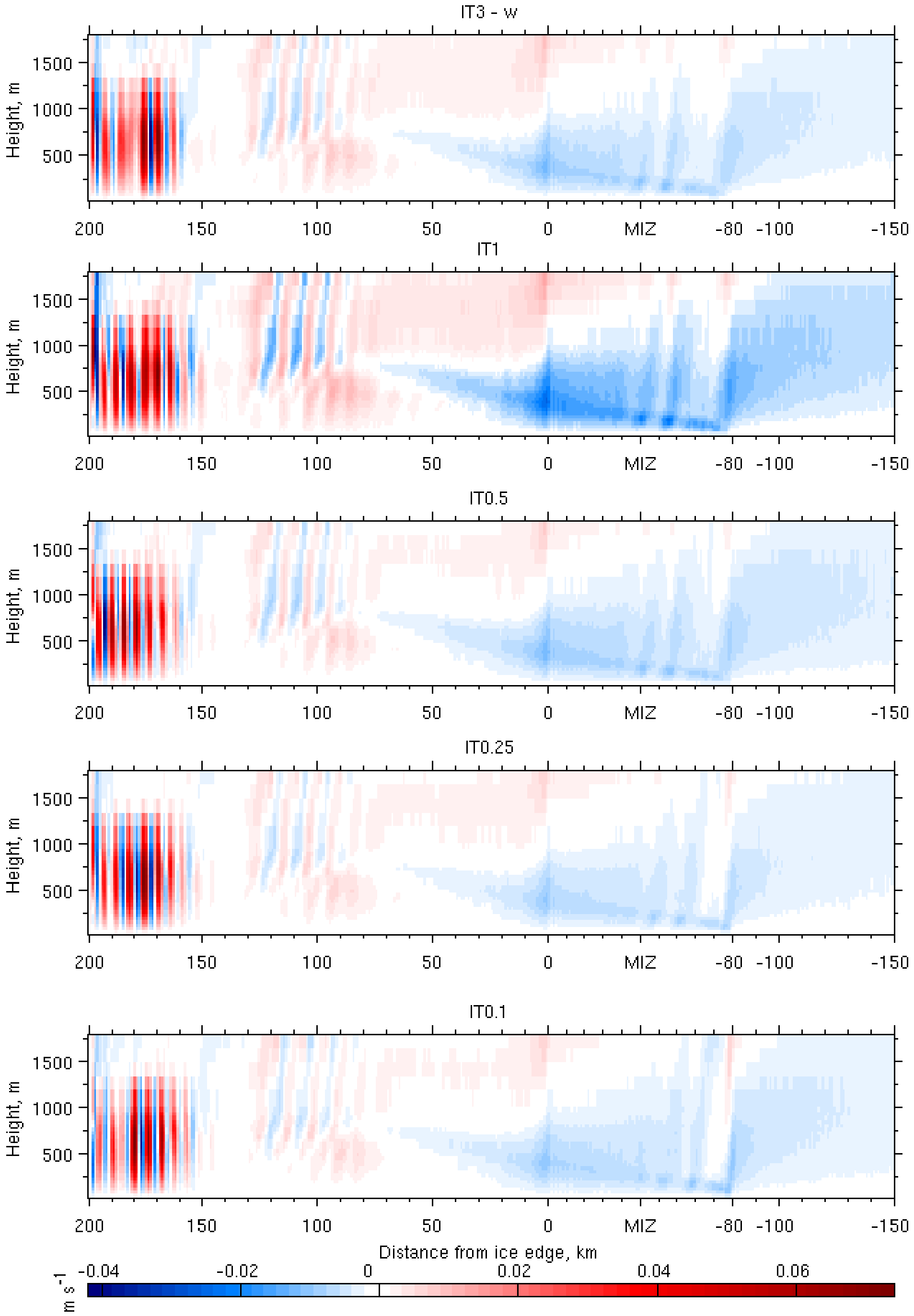

Figure 3.24: w-wind m s^{-1} below 2000 m over the whole domain. Up-drafts are red, while down-drafts are blue.

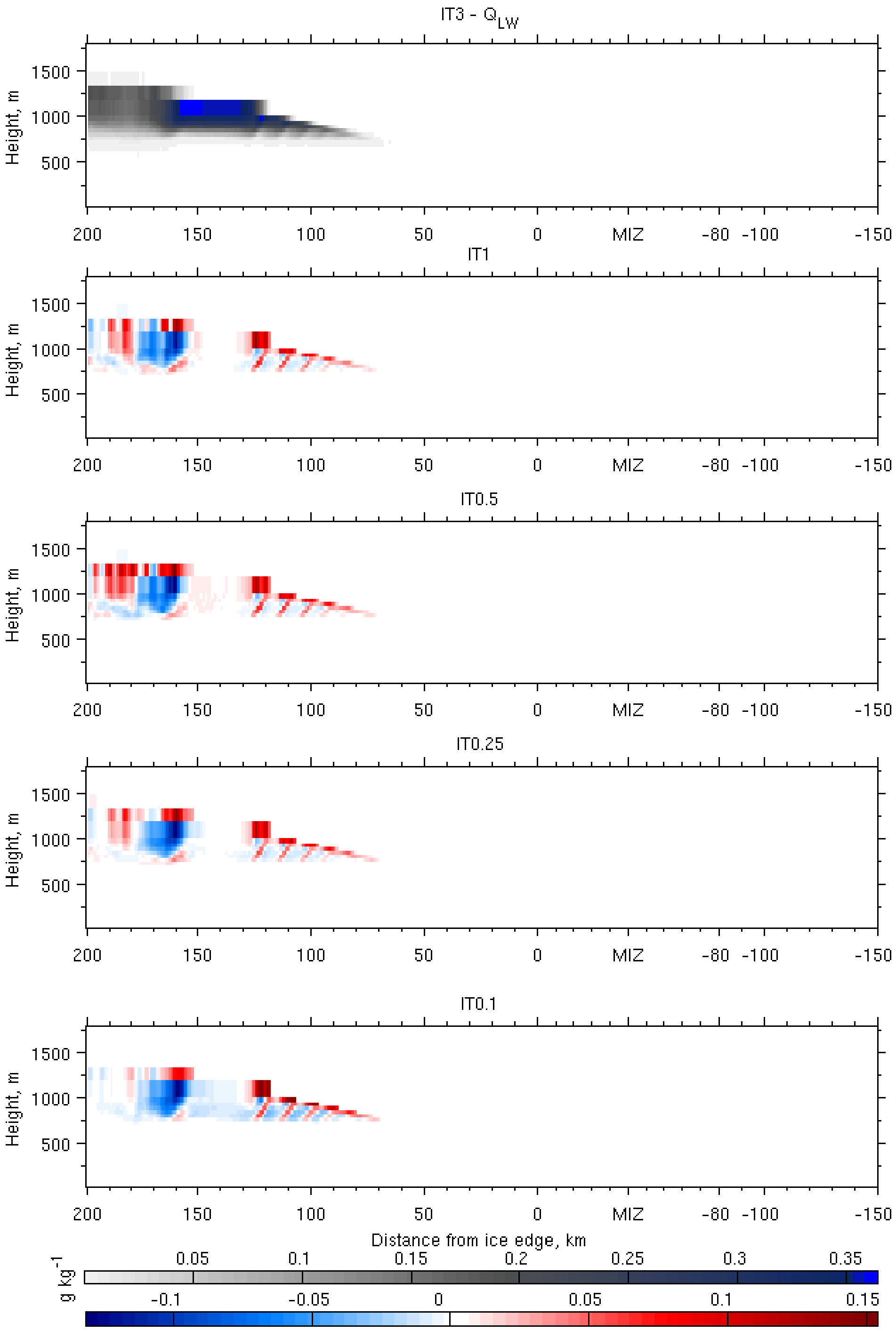

Figure 3.25: Q_{LW} below 2000 m over the whole domain, the top plot shows IT3 and the others show the difference from IT3 for their respective experiment.

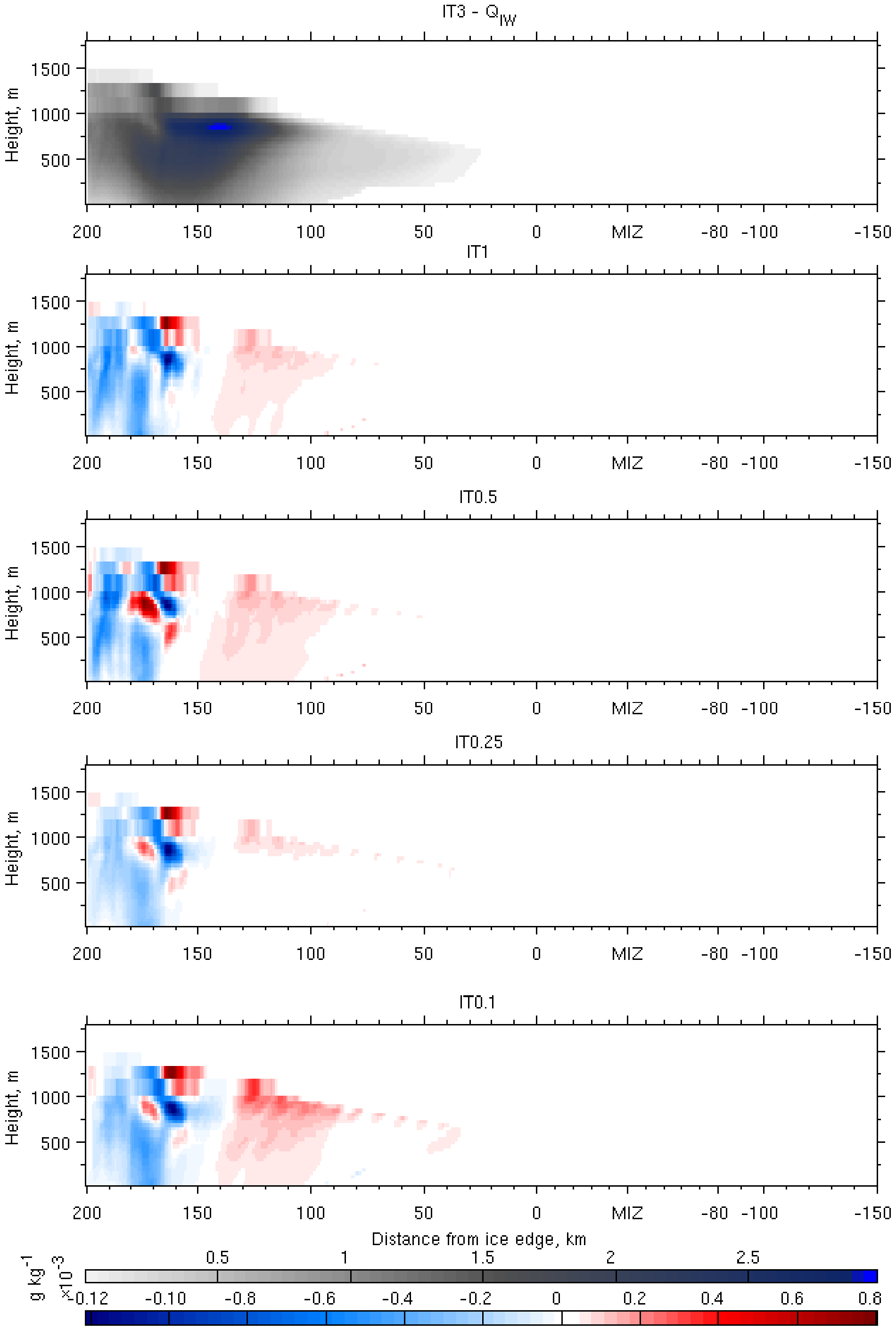

Figure 3.26: Q_{IW} below 2000 m over the whole domain, the top plot shows IT3 and the others show the difference from IT3 for their respective experiment.

curves for LWP and IWP, as would be expected. As for LWP the $LW\downarrow$ increases first for IT0.1 and it remains ahead of the other experiments until the point where the LWP values for the other experiments overtake those for IT3. The maximum for $LW\downarrow$ reaches a maximum furthest off ice, implying the clouds here are warmer, even if they have lower LWP and IWP values. To ascertain the effect this has on the surface the radiation terms in the surface temperature equation 3.2 ,

$$\text{Radiative Forcing} = \epsilon\left[LW\downarrow - \sigma T_{sfc}^{4}\right] + (1-\alpha)SW\downarrow, \tag{3.9}$$

have been calculated. The radiative forcing is shown in Fig. 3.27, and over the open water it can be seen that after the clouds form, the heating of the surface is reduced. Where there is no cloud present at about 50 km from the ice edge, the radiative forcing is around 100 W m^{-2}, this then reduces until it reaches a minimum of 33 W m^{-2}, which is coincident with the maximum value in LWP. There is a trade off between the earlier formation of cloud and the amount of liquid and ice present, as the thinner experiments produce cloud earlier, but less liquid and ice, so the biggest cooling effect is seen in IT0.5 (-28.4 W m^{-2}) and the least shading is provided by IT0.25 (-28.1). There is once again very little variation between the maximum and the minimum with there being a 1% difference between the two. This finding agrees with Serreze & Francis (2006) who find that clouds act to cool the surface during summer.

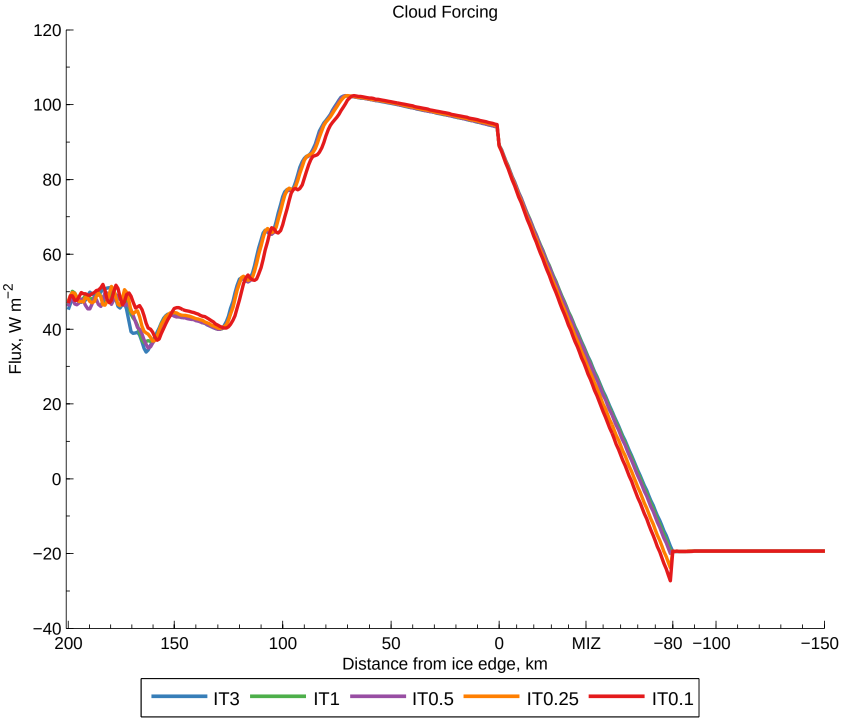

Figure 3.27: The radiative forcing terms of the surface energy balance, W m^{-2}

3.4 DISCUSSION

Due to changes in climate, Arctic sea ice has been seen to become thinner as there is now a higher proportion of new ice than in the past (Nghiem *et al.*, 2007; Comiso, 2012). In order to investigate the impact that thinner ice in the MIZ would have both locally and further downstream, a series of experiments were conducted. Using PWRF 3.5.1 in an idealised setup with a domain comprising 3 m thick sea ice, a MIZ and open water. The MIZ had a linearly varying sea ice concentration between 100 and 10%. For the experiments the thickness of the sea ice in the MIZ was reduced, with the five experiments having MIZ ice thickness values of 3, 1, 0.5, 0.25 and 0.1 m. In order to isolate the impact of the changing sea ice thickness, the albedo was not adjusted to correspond to the thinner sea ice, which was achieved by prescribing a layer of snow over the sea ice across the whole domain and the diurnal cycle is switched off. The idealised experiments were all initialised with a typical atmospheric profile which has been taken from over the solid ice to the north of Svalbard. The profile was dried out so there is no cloud over the MIZ and the wind is entirely from the north.

As thinner sea ice is less insulating than thick sea ice, allowing more transfer of heat from the ocean to the atmosphere, it would be expected that the surface temperature is increased. Other studies have also shown the importance of accurate sea ice fraction to surface temperature and heat fluxes (Bromwich *et al.*, 2009; Screen *et al.*, 2014). For IT0.1, due to the heat flux through the ice being larger by 56.3 Wm^{-2} the surface temperature is also highest by up to 2.9 K. This is a tangible amount of warming, and this increased surface temperature would then act to increase the fluxes of heat and moisture. Indeed the thinner experiments have higher SHF and LHF over the MIZ, with the differences highest at the start of the MIZ. The maximum difference over the MIZ is 45.5 Wm^{-2} for SHF and 16.3 Wm^{-2} for LHF with these values being for IT0.1 compared to IT3. These higher fluxes are only a local effect, as the atmosphere warms up so the fluxes of sensible and latent heat are reduced. This means the thicker experiments then have the higher fluxes over the open water. Over both the water and the MIZ there is a 1.1% and 1.5% difference in modelled SHF and LHF from IT3 respectively. The local increase of heat fluxes over the MIZ could act to increase the melting of the ice in the MIZ. Cold air outbreaks are also implicated in the transfer of moisture from the sea surface to the atmosphere (Liu *et al.*, 2006). In these experiments thinner ice resulted in a higher moisture flux, due to the higher turbulence present in the thinner experiments more moisture can be transported from the surface.

The surface heat fluxes are responsible for heating the atmosphere over the MIZ, with the contribution from diabatic heating being largest for the thinnest experiment at +2.62 K hr^{-1} compared to +2.45 K hr^{-1} for IT3. This means that for the profiles of θ the thinner experiments are consistently warmer than IT3, IT1 and IT0.5, by up to 0.6 K. All the experiments show warming as the BL travels across the MIZ, again due to the heat fluxes from the surface. For IT0.1 the bottom of the atmosphere warms by up to 5.9 K across the MIZ. As the increased fluxes have warmed the BL, so the depth of the mixed layer is increased. The BL is highest for IT0.1 across the whole MIZ, being up to 38 m higher.

The increased moisture flux for the thinner experiments means that the profiles of q show the highest values for IT0.1. The specific humidity also increases the most across the MIZ for IT0.1m, increasing by 0.04 g kg^{-1}. Due to the entrainment of dry air from aloft, by the end of the MIZ the top of the BL is slightly (0.04 g kg^{-1}) drier than the lower BL. All the experiments show that there is turbulence across the top of the BL, with the TKE for the thinner experiments extending higher above the BL top. The thinner experiments also have the highest TKE lower in the boundary layer (+0.06 m^2 s^{-2}). This higher TKE would enhance the turbulent exchange of heat and moisture, as seen above. Higher TKE would also enhance the transport of particles that can act as CCN and IN. The cloud albedo effect implies that an increase in CCN would cause there to be an increase in cloud droplets, which would then be smaller. This would create more reflective clouds. By the second aerosol indirect effect the increase in CCN would also cause the clouds to be more long lived (Mauritsen *et al.*, 2011; Lloyd *et al.*, 2015).

It is known that cloud cover plays an important role in the Arctic surface energy balance and the onset of melt (Pinto, 1998; Vihma *et al.*, 2005; Persson, 2012). Due to the increased moisture flux, the thinnest experiment IT0.1 begins to produce both cloud ice and cloud liquid first, up to 4 km closer to the ice edge. Ice begins to form first by vapour deposition onto IN. Once there is cloud liquid water present, the amount of ice present in the clouds also increases, as there can now be freezing from the liquid phase as well, this pattern is the same for all experiments. The cloud LWP and IWP reach a peak after 100 km from the ice edge. The thinnest experiment shows the lowest values of LWP at this point being 0.5 kg m^{-2} lower than that for IT1 (the maximum). This is due to there being increased loss of liquid from the cloud by the formation of snow and its subsequent sedimentation from the cloud for the thinner experiments, as snow can start to form earlier in the increased presence of liquid and ice. While these clouds are mixed phase, as is common in the Arctic (Morrison *et al.*, 2012), the ratio of water to ice is very high, well above the 85% in Shupe *et al.* (2008). Above it was noted that an increase in TKE and thus CCN from the surface would change the cloud microphysical properties, an increase in CCN would be expected to decrease the formation of snow by inhibiting the riming process (Borys *et al.*, 2000). However as the microphysics used does not take into account changes in CCN, this effect would not be expected. As the thinner ice produced thinner clouds, but produced them sooner so the radiative impact of the thickness of the cloud versus the extent means that IT0.5 caused the most surface shading. Overall the clouds act to shade the surface, in agreement with Serreze & Francis (2006). However, this reduction in cloud impact may be due to the lack of CCN which would be increased for the thinner experiments. If the model did include the effect of surface CCN being brought up by the more turbulent BL, it might be expected to result in longer lived, more optically reflective clouds and thus increase the shading of the surface. An increase in cloud shading would cool the sea surface and thus help to slow melt, while a reduction in cloud thickness would allow the sea surface to warm more and thus increase the melt rate of the ice.

These experiments show that thinner ice impacts the boundary layer over the MIZ both locally and further down stream. Locally the fluxes of heat and moisture over the MIZ are increased. Thinner ice allows more heat through from the water below, which would also increase the melt rate of the ice and act to reduce ice cover further the forthcoming year. The increased fluxes of moisture for the thinner experiments cause clouds to be created earlier. The cloud microphyscial properties are changed by the changes to the surface, with an enhancement to the creation of snow. The clouds become thinner and shade the surface less, which would again enhance warming. It would therefore be important to include the changes in ice thickness in both NWP and Climate simulations due to the downstream impact on clouds.

These experiments do not take into account the changes in albedo, or indeed the changes in CCN caused by an increase in TKE in the BL. A reduced albedo for the thinner experiments would act to further enhance the fluxes of heat and moisture over the MIZ, by increasing the difference in temperature between the surface and atmosphere. This would be because the darker surface would absorb more solar radiation. If the model were able to transport CCN upwards from the surface, the enhanced turbulent mixing caused by the thinner ice would increase the CCN available to the clouds and change the microphysical properties to increase cloud longevity and cloud reflectivity. Therefore these two effects could cancel each other out. Future experiments should include both of these effects, as well as investigating the impact of thinner ice in a more realistic set up and on longer time scales.

4

OBSERVATIONS OF THE BOUNDARY LAYER OF THE MIZ MADE DURING THE ACCACIA CAMPAIGN

4.1 OBSERVATIONS OF THE MIZ

The MIZ is a complicated area with many interactions between the surface and atmosphere. To understand the complex and interconnected system of surface, fluxes, boundary layer and clouds in the MIZ, it is necessary to observe all the components individually and the system as a whole. The Aerosol-Cloud Coupling Climate Interactions in the Arctic (ACCACIA) project and field campaign follow a series of projects each focussing on different aspects of this system.

The first major western campaign based on sea ice was the Arctic Ice Dynamics Joint Experiment (AIDJEX) Lead Experiment in 1979, which aimed to investigate the exchange of heat between the ocean and the atmosphere through leads in the ice (Andreas *et al.*, 1979). During the field campaign, measurement sites were placed on the sea ice up- and down-wind of leads. The impact of the surface on the atmosphere through the turbulent heat fluxes from leads and the development of an internal boundary layer were observed along with the impact of the changing surface roughness. It was found that the turbulent heat transfer from leads in winter is one of the biggest terms in the Arctic heat budget (Andreas *et al.*, 1979).

Several years later, the MIZ experiment (MIZEX) in 1983 used aircraft observations to investigate the impact of the MIZ in the Greenland sea on surface fluxes and the atmosphere above (Fairall & Markson, 1987). With the instrumentation of the time, they were unable to calculate fluxes using the eddy covariance method, but instead used indirect methods (bulk fluxes and inertial dissipation). Flying during late summer they found the total heat flux on average to be 30 W m^{-2} over water and negligible over the ice. They also looked at the change in the 10 m neutral drag coefficient C_{DN10}, which was seen to increase from 1.3 $\times 10^{-3}$ over the ocean to 3.3 $\times 10^{-3}$ over the sea ice.

Following on from AIDJEX was the Arctic Leads Experiment (LEADEX) in spring 1992 based on the Arctic ice cap 200 km north of Prudhoe Bay, Alaksa, where once again observations were made on the surface either side of leads. Looking at an 80 - 120 m wide lead with 2-3 ms^{-1} wind speed and a 1 km wide lead with winds of 6.5 ms^{-1}, they find that the fluxes are sensitive to lead width and wind speed. Fluxes of sensible heat being 30 Wm^{-2} from the narrow lead and 170 Wm^{-2} downwind of the wider lead (Ruffieux *et al.*, 1995; Persson *et al.*, 1997).

Turning the attention to clouds, the Beaufort Arctic Storms Experiment (BASE) campaign looked at mixed phase clouds over the MIZ, along with the fluxes from the surface. Making observations using an aircraft in the Autumn (Paluch *et al.*, 1997), they measured clear skies over ice, with a stable boundary layer and weak fluxes except over leads, where the sensible fluxes were around 55 W m^{-2}. They stated that the leads were causing buoyancy waves or roll vortices to form, but they did not see any plumes associated with the leads. Their calculations of the fluxes indicate that these waves or vortices contribute to the fluxes, since after removing their effects the calculated fluxes were found to be low. Over open water they observed a stratus capped BL, with the mixed phase cloud being liquid topped. The average flux from leads observed during BASE is calculated to be 81 W m^{-2} in Pinto (1998) using a lead fraction of 2% as determined from the downwards facing video camera aboard the aircraft.

More aircraft observations of a cold air outbreak in the Labrador sea were analysed in Renfrew & Moore (1999) where the cloud streets that form off ice during a cold air outbreak were examined. They found that the air both warmed and moistened with distance from the ice edge. Using a bulk flux method they calculate fluxes of 500 W m^{-2} for SHF and 100 W m^{-2} for LHF. These high fluxes lead to a dramatic deepening of the BL off ice, which rises by about 950 m over a 380 km cross section. The cloud streets were set up by roll vortices off ice, and have a wavelength of 7 - 10 km.

Returning to surface based observations, the Surface Heat Budget of the Arctic (SHEBA) project took place for a year from October 1997 with a ship being frozen in the ice north of Alaska and allowed to drift (Perovich *et al.*, 1999). During SHEBA measurements of surface heat fluxes and cloud forcing over the sea ice were made in order to analyse the surface heat budget of the Arctic. Their measured surface latent and sensible heat fluxes were up to two orders of magnitude larger over the leads than over ice in spring (Pinto *et al.*, 2003). It is hypothesised that these turbulent fluxes from leads could result in increased cloud cover. Analysis of the cloud radiative forcing shows that the clouds act to warm the surface for much of the year (Zuidema *et al.*, 2005; Intrieri *et al.*, 2002). However the impact of clouds on the surface depends not only on the cloud amount, but also on cloud base height, the amount and phase of the water, the particle size and shape and the optical depth (Intrieri *et al.*, 2002).

Coincident with SHEBA was the First International Satellite Cloud Climatology (ISCCP) Regional Experiment-Arctic Cloud Experiment (FIRE-ACE), during which observations were made by aircraft (Gultepe *et al.*, 2003) over the Beaufort Sea. Once again surface fluxes and leads were observed, along with the make up of the clouds. Over a 3 km lead, they observed fluxes of latent and sensible heat to be 14 W m^{-2} and 56 W m^{-2} respectively. It is also discussed how the height of the observations, being at the lowest 100 m above the surface, could have an impact on the ability to calculate the surface fluxes as this is higher than the 10% of the boundary layer height as discussed in Fairall & Markson (1987). Over open leads they observed liquid phase clouds, which supports the assumption in Pinto *et al.* (2003) that fluxes of heat and moisture from leads are important for cloud formation.

In Vihma & Brümmer (2002) aircraft observations made of off ice airflow in the Gulf of Bothnia during the BASIS campaign in spring 1998 are examined. They observed a large difference between the ice temperature and the water temperature of about 10 °C. The cloud cover increased over the ice, from 3 to 8 octas and the depth of the boundary layer also increased from 300 m to about 550 m. Due to conductive heat flux through the ice, they observed a weakly unstable boundary layer over the ice, which then transitions into a strongly unstable BL over the water. They also found that the surface heat flux was 4-9 times larger over the water than the ice.

Several years later, the Mixed-Phase Arctic Cloud Experiment (M-PACE) took place in Barrow Alaska in 2004 (Shupe *et al.*, 2008). M-PACE focussed on clouds and found that low level, single layer, mixed-phase, stratiform clouds are typically topped by a 400-770 m deep liquid water layer from which ice crystals precipitate, and these clouds are predominantly liquid (85%). Cloud liquid and ice have substantially different impacts on atmospheric radiation due to differences in particle size, shape, density concentration and refractive index, however the liquid is the dominant effect.The persistence and dominance of liquid in these clouds is likely caused by a limited supply of ice nucleating particles (IN) and a plentiful supply of water vapour.

Continuing to focus on clouds, observations from ground based lidar and microwave radiometer at Eureka, Canada, Barrow, Alaska and the western Arctic ocean were used in de Boer *et al.* (2011) to show that liquid topped clouds occur more frequently than all ice clouds in the Arctic. Their results suggest the presence of liquid in the clouds is important for ice nucleation, which agrees with Shupe *et al.* (2008).

The Aerosol, Radiation and Cloud Processes affecting Arctic Climate (ARCPAC) took place in northern Alaska in 2008 (Lance *et al.*, 2011). Aircraft observations were made to allow for identification and characterisation of both aerosol and trace gas pollutants, and to investigate their effect on cloud microphysical properties. It was found that pollution (and thus more cloud condensation nucleii, CCN) may lead to greater cloud lifetime, greater cloud emissivity and reduced precipitation.

The Arctic Summer Cloud Ocean Study (ASCOS) campaign was another surface based endeavour. In Sedlar *et al.* (2011), ASCOS data is used to examine the effect of clouds on the surface energy budget, particularly during times of low sun angle. The low sun angles are important as they set up a complex cloud radiation and surface interaction. In response to the varying cloudiness, the radiative fluxes showed the largest variations and dominated the energy budgets. Cloud cover, they concluded, is a key component of the surface energy budget of the Arctic during the transition from melt to freeze. Continuing to study the clouds and interactions with the surface, Shupe *et al.* (2013) looks at the coupling between the cloud and surface. Boundary layers where the clouds are coupled to the surface are driven by the cloud, and the cloud processes keep the mixed layer in equilibrium with the surface.

The most recent campaign, taking place at the same time as the ACCACIA, was the Spring Time Atmospheric Boundary Layer Experiment (STABLE) campaign. The aircraft was based out of Svalvard and investigated fluxes from leads with varying ice cover. They observed sensible fluxes as high as 180 Wm^{-2} and found that the fluxes are sensitive to the newly forming ice cover in the leads (Tetzlaff *et al.*, 2015). The downstream effect of leads is also examined, where a convective plume forms and then is advected downstream. They also recommend that to measure fluxes out of a single lead using an aircraft the best flight pattern is one that is parallel to the lead, as the lead can induce oscillations in the fluxes making the determination of an averaging length difficult for a lead-perpendicular run. During the same campaign, observations were made of a cold air outbreak over a polynya (a large open expanse of water which is open for longer periods than a lead). Tetzlaff *et al.* (2014) used dropsondes to observe the evolution of the boundary layer over the polynya. The boundary layer height was seen to increase dramatically from 250 m to 2,500 m, and the effect of the polynya could still be seen 200 km downstream. As a change in sea ice cover can strongly influence local temperature conditions and be seen far downstream then even if the number of cold air outbreaks remains the same, a change in the position of the ice edge would have a strong impact downstream.

The Arctic has benefited from many field campaigns, each trying to answer specific questions. Many focus on one or other aspect of the system as described in chapter 1, such as the fluxes from leads (eg. AIDJEX and LEADEX), or the coupling between clouds and surface (eg. SHEBA and ASCOS). The results of the studies which measured surface heat fluxes are summarised in Table 4.1. In general the presence of leads in the sea ice increases the surface heat fluxes, which are negligible over the sea ice (Fairall & Markson, 1987; Perovich *et al.*, 1999; Vihma & Brümmer, 2002), with the magnitude of the flux being dependent on the width of the leads present (Persson *et al.*, 1997). The magnitude of the fluxes observed is variable, with STABLE observing fluxes of up to 180 $\mathrm{W\,m}^{-2}$ while Fire-ACE observed a SHF of 56 Wm^{-2} over a 3 km lead, meaning that the variability that is possible in the sea ice cover causes variability in magnitude of the surface fluxes.

The ACCACIA project aimed to examine several aspects of the system and their interactions, including understanding the properties of the clouds, how they interact

Table 4.1: Summary of fluxes observed during the campaigns discussed here.

Campaign	Reference	Platform	Observations
AIDJEX	Andreas *et al.* (1979)	Tower	$SHF < 190$ Wm^{-2} , $LHF < 50$ Wm^{-2} downwind of leads.
MIZEX	Fairall & Markson (1987)	Aircraft	Total heat flux of 30 Wm^{-2} observed over water, negligible over sea ice.
LEADEX	Ruffieux *et al.* (1995); Persson *et al.* (1997).	Tower	SHF sensitive to lead width, 30 Wm^{-2} from the narrow lead and 170 Wm^{-2} downwind of the wider lead.
BASE	Paluch *et al.* (1997); Pinto (1998)	Aircraft	Average SHF from leads 82 Wm^{-2}.
	Renfrew & Moore (1999)	Aircraft	SHF 500 Wm^{-2}, LHF 100 Wm^{-2}, uncertainties ± 20%.
SHEBA	Perovich *et al.* (1999); Pinto *et al.* (2003); Zuidema *et al.* (2005); Intrieri *et al.* (2002)	On Ice	Fluxes two orders of magnitude larger over water than ice.
FIRE-ACE	Gultepe *et al.* (2003)	Aircraft	Over a 3 km lead, SHF 56 Wm^{-2} , LHF 14 W m^{-2}
BASIS	Vihma & Brümmer (2002)	Aircraft	Surface heat flux 4-9 times larger over the water than the ice
STABLE	(Tetzlaff *et al.*, 2015)	Aircraft	$SHF < 180$ W m^{-2}

with sea ice cover, and how they interact with the boundary layer. Considering more of the components of the MIZ system together with their interactions should help to shed light on this complex and interlinking problem. This Chapter discusses the instrumentation used on the aircraft and the observations made during two cases. The discussion of the observations sets the scene for the following chapters, where the observations are compared to model output in sensitivity studies.

4.2 METHODOLOGY

The ACCACIA measurement campaign was undertaken in the spring of 2013, using the FAAM BAe-146 instrumented aircraft and the British Antarctic Survey MASIN aircraft. The flights were predominantly made to the south east of the Svalbard Archipelago, as shown in Fig. 4.1. Flight paths were comprised of stacks of horizontal legs (or runs) and profiles over the sea ice, MIZ and open water, mostly perpendicular to the ice edge. These flight paths can be viewed as a cross-section of the atmosphere over the MIZ. Two flights will be discussed in more detail, these are B760 (Case 1) and B765 (Case 2), Case 1 took place on 21st March 2013, and Case 2 on 30th March 2013. The instrumentation on the FAAM aircraft which is used here is summarised in Table 4.2 and briefly described below.

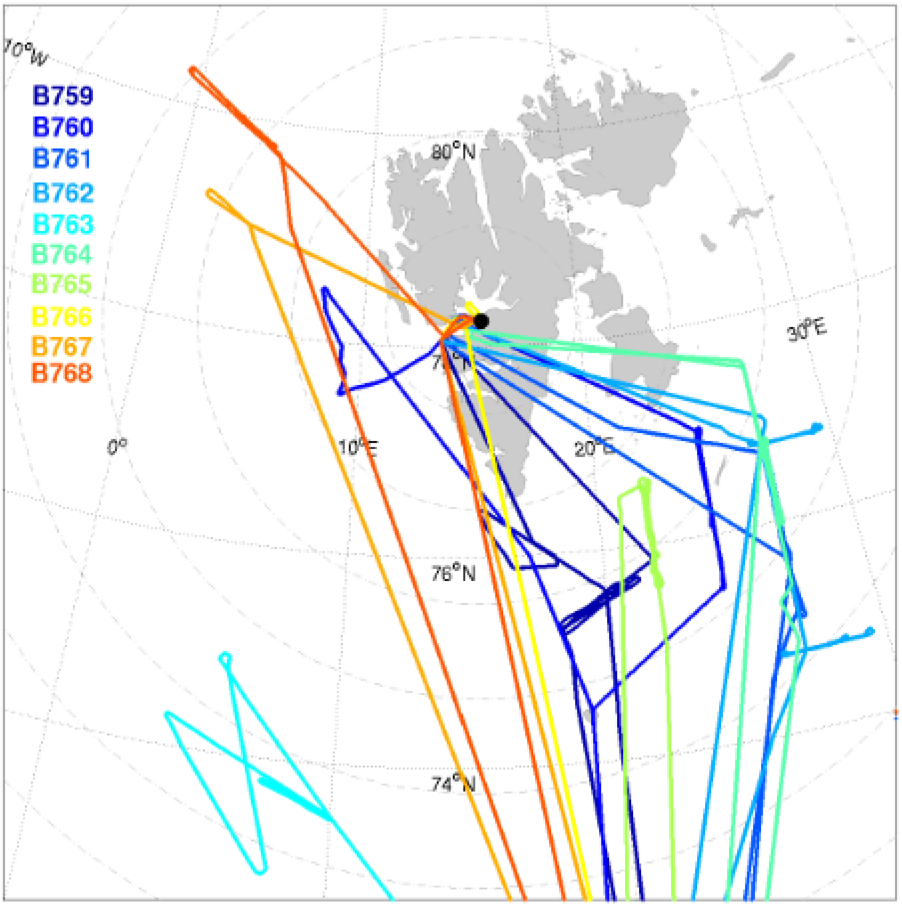

Figure 4.1: All the FAAM flight tracks for the ACCACIA spring campaign, B760 is Case 1 and B765 is Case 2, Case 1 took place on 21st March 2013, and Case 2 on 30th March 2013.

Table 4.2: Table detailing the instruments on the FAAM BAe-146 used in this Thesis.

Instrument	Parameter	Notes	Uncertainty
GIN	Latitude, longitude, altitude.	Range : 0-35kft, ±75degN	5m (Lat, Lon), 7m(alt)
Rosemount type 102 probe (deiced)	Temperature	Range : -70°C to 150°C	± 0.3K
Heimann radiometer	Upwelling infrared brightness temp	8-14 μm Range -50°C to +50°C	±0.5K
Lyman-α absorption hygrometer	Total water content (liquid plus vapour), dewpt	0-20g kg^{-1}	± 0.15 g kg^{-1}
Buck CR2 mirror hygrometer	Water volume mixing ratio ppmv	-40- +40C	±0.1C
Turbulence probe	wind speed and direction		Airspeed ± 0.4 ms^{-1} Incidence ± 0.1deg
Eppley PSP (red and clear dome) Pyranometers	Down/up SW irradience	-40 - 30C / 300 to 2800nm	±1%
General Eastern chilled mirror hygrometer	Dewpoint	220 to 320K	± 0.25K above 273.15K increasing to ±1K at 230K. Instrument slow to respond to large dewpoint oscillations.
Cloud Droplet Probe (CDP)	Liquid water content	range: 3μ m - 50μ m diameter, temps -40 to 40 C	
Two-Dimensional Stereoscopic Probe (2D-S)	Frozen water content	higher-resolution optical array shadow probe, image resolution of 10 μm	

4.2.1 SURFACE TEMPERATURE

Measurements of surface temperature were made using the Heimann downward facing radiometer which measures the up-welling infra-red radiance in the range 8-14 μm and records at 4 Hz. When flying below cloud the measurement is a function of surface temperature, and with no cloud below the aircraft. The emissivity is corrected by calibration against the ARIES inferometer during the flight, so that the T_{sfc} is accurate to within 0.7 K (Cook & Renfrew, 2015).

4.2.2 TURBULENCE PROBE

Turbulence is an important feature of the BL, it is calculated using data from the turbulence probe which comprises a five hole pressure measurement system mounted in the aircraft radome and two static ports, positioned either side of the aircraft. The outputs from turbulence probe are the angle of attack and sideslip along with the true airspeed. Utilising the aircraft altitude and velocity data from the reduced vertical separation minimum (RVSM) compliant air data computer and measurements of the ambient air temperature, wind components (u, v and w) are derived and recorded at 32 Hz. Due to its position on the nose of the aircraft, the turbulence probes can be sensitive to icing. In order to counteract this, the turbulence probe is heated.

4.2.3 SW RADIATION

The SW radiation is used to calculate the albedo, and is measured using two Eppley PSP Pyranometers. These pyranometers measure the $SW\downarrow$ and $SW\uparrow$ and are covered in two glass domes to protect the instrument and to define the operating wavelength range (300 to 2800nm).

4.2.4 AIR TEMPERATURE

The air temperature is measured using Rosemount temperature sensors, both de-iced and non-de-iced. These temperature sensors are both platinum resistance immersion thermometers. Due to the nature of the flight paths including flying in clouds, the de-iced sensor is used in this thesis. The instrument has an overall measurement uncertainty of ± 0.3 K.

4.2.5 DEW POINT AND VAPOUR

Dew point is measured using the Lyman-α total water content (TWC) probe, total water content means that all ice and liquid is evaporated and measured along with any pre-existing water vapour. The Lyman-α is an absorption hygrometer which records total water at 64 Hz with an uncertainty of ± 0.15 g kg^{-1}. To find the water vapour content the Buck CR2 chilled mirror hygrometer is used, the Buck CR2 measures the temperature of the mirror to find the dewpoint. The dewpoint is used to calculate a vapour pressure, which can then be used to calculate the water vapour mixing ratio in ppmv. The mixing ratio output is then converted to g kg^{-1} using the following formula,

$$Q_V = 1 \times 10^{-3} \times VAP \times \frac{R}{R_{water}}, \tag{4.1}$$

where VAP is the water vapour mixing ratio calculated by the the Buck CR2 and R is the specific gas constant for air and R_{water} is that for water. The Buck CR2 can be slow to respond to large oscillations in dew point. The error on the calculated Q_V is $\pm 6.2 \times 10^{-5}$.

4.2.6 CLOUDS

For cloud liquid water mixing ratio Q_{LW}, data from the Cloud Droplet Probe (CDP) is used. The CDP uses a diode laser to count and size individual water droplets, and gives a binned droplet size distribution over a specified sampling interval. The CDP measures the liquid droplet size distribution over the particle size range of 3 - 50 μm. The light from the laser scattered forward in the range 4-12° is collected and particle diameter calculated from this information using Mie scattering solutions (Lance *et al.*, 2010).

For the ice water mixing ratio Q_{IW} water content, the 2 dimensional stereo (2D-S) probe is used. The 2D-S is a high resolution optical array shadow probe which consists of two 128-element photodiode arrays with an image resolution of 10 μm. Two laser beams at right angles illuminate these photodiode arrays, allowing two independent images of a cloud particle to be recorded if it is within the overlapping region (Lawson *et al.*, 2006).

4.2.7 FLUX CALCULATIONS

The fluxes of latent and sensible heat are taken from the Elvidge *et al.* (2016) flux database where they have been calculated using eddy covariance. To calculate the fluxes, the lowest level straight flight runs of each case were divided into several flux runs of 9 km length. The suitability of this flux run length scale was evaluated in order to chose a duration that both captured several eddies across the dominant range of spectrum and provided enough data points for the calculations. The evaluation was carried out by visually inspecting a series of statistical diagnostics describing the variability of the perturbation wind components along each flux run. A run was rejected either in the case of instrument malfunction, or where it did not conform to the following criteria:

- The power spectra of the along wind velocity component should have a well-defined decay slope ($k^{-5/3}$ for wave number k, a Kolmogorov spectrum) implying the turbulence is homogeneous.
- The total covariance of the along wind velocity and vertical velocity should be far greater in magnitude than that of the cross-wind velocity and vertical velocity (which should be small), indicating alignment of the shear and stress vectors.
- The summation of the covariance of the along-wind velocity and the vertical velocity, $\Sigma\left(\overline{a'w'}\right)$ (where a is the along wind component) should be close to a constant slope, indicating homogeneous covariance.
- The cospectra of the covariance of the along-wind velocity and the vertical velocity should have little power at wavenumbers smaller than about 10^{-4} m^{-1}, implying that mesoscale circulation features are not contributing significantly to the stress.
- The cumulative summation of the cospectra should be shaped as ogives ("S"-shaped, with flat ends) implying that all of the wavenumbers that contribute to the total stress have been sampled and again that mesoscale features are not present.

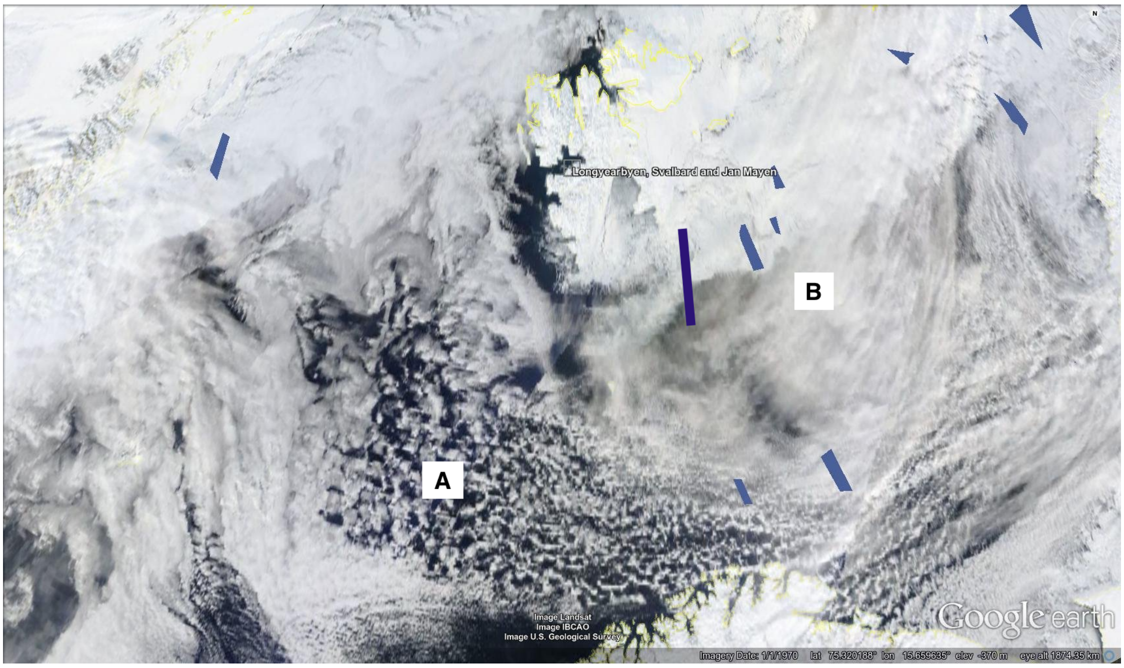

Figure 4.2: MODIS terra image on Google Earth for the date of Case 1, the area of the cross section is marked in blue, and is approximately 165 km long. The A marks the convective cells, B indicates the high, thin cloud. The thin yellow lines mark the edge of the land masses, and the blue patches are areas without satellite imagery. The Terra descending pass is between 9:00 and 10:00 UTC, with the eastern swath being at the earlier time. The flight itself took place from 12:00 to 15:30 UTC.

Using these flux runs, fluxes were then calculated using eddy covariance. The equations for SHF and LHF are thus (following Garrat (1992)),

$$SHF = \rho c_p \overline{(w'\theta')} \tag{4.2}$$

$$LHF = \rho L_v \overline{(w'q')}. \tag{4.3}$$

Where L_v is the latent heat of vapourisation. The error for SHF is 0.01 W m^{-2} while that for LHF is smaller at 0.4×10^{-2}.

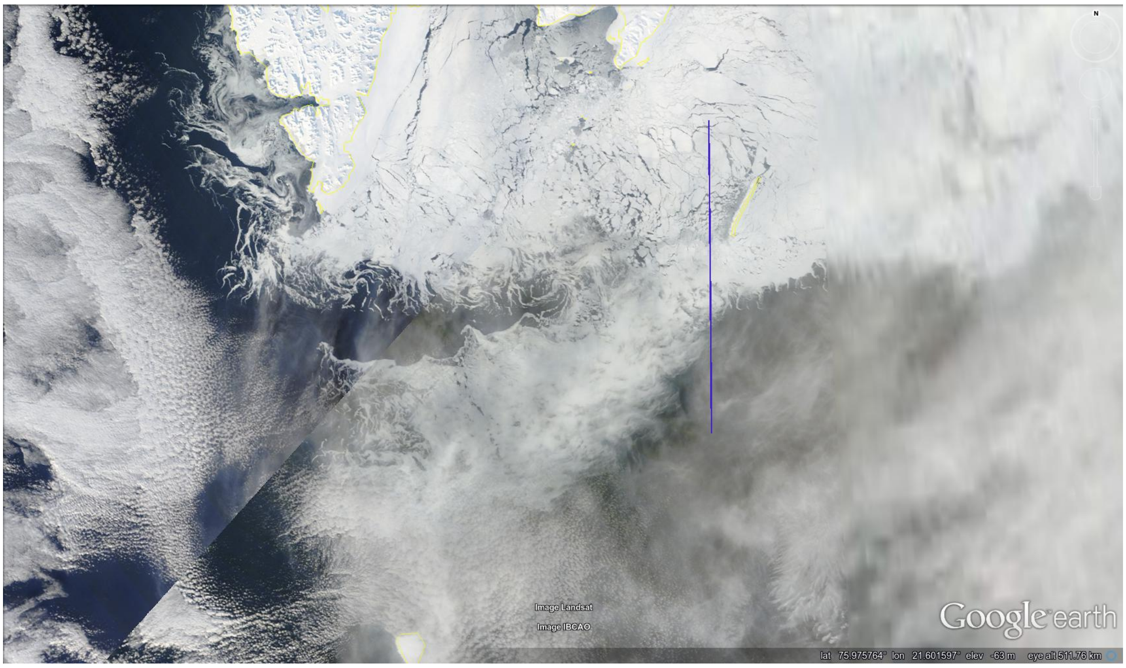

Figure 4.3: MODIS image on Google Earth for the date of Case 1, zoomed in over the area of the flight, the area of the cross section is marked in blue. The broken nature of the ice can be seen and convective clouds can be seen forming to the south west of the flight cross section.

4.2.8 CHOICE OF TWO CASES

Two cases were selected from the available flights, with both cases having cross-sections to the south of Svalbard and being over the MIZ during off ice airflow. Case 1 took place on the 21st March 2013 from 12 to 15:30 UTC and has flight number B760. The air pressure was in general high at 1036 hPa, with winds of 9 ms^{-1} coming from 338 °N in the boundary layer, with wind veering with altitude. A satellite image taken on the day of the flight is shown in Fig. 4.2, the area of the cross section is indicated by the blue line. The sea ice is visible through the thin, high cloud (B), showing that the flight is over the MIZ. Convective clouds can be seen to start far south-west of the ice edge (A). The higher resolution zoomed in image in Fig. 4.3 allows the surface of the MIZ to be seen. Again the blue line indicates the location of the cross section, and it shows the flight covers a range of sea ice types, from large floes to increasing open water, with a darker patch in the middle, which may be related to the small island (outlined in yellow) to the east. The sea ice floes get smaller further to the south of the cross section, with the ice showing swirls where it is being moved by the sea and wind, this is particularly evident to the east of Svalbard, where there is a cloud free area. The surface at the southern end of the cross section looks dark, so implying the

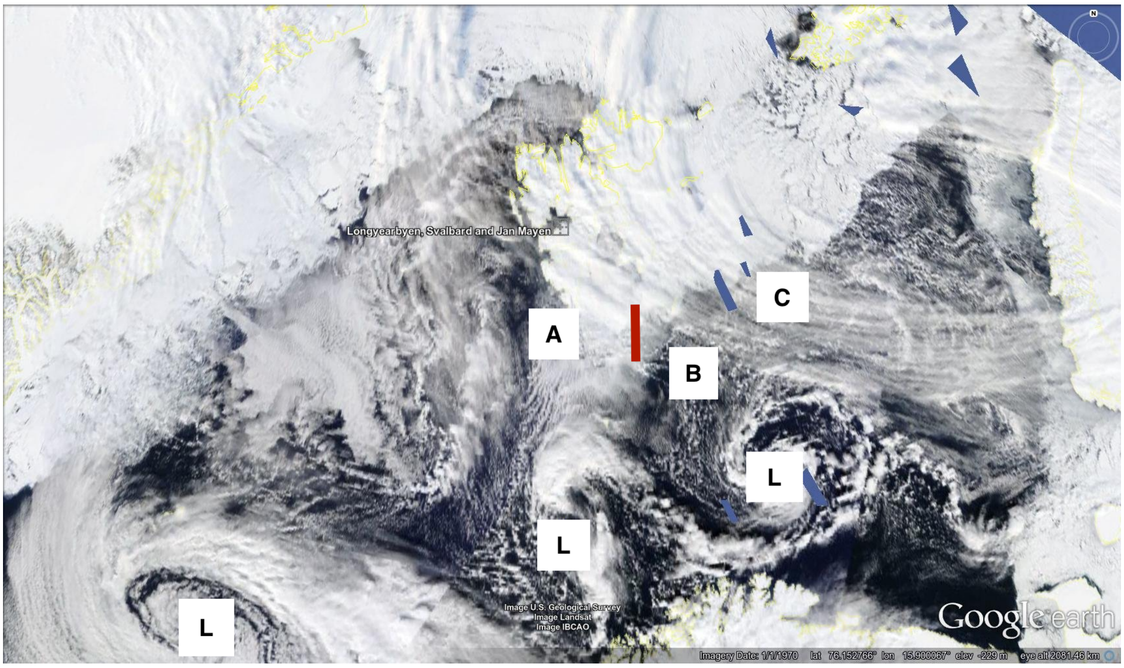

Figure 4.4: MODIS image on Google Earth for the date of Case 2, the area of the cross section is marked in red, and is approximately 112 km long. The low pressure systems are marked as L, A marks an area of cloud streaks, B shows the location of convective cells, and C high cloud. The thin yellow lines mark the edge of the land masses, and the blue patches are areas without satellite imagery.The Terra descending pass is between 9:00 and 11:00 UTC, with the earlier swath being to the east. The flight itself took place from 11:15 to 12:30 UTC.

presence of thin dark ice, very small ice floes or open water.

Case 2 took place nine days later on the 30th March 2013, with the science part of the flight from 11:15 to 12:30 UTC and has flight number B765. The air pressure is now much lower at 1004 hPa, and the satellite image in Fig. 4.4 shows a variety of low pressure systems (mainly polar lows, marked L) to the south of Svalbard. The cross section is marked in Fig. 4.4 and again the wind speed is 9 ms^{-1}, still flowing off ice but now from 39 °N at the bottom of the BL, with the wind direction veering with height to 90 °N. The image shows the presence of cloud streaks at point A, and convective clouds at point B while point C is where the sweep of high cloud can be seen. The high resolution closer image in Fig. 4.5 has the cross section once again marked in red. The northern end of the cross section is over white sea ice, though

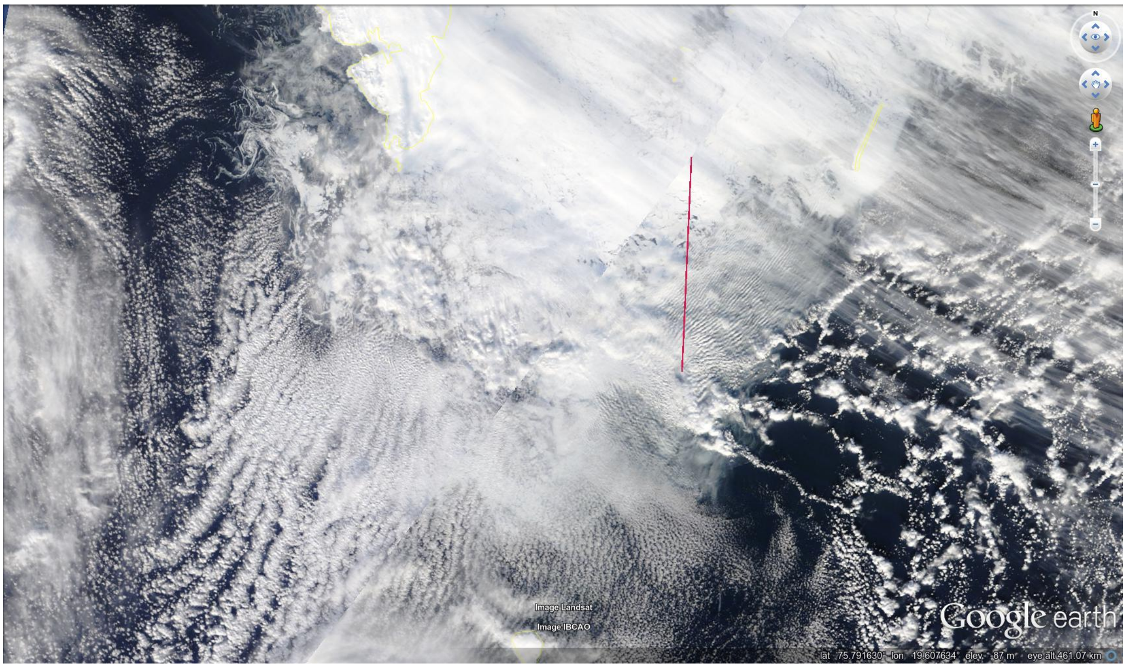

Figure 4.5: MODIS image on Google Earth for the date of Case 2, zoomed in over the area of interest the area of the cross section is marked in red. The south of the cross section is within an area of buoyancy wave clouds. Convective cells are slightly south east of the cross section, and to the east of the cross section, cloud streets can be seen forming off the ice edge.

the swirling patterns indicating smaller floes now occurs north of the middle of this cross section. The southern half of the cross section shows evidence of buoyancy wave clouds, caused by the stable air being disturbed possibly by convection starting below. To the south west of the cross section, cloud streaks can be seen, and to the south east, convective clouds.

These two cases were selected partly due to their similarities, both having off ice air flow in the boundary layer at the same wind speed and being over the MIZ to the south of Svalbard. The cases were also chosen for their differences, Case 2 is slightly to the south and west of Case 1, and has less white sea ice visible under the cross section, it also seems to show the development of convective cloud closer to the ice edge. Examining the differences between these cases could shed light on what controls the distance off ice of the onset of convection. The information for both cases is summarised in Table 4.3. The results for these two cases will be compared and contrasted below.

Table 4.3: Meteorological information for both cases.

	B760	B765
Date	21/03/2013	30/03/2013
Time	12:00 - 15:30 UTC	11:15 - 12:30 UTC
Start - End of Cross-section	75°30'N 24°24'E to 76°59'N 24°31'E	75°36'N 21°49'E to 76°36'N 22°8'E
Pressure	1036 hPa	1004 hPa
Wind Speed	9 ms^{-1}	9 ms^{-1}
BL Wind Direction	338 °	39 °
Cloud cover	Thin high cloud.	Thin high cloud, convective below.

(a) 77 °N **(b)** 75.9 °N

Figure 4.6: Photos from Case 1, 4.6a was taken at 77 °N as the lowest level leg was about to start. Photo 4.6b was taken at the end of the MIZ at 75.9 °N. Photographs taken by the author.

4.3 RESULTS

4.3.1 SURFACE

To understand the surface conditions observed during both cases, images are shown for Case 1 in Fig. 4.6 and for Case 2 in Fig. 4.7, to place these into context the locations of the images are noted on Fig. 4.8 as the lower case letters. At the north of the cross section for Case 1 in Fig 4.6a, large white floes with evidence of rafting can be seen, along with smaller broken floes and narrow leads. The ice here is not completely

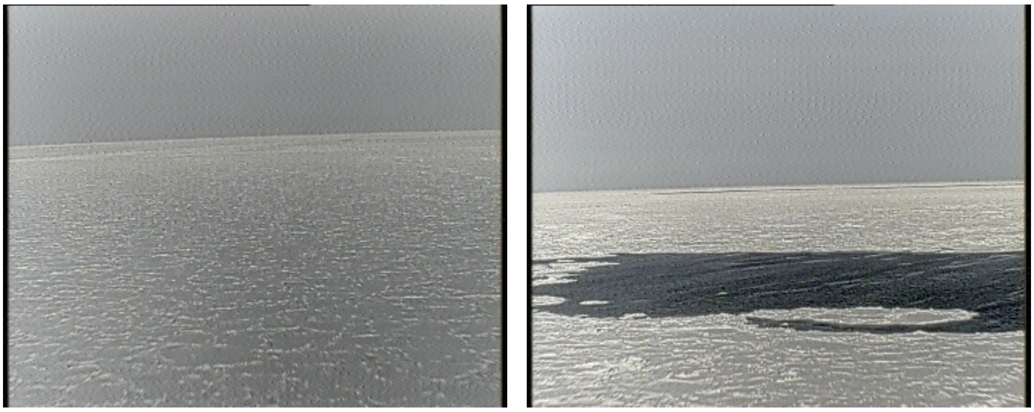

(a) 76.4 °N **(b)** 76.3 °N

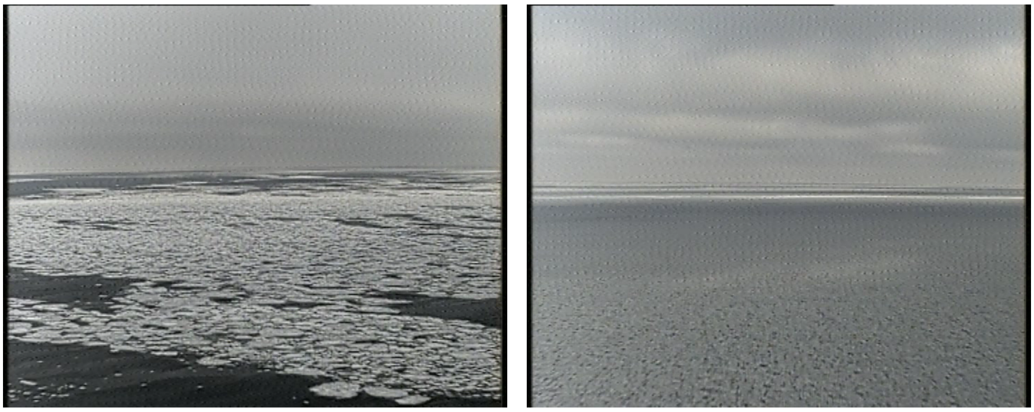

(c) 76 °N **(d)** 75.7 °N

Figure 4.7: Four stills taken from the rear facing video camera on the FAAM BAe-146 during Case 2. Photo 4.7a is from the start of the lowest level run at 76.4N, photo 4.7b is from 76.3N, 4.7c is from 76N and 4.7d is from the end of the lowest level leg at 75.7N

homogeneous. Whereas at the end of the MIZ, Fig. 4.6b shows a dark surface, with the presence of grease ice, which is defined by the WMO as ice crystals which have coagulated to form a soupy layer on the surface of the sea, it reflects little light, giving the sea a matt appearance (JCOMM, 2014). This corresponds to the area of slightly cooler surface temperatures seen north of point b in the top plot of Fig. 4.8. For Case 2, Fig. 4.7 shows stills from the rear facing video camera aboard the FAAM aircraft. They show the changing surface over the MIZ during the lowest level flight leg. At the northern end of the run, Fig. 4.7a shows a white solid ice surface of first year ice, with evidence of ridging and rafting around what once were independent floes (JCOMM, 2014). Fig. 4.7b shows the presence of a lead within this area of white ice, which corresponds to the warmer area just north of b at 76.3 °N in the bottom plot of Fig. 4.8. Continuing over the MIZ, Fig. 4.7c shows the floes now as much more independent blocks of ice, with open water surrounding them, the surface temperature here is more variable than further south of point c in the bottom plot of Fig. 4.8, indicating these flows cool the surface, but not by as much as the larger areas of ice. Finally at the end of the MIZ, Fig. 4.7d shows an area of small independent chunks of white ice, described as close ice. It can be seen that Case 2 shows a more homogeneous surface at the start of the MIZ than Case 1, which also has much less ice at the end of the MIZ than Case 2. Both cases show a complex surface which changes dramatically across the MIZ.

Surface temperature can also be used to show the complexity of the surface (Fig. 4.8). The plots have the location of the start and end of the MIZ marked on them with grey dashed lines, and the locations A and B marked with black dashed lines are the locations of two profiles discussed later. The variation in surface temperature across the MIZ for both cases, shows that the surface is non-homogeneous. Over the MIZ the minimum temperature for Case 1 is 256.7 K while the open water temperature maximum is 272.3 K. The widest lead is at about 76.58 °N and is about 2.6 km wide with a maximum temperature of 269.8 K implying the lead is slightly frozen. For Case 2 the minimum T_{sfc} is 263.6 K and the temperature in the leads is 272.8 K. The temperature at the end of the MIZ is 271.7 K, which corresponds to the image in Fig. 4.7d where some ice is still visible. The widest lead for Case 2 occurs at about 76.29 °N, and is about 2.3 km wide, with a maximum temperature of 272.8 K, implying the lead is fully open water. This is also confirmed from the video. Therefore even though Case 2 starts with more solid ice than Case 1, it is still warmer. The MIZ surface may be warmer for Case 2 due to the ice being thinner or darker, which would be consistent with there being wider, more open leads. Case 2 is also slightly further south than Case 1, and has a slightly warmer atmosphere which would also contribute to Case 2 being warmer. The open water temperature is pretty consistent between both, as should be expected.

The albedo (α) is also useful for establishing the location of leads and whether the surface for Case 2 is darker. However as there is some icing present in the $SW \downarrow$ pyranometer, the α data has gaps, particularly for Case 1 (figure not shown). Despite this icing, both the α plots show that the α decreases across the MIZ, from around 0.8 to 0.2 for case 1 and from 0.8 to around 0.4 for case 2. Both cases do report some values near 1, implying a very reflective surface, possibly with some new snow.

Examining just the $SW \uparrow$, in Fig. 4.9, avoids the problems evident with α. However,

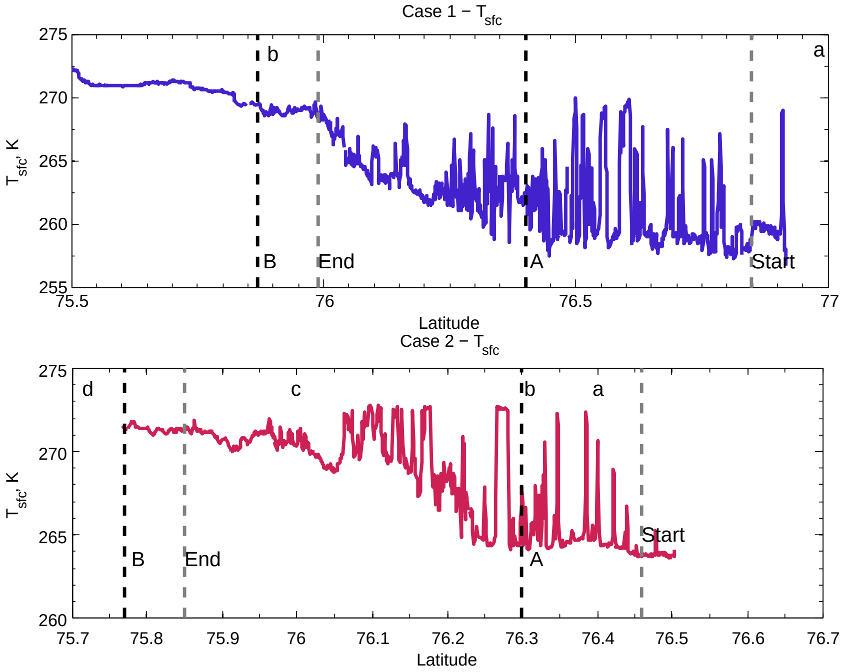

Figure 4.8: The surface temperature (K) for Cases 1 and 2. The grey lines mark the start and end of the MIZ while the black lines mark the locations of profiles A and B. The lower case letters mark the positions of the photographs in Figs. 4.6 and 4.7.

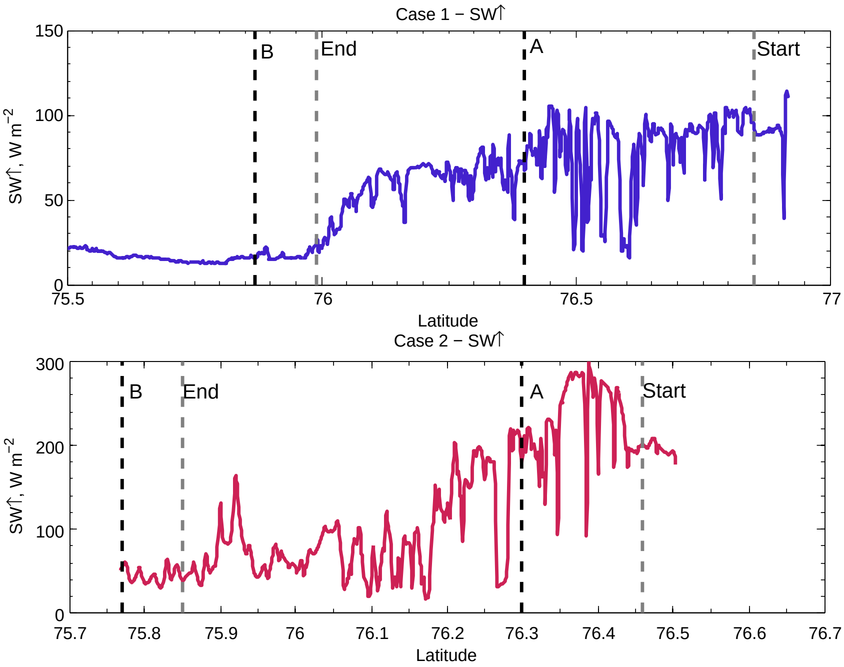

Figure 4.9: The $SW\uparrow$ (W m^{-2}) for Cases 1 and 2. The grey lines mark the start and end of the MIZ while the black lines mark the locations of profiles A and B.

without knowing the proportion of downwards radiation, conclusions about how reflective or otherwise the ice surface is cannot be made between the two cases. It can be seen that for both cases, the leads are darker than the surrounding ice, and the widest are even nearly as dark as the open water. For Case 1 the largest lead shows a $SW\uparrow$ value of 20 W m^{-2} whereas the open water after B, has a $SW\uparrow$ value of 15 W m^{-2}, which adds to the evidence for there being some thin ice in this lead. For Case 2 the largest lead shows a $SW\uparrow$ value of 30 W m^{-2}, matching the end of the run where it shows a minimum open water value of 30 W m^{-2}. This implies this lead is indeed open. The end of case 2 shows some oscillations, which could imply the presence of some thin floes of ice, or of some clouds reducing the down-welling radiation.

To further explore the differences between the surfaces for Case 1 and 2, the scatter plot of $SW\uparrow$ against T_{sfc} is shown in Fig. 4.10. Both cases show a strong negative correlation between T_{sfc} and $SW\uparrow$, as would be expected due to the colder sea ice being whiter and more reflective. The surface in Case 1 is colder, but also reflects less SW radiation however without knowing the amount of SW incident on the surface, it cannot be said if the surface was darker. The change from more reflective and colder, to less reflective and warmer is more continuous than that for Case 2, where there are two more obvious clusters of points. The clusters indicate an area of warmer, but still reflective surface and an area of colder, more reflective surface. This implies there are more areas with large chunks of sea ice than in Case 1.

Both cases therefore show a complex surface, with proportions of open water increasing towards the south. Case 1 is in general cooler than Case 2, with the minimum temperature being 256.7 K compared to 263.6 K for Case 2. The cooler surface in Case 1 implies there could be some freezing in the leads, and indeed according to both T_{sfc} and $SW\uparrow$ Case 1 can be assumed to have ice present in the leads, as the T_{sfc} is lower in the leads than over the water at the end of the MIZ, and the leads are not as dark as the open water. Case 2, being warmer is more likely to have open water in the leads, and again this is confirmed by both T_{sfc} and $SW\uparrow$.

4.3.2 FLUXES

The differences in surface temperatures between the two cases will impact the surface fluxes. The surface flux of sensible heat for both cases is shown in Fig. 4.11. Both

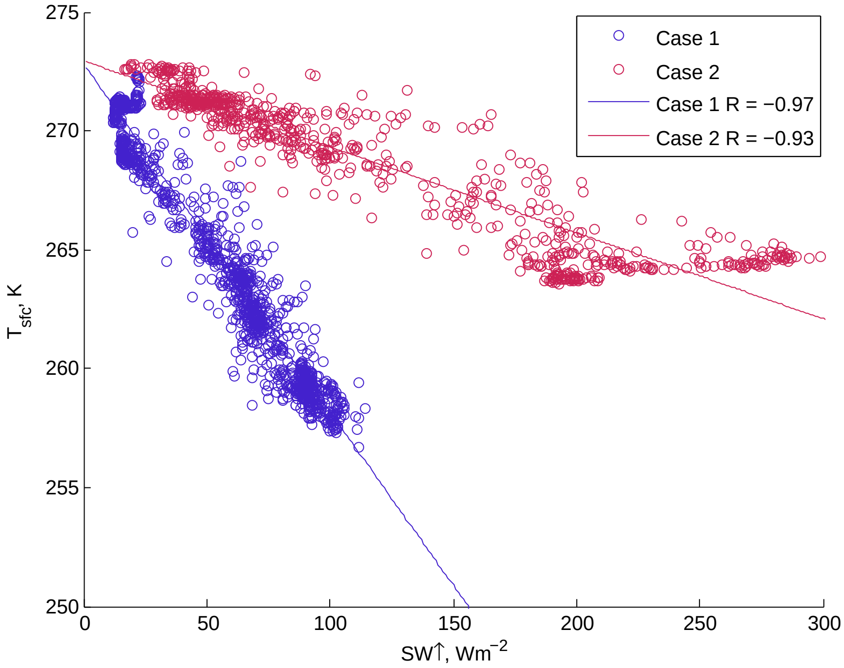

Figure 4.10: The surface temperature plotted against the upwelling shortwave radiation for the lowest level run, the dots are the observations and lines show the correlation.

cases show some increase across the MIZ, from -10 to 66 W m^{-2} for Case 1 and from -7 to 24 W m^{-2} for Case 2. The highest fluxes are recorded over the MIZ for Case 2, while they are highest at the end of the MIZ for Case 1. This could be as the surface is warmer in general for Case 2, the fluxes would increase earlier than for Case 1. The *LHF* in Fig. 4.12 shows a similar shape to *SHF*. Again for Case 1, the values only really increase off ice, from -0.3 to 72 W m^{-2} while for Case 2 the values rise from 1 over the ice to 30 W m^{-2} with the maximum being in the middle of the MIZ. Case 1 has higher *SHF* and *LHF* values than Case 2, despite having a colder surface, this is due to there being larger difference between the air and surface temperatures, indeed looking at the θ values for Case 1 at position B, there is a 8 K difference between the surface and lowest layer values of θ (Fig.4.13).

These values of *SHF* and *LHF* are low compared to other observations, such as Renfrew & Moore (1999) where *SHF* of 500 W m^{-2} was observed off ice, or Tetzlaff *et al.* (2015) where *SHF* values of 180 W m^{-2} were recorded. However other observations of *SHF* such as those in Paluch *et al.* (1997) at 55 W m^{-2} and Gultepe *et al.* (2003) at 56 W m^{-2} are much closer. This could be due to these observations being over leads as opposed to large polynyas or open water or the flight not being parallel to the lead edge Tetzlaff *et al.* (2015).

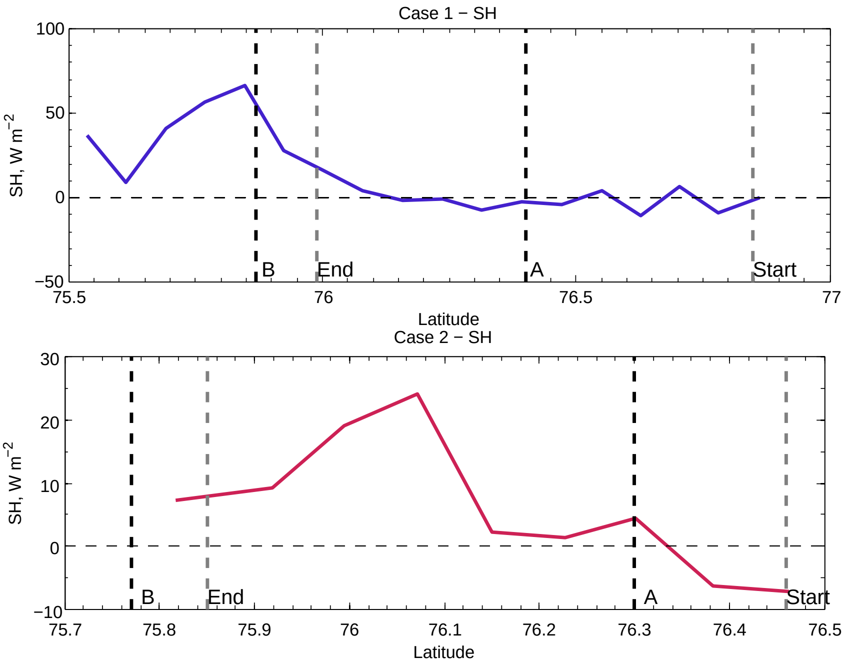

Figure 4.11: The sensible heat flux for Cases 1 and 2. The grey lines mark the start and end of the MIZ while the black lines mark the locations of profiles A and B.

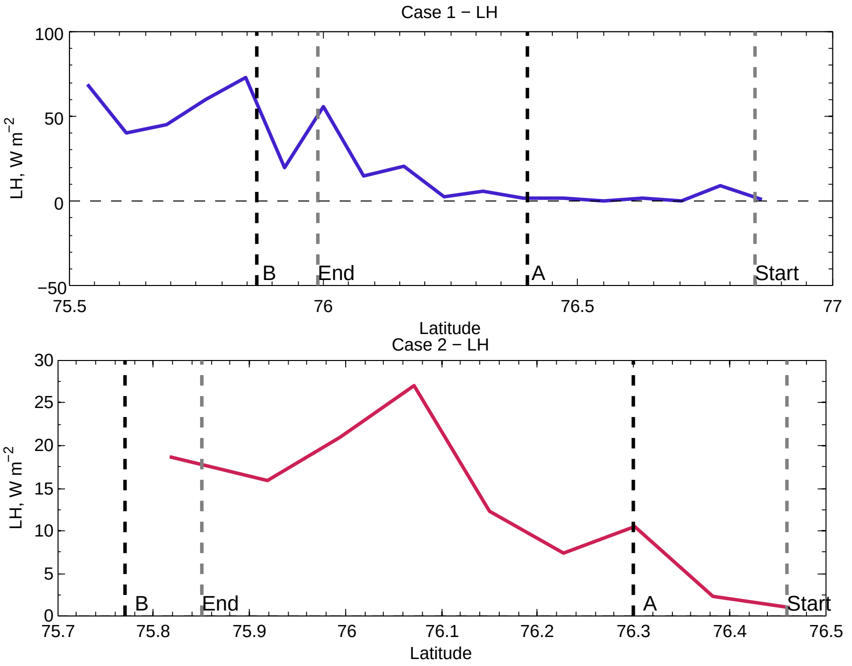

Figure 4.12: The latent heat flux for Cases 1 and 2. The grey lines mark the start and end of the MIZ while the black lines mark the locations of profiles A and B.

4.3.3 BOUNDARY LAYER

As has been discussed above, the surface for Case 2 is warmer than Case 1, but lower values for SHF and LHF were observed when compared to Case 1. This might impact the boundary layer development. Profiles of θ are shown in Fig. 4.13 for both cases. Solid lines are profiles from point A, which is in the middle of the MIZ, while the dashed lines are for point B which is after the MIZ. The Case 1 profile (blue) shows that the the surface warms by 8 K between points A and B. The initial BL height is just over 100m, which then rises to just over 200 m by point B.

Case 1 can be said to have a convective internal BL (CIBL), with both profiles having an unstable layer, with a well mixed layer and a capping inversion. Case 2 (red) is warmer than that for Case 1. The surface also warms by less across the MIZ, only increasing by 3 K. Initially at point A there is a clear CIBL, with a capping inversion at 200 m within a well mixed warmer atmosphere. By point B the CIBL has warmed to the extent that it has equilibrated with the well mixed atmosphere, thus the capping inversion is no longer visible.

Therefore Case 1 shows a slower development of a CIBL with θ at 100 m increasing by 3 K, whereas for Case 2 θ at 200 m warms by 6 K between the two profiles. While Case 2 has lower SHF and LHF values when compared to Case 1, the maximum value occurs between these two profiles, so the position of these higher fluxes could have contributed to the faster warming of the mixed layer.

Note that profile A is an artificial profile, taken from the same point in several different flight runs at different heights. Also the value of θ at the surface has been calculated using the pressure calculated for the surface using the hydrostatic equation and the surface temperature. The location of the surface θ corresponds to the location of the lowest point of the profile.

The change in surface from ice to more open water would also increase the availability of moisture. The q profiles in Fig. 4.14 show that for Case 1 the CIBL had a higher q than the air above at 1.4 g kg^{-1} compared to 0.6 g kg^{-1}, implying that the moisture is coming from the surface. Case 2 is in general more moist with the profile from point A being at most 2 g kg^{-1} compared to 1.4 g kg^{-1} for Case 1. For Case 2, however, the CIBL was drier than the free atmosphere. This means that the air being advected over the MIZ began drier and colder than the air above. Over the MIZ,

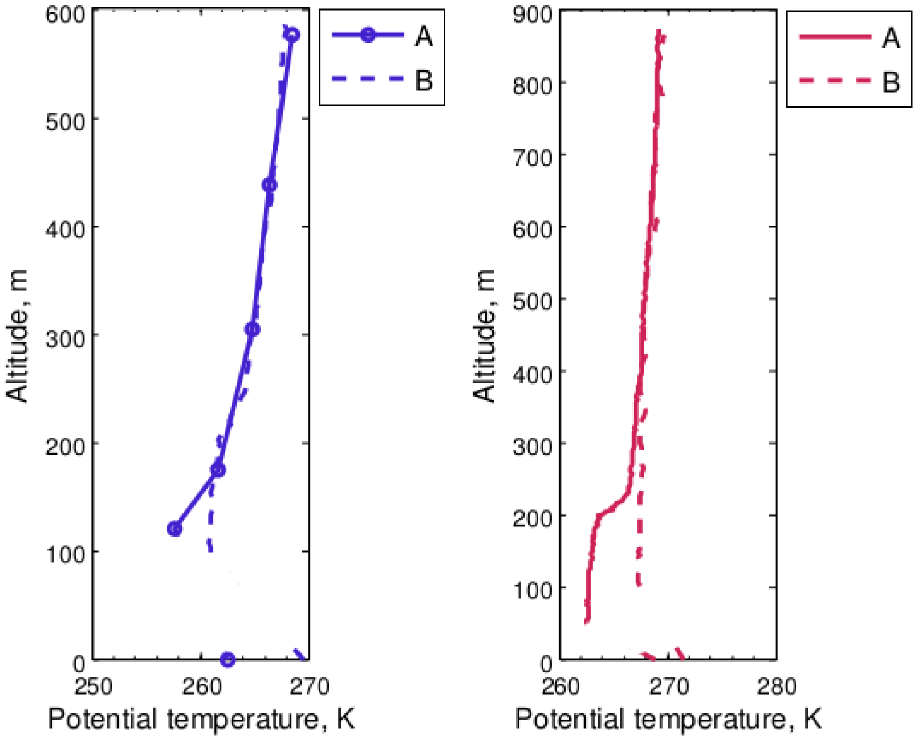

Figure 4.13: θ for both Case 1 (blue) and Case 2 (red). The solid lines are profiles from point A and the dashed lines are profiles from point B. The surface value of θ is taken from the surface temperature at the same point from the lowest level run. Case 1 profile A has been made of data at different heights (circles), and is not a continuous profile. Note the axes are different.

the CIBL does become more moist, equilibrating with the air above the CIBL as the θ profile also shows. For Case 2 the moisture is probably coming from both the surface and above the CIBL. With the surface no longer de-coupled from the air above, the open water areas can act as a source of moisture for the atmosphere, which is why the whole profile has become more moist by point B. The oscillations are caused by the slow response of the instrument to the changing moisture during the aircraft profile.

While the two cases differ in regards to temperature and moisture, the wind speed, W_s is more similar. The profiles of **U** in Fig. 4.15 show that both cases have winds of between 8 and 11 ms^{-1}. The two cases also show that W_s is decreased nearer to the surface, this is due to the effect of surface friction. For Case 1, the W_s increases slightly between A and B, from 8 to 9 ms^{-1}. The surface is becoming more open water and thus the surface friction would be reduced. For Case 2 , profile A shows a W_s maximum across the top of the CIBL. This is a weak low level jet (Stull, 2012), by profile B the Low level jet has reduced but as the surface and atmosphere are no longer decoupled by the presence of the CIBL, the atmosphere now feels the effects

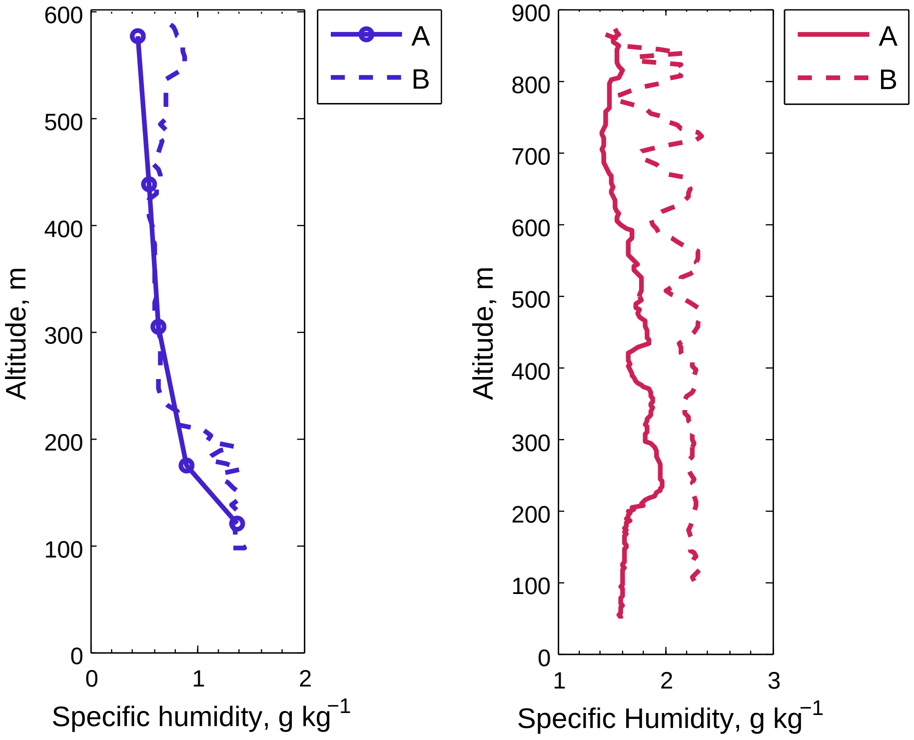

Figure 4.14: q for both Case 1 (blue) and Case 2 (red). Case 1 profile A has been made of data at different heights (circles), and is not a continuous profile. The solid lines are profiles from point A and the dashed lines are profiles from point B.

of the surface friction.

For both cases the BL warms across the MIZ and shows the formation of a CIBL. For Case 1 this CIBL is also more moist than the atmosphere above, meaning the surface is supplying moisture to the atmosphere, which is important for the formation of clouds. Case 2 also shows a CIBL, which is actually drier than the free atmosphere as the air being advected from the North is both cold and dry, however the minimum value at the surface of 1.6 g kg^{-1} is the maximum for Case 1. As the CIBL in Case 2 heats up and equilibrates with the free atmosphere, so it becomes more moist, with q values increasing. The whole atmosphere has gained around 0.4 g kg^{-1} q, while the lowest part has gained 0.7 g kg^{-1}, so once again the surface is a source of moisture.

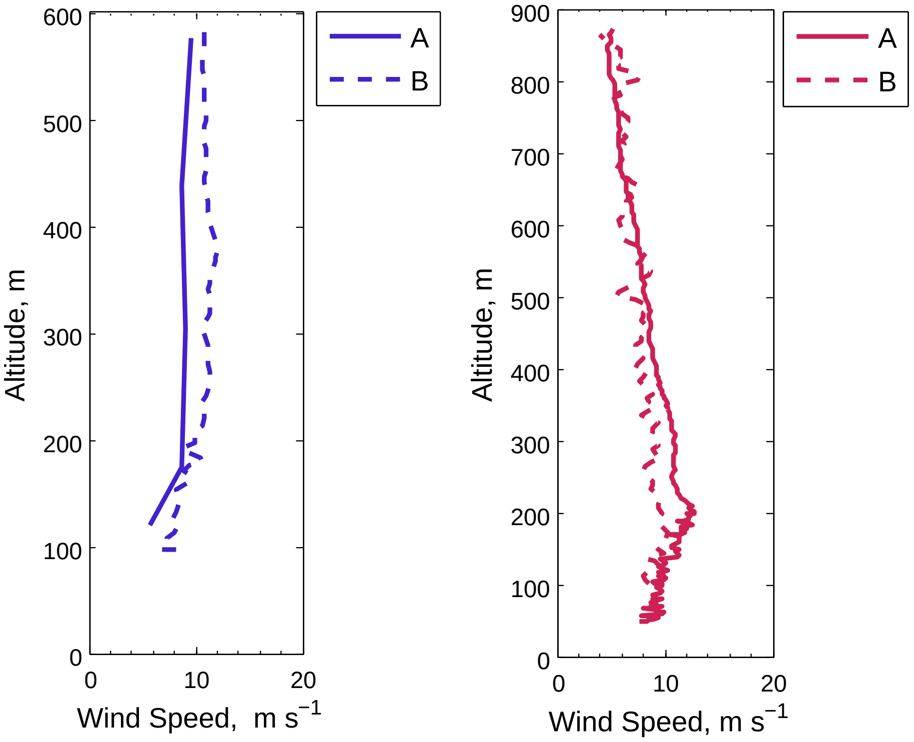

Figure 4.15: W_s for both Case 1 (blue) and Case 2 (red). Case 1, profile A has been made of data at different heights, and is not a continuous profile.The solid lines are profiles from point A and the dashed lines are profiles from point B.

4.3.4 CLOUDS

The surface moisture increase seen in the q profiles for Case 1 is below 200 m, while the whole air column is more moist in Case 2. The RH (not shown) has areas of > 100% RH meaning there are clouds in Case 2. The liquid water mixing ratio, Q_{LW} for both cases as measured using the CDP is shown in Fig. 4.16. Case 1 shows generally low concentrations (under 0.1 g kg^{-1}) over the MIZ, visible mostly in the lowest level leg. As the boundary layer height increases towards the south of the cross-section, the moisture is able to extend further up. This is due to the increase in BL height and the mixing up of water from the sea surface.

Case 2 shows low values of Q_{LW}, even in the lowest level leg however there is more liquid above 200 m than for Case 1. Case 2 shows a definite area of increased Q_{LW} south of 76N at 300m. This corresponds to a cloud which is seen in the flight videos. The mixing ratio of 0.3 g kg^{-1} seen beyond the end of the MIZ is within the range for a cloud in the Arctic (Lloyd *et al.*, 2015). The areas of higher Q_{LW} ratio increase in height as the BL height increases.

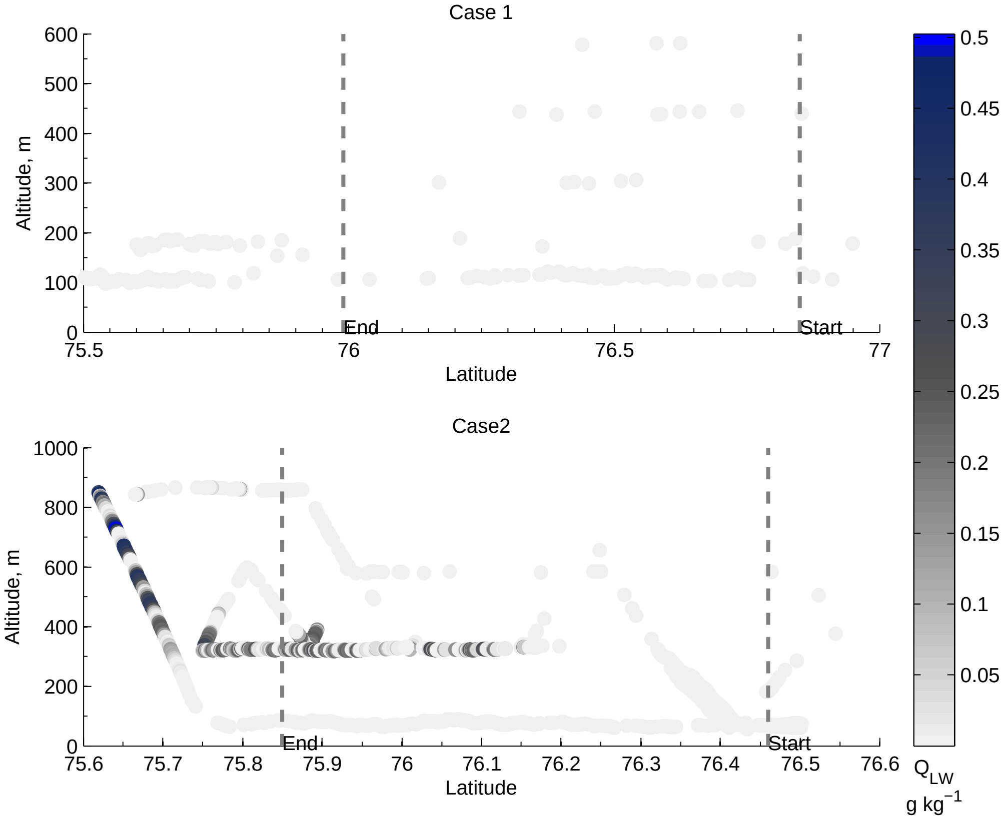

Figure 4.16: Liquid water mixing ratio, Q_{LW} in g kg^{-1} for both Case 1 (top) and Case 2 (bottom)

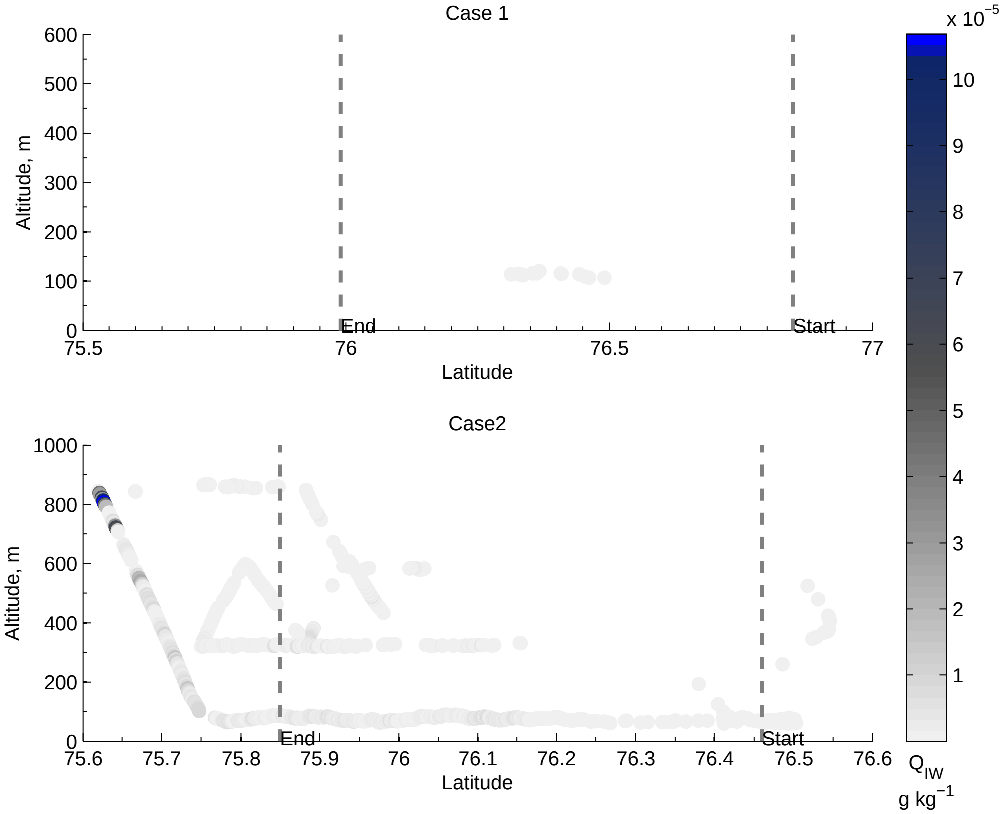

Figure 4.17: Ice water mixing ratio, Q_{IW} in g kg^{-1} for both Case 1 (top) and Case 2 (bottom)

4.4 DISCUSSION

This chapter examines some of the observations made during two flights of the FAAM BAe-146 instrumented aircraft during the ACCACIA campaign. The two flights are termed Case 1 and Case 2 with both taking place over the MIZ to the south of Svalbard. While both flights took place when cold air was flowing from north to south over the MIZ, Case 1 is in general drier and colder than Case 2 and has much less cloud.

For both cases a CIBL is formed, extra heat from the surface is responsible for destabilising the lower atmosphere and forming a convective internal BL. Both cases also show an increase in the height of this CIBL over the MIZ. For Case 1, Fig. 4.13 shows the surface θ is 261 K with an unstable layer capped by an inversion at 100 m, as this profile is a composite of values, the presence of a neutral layer is assumed below the inversion. The surface warms to 270 K and the inversion is now at 200 m. Between A and B the BL height increases by 100 m. For Case 2, Fig. 4.13 shows that at point A a clear CIBL is present with an inversion at 200 m. As the surface heats up the CIBL is warmed until it becomes the same temperature as the free atmosphere, thus the profile at point B does not have an obvious inversion.

It is thought that the MIZ is a source of moisture to the atmosphere (Pinto *et al.*, 2003; Kay & Gettelman, 2009; Sedlar *et al.*, 2011). For Case 1 where the wider atmosphere is drier, with a q of 0.6 g kg^{-1}, the lowest parts of both profiles have higher values for q at 1.4 g kg^{-1}. This implies that the surface is the source of the moisture for Case 1. For Case 2, the atmosphere becomes more moist between profiles A and B, however the BL begins drier, probably due to the air mass coming from the the North being drier. The BL does become more moist, increasing by 0.6 g kg^{-1} between point A and B, eventually becoming as moist as the wider atmosphere. This implies that the surface is providing moisture to the BL for both cases.

The MIZ is implicated in the formation of clouds off ice, as it is a source of heat and moisture (Paluch *et al.*, 1997; Renfrew & Moore, 1999; Pinto *et al.*, 2003; Gultepe *et al.*, 2003). As it begins drier than Case 2, Case 1 does not show as much formation of cloud as Case 2. Some ice and moisture within the BL is present over the MIZ for Case 1, with Q_{LW} extending higher after the end of the MIZ as the BL is higher. There may be some liquid cloud formed here within the BL. For Case 1 the surface is the only source of moisture. In contrast, Case 2 shows Q_{IW} through the whole BL at low concentrations,

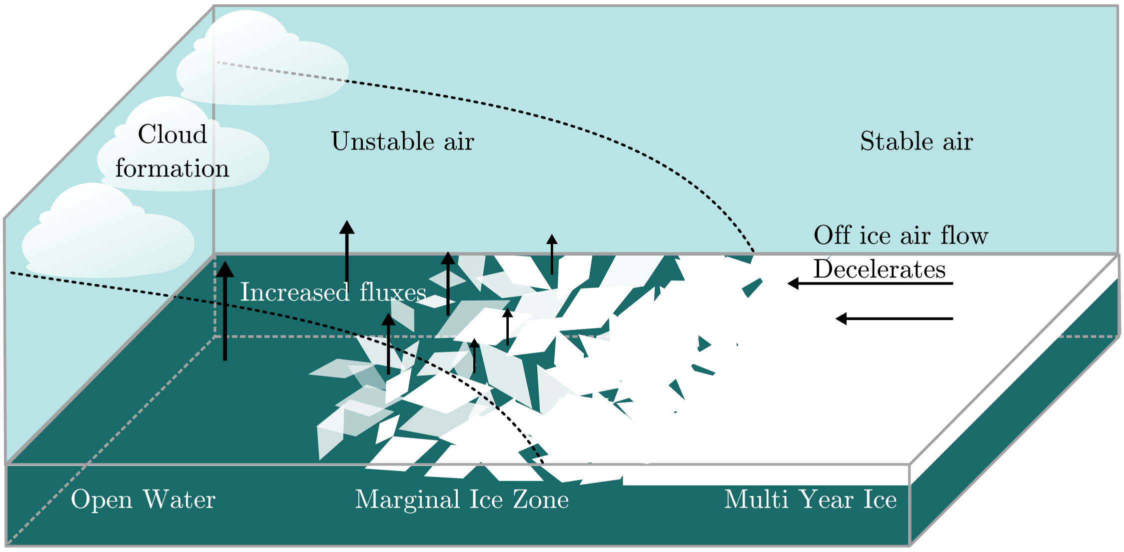

Figure 4.18: A schematic diagram showing the modification of a cold air outbreak as it travels over the MIZ.

with higher concentrations occurring at 800 m high at the end of the cross section. Due to the increased availability of liquid and vapour to freeze into ice. The Q_{LW} is higher in general, with a cloud apparent near the end of the MIZ.

It can be seen from the similarities between both of these cases that in general, as a colder, drier air mass is advected from the north over the MIZ to the open water to the south it warms, and becomes more moist and then forms a convective internal boundary layer and if conditions are right, clouds. This is summarised by the schematic in Fig. 4.18. Other observations of CAOs have reached similar conclusions (Tetzlaff *et al.*, 2014; Vihma & Brümmer, 2002; Gultepe *et al.*, 2003; Renfrew & Moore, 1999), so these results add to the available knowledge.

The formation of cloud both off ice and above ice is important for the surface energy balance of the Arctic. Cloud cover may help to warm the surface, or to cool it (Intrieri *et al.*, 2002; Serreze & Francis, 2006) which could change the onset of melt and freezing. As these case studies show, the surface is an important source for moisture for these clouds, with the vertical transport in the BL being a key process in the mixing up of moisture to the wider atmosphere.

5

SIMULATING COLD-AIR OUTBREAKS OVER THE MIZ: SENSITIVITY TO BOUNDARY LAYER PARAMETRISATION

The ability to accurately predict the weather of the Arctic is of increasing importance, as reductions in sea ice cover mean an increase in sea going traffic as well as possible oil drilling and mining (Larsen *et al.*, 2014). However due to the generally inhospitable nature of the Arctic and the sea ice edge, there are fewer observations for the Arctic than for mid-latitudes. The lack of observations means that often the development and testing of weather and climate models is done for places in the lower latitudes. Then when these models are applied to the Arctic problems can occur. For example Kay *et al.* (2010) discusses this in relation to the Community Atmosphere Model v4 (CAM4). The boundary layer scheme was written for the atmosphere over the ocean in the subtropics and assumed a well mixed boundary layer, the parametrisation diagnosed a well mixed boundary layer using criteria which are violated in the Arctic due to the presence of multiple inversions and very near surface inversions, causing problems with the cloud cover. Upon modifying the parametrisation the modelled clouds were better predicted than using the original parametrisation.

As WRF offers the user a choice of boundary layer schemes, it is important that the best possible scheme for the application be chosen. Many sensitivity studies have been carried out, using several different combinations of boundary layer schemes to establish which might be optimal for a particular situation, these will be discussed below. An indepth discussion of the MYJ, YSU, QNSE and ACM2 schemes as well as some explanation of why boundary layer parametrisation schemes are needed is included in Ch. 2.

Surface and boundary layer temperature is affected by choice of boundary layer scheme, so it is important to examine errors in these variables. As part of the development and testing of the Polar version of the Weather Research and Forecasting model (PWRF) Hines & Bromwich (2008) and Bromwich *et al.* (2009) both compared the YSU and MYJ BL schemes to observations from Greenland and SHEBA (Surface Heat Budget of the Arctic), respectively. The YSU is a first order, non-local scheme with an explicit treatment of BL top entrainment, while the MYJ is a 1.5 order local closure TKE scheme. In Hines & Bromwich (2008) the MYJ is found to perform best in winter, with the lowest bias in 2 m temperature and 2 m specific humidity. However both the MYJ and YSU have a warm bias in 2 m temperature of +2.1 K and +3.5 K respectively. Contrary to this result is Bromwich *et al.* (2009) which looks at sensitivity over Arctic fractional sea ice, here the YSU is found to perform marginally better than the MYJ, with the lowest bias in 2 m temperature (-1.2 K compared to -1.5 K for the MYJ), and equal performance in specific humidity and surface temperature.

PWRF has also been tested in the Antarctic, Bromwich *et al.* (2013) compared the MYJ and the MYNN schemes against AWS data, also testing whether the ERA-interim or GFS-FNL (Global Forecast Service, final) is best for initialisation. The MYNN (Mellor-Yamada Nakanishi-Niino) scheme is a 1.5 order local closure, which is Turbulence Kinetic Energy (TKE) based like the MYJ. The BL schemes perform very similarly, with the MYNN having the largest cold bias in the summer (-1.3 (± 0.26) K for MYJ -3.3 (± 0.30) K for the MYNN) and the smallest bias in 2 m dewpoint temperature (+2.9 (± 0.40) K for MYJ compared to +1.2 (± 0.43) K for the MYNN). However this bias is reduced when the ERA-interim data is used, implying that the initial conditions are very important to the performance of the model.

Another BL scheme is tested in Tastula *et al.* (2012), where the ACM2 is tested along with the MYJ over sea ice and compared with observations. The ACM2 has a Total-Transilient-Turbulence style non-local closure, which allows interactions between every level in the boundary layer, and was developed for convective situations. The ACM2 performs best for surface temperature, with a bias of 0.02 K compared to 2.4 K for the MYJ.

Observations from Svalbard are used in Mayer *et al.* (2012). A combination of tethersonde and unmanned aerial system (SUMO, Small Unmanned Meteorological Observer) are compared against WRF. The YSU, MYJ and QNSE BL schemes are once again tested. The QNSE scheme was found to slightly improve temperature forecasting in stable conditions, but all the schemes have a warm bias at the surface and a cold bias above the BL. The MYJ was also found to have a larger cold bias in Hu *et al.* (2010) where the BL simulated by the MYJ is colder than both the YSU and ACM2 with the mean 2 m temperature bias being -1.25 K, -0.63 K and -0.9 K for the MYJ, YSU and ACM2 respectively. However the MYJ is better at 5 m temperature, with a bias of +0.7 K compared to -2.1 K for the ACM2.

García-Díez *et al.* (2013) looks at the seasonal dependence of WRF surface temperature biases over Europe, along with the sensitivity to BL schemes. The YSU, MYJ and ACM2 are compared against the E-OBS dataset, these are gridded observations for the whole of Europe. A systematic cold bias is seen during the warm seasons with temperatures being up to 2 K too low, and a warm bias of up to 1 K during cold seasons. The warm bias during cold seasons is also reported in Hines & Bromwich (2008), while a cold bias in summer is seen in Bromwich *et al.* (2013). They conclude that while the ACM2 or MYJ might be better suited in winter, the scheme performing closer to the observations depends on the season and is probably the result of error cancellation.

Five schemes, the YSU, ACM2, MYJ, QNSE and BouLac are compared in Shin & Hong (2011) against observations taken from the CASES-99 (Cooperative Atmosphere-Surface Exchange Study) field programme in Kansas. The BouLac (Bougeault and Lacarrere) scheme is a 1.5 order local closure scheme, which was developed for orographically induced turbulence. The YSU and ACM2 produce surface temperatures which are too high, by +3.5 K and + 1 K respectively, while QNSE underestimated surface temperature by 2.5 K.

In Kleczek *et al.* (2014) six schemes (YSU, ACM2, MYJ, MYNN25, QNSE and BouLac) are compared with observations from the Cabauw tower in the Netherlands. It is found that the non-local schemes produce higher temperatures though in general the model underestimates the 2 m temperature in the daytime (by up to 2 K) and night (by up to 4 K). A consistent 2 K cold bias in the upper BL is also seen.

It therefore seems that for the forecasting of surface and near-surface temperature, the choice of BL scheme can reduce errors substantially (Hu *et al.*, 2010; Tastula *et al.*, 2012; Bromwich *et al.*, 2013). However seeing a cold bias near the surface is very common, with only Shin & Hong (2011), Tastula *et al.* (2012) and Hines & Bromwich (2008) having a warm bias.

One of the major roles of the boundary layer and their associated surface layer parametrisation schemes is the provision of fluxes to the model, and the values of the fluxes are dependent on the surface and atmospheric boundary layer temperatures. In Bromwich *et al.* (2009) the sensible heat flux was found to be negatively biased for both BL schemes tested which follows the negative bias in surface temperature, however unlike for surface temperature it is the YSU which is slightly more biased at -13.8 W m^{-2} compared to -13 W m^{-2} for the MYJ. The latent heat flux was positively biased and much better predicted with a bias of +0.19 W m^{-2} and +0.14W m^{-2} for the MYJ and YSU respectively.

Unlike in Bromwich *et al.* (2009), in Shin & Hong (2011) surface sensible heat fluxes are found to be overestimated by all the schemes tested (YSU, ACM2, MYJ, QNSE and BouLac) during the daytime, by over 100 W m^{-2} for the QNSE, which follows from the positive bias in surface temperatures. The YSU produced the smallest sensible heat flux, and the QNSE the largest. This is attributed to the surface layer schemes producing the smallest and largest C_H respectively. The latent heat flux also has the same problem. They conclude that the representation of surface variables is still uncertain, even with state of the art BL schemes and especially under stable conditions.

The depth of the boundary layer and the strength of the capping inversion can be important for clouds, and features of the boundary layer such as low level jets are important for the creation of turbulence. However boundary layer parametrisations seem to struggle with these features.

Observations from tethersondes and masts in Arctic fjords on Svalbard were compared against PWRF in Kilpeläinen *et al.* (2012). The MYJ and YSU were once again tested, along with the QNSE. The QNSE scheme is a non-local spectral closure, designed for stably stratified BLs. The QNSE is found to perform the best, with the lowest bias over all variables. As with other studies (eg.Hines & Bromwich

(2008)), a warm bias near the surface was seen, which was related to underestimated temperature inversion depth and strength. The same conclusion was found in García-Díez *et al.* (2013), where a warm winter bias was also seen.

A low level jet is a local wind speed maximum which occurs in or just above the boundary layer. In Tastula *et al.* (2012) PWRF was found to underestimate the frequency of LLJs by roughly 50%, even with a very high vertical resolution (33 levels below 400 m). The inversions are also too thick in the model. Kilpeläinen *et al.* (2012) also showed that PWRF was unable to reproduce multiple inversions and LLJs. This could influence the fluxes and near surface temperatures, due to a lack of mixing. Indeed (Tastula *et al.*, 2012) had a warm bias, maybe due to the lack of cold air being advected by LLJs.

The best BL scheme can depend on the stability of the BL, with non-local schemes best in unstable conditions and local schemes best in stable conditions (Shin & Hong, 2011). However the non-local BL schemes underestimate BL depth and LLJ altitude, as was seen in Tastula *et al.* (2012) and Kilpeläinen *et al.* (2012), though in Kleczek *et al.* (2014) they are found to give higher wind speeds particularly at night.

The boundary layer scheme is responsible for providing the tendencies of moisture and temperature to the free atmosphere in the model. This means the choice of boundary layer scheme is important for the simulation of clouds, which are in turn important for the simulation of surface temperatures by their impact on shortwave radiation.

In Bromwich *et al.* (2009), over the sea ice both the YSU and MYJ schemes have a cold bias, due to the differences in shortwave radiation. However the YSU shows better correspondence to the shortwave radiation bias with values of -65 W m^{-2} and -25.8 W m^{-2} for the MYJ and YSU respectively. An improvement in the representation of clouds for the YSU is what causes the YSU to give the better 2 m temperature. Also in Bromwich *et al.* (2013) the summer cold bias in 2 m temperature is attributed to inadequate cloud representation, caused by an inadequate input moisture fields from the GFS-FNL. Tastula *et al.* (2012) also found negative biases in 2 m temperature for all the schemes tested. Again they attribute problems with modelling surface temperatures and therefore fluxes to problems with cloud cover. (Tastula *et al.*, 2012).

Standard WRF has also been tested in many different applications. As the BL is important for the transport of pollutants, simulating the BL correctly is important for air pollution modelling. To this end Hu *et al.* (2010) uses WRF 3.0.1 and evaluates the MYJ, YSU and ACM2 over Texas. Again they find that daytime temperature biases are caused by the poor simulation of cloud, as was seen in Bromwich *et al.* (2009) with the MYJ producing insufficient mixing in the convective BL, and thus the least cloud.

In Huang *et al.* (2013) five BL schemes (YSU, MYJ, MYNN, MRF and TEMF) are tested against cases which have been modelled with a single column model with 116 vertical levels up to an altitude of 12,000 m and a simulation time step of 30 s. The TEMF (Total-Energy Mass-Flux) scheme is a non-local scheme which uses eddy diffusivity and mass flux concepts to determine vertical mixing. It belongs to a category of closures called ED-MF, (eddy diffusivity - mass flux). The eddy diffusivity is used in the stable parts of the column, when the surface bouyancy flux is positive, a surface-based updraft, which is non-local and handles counter gradient transport, is created which transports heat, moisture, energy and momentum upwards. The eddy diffusivities for heat and momentum are prognosed from the turbulent energy (which is similar to TKE, but does not have a buoyancy destruction term). The primary purpose of the TEMF scheme is to improve the representation of boundary layers with shallow cumulus clouds and stable boundary layers. The Huang *et al.* (2013) study focussed on marine stratocumulus capped BLs over tropical/subtropical sea and all the BL schemes were found to perform poorly at simulating cloud liquid water, being up to two orders of magnitude too large. The TEMF produced the most realistic cloud base and heights, so they concluded the TEMF is best, with the caveat that the artificial modularity of parametrisations as implemented in WRF produces unreliable results.

Due to WRF and PWRF having a modular setup, sensitivity studies are relatively easy to carry out. Many studies have been done comparing the model to data from field campaigns or LES, the results sorted by BL scheme are shown in Table 5.1. In general WRF has a warm bias during winter (Bromwich *et al.*, 2013; García-Díez *et al.*, 2013; Kilpeläinen *et al.*, 2012; Hines & Bromwich, 2008). This has been attributed to problems with simulating cloud (Bromwich *et al.*, 2009). As the BL scheme and surface layer scheme must be chosen together, there are differences in surface fluxes, with the models usually overestimating (Shin & Hong, 2011). Surface flux differences will impact the BL temperature and stability, which will also impact the clouds. The boundary layer of the Arctic often has multiple inversions and WRF is not good at reproducing these (Tastula *et al.*, 2012; Kilpeläinen *et al.*, 2012). WRF is also unable to reproduce LLJs, which may play a role in the entrainment of heat and moisture (Tastula *et al.*, 2012; Kilpeläinen *et al.*, 2012; Kleczek *et al.*, 2014).

The selection of a BL scheme is difficult due to the different approaches taken in the closure of the turbulence, and as certain schemes seem to perform best in different situations. The QNSE is found to show promise in Mayer *et al.* (2012) over Svalbard. Hines & Bromwich (2008) and Bromwich *et al.* (2009) do not agree on whether the YSU or the MYJ is best. The YSU performed better over the sea ice and ocean, while the MYJ best over Greenland. The ACM2 was found to be best at surface temperature in Antarctica (Tastula *et al.*, 2012). It is important for both weather and climate simulations to be able to accurately predict variables such as surface temperature and cloud cover, due to the impact of both of these on the sea ice surface. The BL scheme is important for both of these variables, along with the surface fluxes and the provision of heat, momentum and moisture upwards to the free atmosphere. The MIZ, with a very complex surface and BL transition from stable to convective presents a big challenge to BL schemes which may be optimised for stable (QNSE) or convective (ACM2) or more general (YSU, MYJ) situations. Being able to capture the stability and convection present is important for the correct simulation of surface heat and moisture flux and clouds. Using observations from two ACCACIA case studies, both with BL transitions over the MIZ during a cold air outbreak but with Case 1 having a slower transition than Case 2, a series of BL parametrisation sensitivity tests will be carried out testing the MYJ, YSU, QNSE and ACM2 schemes. The ability of these schemes to simulate the surface temperatures, surface fluxes, boundary layer transition and clouds will be examined and conclusions made as to which BL scheme is optimal, or in the case that no scheme is preferred, recommendations as to what could be done to improve the simulation of BL transitions will be made.

5.1 EXPERIMENTAL DESIGN

For these experiments the Polar version of WRF 3.5.1 (PWRF) was used. The model was set up with three nested grids at a horizontal resolution of 27, 9, 3 km. The grids are one way nested and run one after the other, with the data from the larger grid being interpolated downwards to provide initial conditions for the smaller grid, and

Table 5.1: Table summarising the results of the sensitivity studies discussed in the introduction.

BL Scheme	Type	Notes
YSU	First order	Warm bias in T_2 of +3.5 K over Greenland (Hines & Bromwich, 2008)
	Non-Local	Cold bias in T_2 -1.2 K over sea ice, negative bias in SHF -13.8 W m^{-2},LHF bias +0.14 YSU better at clouds (Bromwich *et al.*, 2009)
	BL top entrainment	T_{sfc} overestimated (+3.5 K),smallest SHF (but big +ve bias) (Shin & Hong, 2011)
MYJ	1.5 order	Warm bias in T_2 of 2.1 K over Greenland (Hines & Bromwich, 2008).
		- 1.5 K bias in T_2, -13 W m^{-2} SHF, + 0.14 W m^{-2} LHF over sea ice, bad at clouds,(Bromwich *et al.*, 2009)
	Local Closure	-1.28 K bias in summer over Antarctic. +2.29 K for dewpoint,(Bromwich *et al.*, 2013)
		+2.4 K bias in T_2 over sea ice (Tastula *et al.*, 2012)
	TKE Scheme	Insufficient mixing, so not enough cloud and colder, -1.25 K T_2 bias (Hu *et al.*, 2010)
		Possibly better suited for winter, (García-Díez *et al.*, 2013)
MYNN	1.5 order	Cold bias in summer over Antarctic, +1.5 K for T_{dew} (Bromwich *et al.*, 2013)
	Local Closure	
	TKE Scheme	
ACM2	Non-Local	0.02 K bias in T_{sfc} over sea ice, (Tastula *et al.*, 2012)
	TTT type model	-0.9 K T_2 bias (Hu *et al.*, 2010)
	Convective	Possibly better suited for winter, (García-Díez *et al.*, 2013).
QNSE	Non-local	Best over Svalbard. (Kilpeläinen *et al.*, 2012)
	Spectral Closure	T_{sfc} negative bias -2.5 K (Shin & Hong, 2011)
	Stable	
TEMF	Non-Local	Produces most realistic cloud base and height over tropical/subtropical sea (Huang *et al.*, 2013)
	Eddy-diffusivity	
	Mass-flux	

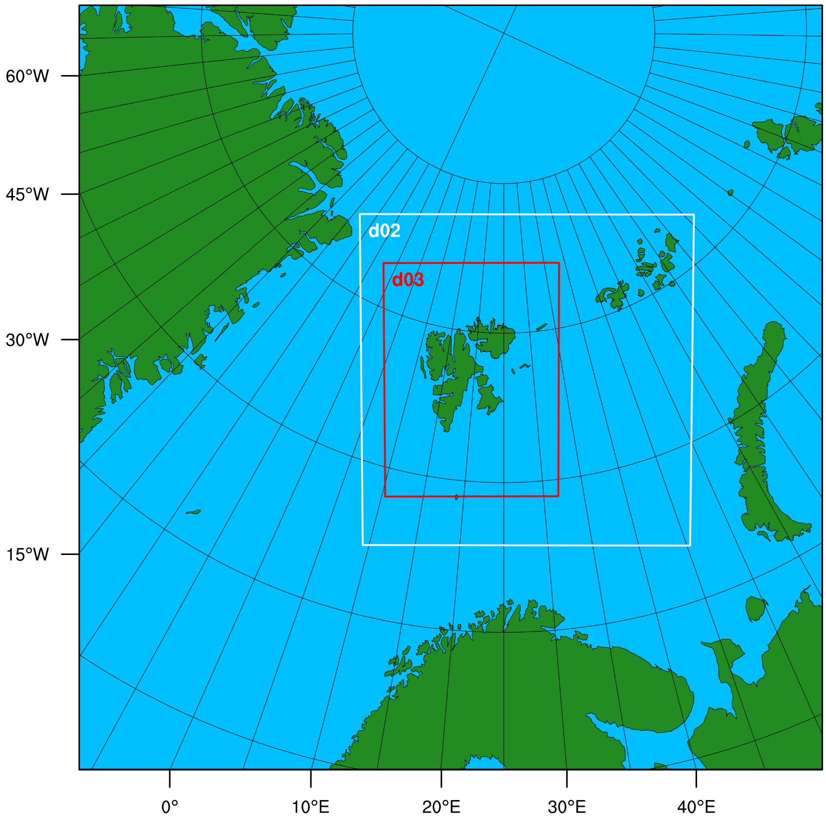

Figure 5.1: The domain configuration for WRF experiments from the WRF Preprocessing Suite. The outer domain is 98 × 100 grid points at 27 km resolution, with d02 having 130 × 130 grid points at 9 km resolution and d03 having 205 × 274 grid points at 3 km. The model uses a regular Cartesian grid.

boundary conditions for the whole run. One-way nesting was used due to difficulties with running WRF with the high resolution sea ice product. In two-way nested runs the model crashed, with errors propagating from where the ice edge intersected the edge of the domain. The errors were attributed to the change in resolution of the sea ice between the outer and inner domains. Using one-way nesting resolved this problem as the interpolation from outer to inner grid is done as a separate step. The domains are shown in Fig. 5.1 and was chosen to avoid having large variations in orography on the edges. The map projection is polar stereographic.

The initial and boundary conditions for the outer domain come from ERA-interim, as ERA-interim was found to give the best performance in 2 m temperature and dewpoint Bromwich *et al.* (2013). ERA-interim data was downloaded from the ECMWF MARS archive at a $0.25° \times 0.25°$ horizontal resolution. The sea ice, sea surface temperature and land mask are taken directly from OSTIA, which is used in the ERA-

Table 5.2: The basic physics set up for WRF experiments, the cumulus scheme (which parametrises convection) is only used for the 27 and 9 km domains.

Subroutine	Process	No.	Parametrisation Scheme
mp_physics	Microphysics	10	Morrison double moment scheme
ra_lw_physics	Long Wave	4	Rapid Radiative Transfer Model for GCMs
ra_sw_physics	Short Wave	4	Rapid Radiative Transfer Model for GCMs
sf_surface_physics	Land Surface Model	2	Noah LSM
cu_phsyics	Cumulus	1	Kain-Fritsch

Table 5.3: PBL parameterisation schemes and the associated surface physics scheme used in these experiments.

PBL scheme	Surface Scheme	Reference
MYJ (2)	Eta similarity (2)	(Janjic, 1994)
YSU (1)	MM5 Similarity (1)	(Hong *et al.*, 2006)
QNSE (4)	QNSE surface layer (4)	(Sukoriansky *et al.*, 2005)
ACM2 (7)	MM5 Similarity (1)	(Pleim, 2007)

interim reanalysis, at a high horizontal resolution of 0.05°× 0.05°. More information about WRF and the forcing data can be found in Ch. 2.

Following Hines & Bromwich (2008) and Bromwich *et al.* (2009) the physics choices used as the control setup are in Table 5.2. In this chapter the boundary layer schemes are tested (along with the surface layer schemes, see Table 5.3). The surface layer scheme and boundary layer need to be coupled together and not all schemes can be coupled together. These are in Table 5.3,

For the experiments, PWRF 3.5.1 is run for each of Case 1 (flight B760 from the ACCACIA campaign) and Case 2 (flight B765), which are described in Chapter 4. The model run begins at 00:00 and ends at 18:00 with the cross sections taken at 13:00. This gives 13 hours of spin up time. The boundary layer and surface layer schemes are changed together following Table 5.3. The results of the experiments are analysed below. In order to compare the observations from the aircraft, which include temporal and spatial variability, to the model where the data is presented for all locations at the same time some assumptions have to be made, namely that the atmosphere is in a quasi-steady state and thus does not change substantially over the time period of making the cross-sections. The aircraft was flying at an equivalent ground speed of approximately 100 m s^{-1}, while the maximum wind speed is 10 m s^{-1}, this means we are not following an air parcel in a Lagrangian sense as the speed of the aircraft far outstrips the air. Checking a cross-section of the model for the output of the Case 2 MYJ simulation, 30 minutes before and after the time of the cross sections presented here (which is at a time of 13:00), In the model, the wind speed exhibits its biggest differences around the top of the BL (± 1 m s^{-1}) with an average difference across the cross section of <1%. The potential temperature, θ is similar with ± 1 K differences around the top of the BL, but overall <0.1% difference. The clouds as represented in the model by Q_{lw} are decreasing in liquid content between 12:30 and 13:30 by over 60%. The location of the cloud in the model is very similar across the three times looked at. The assumption is then made that the model and the observations are steady enough to be able to make comparisons between the two, though the difference between the two must be remembered, especially for the cloud cover.

The measures used for comparing the model to the observations are the bias, mean absolute error (MAE) and root mean squared error (RMSE). The bias is the difference between model and observations,

$$\text{bias} = \overline{\text{model} - \text{observations}}. \tag{5.1}$$

The bias used here is the mean over all points, ignoring any NaN values. This shows if there is a systematic positive or negative skew in the model compared to the data, however the bias can be low if there are both large positive and large negative errors, so it is not indicative of a large spread in difference.

The MAE is calculated by,

$$\text{MAE} = \overline{|\text{model} - \text{observations}|}. \tag{5.2}$$

As the absolute value is used, the MAE is always positive. A smaller value for the MAE implies a closer agreement between the model and observations. If the bias is consistently positive, it will be equal to the MAE. The MAE can be heavily influenced by a small number of anomalous values, though not as much as the RMSE which is given by,

$$\text{RMSE} = \sqrt{\overline{(\text{model} - \text{observations})^2}}. \tag{5.3}$$

As the RMSE is more strongly affected by outlying data points, the difference between the MAE and RMSE can give an indication as to the spread of errors. The larger the

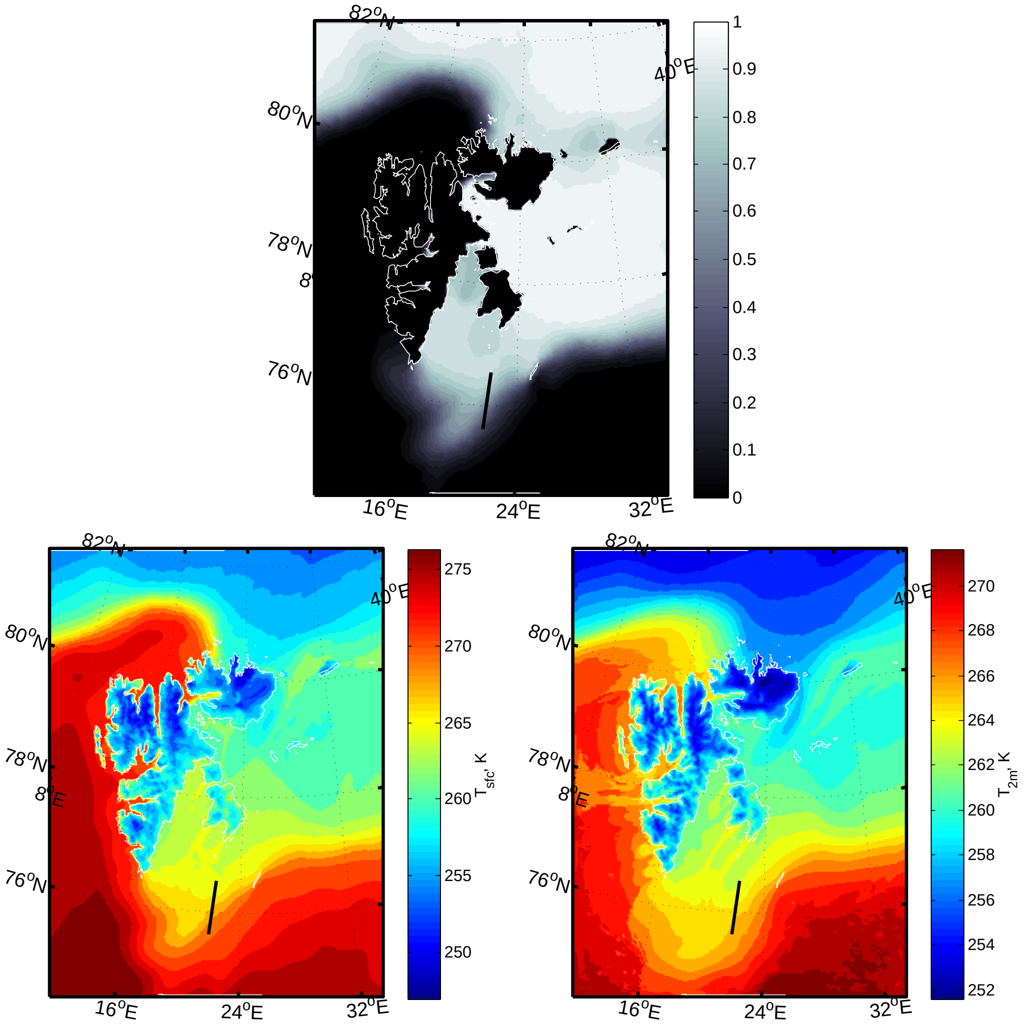

Figure 5.2: Sea ice cover (0-1), T_{sfc} and T_{2m} (K)for the inner domain of Case 2 with the MYJ scheme. The black line shows the location of the flight cross-section.

difference between the RMSE and the MAE, the larger the spread differences.

5.2 CASE STUDIES

5.2.1 SURFACE

The 2-dimensional latitude-longitude plots for surface variables are shown in Fig. 5.2, the three images show the inner most domain (3 km horizontal resolution) for Case 2 for the MYJ scheme and allow for an understanding of the wider context for the WRF data. The top plot shows the sea ice fraction (between 0 and 1), the island of Svalbard is clearly visible. The sea ice in WRF extends to the south of the island, reducing in fraction further south. The cross-section is over an area which the model has as changing sea ice fraction, to the west of this cross section the sea ice fraction is higher than that under the cross section, while to the east the sea ice fraction is lower. The sea ice fraction has a strong effect on T_{sfc} (bottom left) and by extension T_{2m} (bottom right), with the cooler (blue-yellow) areas corresponding to locations with higher ice fraction. Much of the MIZ in the model has a similar signature to the area under the cross section for both T_{sfc} and T_{2m}, with temperatures increasing from north to south across the MIZ. The area to the east of the cross section has a tongue of ice which extends further south than the rest of the ice edge and causes the warming to be slightly slower than for other areas.

The model has a horizontal resolution of 3 km, the specific cross section used need to not be anomalous compared to cross sections near by. The cross sections of θ, **U** and Q_{LW} are compared to those 3, 6 and 9 km to the east and west for both cases. All the cross sections are qualitatively similar, with features in similar locations across them. For Case 1, the maximum and minimum values of θ are 0.4 K and and 0.8 K different respectively, and there is no difference between the mean values. The standard deviation varies by 0.1 K between the cross sections. The cross sections of **U** also exhibit little variation in the maximum and minimum values, of 0.8 m s^{-1} for both. The mean value varies by 0.6 m s^{-1} between the cross sections, and the standard deviation by 0.1 m s^{-1}. There is no variation at all between the cross sections for Q_{LW}, as there is 0 Q_{LW}. It can be concluded for that for Case 1 the chosen cross section is representative of the general area.

For Case 2, the variation in maximum and minimum θ is 0.1 K and 0.25 K respectively. The mean θ varies by 0.25 K and the standard deviation varies by 0.1 K between the cross sections. For **U** there is no variation between the maximum or the mean values for the different cross sections. The minimum value varies by 0.2 m s^{-1} and the standard deviation by 0.1 m s^{-1}. Case 2 has some Q_{LW} present in the cross sections. The maximum Q_{LW} varies by 0.2×10^{-9} g kg^{-1} between the cross sections, while the minimum is 0 g kg^{-1} for all cross sections. The mean value varies by 4×10^{-9} g kg^{-1} and the standard deviation by 0.14×10^{-9} g kg^{-1}. Again as the mean, maximum, minimum and standard deviation values are similar between the cross sections, and so the chosen cross section can be assumed to be representative of the surrounding areas.

Looking now at the cross sections, the T_{sfc} for both cases is shown in Figs. 5.3 and 5.4. The figures show the data from the observations, smoothed to 3 km to match the model resolution along with the modelled sea ice fraction on the second y-axis, as a black dashed line. It can be seen that for Case 1 the model gives a sea ice fraction from near one to near zero over the cross-section, whereas for Case 2 the model has a greater than 0.5 concentration of sea ice across nearly the whole area.

The most obvious difference between the two cases, is that in general the T_{sfc} is overestimated for Case 1, while it is underestimated for Case 2. The bias for each boundary layer scheme is given in Table 5.4, where the mean bias across all schemes are not substantially different, the bias for Case 1 is +1.8 K while for Case 2 it is -1.1 K. For both cases the temperature given over the higher sea ice fractions is both more variable between the schemes, but closer to the observations. As the sea ice is handled by the land surface model which is unchanged between the experiments, these differences must be due to differences in solar forcing or the differences in exchange coefficients as provided by the surface layer scheme.

For Case 1 the schemes differ by up to 0.9 K at the northern-most end of the cross section. The ACM2 has the highest value at 260.3 K while the MYJ has the lowest at 259.4 K. The observations are closer to the higher model result at 76.86 °N, while they then join the lower estimate by 76.84 °N. The model is then consistently above the observations, apart from at 76.6 °N. Here there is a lead present in the observations which is not in the model, the temperature difference is 6 K. Between 76.5 °N and 75.98 °N the model overestimates the T_{sfc}, by up to 5.3 K. This area of difference over the MIZ is due to problems with sea ice fraction and thickness representation being different to that observed. Over lower sea ice concentrations in Case 1, the surface temperatures converge, due to the high percentage of open water. The values also match well with observations.

Case 2 again shows the largest spread over the higher sea ice fractions. At 76.4 °N there is a 1.3 K difference between the schemes, with the YSU being the warmest and the QNSE being the coldest. Between 76.3 °N and 76.4 °N the observations fall between the modelled temperatures. However at 76.3 °N, the observations show a lead, which is again not captured by the model due to the sea ice surface not including the lead. The maximum temperature difference over this lead is 5.4 K. South of 76.2 °N the observations show a T_{sfc} of around 270.5 K, with a maximum of 271.9 K and a minimum of 269.1 K. The model however underestimates the surface temperature here, with T_{sfc} rising from around 266.7 K to 269.1 K across this part of the domain. The model has a sea ice fraction greater than 0.4 whereas the observations showed open water and much lower sea ice fractions than this, therefore the model cannot be expected to reproduce the temperature here.

Neither case captures the variation seen in the observations, this is due to the very smooth sea ice fraction change in OSTIA, whereas in real life this was more varied. This will be discussed in more detail in Chapter 6. Problems with representation of the surface temperature are more to do with the differences between the model and observed surface than the variation in the BL parametrisation, with all the BL schemes behaving similarly. The RMSE and MAE being close together highlights this systematic error.

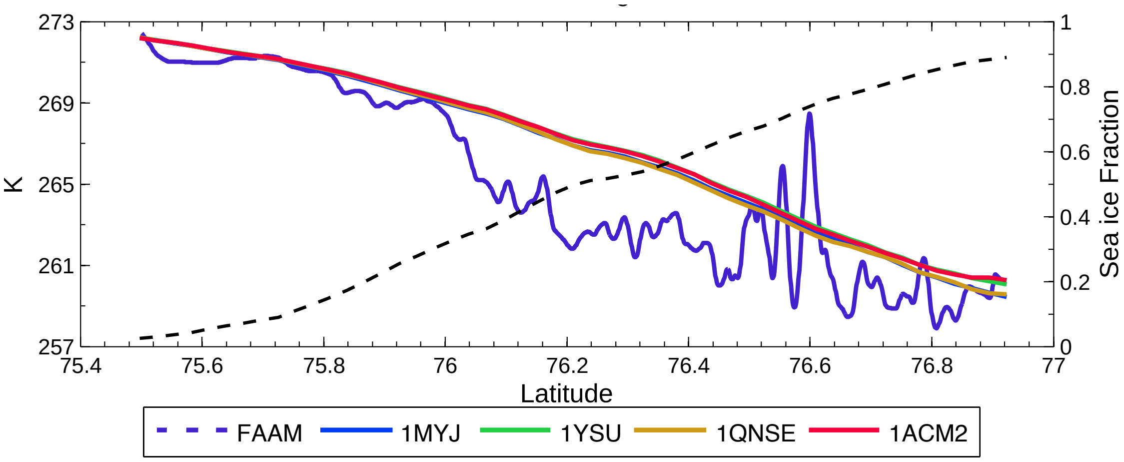

Figure 5.3: Case 1 T_{sfc}, K for both the observations (dashed blue) and the model simulations. The second axis displays the sea ice fraction as used in the model (black dashed line).

Table 5.4: Table showing the bias, MAE and RMSE for surface temperature for both cases, K. Error estimates are from the instrument errors shown in Table 4.2

	MYJ	YSU	QNSE	ACM2	MYJ	YSU	QNSE	ACM2
	Case 1				Case 2			
Bias (± 0.3)	+1.71	+1.94	+1.70	+1.92	-1.10	-0.79	-1.32	-1.12
MAE (± 0.3)	1.92	2.10	1.91	2.07	1.69	1.86	1.73	1.83
RMSE (± 0.3)	2.47	2.66	2.45	2.63	2.00	2.04	2.05	2.1

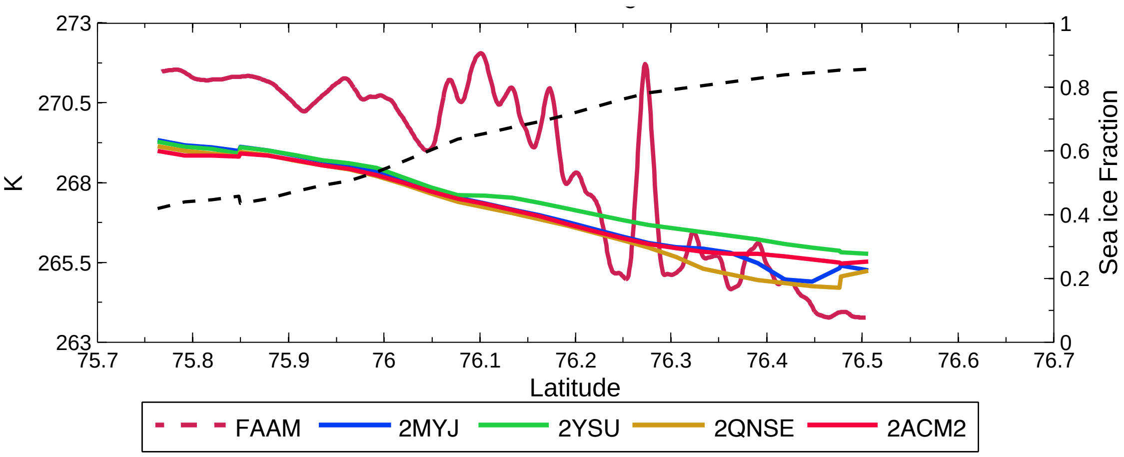

Figure 5.4: Case 2 T_{sfc}, K for both the observations (dashed red) and the model simulations. The second axis displays the sea ice fraction as used in the model (dashed black).

5.2.2 FLUXES

Looking first at the wider context of the fluxes in 5.5 where the SHF (left) and LHF (right) are shown, it can be seen that over most of the domain the blue colours of low to negative fluxes dominate. To the north of Svalbard an intense patch of high fluxes is visible for both SHF and LHF, this corresponds to an area of open water as seen in the sea ice fraction (Fig. 5.2). The fluxes around the cross section are between 0 and 100 W m^{-2} for SHF and between 0 and 30 W m^{-2} for LHF. There is little increase in these values until much further south, where the sea ice fraction is reduced.

The sensible heat flux, SHF for both flights is consistently over-estimated, with the average bias being + 53.1 (± 0.01) W m^{-2} for Case 1 and + 50 (± 0.01) W m^{-2} for Case 2. Error estimates are from the instrument error given in Table 4.2. There is a bigger spread between the different schemes than for the surface temperature, with up to 14.7 W m^{-2} and 11 W m^{-2} between the MYJ and QNSE for Cases 1 and 2 respectively. There is a jump in modelled SHF for the MYJ and QNSE in Case 1 at 76.2 °N. This is due to the same factors as the jump seen in the idealised experiments. That is the switch from stable to unstable conditions causes a change in the stability correction, which results in a sudden change in the fluxes. Both Cases show an increase in modelled fluxes with a decrease in sea ice concentration. While this anti-correlation was observed in both cases, there is also a reduction in observed flux south of 75.8 °N, which does not happen in the model.

The latent heat flux, LHF is again generally overestimated by the model, +19

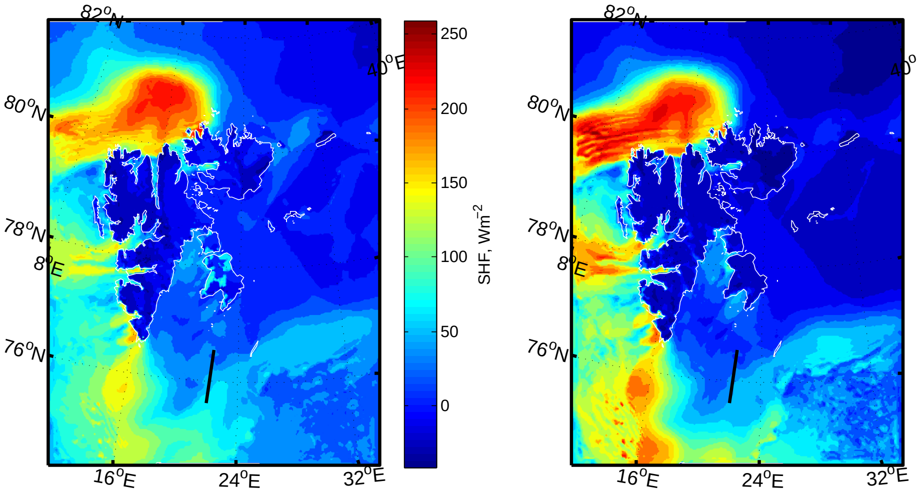

Figure 5.5: *SHF* and *LHF* (W m^{-2}) for the inner domain of Case 2 with the MYJ scheme. The black line shows the location of the flight cross-section.

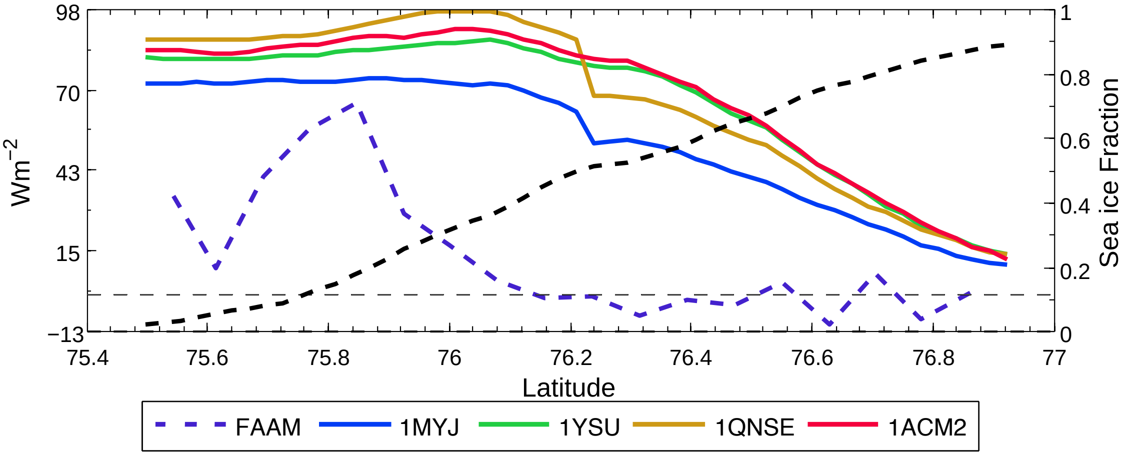

Figure 5.6: Case 1 *SHF*, W m^{-2} for both the observations (dashed blue) and the model simulations. The second axis displays the sea ice fraction as used in the model (black dashed line). The zero line is dashed grey.

(±0.004) W m^{-2} for Case 1 with the biggest difference in bias being between the MYJ and the QNSE (7.5 W m^{-2}) . For Case 2 there is an average bias of + 21.1 (±0.004) W m^{-2} with a 5.5 W m^{-2} difference between the MYJ and the QNSE. Error estimates are from the instrument error in Table 4.2 The same general features are visible in *LHF* as in *SHF*. Values increase across the MIZ, as the sea ice fraction decreases. However for both cases the sea ice surface means the variability in fluxes is not observed. This will be further discussed in Chapter 6.

In general the MYJ predicts the lowest *SHF* and *LHF* values, while the QNSE predicts the highest. These two have very similar surface layer schemes, with subtle differences in the stability correction on the fluxes. The QNSE is able to produce an

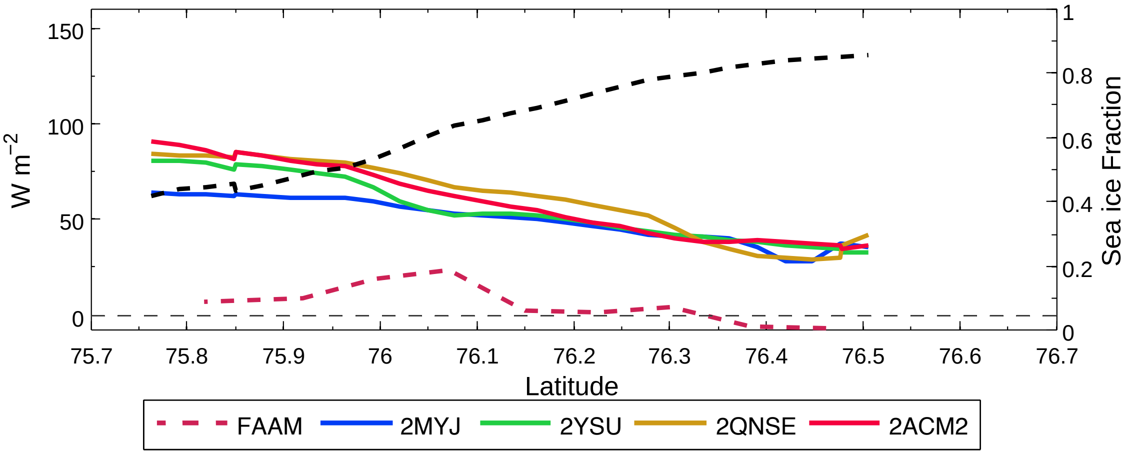

Figure 5.7: Case 2 *SHF*, W m^{-2} for both the observations (dashed red) and the model simulations. The second axis displays the sea ice fraction as used in the model (dashed black). The zero line is dashed grey.

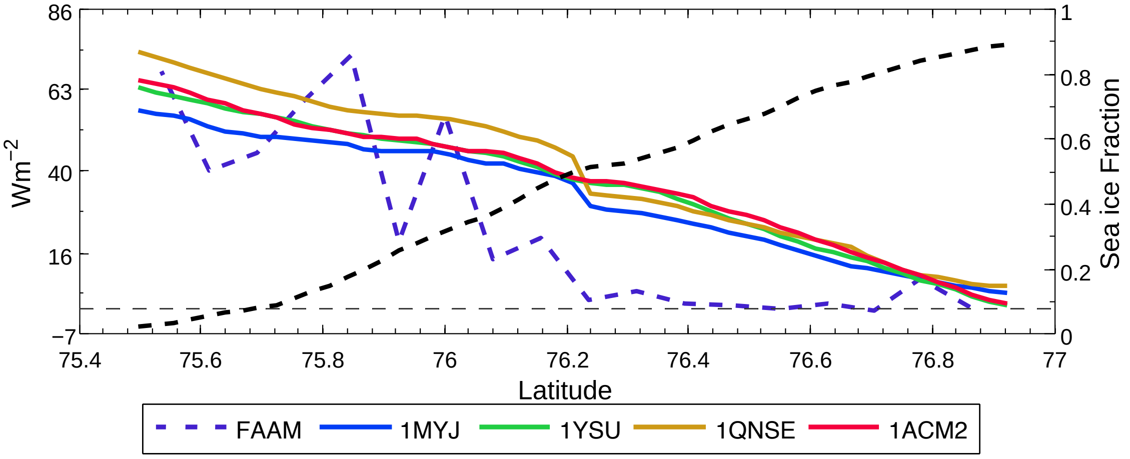

Figure 5.8: Case 1 *LHF*, W m^{-2} for both the observations (dashed blue) and the model simulations. The second axis displays the sea ice fraction as used in the model (dashed black). The zero line is dashed grey.

increased heat flux under a more stable BL, however this may now be causing the fluxes to be overestimated, due to the atmosphere not being stable. Also as the MYJ is a local scheme, it can be seen with both cases that this local scheme produces the lowest fluxes generally. For the *SHF* the three other schemes group together, particularly over ice.

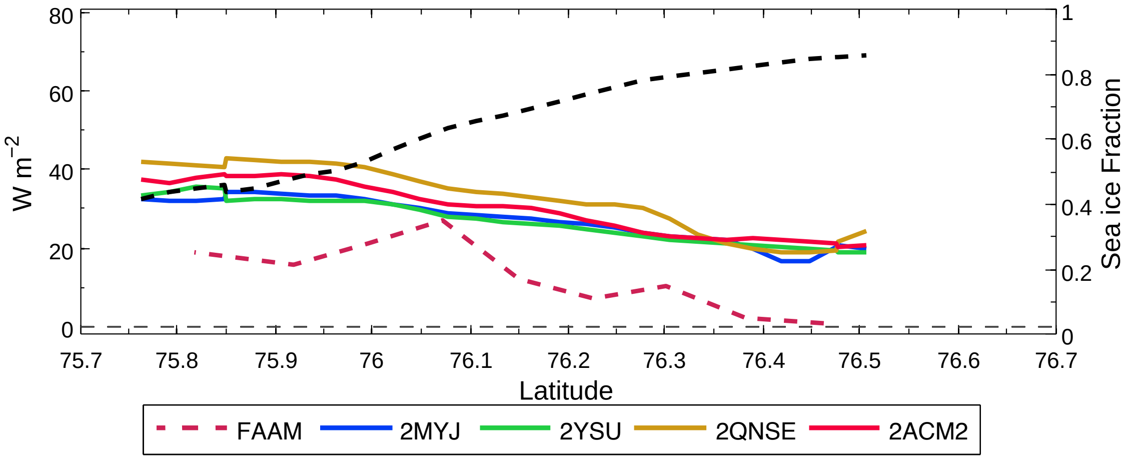

Figure 5.9: Case 2 *LHF*, W m^{-2} for both the observations (dashed red) and the model simulations. The second axis displays the sea ice fraction as used in the model (dashed black). The zero line is dashed grey.

Table 5.5: Table showing the bias, MAE and RMSE for *SHF* and *LHF* for both cases, W m^{-2}. Error estimates are from the instrument error shown in Table 4.2

	MYJ	YSU	QNSE	ACM2	MYJ	YSU	QNSE	ACM2
	SHF							
	Case 1				Case 2			
Bias (±0.01)	+42.3	+55.4	+57.0	+57.5	+42.4	+48.0	+53.5	+52.0
MAE (±0.01)	42.3	55.4	57.0	57.5	42.4	48.0	53.5	52.0
RMSE (±0.01)	47.4	60.9	62.9	63.0	43.6	50.4	55.7	54.6
	LHF							
	Case 1				Case 2			
Bias (±0.004)	+15.2	+18.5	+22.7	+19.5	+19.0	+18.8	+24.6	+21.9
MAE (±0.004)	19.3	22.0	25.2	23.0	19.0	18.8	24.6	21.9
RMSE (±0.004)	21.7	24.6	27.8	25.6	19.7	19.5	25.3	22.5

INVESTIGATING THE SYSTEMATIC *SHF* AND *LHF* BIAS.

The surface fluxes discussed above do not show good agreement between the model and the aircraft for all the BL parametrisation schemes in both Case 1 and Case 2. These differences could be caused by errors made in the observations, difficulties for the model in calculating fluxes over the MIZ or a combination of the two. In order to establish whether the flux biases are caused by the observations or the model, a number of different investigations will be made. Firstly the observations will be examined to establish if the altitude of the aircraft was suitable for measuring surface fluxes. The fluxes which were observed will be checked to see if they are large enough to cause the observed heating in the boundary layer. To investigate the model, as the

LHF and *SHF* depend on other other variables which are calculated at altitude in the model namely temperature and wind speed, the differences in these variables can be examined to establish if the model bias is caused by an inability to forecast other variables correctly.

Firstly the observations will be considered alone, the bias between the model and observations could be caused by the observations not being properly representative of the surface fluxes. The bias could have been induced by the aircraft flying too high, so the fluxes measured are not the surface fluxes that the model produces. In Fig. 5.10 the θ profiles are shown along with the aircraft altitude range (black) and the depth of the lowest 10% of the BL in grey. For Case 1 the BL height at A is at about 100 m while the flight run is at an altitude of 96 - 125 m, meaning much of this data is either at the very top of the BL or above the BL. At point B the BL height (defined as the start of the inversion in θ from Fig.5.10) is about 200 m, so the flight level was within the BL. However, as the aircraft was above the lowest 10% of the BL the flux calculations break some of the assumptions made in calculating the fluxes (Fairall & Markson, 1987). For Case 2 the BL height at profile A is 200 m, and the flight leg is at 60 - 90 m. This means that the flight data is at least in the lowest half of the BL. By the end of the MIZ, the BL height is above that of the cross-section. This is why there is positive flux across the whole MIZ for Case 2, as the aircraft was actually flying within the BL and thus able to capture it. The bias in *SHF* is better (by up to 5.5 W m^{-2} for the ACM2) for Case 2 when compared to Case 1. As multiple inversions are common in the Arctic (Kay & Gettelman, 2009; Tjernström, 2012) it could also be possible that the aircraft, while flying within one layer, is above another layer which is closer to the surface. From this alone, it could be concluded that the observations are inappropriate for use as surface fluxes, which would mean no meaningful comparison with the model could be made, however such a statement cannot be made without investigating more thoroughly.

Continuing to focus on the observations, it could be established that the observed fluxes are representative of the surface fluxes if the warming and deepening of the BL seen across the MIZ is consistent with the size of the flux. If the warming is consistent, then the observations can be concluded to be correct, and the model is at fault. If the fluxes are assumed to be providing the majority of heating in the boundary layer (as was the case in Chapter 3) and that the atmosphere is under steady state conditions in the observations (which is an assumption of all the analysis in this chapter), then using the results of Chapter 3 it can be established if the amount of heating provided by the fluxes is consistent with the increase in temperature and height of the observed BL.

Taking the average of the five idealised experiments, it can be seen that an average total heat flux ($SHF + LHF$) of 185 W m^{-2} across the 80 km MIZ produces a warming of 4.7 K at the bottom of the model atmosphere (18 m) and a BL height increase of 285.5 m. The wind speed was defined in the idealised experiments to be similar to that seen in the observations of both cases (9 m s^{-1}). In the observations, for Case 1 the average total heat flux is 20 W m^{-2} between the two profiles, a distance of 58.93 km. The observed increase in temperature at the bottom of the profiles was 3.3 K, along with an increase in BL height of up to 143.3 m. For Case 2 the heat flux was similar at 20.4 W m^{-2} over a distance of 73.39 km. A warming of 4.7 K was observed between the two profiles, along with a dramatic increase in BL height.

Therefore if the idealised case gives a warming of 4.7 K over 80 km, a warming of approximately 3.4 K would be expected over 58.93 km for Case 1 which is close to what was observed, also for Case 2 the observed warming of 4.7 K over 73.39 m is consistent with that seen in the idealised experiments. This implies that if it is assumed that the fluxes are the largest contributor to the BL heating, then the observed surface fluxes must be too low to produce the heating seen, using the results of the idealised experiments, a total heat flux of over 100 W m^{-2} would be required. Using this argument, it could be concluded that the observations are not capturing the fluxes correctly if the atmosphere was indeed under steady state conditions, which is attributed to flying too high to capture the surface layer, as shown in Fig 5.10 where the approximate altitude of the aircraft is marked in black and the lowest 10% of the BL marked in grey. It could be that the fluxes are not actually the main source of heating for the boundary layer in these cases, with other sources of heat such as shortwave radiation from the sun or latent heat released by phase changes of water (freezing or condensation). It would therefore be useful to compare other variables which are involved in the flux calculations.

Comparing the aircraft fluxes and modelled surface fluxes against one another could be the cause of the apparent bias, as two different fields are being compared as if they are the same. Therefore it would be useful to compare variables which are both

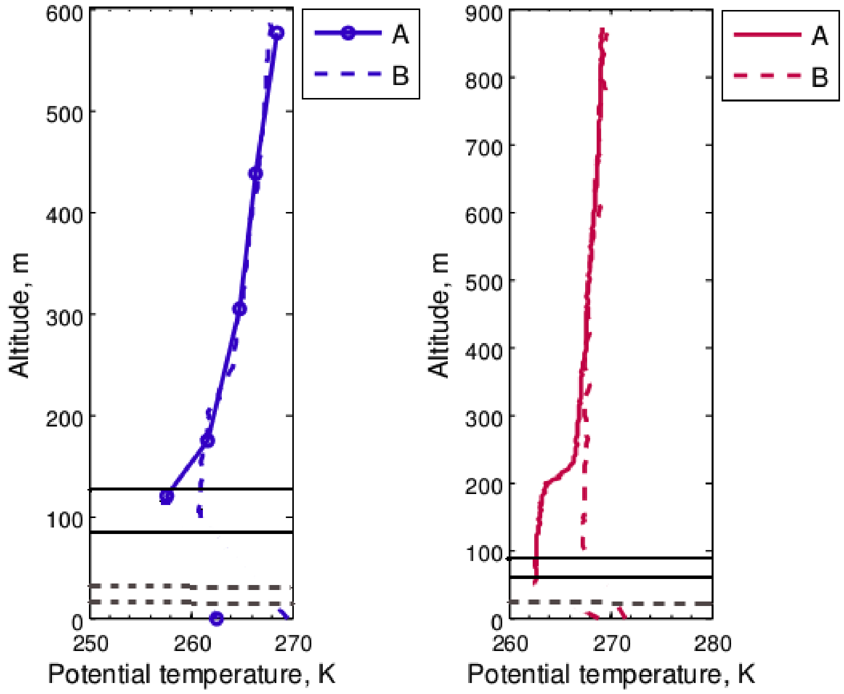

Figure 5.10: θ profiles for Cases 1 and 2 with the range of the aircraft altitude over during the lowest level run marked in black and corresponding surface layer depth (10% of BL height) marked in dashed grey. Case 2 only has one surface layer depth marked, as the over water BL height is above these measurements, and so it is impossible to calculate the depth of either the BL or the surface later.

at the same level, such as the temperature at altitude, temperature at the surface and the wind speed. These variables are all used in the calculation of fluxes in the model, so comparing the model and aircraft data will help to explain some of the differences.

The temperature difference, ΔT is defined as surface temperature minus the temperature at altitude ($T_{sfc} - T_{alt}$), so if the the BL is unstable $\Delta T > 0$, and if it is stable the $\Delta T < 0$. Along with the wind speed, $\mathbf{U}$, ΔT is used calculate the fluxes in the model as discussed in Chapter 2. If the model and observations have similar values for ΔT and $\mathbf{U}$ then it can be concluded that the model is unable to capture this, however if modelled ΔT is lower than the observations, but $\mathbf{U}$ is higher (or vice versa) the errors may balance out.

The values for ΔT and $\mathbf{U}$ for both Cases 1 and 2 are shown in Figs. 5.11 and 5.12 respectively. For Case 1 $\mathbf{U}$ is just over 7.5 m s^{-1} (with all the schemes having the same wind speed) which shows good agreement between the observations and the model at the northern end of the cross section, the model is too high in the middle and too low at the end of the cross section. The temperature difference in the model is negatively biased, and so the model is slightly more stable than the observations.

The bias is largest for the QNSE, which counter-intuitively corresponds with it having the highest fluxes. The QNSE having been designed to provide fluxes in more stable conditions, is performing as expected. At the northern end of the cross-section (right of 76.6 °N) both **U** and ΔT are similar to the observations, and for both SHF and LHF the bias here is positive but small in Figs. 5.6 and 5.8. Implying that the model might actually be overestimating the fluxes. Between 76.2 °N and 76.6 °N **U** and ΔT are overestimated in the model, and this is reflected in the largest bias for both SHF and LHF being here. Where **U** is lower in the model, south of 76 °N and ΔT is still too stable compared to the observations, the SHF is again too high, while the LHF is in good agreement with the observations. This points to the model being better at simulating LHF than SHF.

In contrast, Case 2 (Fig. 5.12) has a consistent negative bias in **U** of around 5 m s^{-1}, while ΔT is in reasonable agreement with the observations apart from in the middle of the cross-section. This would be expected to produce lower fluxes in the model than the observations. Once again the QNSE is the most stable, despite generally having the highest fluxes in Figs. 5.7 and 5.9. Despite the low windspeed in the model, there is a positive bias in both SHF and LHF, the best agreement occurs in LHF at around 76.1 °N where the model is more stable than the observations.

These investigations show that the observations made using the aircraft were above the lowest 10% of the BL for both cases, which does make any surface flux calculation from the aircraft problematic, this is especially true at times when the aircraft may not be within the BL at all as seen in Case 1. Investigations into the heating effect of the BL fluxes showed that the amount of LHF and SHF predicted by the idealised experiments to provide the same amount of heating over the same distance is much higher than that observed. Both of these investigations point to the observations being not representative of surface fluxes. However considering variables which both the model and observations contain, namely temperature difference and wind speed, the picture becomes less clear. Case 1 has three different areas where wind speed is either well represented in the model, positively biased and negatively biased when compared to the observations, while the modelled temperature difference is always negatively biased. This pattern is not obvious in the fluxes, where both SHF and LHF are positively biased compared to the observations, apart from where the modelled LHF is within the observations south of 76 °N. This area of good agreement in the fluxes corresponds to an area where both the **U** and ΔT are negatively biased in the model. The results for Case 2 show that while modelled ΔT is generally in good agreement with the observations, the modelled **U** is negatively biased. This does not result in fluxes which are too low, in fact the best agreement for LHF comes where the observations and model show the least agreement. It could be concluded from here that neither the model is performing well or the observations are representative.

The difficulties in comparing the model and observations could point to other problems the model could have which can be causing it to overestimate the fluxes. These include an inability to simulate, or indeed parametrise the complex and varied terrain of the MIZ, which is very different from the decreasing fraction seen here. The mosaic method whereby the fluxes over mixed ice-water areas are calculated twice, once for open water and once for solid ice, and then averaged using the ice fraction as a weighting (as discussed in Chapter 3) could be too simple. The different types of ice could impact on the fluxes, as what a satellite might interpret as open water may be very dark, thin new ice, and what a satellite might interpret as high sea ice cover might be made up of lots of small floes which while close together let more open water to the surface, and thus behave as a lower ice fraction.

Unfortunately
to properly conclude whether the observations are not representative of the surface, either dropsondes or surface measurements would be needed. If more dropsondes had been used in these cases, then the presence of a surface based inversion below the aircraft altitude could be detected, allowing the flux calculations to be discounted. Surface measurements in the MIZ would be difficult to obtain, but only with these could the model and observations be accurately compared. More work does also need to be done to evaluate the fluxes of sensible and latent heat over the MIZ and design better parametrisations for this area.

It would also be good to be able to compare fluxes at model levels with those calculated using the aircraft observations. While this is not possible with standard WRF output, it is possible to obtain the fluxes on model levels through post-processing. The calculation involves taking the BL tendency of potential temperature then using the SHF as a surface boundary condition, to solve the differential equation,

$$\textbf{BL Tendency} = \frac{d(flux)}{dz}. \tag{5.4}$$

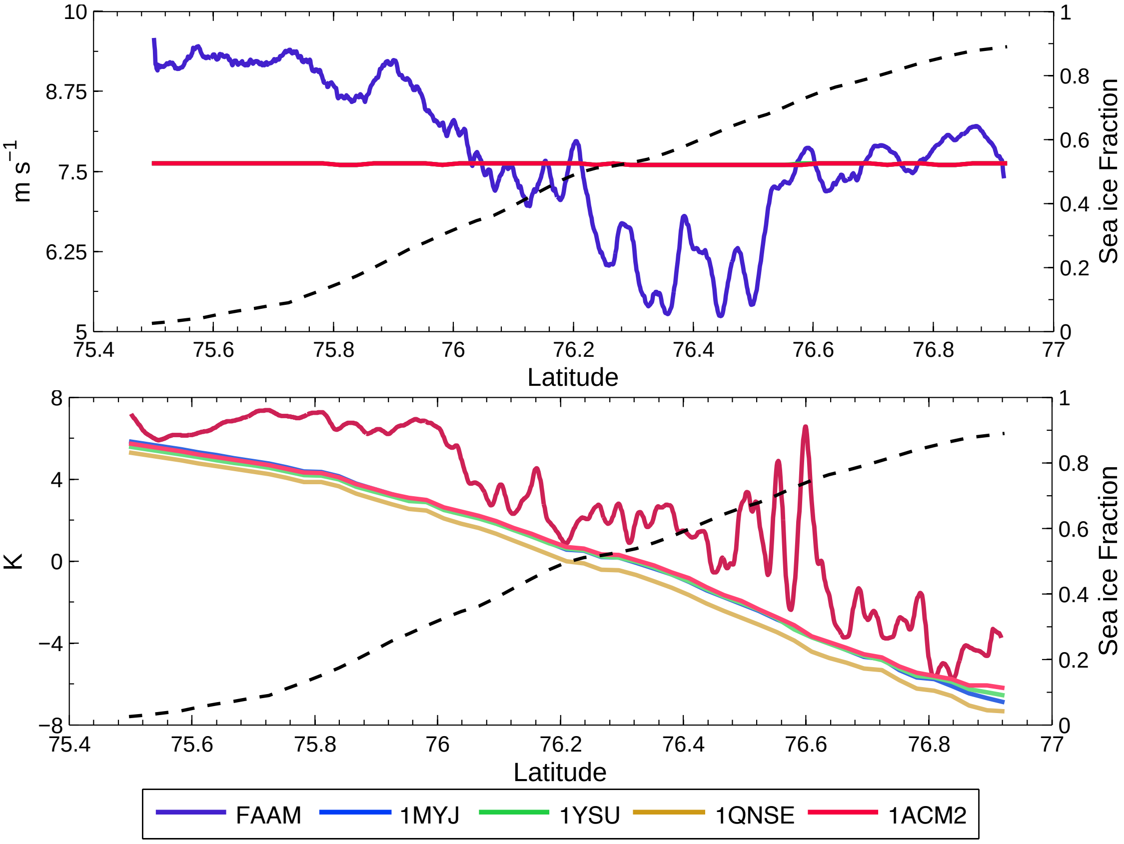

Figure 5.11: Windspeed (top, m s−1) and ΔT (bottom, K) at flight level for Case 1.

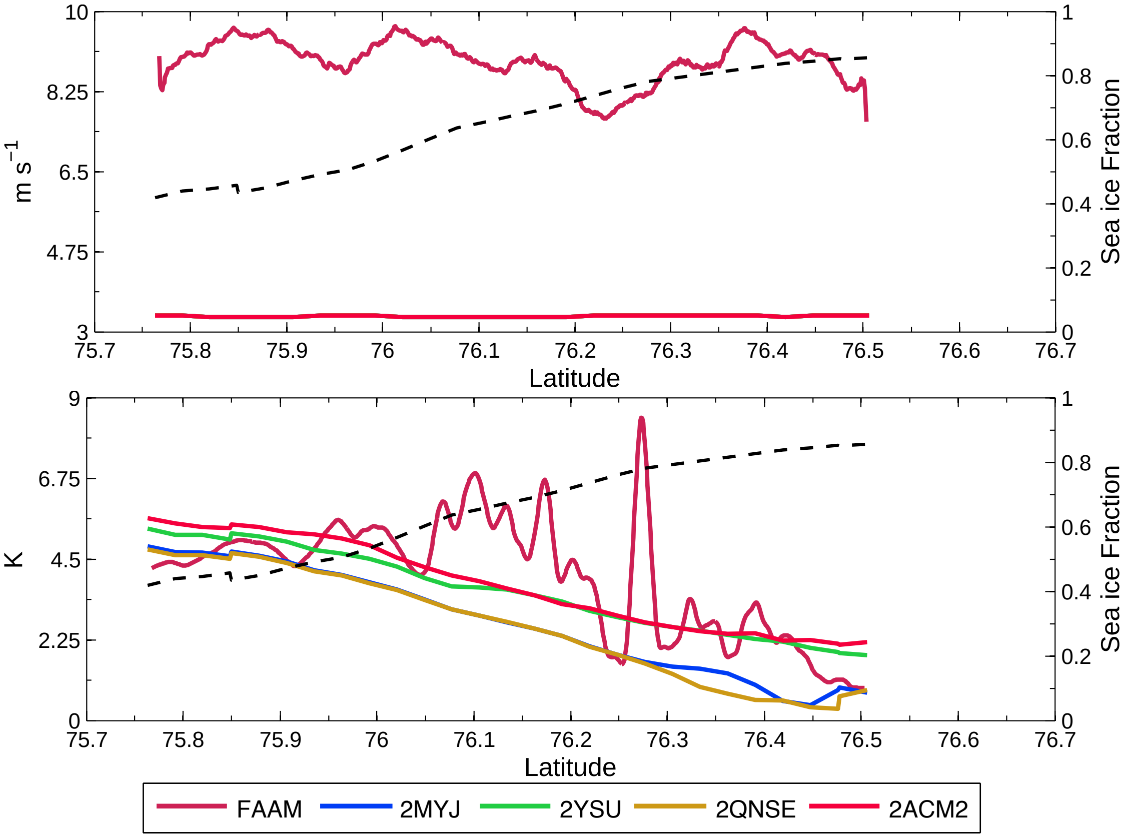

Figure 5.12: Windspeed (top, m s−1) and ΔT (bottom, K) at flight level for Case 2

5.2.3 BOUNDARY LAYER

Profiles of potential temperature, θ are shown in Figs. 5.13 and 5.14. These are either taken from profiles made with the aircraft, or by stacking observations at the same point at different altitude runs as for Case 1 over ice. The profiles are taken from point A (over ice) and point B (over water) which are marked on Fig. 4.8 as the dashed grey lines. All the observed profiles have a surface value calculated using the surface temperature and pressure. The two triangles indicate the range of surface temperature values over the 3 km at the bottom of the profile. The 3 km corresponds to the horizontal resolution of the model. The profiles use mean values at the surface.

For Case 1 the temperature inversion is well simulated by all the BL schemes (Fig. 5.13). Over ice the observed inversion is between 120 m and 170 m while the model ranges between 92 m (MYJ and QNSE) and 130 m (ACM2 and YSU). Over water only the YSU gives a different value, at 245 m compared to 207 m for the other schemes. The MYJ, QNSE and ACM2 have BL heights which are again very close to the observations. The extra height in the YSU experiment may be due to the explicit treatment of BL top entrainment in the YSU scheme allowing more rapid growth upwards. The thickness of the inversions is generally accurate unlike Tastula *et al.* (2012) or Kilpeläinen *et al.* (2012).

The surface value over ice for Case 1 is at the lower end of the range given by the triangles at 261.8 K for the ACM2 and 261.4 K for the other schemes. The lower bound for the observations was 261.7 K. Over water the modelled values are much cooler than the range for the observations. With model values are 266.4 (MYJ) and 266.5 (YSU, QNSE, ACM2) which is 2.4 - 2.5 K below the observations which are between 268.8 K and 269.6 K. This is linked to the model not having open water here like in the observations.

Over ice the mixed layer temperature is hard to see in the observations, due to no observations being available within the mixed layer. However looking at the inversion point θ is 257.7 K in the observations and between 257-257.7 K for the model, with the QNSE being warmest. The mixed layer temperature is therefore well represented. Over water the mixed layer temperature is also well represented, with the observations being 261 K, MYJ and ACM2 are 260.7 K and 260.8 K respectively, while the YSU and QNSE are 261.2 K.

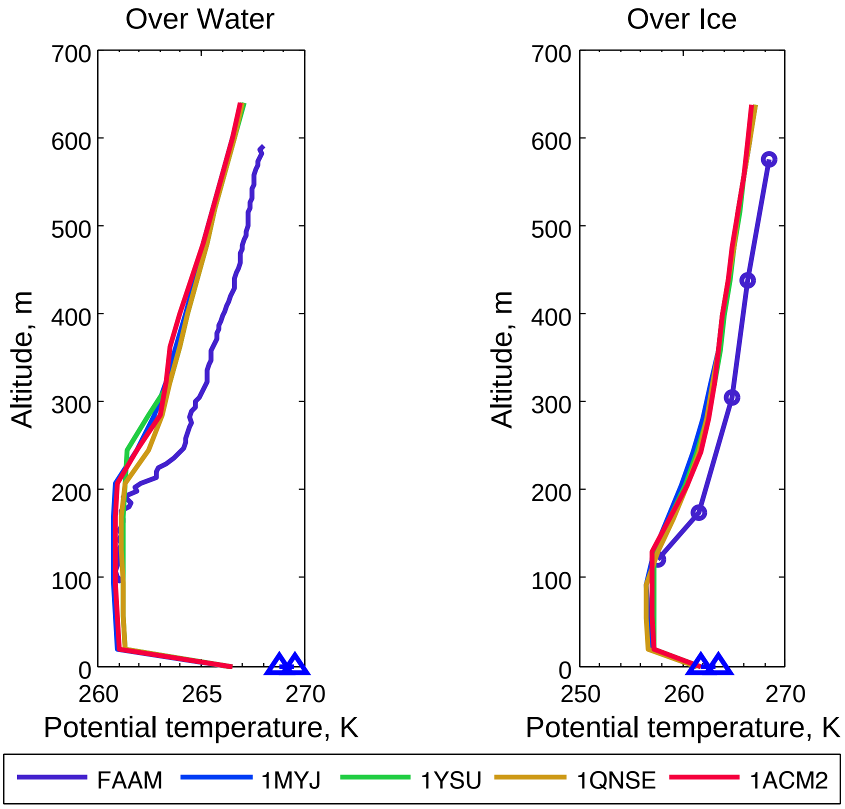

Figure 5.13: θ for Case 1, K for both the observations and the model simulations. The over ice profile is compiled from observations at different levels, indicated by the dots. The triangles give the range of possible surface values.

Above the CIBL the model generally underestimates the potential temperature, being on average 2.7 K cooler than the observations over ice. This gap is maintained for the over water profile, implying this is a larger scale issue with the atmosphere possibly being initialised too cool. This is similar to Mayer *et al.* (2012) where there was a cold bias above the BL.

Looking at the cross section in Fig.5.15 it can be seen that the transition from stable to well-mixed is happening in both the observations and the model. Most notably it can be seen in all four plots that the BL height, as shown by the change from blue to yellow colours, starts to increase further south (left of B) for all the BL schemes. The MYJ has the smallest increase in BL height, reaching 300 m, whereas the other three schemes all approach 400 m. One feature which is lacking in the model is the warmer θ values at the northern end of the cross section (100 m, 76.85N) of 261 K, whereas the model has values between 254.5 K (MYJ) and 255 K (ACM2). The lack of any open water such as leads in the sea ice field means that the θ is not increased by the presence of warmer water, as happens in the observations.

For Case 2 (Fig. 5.14) over ice, it can be seen that the range of observed surface temperatures is very wide, 264.1 - 272.6 K, due to the presence of a lead near the profile. The surface values for the model are all within this range. The average from the observations is 266.8 K, and there is little spread between the different schemes. Over the water the range for the observations is much smaller, 271.3 - 271.8 K with the average being 271.5 K. Here the model values are 1 K too cold. Again this can be attributed to differences in the surface representation between the observations and the model.

As for Case 1, in Case 2 the mixed layer temperature over the ice is well represented. Observations are around 262.7 K, while the model values are between 262.6 K (MYJ) and 263.3 K (YSU) with the ACM2 and QNSE at 262.8 K. The modelled boundary layer height in Case 2 is however very different from the observations, being far higher. The observed value is 197 m, whereas the model ranges between 281 m (MYJ) to 397 m (YSU, ACM2) with the QNSE being between these at 319 m. This is up to 200 m too high. Either the model has warmed far too fast, or began warmer than the observations. The high fluxes in the model cannot be the sole cause of this higher BL height, as Case 1 also has higher fluxes in both the model and observations, but a much better BL height. Rather the overestimation of the BL height implies a problem with the initialisation data.

For Case 2 the model does not warm the mixed layer as close to the MIZ as the observations. Over water the observations have a mixed layer temperature of 267.4 K, while the model has between 263.9 K (ACM2) and 264.7 (MYJ) which is up to a 3.5 K difference. For the observations the CIBL erodes away and equilibrates with the wider atmosphere which does not happen in the model. While the BL height does change, it is actually decreasing over the MIZ. As the key source of heating for the BL over the MIZ is the surface, this implies the surface is not providing enough heat to sustain the height of the BL. The other explanation is that the CIBL is being eroded but slower than in the observations, by mixing down air from above the BL and thus reducing the height of the inversion. Again the free atmosphere above the BL is cooler in the model than in the atmosphere, with up 2.6 K difference over the ice which then reduces to 1.1 K over the water, this is possibly due to other sources of heating, such as latent heat release in clouds warming the atmosphere.

The cross section for θ for Case 2 is shown in Fig. 5.16, the overestimation of the

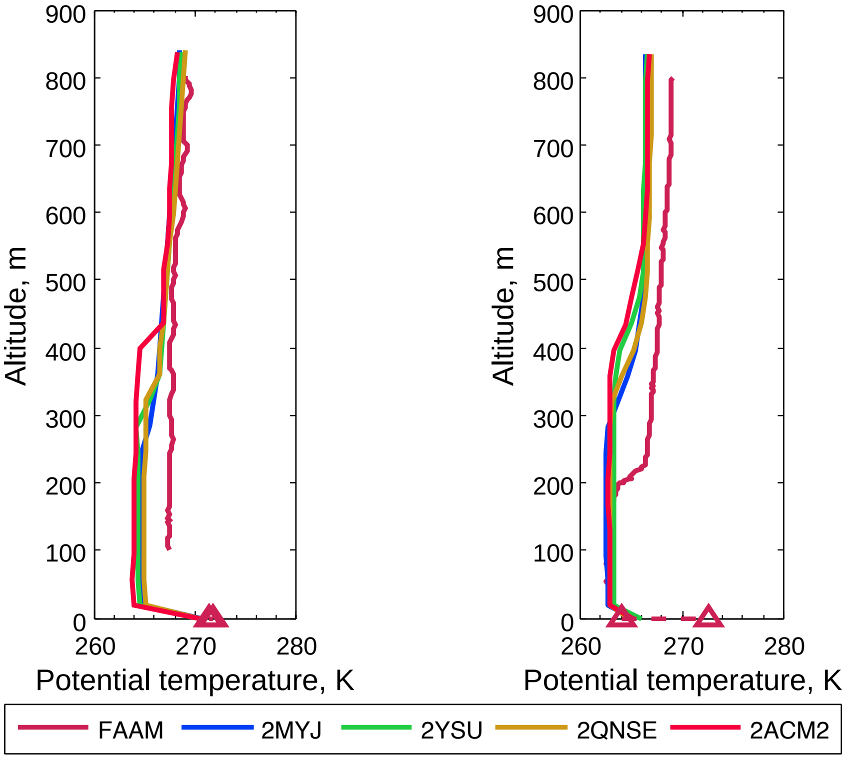

Figure 5.14: θ for Case 2, K for both the observations and the model simulations. The triangles indicate the range of possible surface values. The right plot is over ice, and the left over water.

depth of the BL in the model can be seen to extend to the north of the profile at A. The four schemes do show an increase in θ at the bottom of the BL from the north to the south, however this is between 1 K (ACM2) and 2.5 K (QNSE). However this is much slower than the observations, which increase by 4 K. The QNSE is most efficient at mixing in a more stable environment. The slow response to the surface can be attributed to the surface being too cold, which could be seen in Fig.5.4.

The specific humidity, q, profiles for the two cases are shown in Fig. 5.17 and 5.18. The Case 1 q (Fig. 5.17) shows good agreement in general with the observations. Again the over ice profile is created with measurements at different levels during different flight legs (denoted by the circles) as opposed to one profile in the aircraft like the over water profile. Over the ice the bottom of the profile is too dry in the model, by up to 0.54 g kg^{-1}, with the MYJ having the lowest (1.0 g kg^{-1}) and the QNSE the highest (1.16 g kg^{-1}) q values below 100 m. The reduction in q is slightly higher up for the YSU and ACM2 at 129 m compared to 92 m for the QNSE and MYJ. Above this the model atmosphere is too moist compared to the observations, with a +0.4 g kg^{-1} bias. over the open water, the MYJ is again has the lowest q (1.5 g kg^{-1}) and the QNSE the

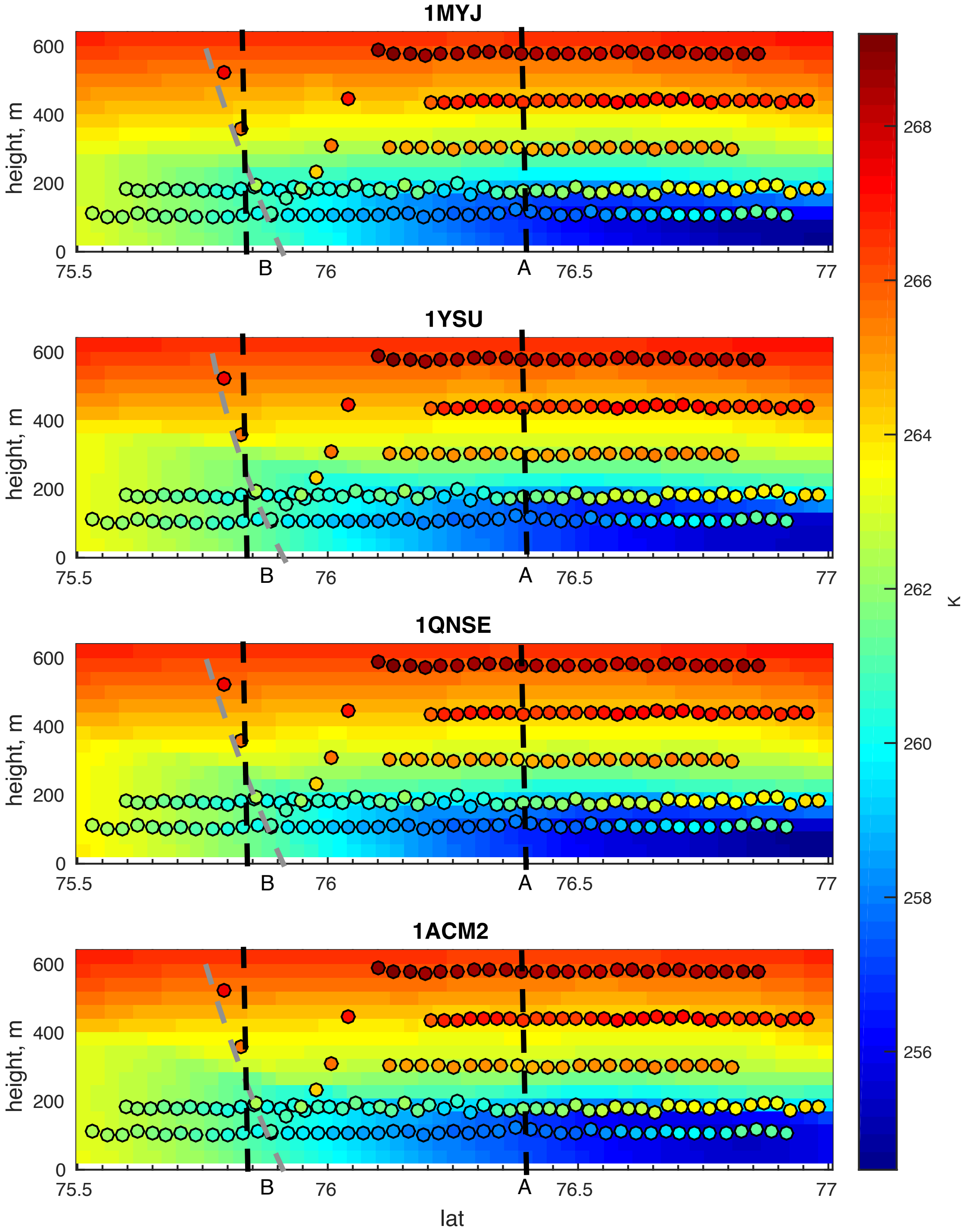

Figure 5.15: θ for Case 1, K. The observations are the coloured dots, while the modelled values are in the background for all the different BL schemes. The northern end of the cross section is on the right hand side.The black lines marked A and B indicate the location of the modelled profiles, while the grey line indicates the true profile which was used from the observations.

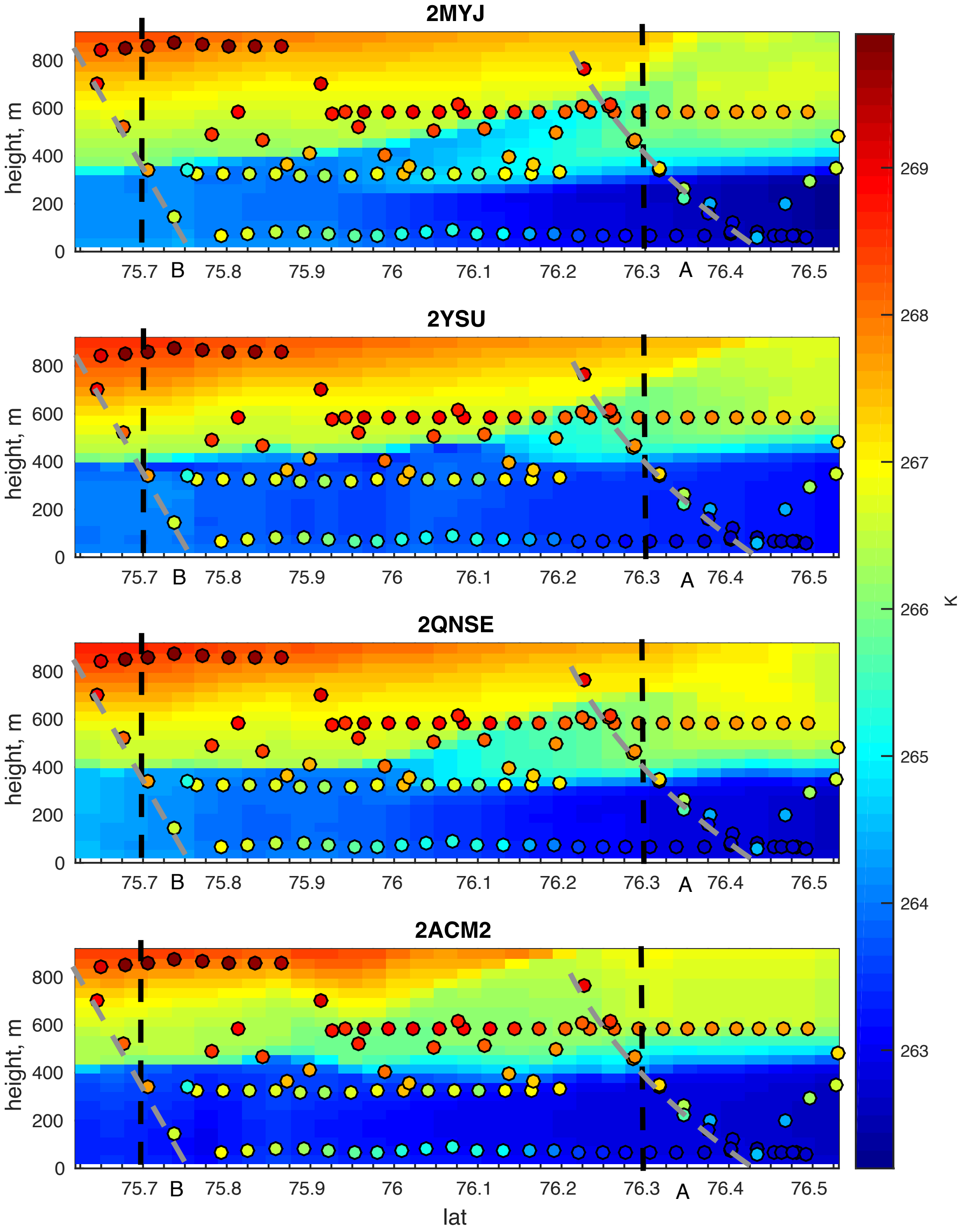

Figure 5.16: θ for Case 2, K. The observations are the coloured dots, while the modelled values are in the background for all the different BL schemes. The northern end of the cross section is on the right hand side. The black lines marked A and B indicate the location of the modelled profiles, while the grey lines indicate the true profile which was used from the observations.

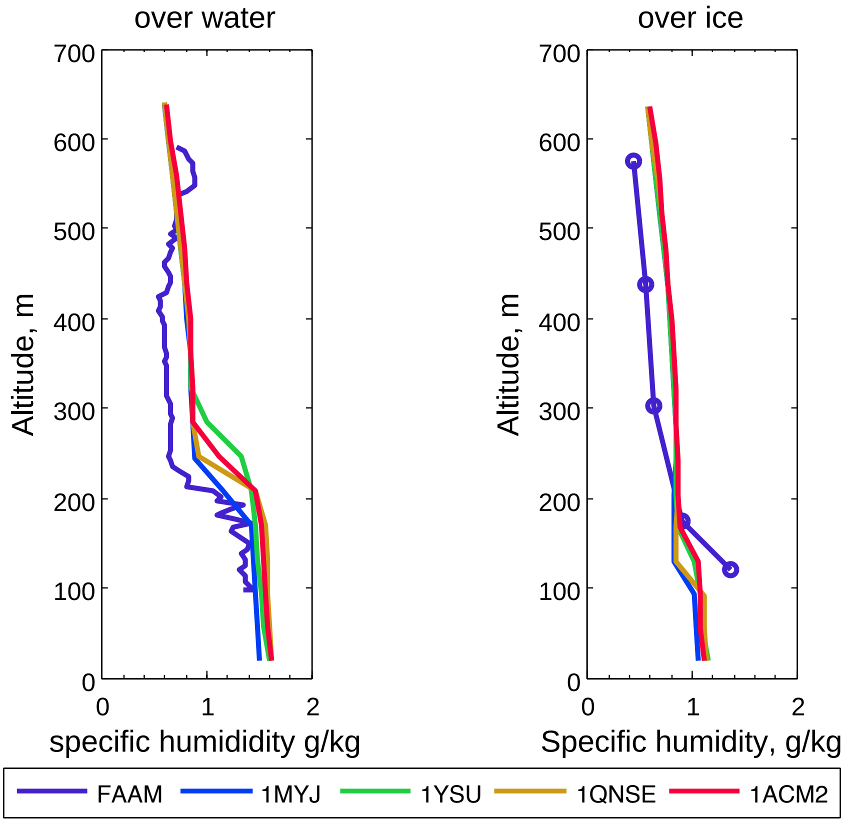

Figure 5.17: Specific humidity, q for Case 1, g kg^{-1}. The over ice profile has been made using observations from multiple levels, marked by dots.

highest (1.6 g kg^{-1}), and both have increased by 0.4 g kg^{-1} across the MIZ, while the observations did not change at the bottom of the internal BL. The MYJ, which has the largest magnitude in the bias over the ice, now over water has the smallest bias, despite being the lowest value for both, as q increases faster in the model. The model also has the reduction in q from the over ice profile higher now than the observations. At a maximum of 245 m (YSU) compared to 192 m for the observations, the MYJ matches well with the observations here. The free atmosphere above the internal BL does not show much change in q for either the observations or the model, with the model being too moist compared to the observations again.

The cross section of q in Fig.5.19 shows that the observations have a local maximum in the lowest level leg of 1.5 g kg^{-1} at 76.75N, which the model does not have. The YSU and ACM2 have lower values of q here than at 77N. The surface can again be to blame for this, as without an area of open water the model cannot be expected to reproduce the changes in q without the source of moisture. However between A and B the model is able to give more q than in the observations, with a

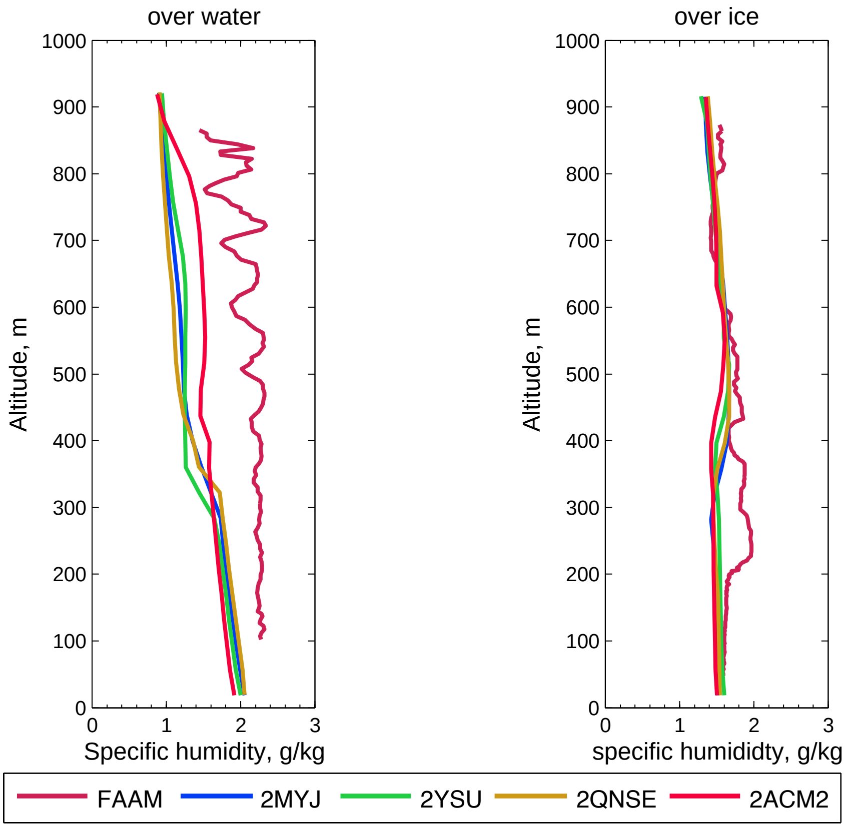

Figure 5.18: Specific humidity, q for Case 2, g kg^{-1}.

maximum between 1.61 g kg^{-1} (MYJ) and 1.73 g kg^{-1} (YSU) while the observations have a maximum of 1.59 g kg^{-1} at the southernmost end. This shows that the surface has been the main provider of moisture to the BL, however the model has a much bigger change in q across the MIZ than the observations do, which means the model moisture flux (and thus LHF) is too high. Vertically the model has higher values of q than the model across all the schemes, and for all the cross section, which implies a problem with the initialisation of the case.

The q profiles over the ice and water for Case 2 (Fig. 5.18) in general have higher q values than Case 1. Over the ice the internal BL has the drier air than the free atmosphere in both the model and observations. The model being up to 0.1 g kg^{-1} lower than the observations (ACM2). The bottom value for the YSU is very similar to that for the observations. This area of drier air extends to 281 m (MYJ, QNSE) and 396 m (ACM2,YSU)in the model, while in the observations it extends to only 201 m. Above 201 m the model is negatively biased by up to 0.5 g kg^{-1} (MYJ). This negative bias extends to around 500 m, where the model and observations begin to converge. Over the open water the bottom of the profile has become more moist, by

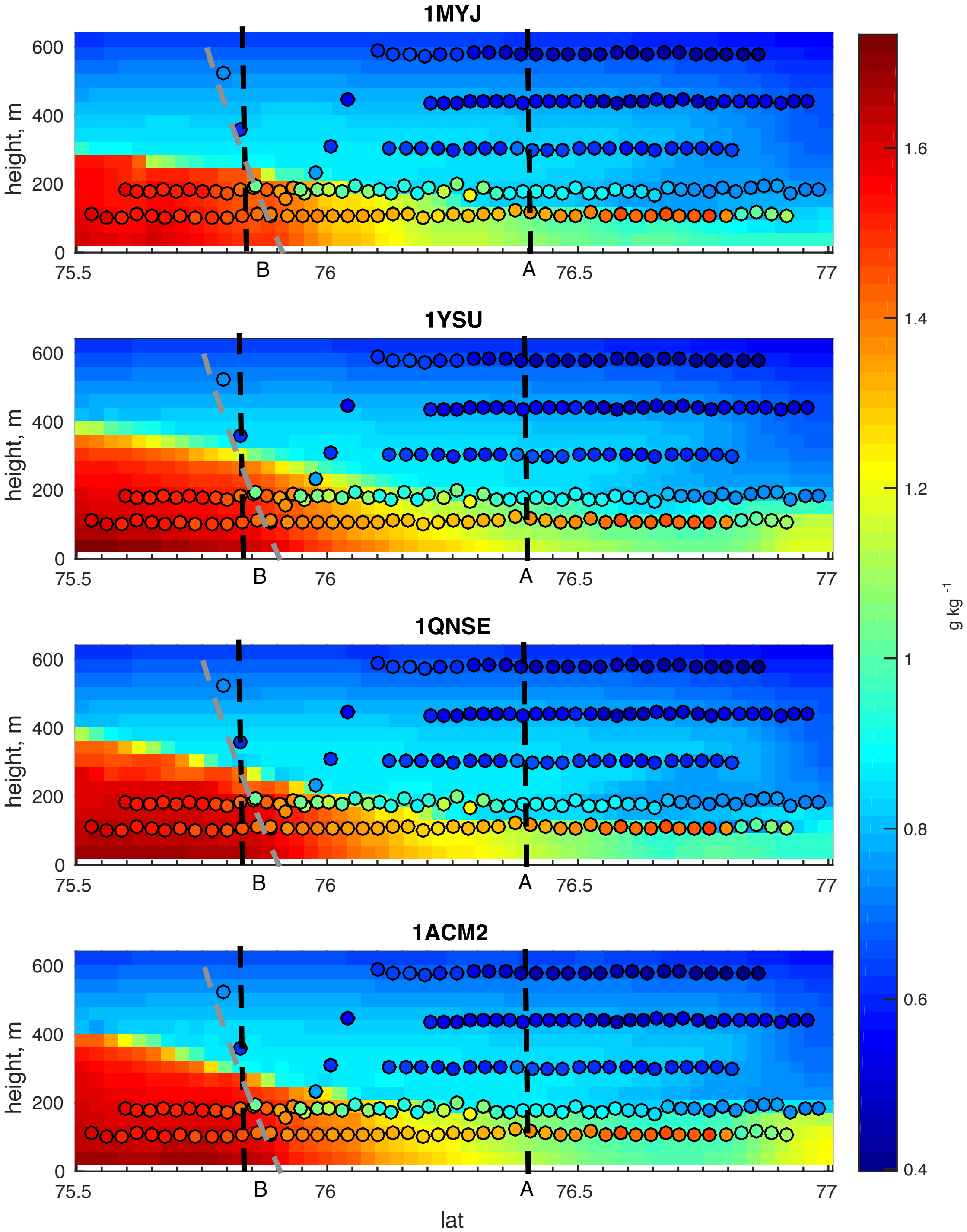

Figure 5.19: Case 1 specific humidity q cross section, g kg^{-1} The observations are the coloured dots, while the modelled values are in the background for all the different BL schemes. The northern end of the cross section is on the right hand side.The black lines marked A and B indicate the location of the modelled profiles, while the grey line indicates the true profile which was used from the observations.

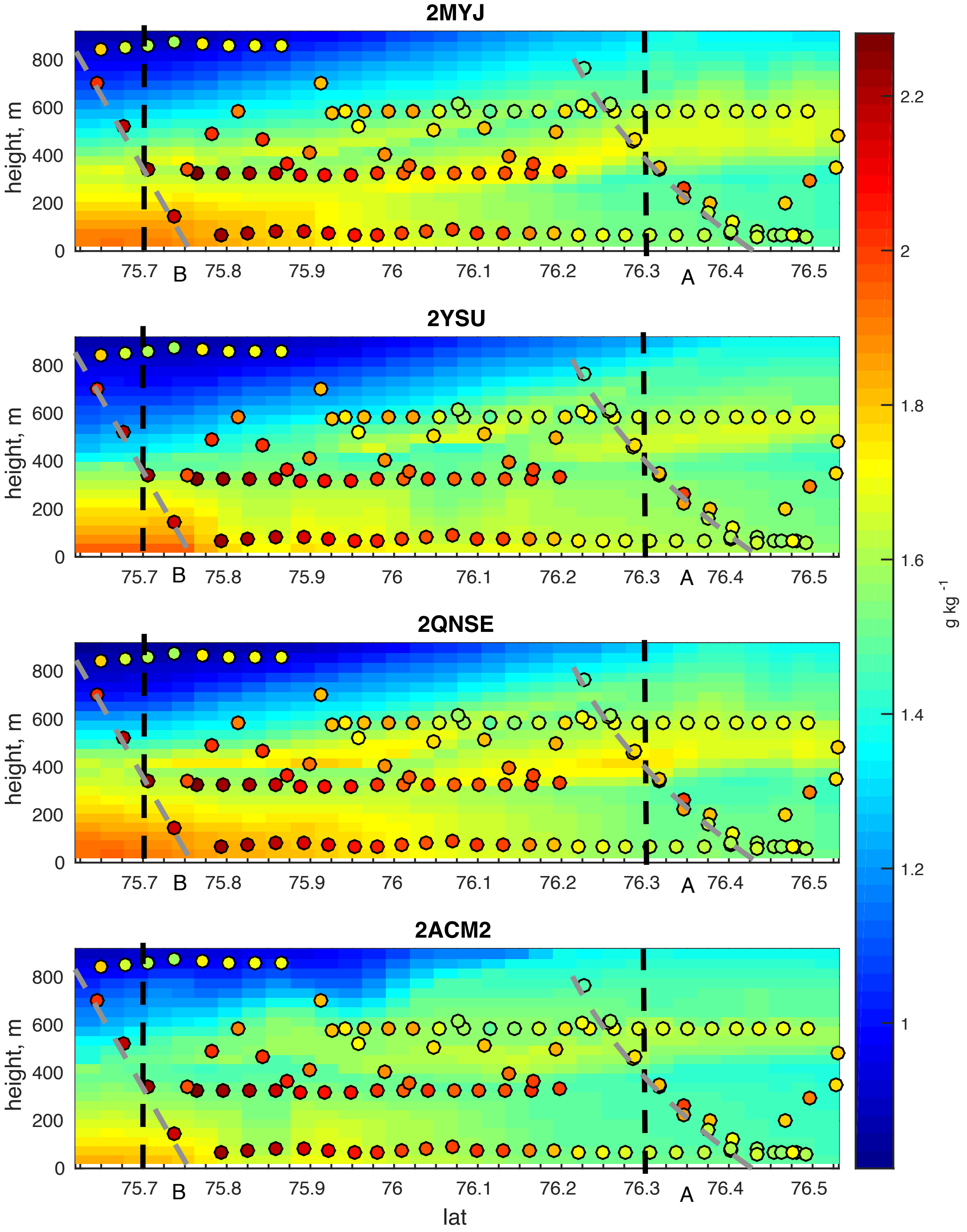

Figure 5.20: Case 2 specific humidity q cross section, g kg^{-1} The observations are the coloured dots, while the modelled values are in the background for all the different BL schemes. The northern end of the cross section is on the right hand side.The black lines marked A and B indicate the location of the modelled profiles, while the grey line indicates the true profile which was used from the observations.

up to 0.4 g kg^{-1} for the QNSE, which is now the most moist, while the ACM2 has the lowest q. The observations however increased from over the ice by 0.6 g kg^{-1}. The model increased by the same amount for Case 1, which was too much in that case, but too little in this case. The internal BL is now more moist than the air above, which is not seen in the observations as the internal BL has eroded and the surface is now coupled to the atmosphere above. As the inversion in θ is lower in the model for the Case 2 over water profile compared to that over the ice, so the layer of moist air has reduced in height. The model is unable to capture the internal BL being eroded and the re-coupling between the surface and atmosphere.

The cross section in Fig.5.20 shows the model and observations started at similar values, close to 1.6g kg^{-1} at the northern end of the cross section (90 m, 76.6 °N). However the observed values of q rapidly increase to reach a maximum of 2.2 g kg^{-1}, while the model q is increasing slower, reaching between 1.83 g kg^{-1} (ACM2) and 1.94 g kg^{-1} (YSU) at the southernmost end. The model has too little open water, compared to the observations, meaning there is not enough moisture available to increase q.

The wind speed for Case 1, **U** is shown in Fig.5.21, in both the observations and the model, **U** is lower at lower altitudes, and increases from north to south. The observations have higher values for **U** in the lowest level (100 m) than above across the cross section, starting at 7.5 m s^{-2} at 76.9N, increasing to 9.1 m s^{-2} at 75.5 m s^{-2}. While the model starts below 5 m s^{-2} and increases to 7.5 m s^{-2}, which is a similar rate of increase but starting from too low. Vertically in both the observations and the model, **U** increases with altitude, as the friction from the surface is not felt. The observations increase to a maximum of 11.3 m s^{-2} at 600 m and 76.1N, while the model has a value at the same location of between 6.5 m s^{-2} (MYJ) and 7.5 m s^{-2} (QNSE). The lower **U** may be why the model is too dry over the ice, as there is not enough wind driven mixing to bring the moisture from the surface.

For Case 2 **U** is shown in Fig.5.22. In general the observations have higher **U** than the model. At the lowest level run of the observations (90 m) the minimum value is at 76.45 °N, and is 7.1 m s^{-2}, which increases to 8.8 m s^{-2} at 75.84 °N. The model in the same locations decreases slightly, from 7.9 m s^{-2} to around 7.5 m s^{-2}. Vertically for the observations the higher **U** extends to around 400 m before reducing to a minimum of 4.1 m s^{-2} at 75.74N and 800 m. The model also has a decrease in **U** at the same height, but decreases much further to between 1.2 m s^{-2} (YSU) and 1.9 m s^{-2} (MYJ, QNSE). Unlike for Case 1, there is a deceleration over the cross section, so where the mixing should be enhanced by wind shear in the model, there is no increase in BL height, mixed layer θ or q. The surface may be to blame here, as if there is too high an ice fraction, there may be too much friction. These factors combine to reduce the speed of the boundary layer transition which is evident in the observations, and in the model for Case 1.

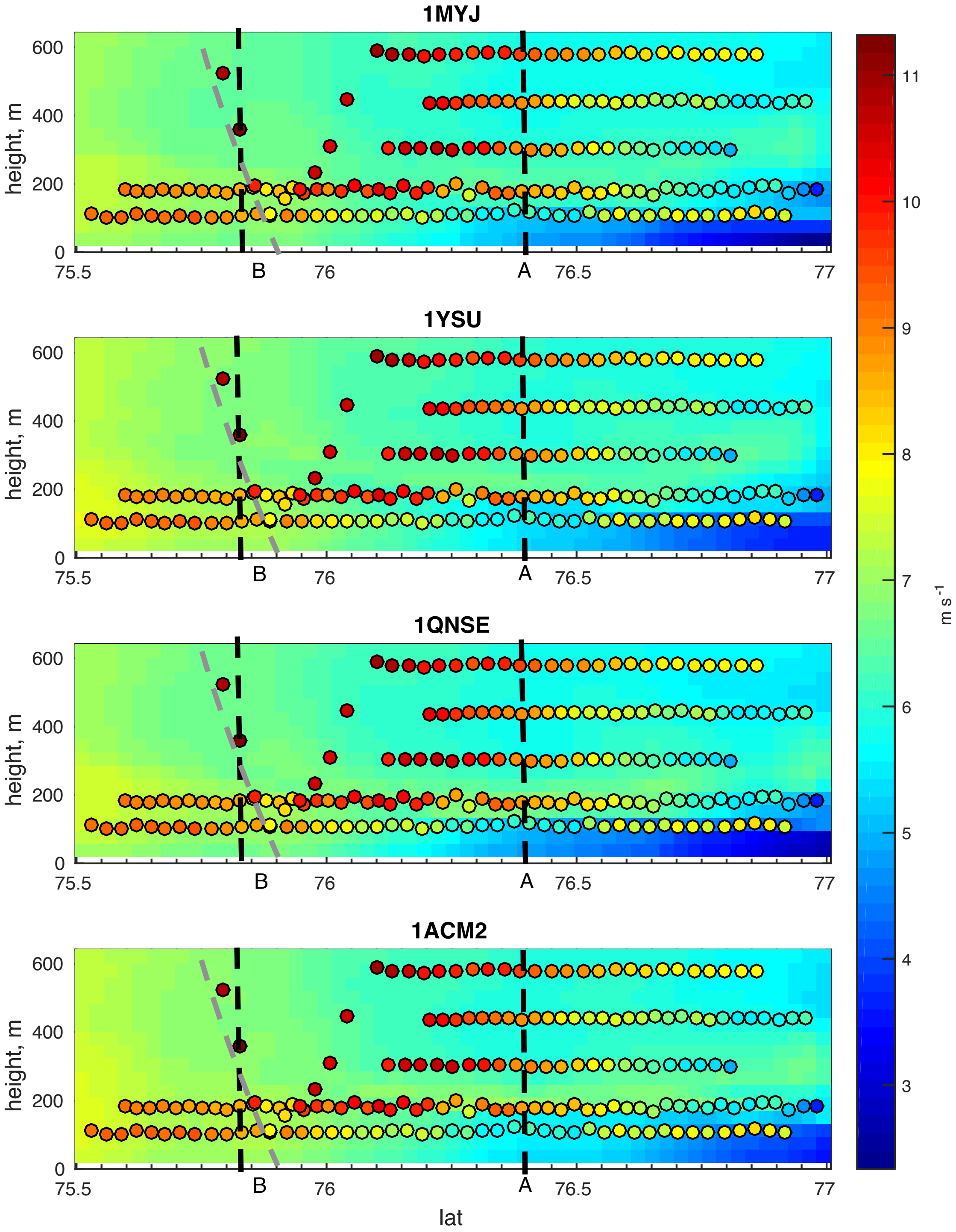

Figure 5.21: Case 1 **U** cross section, m s^{-2}. The observations are the coloured dots, while the modelled values are in the background for all the different BL schemes. The northern end of the cross section is on the right hand side.The black lines marked A and B indicate the location of the modelled profiles, while the grey line indicates the true profile which was used from the observations.

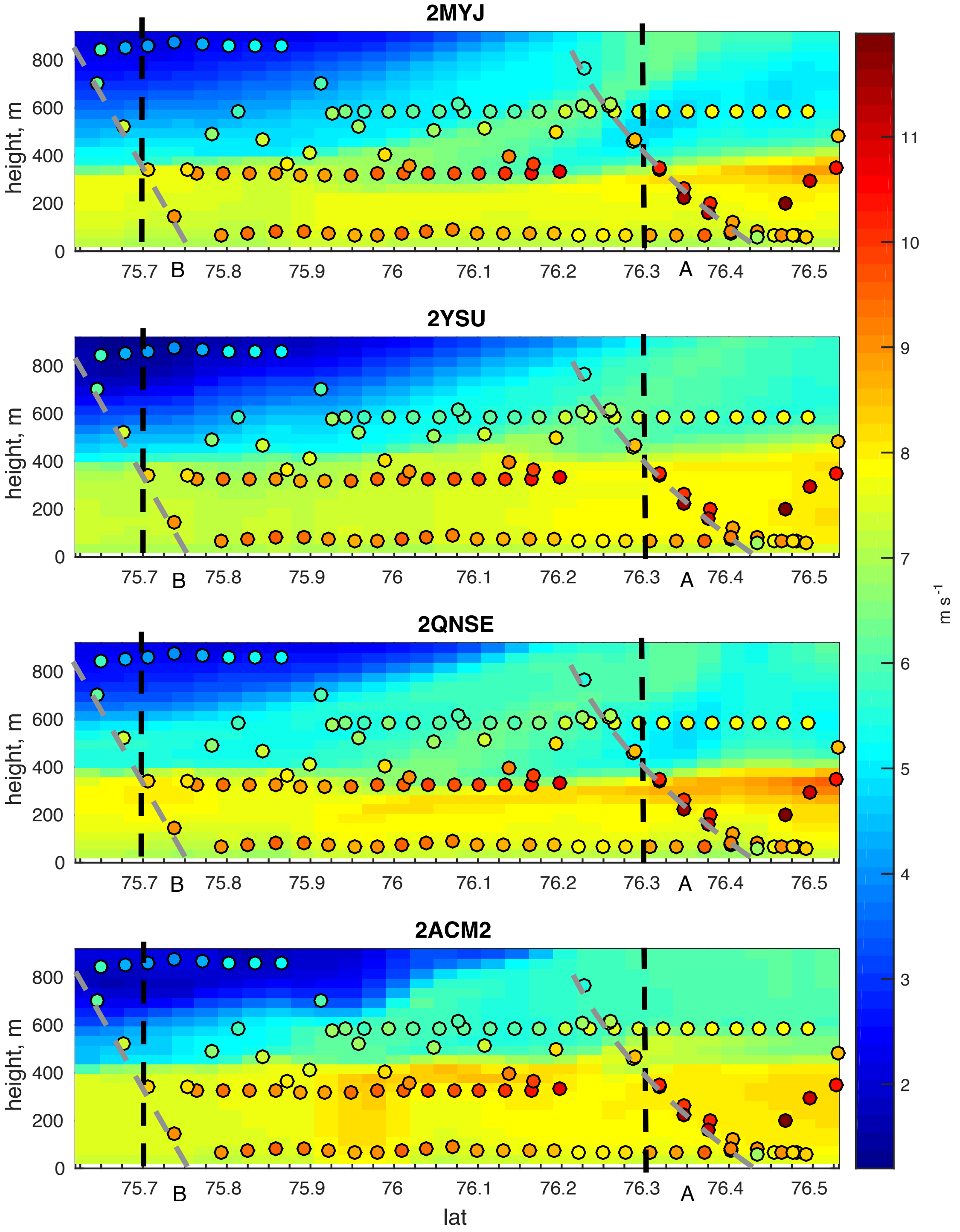

Figure 5.22: Case 2 **U** cross section, m s^{-2}.The observations are the coloured dots, while the modelled values are in the background for all the different BL schemes. The northern end of the cross section is on the right hand side.The black lines marked A and B indicate the location of the modelled profiles, while the grey line indicates the true profile which was used from the observations.

5.2.4 CLOUDS

Many studies point to uncertainties in predicting clouds as the cause of problems with surface and mixed layer temperature (Hu *et al.*, 2010; Tastula *et al.*, 2012; Bromwich *et al.*, 2013). To investigate whether the BL schemes were causing inaccuracies in the clouds and evaluate if this is causing a problem with the modelled surface temperatures, the figures for liquid water mixing ratio, Q_{LW} and ice water mixing ratio, Q_{IW} (Figs. 5.23, 5.24 and 5.25) show the data from the observations as coloured dots, which have been smoothed to 3 km and then only every third kilometre is shown, in order to bring it into line with the model. Data from the model is shown as a coloured surface behind the dots, and as they are on the same colour map, qualitative agreement between the two can be ascertained when the dots blend into the background.

For Case 1 the observed Q_{LW} is very low, with a maximum Q_{LW} of 1.1×10^{-4} g kg^{-1} across the domain. The model also has very low Q_{LW}, however it does have higher values of Q_{LW} than the observations to the north of the domain (77 °N). The YSU produces the most Q_{LW} here, with a maximum of 0.4×10^{-1} g kg^{-1}, much higher than the observations. The YSU and ACM2 produce this cloud, which explains why these produce the higher surface temperature in Fig. 5.3.

For Case 2 the maximum observed Q_{LW} is higher than that for Case 1 at 0.05 g kg^{-1} and is again seen more to the south of the cross-section. The observed moisture is mostly under 400 m between 76.1 °N and 75.7 °N, and then up to 800 m south of 75.7 °N,. All the model experiments show a sweep of Q_{LW} from above 800 m at 76.5 °N to 300 m high at 75.7 °N. As this sweep of Q_{LW} this is common to all the experiments, it is likely coming from the initialising data where there is a higher amount of liquid water. As the BL height is decreasing across this area, it would be expected that the height of the moisture would decrease too. Qualitatively, the MYJ does the best job of replicating the cloud seen in the observations. However this looks like more of an accident than due to any skill, as the model cannot capture the cloud extending higher into the BL, as it does not capture the increase in BL height seen in the observations. The QNSE is providing too much moisture to the cloud microphysics scheme, as it also has the highest moisture flux (not shown). It has the largest maximum values for Q_{LW} at 0.33 g kg^{-1}, whereas the MYJ is has the smallest maximum Q_{LW} at 0.22 g kg^{-1}.

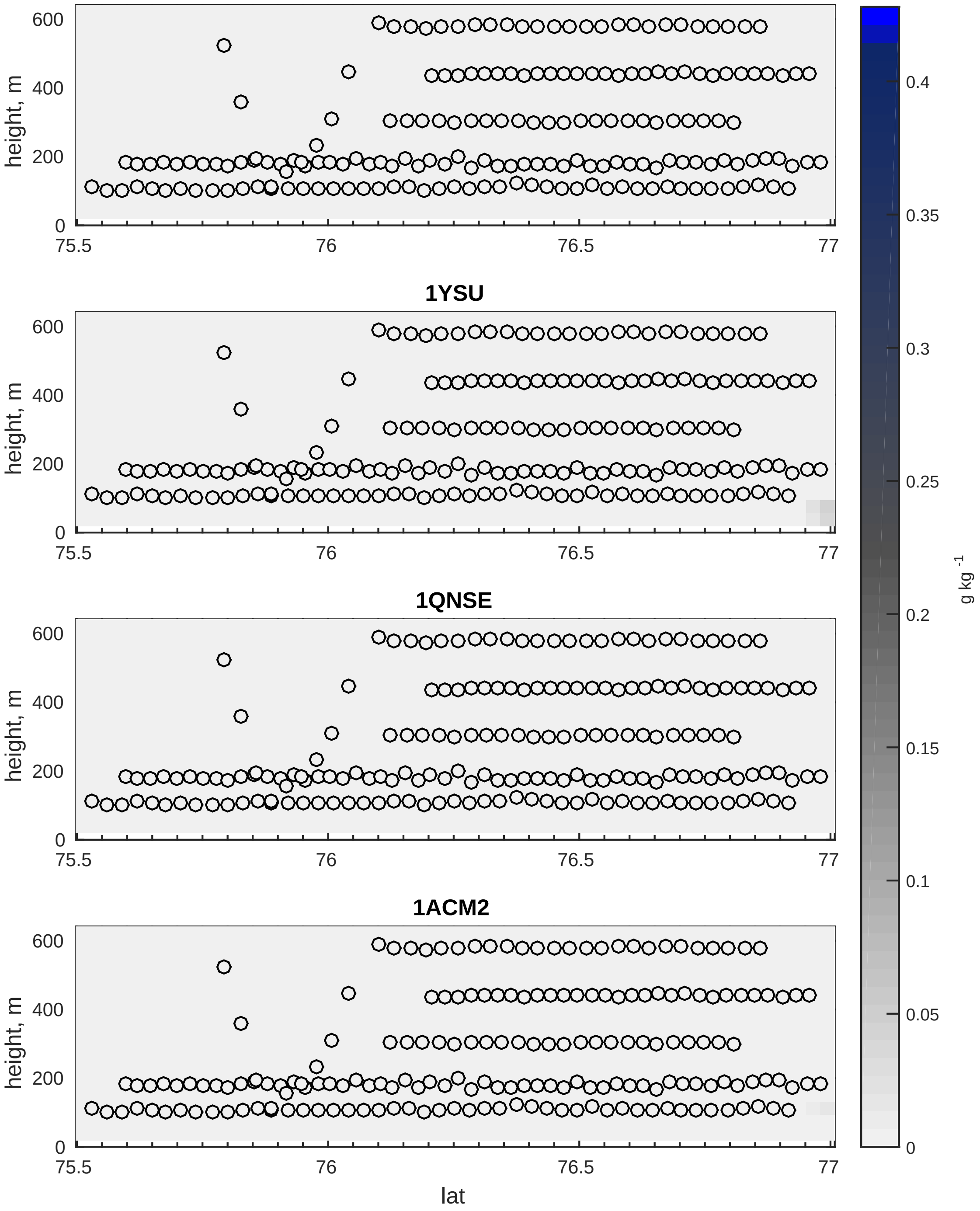

Figure 5.23: Q_{LW} for Case 1, g kg^{-1}.The background colour is from the model, while the filled circles are the observations. A minimum threshold of 1×10^{-3} g kg^{-1} is applied, with anything below that being white. The northern end of the cross section is to the right.

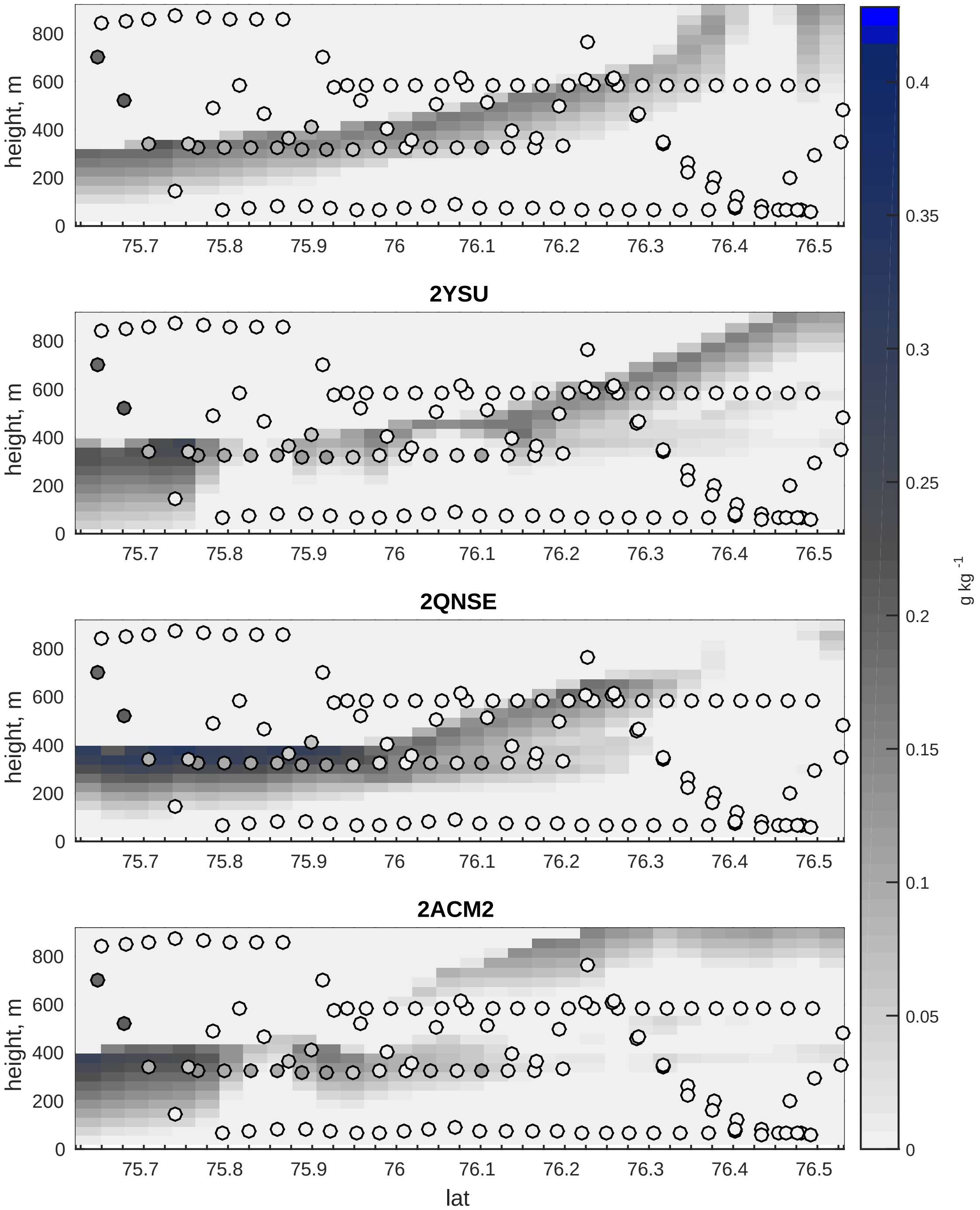

Figure 5.24: Q_{LW} for Case 2, g kg^{-1}. The background colour is from the model, while the filled circles are the observations. A minimum threshold of 1×10^{-3} g kg^{-1} is applied, with anything below that being white. The northern end of the cross section is to the right.

For Q_{IW}, Case 1 again has low concentrations and the model is giving higher concentrations to the north (77 °N) as for Q_{LW} , and again it is only the YSU and ACM2 which show this (figure not shown).

Case 2 has a sweep of Q_{IW}, like for Q_{LW}. However again the observations have the majority of Q_{IW} within the BL, under 400 m, which is not the case in the model. Even though all the BL schemes are poorly representing the Q_{IW}, there are some interesting differences between them. The MYJ has its highest values of 4.8×10^{-4} g kg^{-1} between 76.4 °N and 76.5 °N and above 800 m. The QNSE has a similar structure, but with less Q_{IW} at 4×10^{-4} g kg^{-1}. The similarities between the MYJ and QNSE are due to them being the same type of BL scheme. Both the YSU and ACM2 show a maximum value lower down at around 400 m, with the ACM2 having 5.3×10^{-4} g kg^{-1} around 76.85 °N and the YSU 5.2×10^{-4} g kg^{-1} at around 76.1 °N . As the ACM2 has the highest BL, the Q_{IW} extends higher into the atmosphere here. The high values of Q_{IW} in the cloud over the middle of the cross-section could be causing the YSU to have the highest surface temperature here in Fig. 5.4.

The boundary layer scheme therefore does make a difference to the presence of clouds, with the YSU and ACM2 producing more Q_{LW} and Q_{IW} than the QNSE and MYJ, implying these schemes provide more liquid to the cloud microphysics. The increased cloud, causes an increase in surface temperature. However none of the model experiments are able to reproduce the cloud accurately.

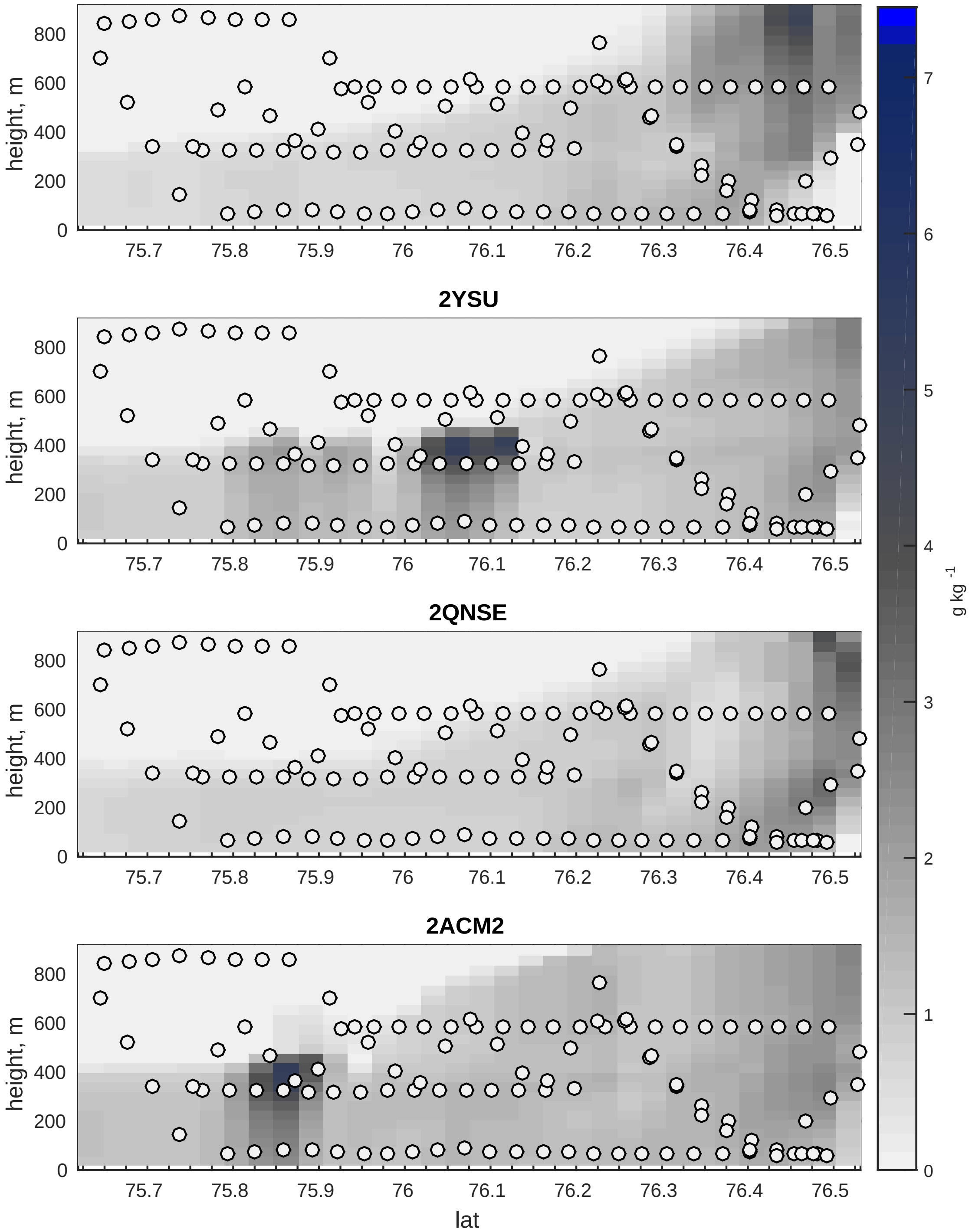

Figure 5.25: Q_{IW} for Case 2, g kg^{-1}. The background colour is from the model, while the filled circles are the observations. A minimum threshold of 1×10^{-7} g kg^{-1} is applied, with anything below that being white. The northern end of the cross section is to the right.

5.3 DISCUSSION

In this chapter results of BL parametrisation sensitivity tests in PWRF were presented. Four different BL schemes were evaluated, the MYJ, YSU, QNSE and ACM2. The different schemes cover a range of closures types, include both local and non-local approaches, and have been developed for different situations. The results from the four different schemes were compared against the two cases chosen from the observations. Case 1 is colder, drier and has less cloud present than Case 2. Using the two case studies was due to different BL schemes being best for different situations.

In general all the schemes performed similarly, and are often not very close to the observations. For the surface temperature the model overestimates for Case 1, with a bias up to +1.94 K. However for Case 2 the surface temperature is underestimated, with the largest bias being -1.32 K. The problems with simulating the surface temperature can be attributed to issues with the sea ice cover. While the observations show a highly heterogeneous sea ice cover, the model assumes a much smoother sea ice field, as can be seen in Fig. 5.2. The sea ice fraction may also be overestimated, particularly for Case 2, where the end of the domain was more open water than the model assumes (Fig. 5.4). The presence of clouds in the model do have some impact on the surface temperatures, particularly over the ice, however this is a moderating effect, rather than the main reason the surface temperature is incorrect in the model. With the surface being so different to the observations, it is no wonder the surface temperatures are incorrect. Problems with surface temperature may cause the surface fluxes to be incorrect, as well as the provision of moisture to the atmosphere if the fraction of open water is incorrect. Problems with the flux of heat and moisture from the surface to atmosphere impact the formation of clouds, which then further warm the surface. Other experiments have seen a cold bias of up to -3.32 K (Bromwich *et al.*, 2013) over sea ice, or a warm bias of up to 3.5 K (Hines & Bromwich, 2008) over Greenland.

While the two cases perform very differently for surface temperature, the surface fluxes of sensible and latent heat are consistently overestimated. For SHF (Figs 5.6 and 5.7) the average bias over all the BL schemes is +53.05 W m^{-2} while for Case 2 it is slightly lower at +49 W m^{-2}, despite the surface temperature being overestimated and underestimated for Case 1 and 2 respectively. LHF is better, but still too high with the bias for Case 1 being +19 W m^{-2} and for Case 2 + 21.1 W m^{-2}. The QNSE consistently gives the highest flux values and as the QNSE has been developed for stable boundary layers, it is possibly over-doing the fluxes in an unstable BL as was seen here in the observations and in the model. These biases are much higher than those observed in Bromwich *et al.* (2009), where fluxes were underestimated in the model, however the latent heat flux had a smaller bias as seen here. However over land all the schemes tested in Shin & Hong (2011) have large positive biases in the surface fluxes. The surface fluxes are overestimated in Case 2, despite the surface temperature being negatively biased. The sensible heat fluxes are slightly lower than those for Case 1, so this is probably due to the lower surface temperature. The biggest problem here is the comparison of fluxes from the aircraft at altitude to the surface flux values from the model. Comparing the ΔT and $\mathbf{U}$ from the model with the observations, along with taking into account the changes in the θ profiles it was concluded that the observed flux values are erroneously low. Even with good agreement between $\mathbf{U}$ and a too stable BL, the modelled fluxes were higher. These higher fluxes however could not warm the BL as much as was seen in the observations, implying the observed fluxes are erroneously low, caused by the limitations of flying low over the sea surface in an aircraft. Further work would need to have the model provide the turbulent components of vertical wind and temperature at model levels to enable better comparisons between the model and aircraft.

Both WRF and PWRF have been seen to have problems representing the BL over the Arctic, with inversions being too thick (Tastula *et al.*, 2012), or being too shallow and weak (Kilpeläinen *et al.*, 2012). For Case 1 the BL is represented very well within the model, with the inversion height being correct, as well as the mixed layer temperature and the surface inversion. The model has the atmosphere above the BL around 2 K too cold, so the inversion is not strong enough. The specific humidity is well represented over the open water, while the model is too dry in the mixed layer over the ice. The free atmosphere has a positive bias when compared to the observations which is consistent through all the schemes. There is little to separate the schemes, with the YSU having slightly higher inversion heights. The wind speed in the BL is slower than that for the observations across all the schemes, which may explain the negative moisture bias in the model over the ice. In general there is very little to separate the schemes.

Case 2 is very different, the BL height is over-estimated by up to 200 m. While the surface and mixed layer temperatures are well represented over ice, the inversion is too high. In the observations the convective internal BL has been eroded away in over water profile. This is not captured by the model, with the BL heights even decreasing. The BL in the model has a negative bias in q, and while there is some increase over the cross section, it is not as much as in the observations. The wind speed is too low across the whole cross section, and decelerates while the observations have an acceleration in wind speed. The negative bias in wind speed may explain why the BL does not change as fast as in the observations, as there is less mixing due to wind shear, meaning the BL height does not change as fast. Incorrect BL heights could cause an incorrect cloud base height, as this is related to the inversion height. Problems with cloud cover in WRF have been blamed for problems with surface temperature, as in Tastula *et al.* (2012) and Bromwich *et al.* (2009). For Case 1, very little cloud liquid water or ice was observed, and the model also has very little due to the atmosphere being too dry. However for Q_{LW} the YSU and ACM2 give small amounts of liquid in the north of the domain as they are most efficient at providing moisture upwards. This is similar for Q_{IW} with the YSU and ACM2 giving values again to the north of the domain. Case 2 has cloud in the observations, however the model has a sweep of cloud liquid and ice, which was not seen in the observations. The QNSE now gives the highest values of Q_{LW}, again this can be attributed to it over-mixing as the BL is not stable. For Q_{IW} the YSU and ACM2 have similar features, while the QNSE and MYJ are more similar. As both the QNSE and MYJ are TKE schemes, this similarity may be expected.

Four different boundary layer parametrisation schemes were compared for two different cases. As all the boundary layer schemes perform similarly to one another, it is not possible to make a recommendation of a best BL scheme. One of the key problems with these simulations is the mis-representation of the surface, which then causes issues with the surface temperature and fluxes along with the cloud cover, which feeds back to the surface temperature. In order to better assess the abilities of the BL parametrisations a more accurate surface should be supplied to the model. This will be investigated in the next chapter.

6

SIMULATING COLD AIR OUTBREAKS OVER THE MIZ: SENSITIVITY TO SEA ICE.

The sea ice in the MIZ is important for the atmosphere above it. In Chapter 3 it was seen that reducing the thickness of the sea ice increased the surface temperature. The surface fluxes of heat and moisture were increased and produced cloud and precipitation earlier. Having a good sea ice representation is therefore not only important local to the ice edge, but potentially many kilometres downstream.

Sea ice is not only important in an idealised set up. In Chapter 5 inaccuracies with the simulated surface temperature being too high or low, surface fluxes being too smooth, the boundary layer not warming and deepening enough and cloud height not increasing sufficiently were attributed to the sea ice surface being too homogeneous and the sea ice fraction being too high. The issues with the surface forcing made it difficult to evaluate the skill of the four BL schemes tested.

Difficulties with representing sea ice in models have been seen to cause problems such as a daytime warm bias due to the albedo being too low due to neglecting the effect of frost flowers (Pinto *et al.*, 2003), large changes in fluxes due to large changes in sea ice fraction (Rinke *et al.*, 2006) and increases in cloud fraction in areas with decreased ice cover (Palm *et al.*, 2010) and reducing sea ice cover reducing intensity of convection (Liu *et al.*, 2006). Surface temperatures and the albedo are important for the surface energy balance, along with the cloud cover. In simulations where sea ice is permitted to form or melt, these are key indicators for whether the sea ice should be present or not. Simulating these incorrectly makes understanding future sea ice cover difficult.

Using Polar WRF (PWRF), Seo & Yang (2013) compare three different sea-ice concentration algorithms for satellite derived sea-ice fraction, (the NASA TEAM algorithm, Bootstrap algorithm and EU OSI-SAF (Ocean and Sea Ice Satellite Application Facility) algorithm) against in-situ measurements. In general the bootstrap algorithm has the highest concentrations, the NASA lowest and the EU inbetween. They found that the observed BL evolution is simulated well, provided the uncertainties in sea ice concentration are small. Problems occur especially around the MIZ where the thickness and concentration of the sea ice greatly influence the skill of the hindcasts, with 2 m temperature (T_2) and moisture (Q_2) being more responsive than SLP. They concluded that while it is important to have small uncertainties in sea ice representation, it is not possible to recommend one of these three algorithms as best as none of them performed persistently better across all the variables being examined.

It was found in Chapter 5 that the sea ice product used in the simulation (OSTIA) was significantly different to the observed sea ice for Case 2 (flight B765, 30/03/2013). This is confirmed in Figure 6.1, which shows the MODIS satellite image for Case 2 at 250 m resolution, with contours of the OSTIA sea ice fraction over the top and a red line indicating the location of the cross section. It appears that the sea ice cover is overestimated by OSTIA, with the 0.7 contour corresponding to the edge of the white sea ice to the east of the cross section. Location A is where mostly white ice can be seen, and B marks ice with more dark open water visible. Buoyancy wave clouds are seen at C and further south point D indicates the location of convective cells. Looking to the east of the cross section (at the 0.3 contour label) the cloud is thin enough to see that below the surface is mostly dark. While there could indeed be a high ice concentration here, the ice must be either very thin or very broken (or both) to appear so dark. The presence of buoyancy wave clouds could be taken to indicate the presence of a change in surface causing there to be some instability which is perturbing the stable layer above, causing the waves, such as the edge of the ice.

In chapter 5 the OSTIA sea ice is used, and the sea ice is 3 m thick. This can be seen in Fig. 6.1 to not agree well with the visible satellite imagery. Some studies have had

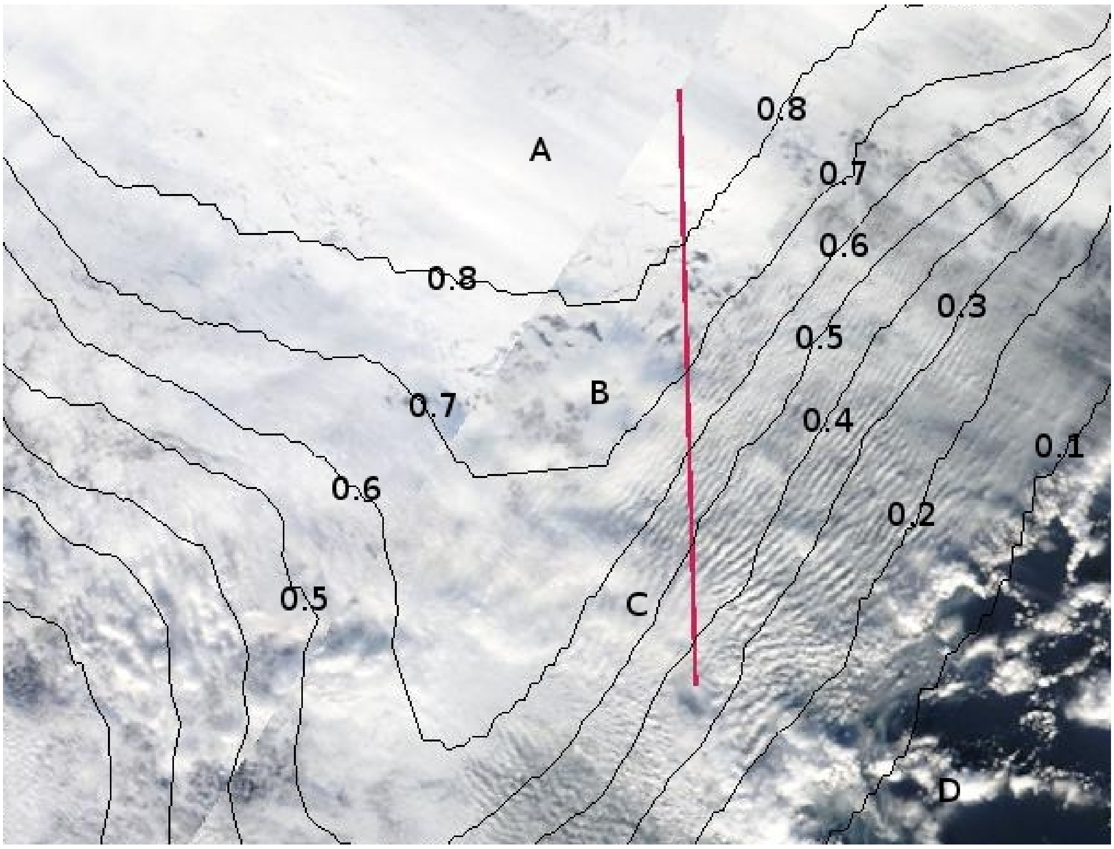

Figure 6.1: MODIS image on Google Earth for midday Case 2 (30/03/2013) with the OSTIA sea ice contours over the image, the area of the cross section is marked in red. Location A marks more solid ice with fewer breaks, B shows where the ice has started to show more open water, C indicated the presence of buoyancy wave clouds, and D the location of convective cells.

to hand edit the sea ice for their model simulations, Kilpeläinen *et al.* (2012) started with sea ice from the AMSR-E dataset, with a 25 km resolution and modified to follow the sea ice charts produced daily by the Norwegian Meteorological Institute due to errors near coastlines and fjords. Following the same process, Mayer *et al.* (2012) also resorted to hand editing the sea ice cover near the coast for their BL sensitivity study.

This chapter will examine the changes caused by editing the sea ice beneath the cross section on the results of the Case 2 BL sensitivity study seen in chapter 5. Case 2 was chosen as this case had the most difference between the observed and modelled sea ice. To begin with, observations from the aircraft will be used to derive a new sea ice concentration, which will then be added to the OSTIA data. The sensitivity to BL scheme will then be re-done for Case 2. As the sea ice fraction was assumed to be the cause of problems with surface temperature, fluxes, boundary layer structure and cloud cover, it made it difficult to establish if there was a preferred BL parametrisation

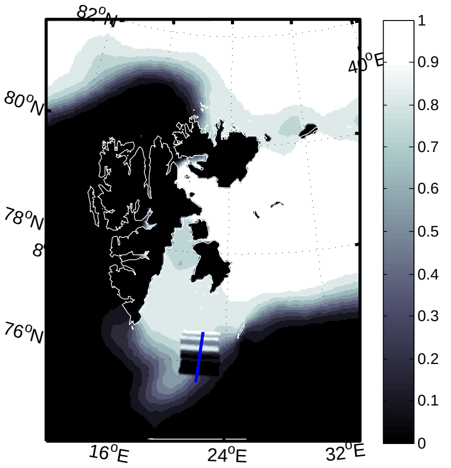

Figure 6.2: The sea ice field for B765 with the adjusted sea ice clearly visible. The blue line gives the location of the cross-section.

scheme for the MIZ. This chapter aims to establish if the sea ice fraction is responsible for issues seen with the previous case study, and to recommend a BL scheme for use over the MIZ.

6.1 IMPLEMENTING THE NEW SURFACE

As the sea ice fraction provided by OSTIA for Case 2 does not match well with either the observations made during the campaign or the satellite image in Fig. 6.1, it needs to be edited to better match the observations. Following Elvidge *et al.* (2016), the sea ice concentration is derived from the albedo calculated from the observed short-wave radiation. The scheme uses tie values (derived from analysis of the aircraft data and videos) of 0.15 and 0.85 as the albedo of 0% and 100% sea ice respectively. The scheme provides a 3 km averaged sea ice fraction between 0 and 1. A wide strip equivalent 180 km (60 gridpoints) wide was then spliced into the OSTIA sea ice fraction, centred around the locations of the flight cross-section as shown in Fig. 6.2. The strip is wide to ensure there is sufficient distance between the edge of the new sea ice and the old sea ice field so the effect of the new sea dominates the local BL response.

For the sensitivity studies the same WRF physics set up as in Chapter 5 was used, meaning the results are comparable. The sensitivity to choice of boundary layer scheme was once again tested with the new surface, to see if this induced any larger differences between the different parametrisations and improved the simulation of the surface, fluxes, boundary layer and clouds.

6.2 RESULTS

6.2.1 SURFACE

As with the previous chapter, it is useful to see the whole inner domain of the model to understand what the changes to the surface have done to the wider model. In Fig. 6.3 the T_{sfc} (left) and T_{2m} (right) are shown, and the changes to the sea ice are apparent in both. The T_{sfc} shows a large area under the cross section which is now warmer than with the original surface, which can be inferred from the cooler area surrounding the area with the changed sea ice. The surface becomes warmer due to the reduction in sea ice cover. The reduction in sea ice fraction is also evident in the T_{2m} plot, but to a lesser extent. The air around the cross section is warmer than the air outside of the changed area, but the features of the sea ice are less evident than in T_{sfc} as T_{2m} is less dependent on the sea ice fraction than T_{sfc}.

To check if there is no horizontal interference caused by the sudden change in the sea ice where the hole has been made, cross sections 9, 6 and 3 km to the east and west of the cross section used here were made. The differences between these cross sections and the central one were calculated for wind speed, potential temperature and cloud liquid mixing ratio, and the standard deviations of the differences found. As was found previously in Chapter 5 the standard deviation of the differences between the cross sections were found to be at least an order of magnitude lower than the values of the variables, they were all also qualitatively similar with features in similar locations over all the cross sections. This means that as before the cross sections from the model can be assumed to not be in any way anomalous, with the change in sea ice not causing any strange behaviour.

In the original sensitivity study, the surface temperature (T_{sfc}) was seen to be too low and too smooth for Case 2 (Fig. 5.4). The T_{sfc} from the four different experiments are shown in Fig. 6.4, the dotted line on the second y-axis shows the new sea ice fraction. The sea ice fraction is now much more variable, with areas of lower concentrations visible north of 76.2 °N, and open water south of 75.95 °N. With the new surface having a lower, and more variable, sea ice concentration, T_{sfc} is now increased (cf. Fig. 5.4) and more variable as it responds directly to the change in sea ice cover, qualitatively more similar to the observations. The reduction of the sea

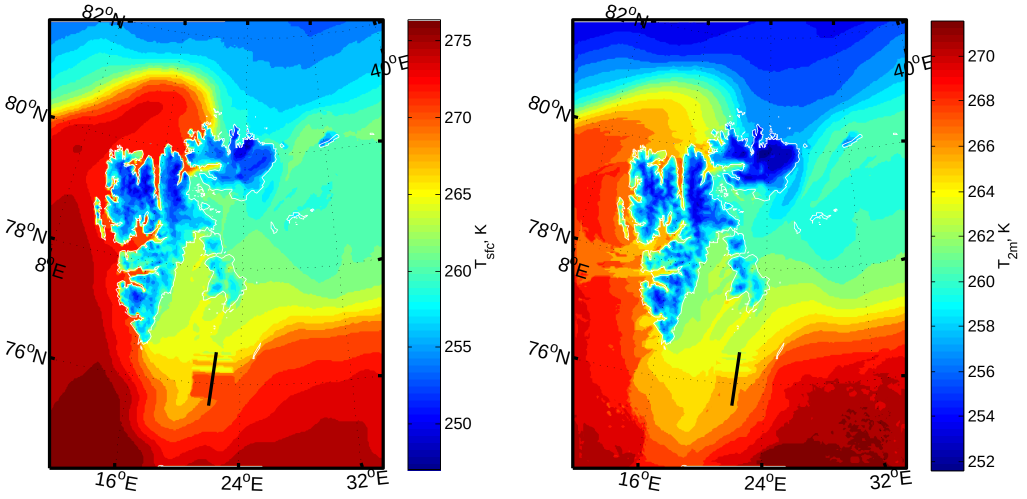

Figure 6.3: T_{sfc} and T_{2m} (K)for the inner domain of Case 2 with the MYJ scheme. The black line shows the location of the flight cross-section.

ice cover allows the warmer open water to be at the surface, directly impacting the temperature. Note the lead observed at 76.25 °N is not included in the new surface, due to the smoothing to 3 km which has been employed, so the surface temperature is too low here. Overall there is a positive bias, between 0.74 and 1.06 K in surface temperature with the QNSE having the lowest and YSU the highest bias. This is a flip in the sign compared to the previous surface (Table 6.1) and is because now the sea ice fraction is lower, so the model is giving a warmer surface much closer to that observed. In the over water area, the surface temperature now seems too warm, 271.6K (+0.3 K over observations) as the model now has totally open water. However as the error on the Heimann downwards facing radiometer is ± 0.5 K, this value is within the range of errors. The calculation for sea ice cover used only the albedo and did not include surface temperature, meaning it is ignoring really low concentrations of sea ice. However, even if there was a low ice fraction or very thin ice present here, the model has no way of simulating thin, dark ice as the ice albedo and ice thickness are not changed. With the previous surface the YSU gave the smallest bias by being the warmest scheme, but it is now the worst as it is too warm. Which shows how its not one BL parametrisation being particularly skilled, but that the best performing scheme can be due to error cancellation.

In the north of the cross section, over the higher ice fractions the temperature is again more varied with the YSU systematically the highest and the QNSE systematically lowest with 0.5 K between them, as was also seen in Fig. 5.4. The

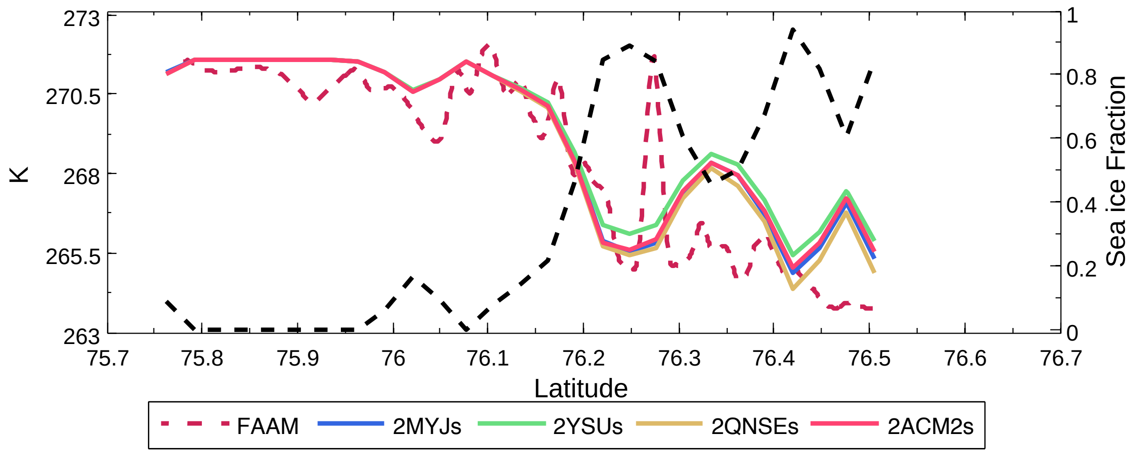

Figure 6.4: T_{sfc} for the new surface compared to the observations for Case 2, the right hand y-axis corresponds to the dashed black line showing the sea ice fraction. The cross section runs from south to north.

biggest spreads of temperatures occur at 76.25 °N where there is 0.7 K between the YSU and QNSE and at 76.42 °N where there is a 1 K difference between QNSE and YSU. Both these locations have a high ice fraction, indicating differences with how the schemes handle exchange coefficients over ice.

The change in the sea ice concentration has indeed reduced the bias between the model and the observations, the new, more varied sea ice cover has resulted in a warmer more varied surface temperature in the model. The QNSE scheme now has the lowest bias (where previously it had the largest bias) as it gave the lowest surface temperature with both the old and new surfaces, with the opposite being true for the YSU. Therefore if a model has thick sea ice and a high sea ice concentration that may be incorrect, the YSU may be the best to use, though if the surface is much more realistic the QNSE may be best.

Table 6.1: Table showing the bias, MAE and RMSE for surface temperature for both cases, K.

	MYJ	YSU	QNSE	ACM2	MYJ	YSU	QNSE	ACM2
	Case 2 original surface				Case 2 new surface			
Bias (± 0.5)	-1.10	-0.79	-1.32	-1.12	+0.86	+1.06	+0.74	+0.89
MAE (± 0.5)	1.69	1.86	1.73	1.83	1.00	1.16	0.92	1.04
RMSE (± 0.5)	2.00	2.04	2.05	2.1	1.35	1.55	1.25	1.40

Table 6.2: Table showing the bias, MAE and RMSE for *SHF* and *LHF* for both cases, W m^{-2}.

	MYJ	YSU	QNSE	ACM2	MYJ	YSU	QNSE	ACM2
	SHF							
	Case 2 Old surface				Case 2 New surface			
Bias (±0.01)	+42.4	+48.0	+53.5	+52.0	+65.8	+80.0	+86.19	+87.1
MAE (±0.01)	42.4	48.0	53.5	52.0	65.8	80.0	86.19	87.1
RMSE (±0.01)	43.6	50.4	55.7	54.6	68.1	85.2	90.9	93.4
	LHF							
	Case 2 Old surface				Case 2 New surface			
Bias (±0.004)	+19.0	+18.8	+24.6	+21.9	+31.7	+37.5	+39.0	+43.4
MAE (±0.004)	19.0	18.8	24.6	21.9	31.7	37.5	39.0	43.4
RMSE (±0.004)	19.7	19.5	25.3	22.5	32.8	39.6	40.9	46.4

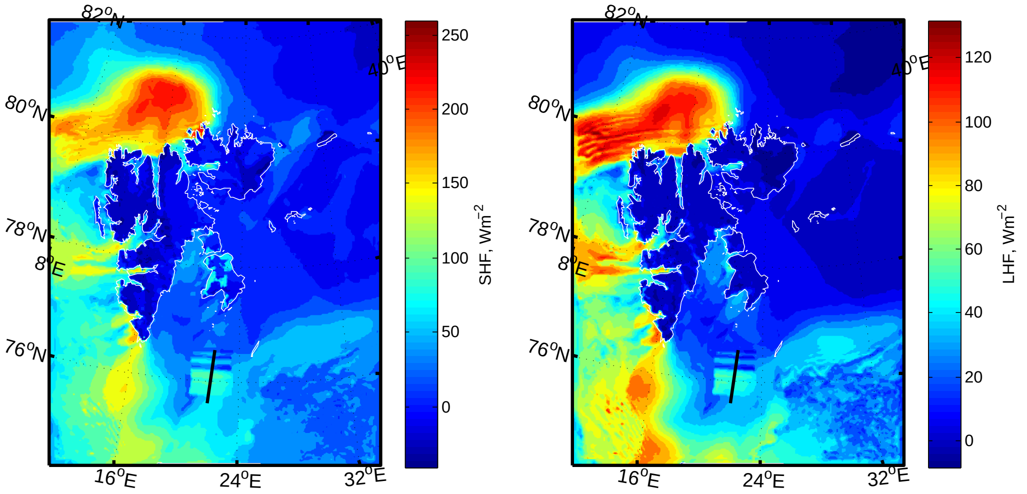

Figure 6.5: *SHF* and *LHF* (W m^{-2})for the inner domain of Case 2 with the MYJ scheme. The black line shows the location of the flight cross-section.

6.2.2 FLUXES

The change in sea ice fraction (Fig. 6.2) has a direct impact on both *SHF* and *LHF* as can be seen in Fig.6.5, with areas of higher fluxes extending either side of the cross section (black line). These fluxes do not reach the values seen further south over open water, perhaps due to the fetch being shorter, but are certainly higher than the fluxes over the unchanged sea ice.

The new sea ice fraction now has much more open water and is therefore warmer than the old surface. This makes the air-surface temperature difference larger and therefore the fluxes much higher for the new surface. Figures 6.6 and 6.7 show the sensible heat flux (*SHF*) and the latent heat flux (*LHF*) respectively. In Figs. 6.6 and 6.7 it can be seen that the heat fluxes are directly responding to the warmer surface caused by the changes in sea ice fraction, with higher fluxes where there is more open water. The biggest spread in surface flux values is over the water and as the flux for the open water is provided by the surface layer schemes the differences in surface layer parametrisation can be seen. Over the water there is a large spread in surface heat fluxes, the ACM2 gives the highest SHF and LHF by 48 Wm^{-2} and 28 Wm^{-2} (respectively) when compared to the MYJ. Whereas with the old surface the QNSE had the highest surface flux values (Figs. 5.7 and 5.9), where the QNSE was only higher by 11 Wm^{-2} and 5.5 Wm^{-2}. Over the areas with medium ice fraction the QNSE is able to provide the highest flux (+17.5 Wm^{-2} and +11.41 Wm^{-2} over the MYJ), as it did with the old surface, while the MYJ remains the lowest. Over the higher ice fractions the different parametrisations are close together, though with the QNSE slightly higher (7 Wm^{-2} and 5 Wm^{-2} for SHF and LHF).

As the ACM2 is designed for convective situations it is able to produce large fluxes over open water, whereas the YSU which uses the same surface layer scheme provides fluxes that are lower over the open water. With the old surface the QNSE provided the largest surface fluxes, as it is optimised for stable BLs it is prone to over mixing. The MYJ provides the lowest fluxes over open water and as it is the only local scheme in this study, this points to the local closure limiting the amount of SHF and LHF. The differences between the observed and model fluxes (Table 6.2) come from the observations being too low, as discussed in Chapters 4 and 5. The modelled fluxes are now higher, and indeed closer to the average total heat flux of over 100 Wm^{-2} which was found in Chapter 4 to be the amount required to produce the observed warming. The reduction in sea ice fraction has therefore improved the modelled fluxes, which should improve the modelled BL.

Due to the different schemes performing differently over areas with high and low sea ice concentrations, and issues with the observations, it is difficult to establish which is better for the surface fluxes over the MIZ. As with the surface temperature error cancellation plays a part, therefore if spuriously high sea ice concentration is suspected, the QNSE may be the better option for the error cancellation.

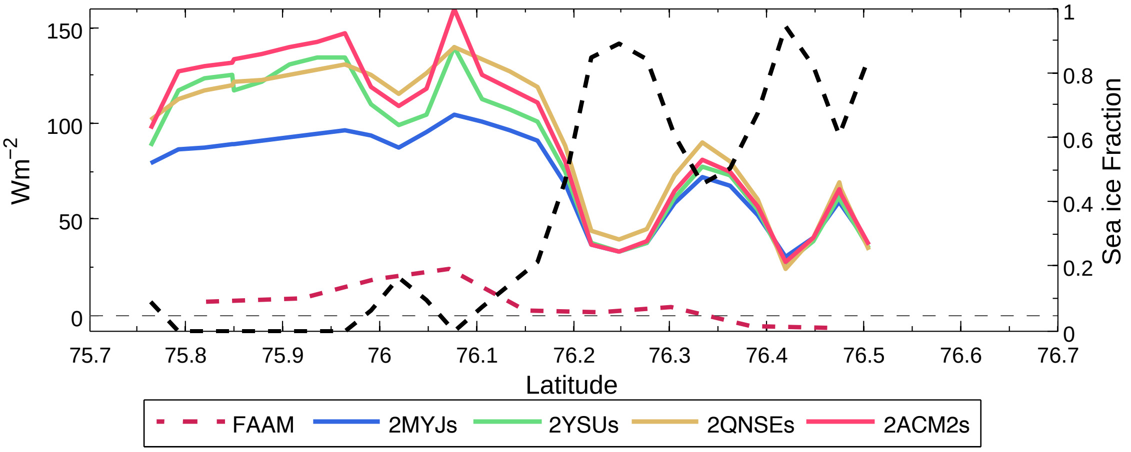

Figure 6.6: The *SHF* for the new surface for the four different BL schemes and the observations. The thick dashed line corresponds to the new sea ice fraction (right axis). The grey dashed line marks zero flux.

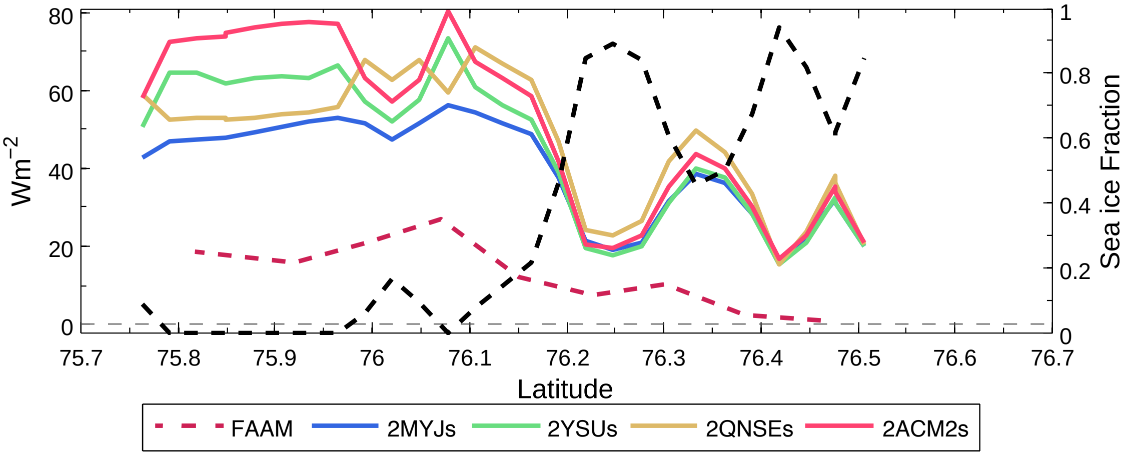

Figure 6.7: The *LHF* for the new surface for the four different BL schemes and the observations. The thick dashed line corresponds to the new sea ice fraction (right axis). The grey dashed line marks zero flux.

6.2.3 BOUNDARY LAYER

With the OSTIA surface conditions the simulated BL height decreased from north to south across the MIZ due to the high sea ice fraction providing a cold surface which did not match the observations (Fig. 5.14). Looking at potential temperature (θ) in Fig.6.8, over the ice the simulated BL is again too deep, and shows little change from the original surface (Fig.5.14) which would be expected as the surface has changed less here. However with the new surface, the simulated BL height increases across the MIZ, most notably for the ACM2 which increased from 396 m to 556 m between the over ice and over water profile. The BL heights for the other schemes increased by much less, the MYJ from 281 m to 284 m and the YSU from 358 m to 361 m. The

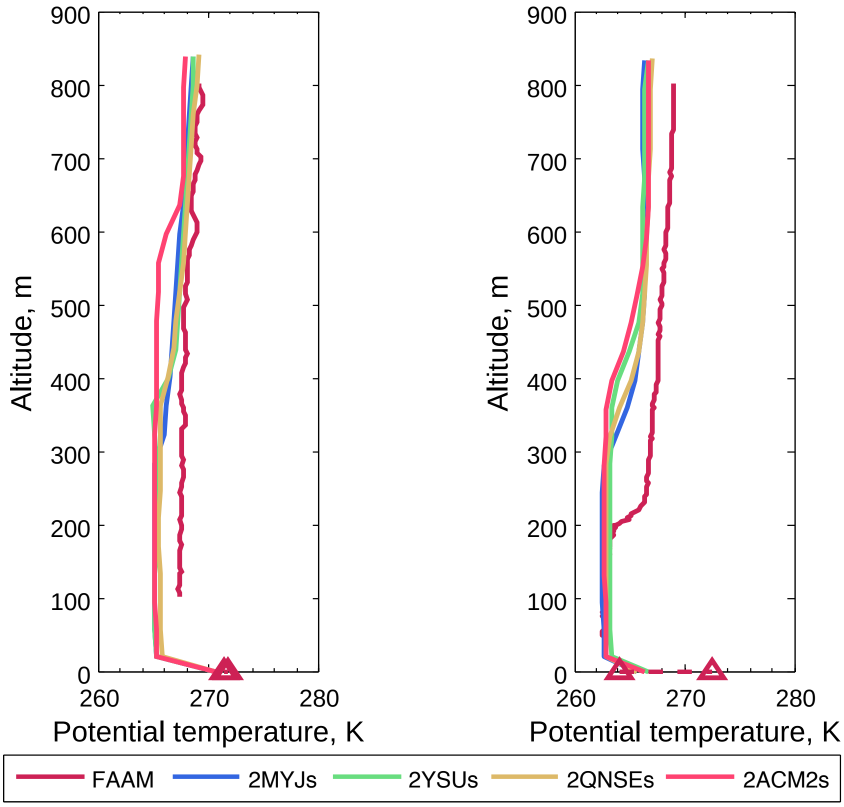

Figure 6.8: Potential temperature θ, K for Case 2 with the new surface. The triangles show the range of measurements for the surface observations.

YSU having a small increase in height is interesting as the YSU is the only scheme with explicit treatment of BL top entrainment, however it is unable to grow as fast as the ACM2 which seems best suited to responding rapidly to a change in surface forcing.

The simulated mixed layer temperature over the ice shows good agreement with the observations for the new surface, along with the surface value for θ being closer to the observations ($<$ 1 K difference for the new surface compared to $>$ 2 K for the old surface, with an error of ± 0.4 K). However the warmer surface has not translated into the mixed layer warming up at the same latitude as the observations, despite the simulated fluxes being so high. The cross section in Fig.6.9 shows that the mixed layer is warming faster than for the old surface shown in Fig.5.16. As the modelled atmosphere above the BL is 2 K too cold, this means there is not enough warm air to mix down. This colder air above the BL was seen with the old surface and was attributed to a problem with forcing data. Now the model has more open water the mixed layer temperatures over water have smaller spread, and are warmer (spread 1.1 K original surface, 0.4 K new). The temperatures are also warmer by up to 1.3 K, with the QNSE being warmest over the open water.

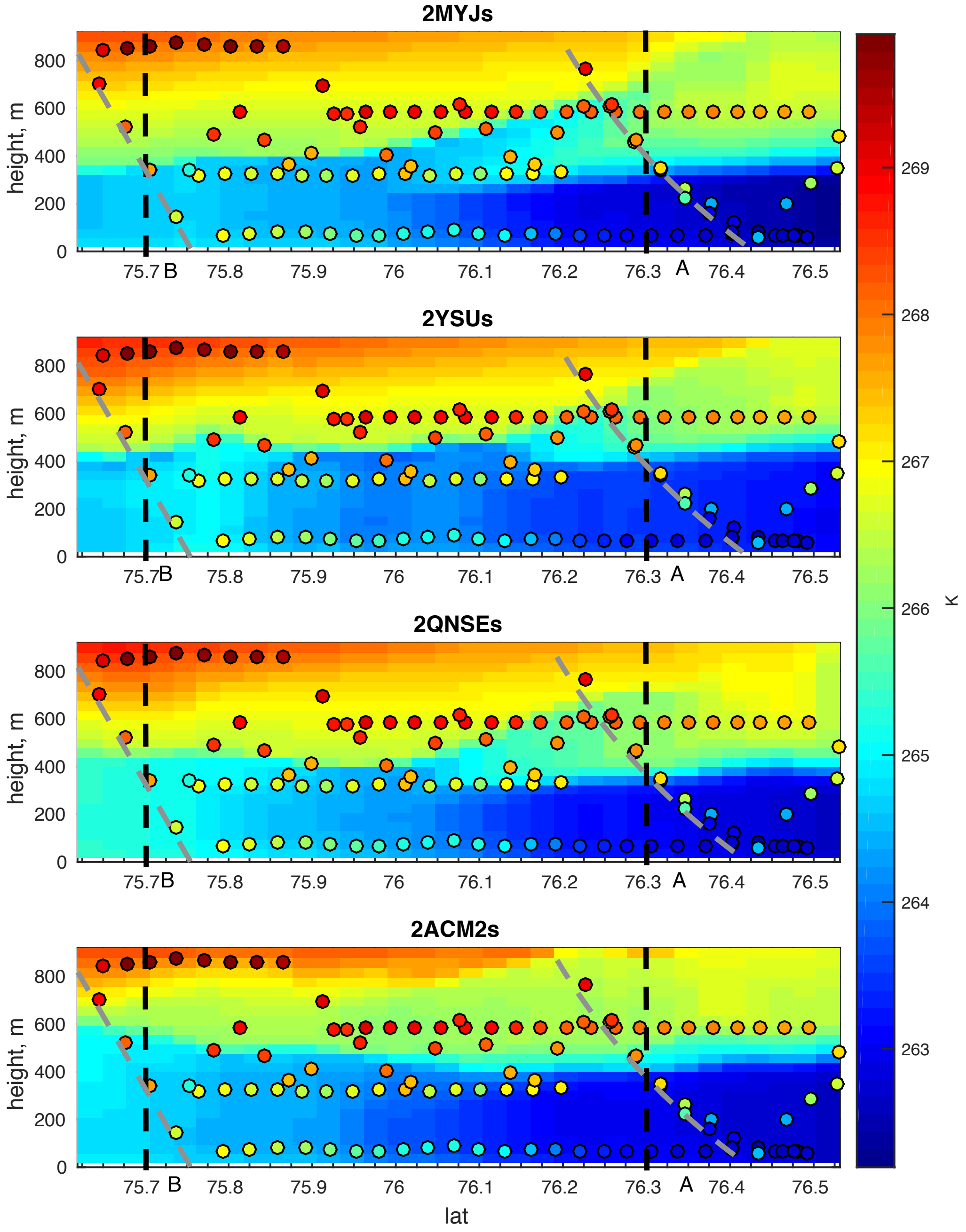

Figure 6.9: θ for Case 2 with the new surface, K.The observations are the coloured dots, while the modelled values are in the background for all the different BL schemes. The northern end of the cross section is on the right hand side. The black lines marked A and B indicate the location of the modelled profiles, while the grey lines indicate the true profile which was used from the observations.

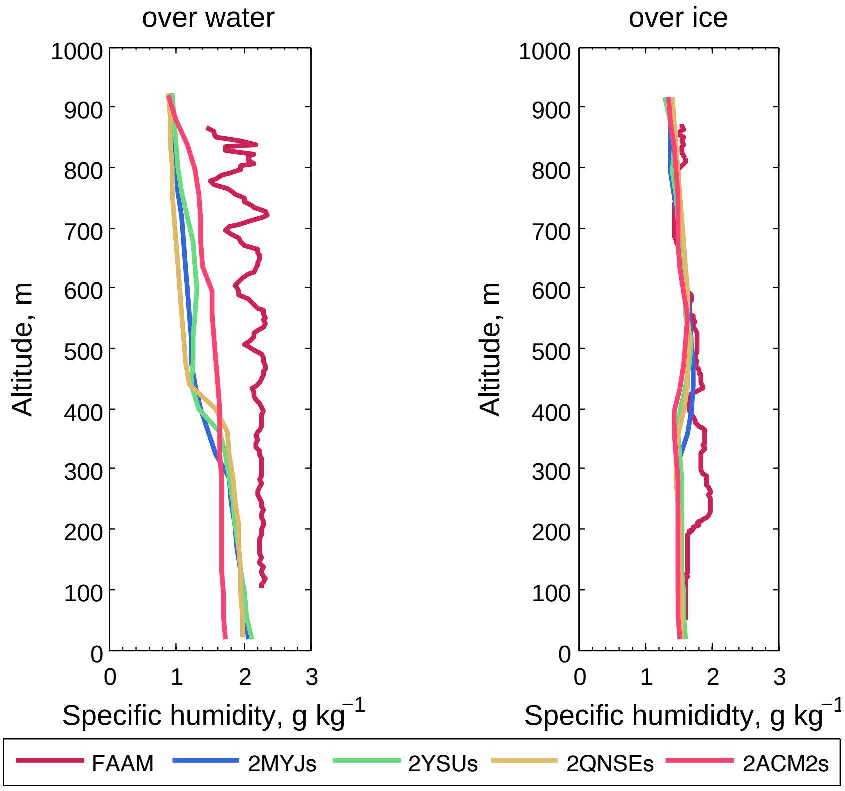

Figure 6.10: Specific humidity, q for Case 2 with the new surface, g kg^{-1}.

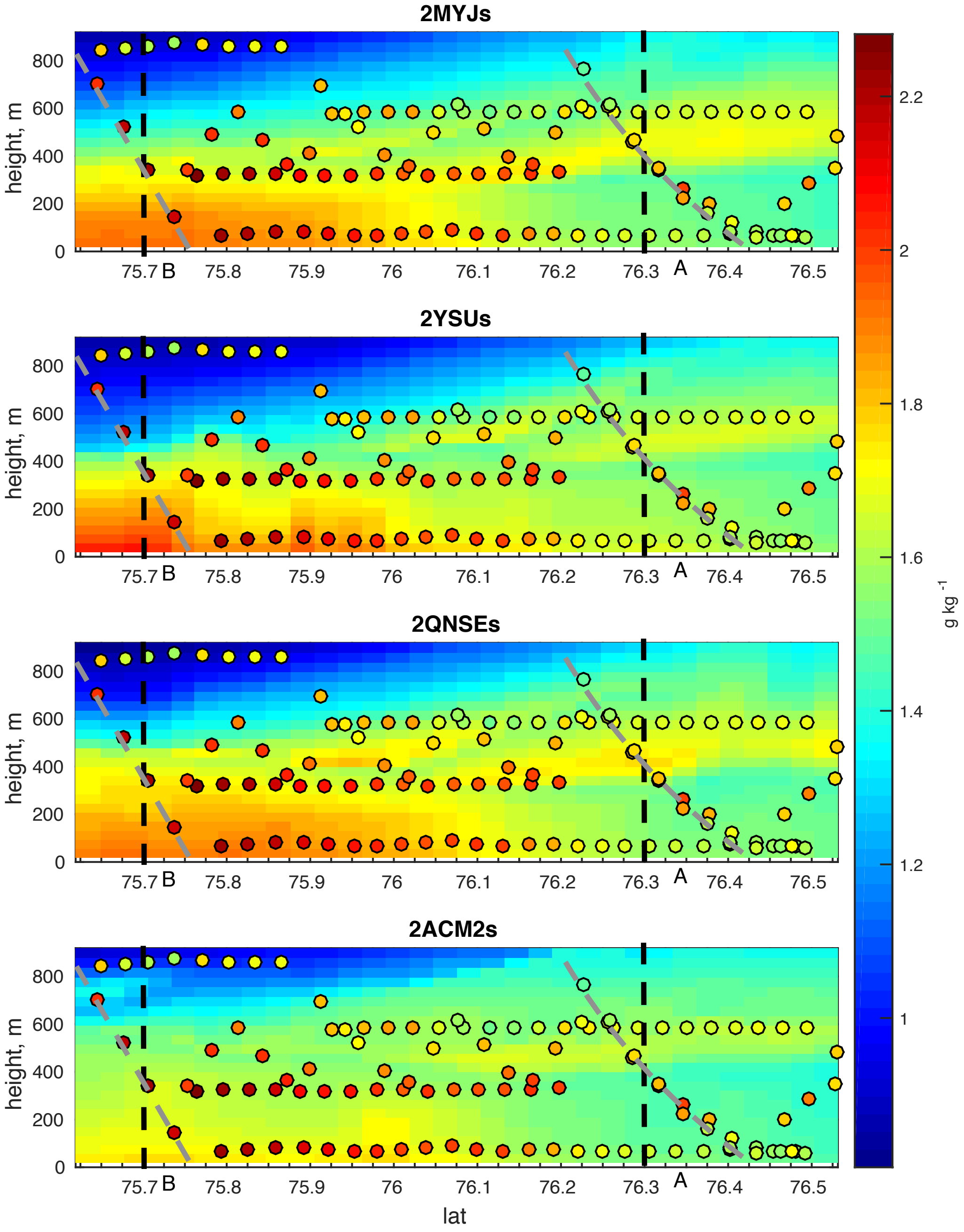

Figure 6.11: q for Case 2 with the new surface, g kg^{-1}.. The observations are the coloured dots, while the modelled values are in the background for all the different BL schemes. The northern end of the cross section is on the right hand side. The black lines marked A and B indicate the location of the modelled profiles, while the grey lines indicate the true profile which was used from the observations.

The specific humidity (q) profiles are shown in Fig. 6.10. Over the ice the q profile shows generally good agreement at the surface and above the BL, while over water the model profiles have too little q. Over the ice the drier internal BL extends too high into the atmosphere, which follows from the internal BL height being too large in θ. The moisture representation at the surface is improved from the original surface having increased by 1 - 2 g kg^{-1} as now the surface has more moisture available due to the reduced sea ice cover. The YSU has the lowest bias at the bottom of the column, with only +0.1 g kg^{-1}. Above the BL the observations are within the model spread, though the observations begin to become more moist above 800 m whereas the model does not show this.

For over the water the bottom of the observed BL value has increased by 0.69 g kg^{-1} between the two profiles, showing the surface has been a source of moisture for the BL, and the air above has also become more moist. This can also be seen in the cross section in Fig.6.11, where the specific humidity starts to increase below 300 m at about 76N. In the model the YSU again has the best surface value, with a -1.7 g kg^{-1} bias at the surface. The bias has reduced from that for the old surface. The QNSE and ACM2 have increased bias for the surface value, compared to the previous surface (QNSE old surface 2.05 g kg^{-1} new surface, 1.99 g kg^{-1}, ACM2 1.91 g kg^{-1} and 1.73 g kg^{-1} for the old and new surface respectively). The QNSE despite having the higher θ value in the mixed layer has the lowest value of q, whereas the surface value for the ACM2 also increased the least over cross-section, As the ACM2 has the highest q values further up in the BL, the surface value may be reduced due to too much mixing upwards.

Above about 400 m the modelled atmosphere dries out compared to the surface by up to 0.5 g kg^{-1}. In the observations the BL top is much higher, with the whole of this air column being coupled to the surface, this means the whole column is at approximately the same specific humidity. As the model BL height does not change as much, the moisture from the surface is unable to penetrate upwards, the ACM2 is the only scheme which is able to do this as it is the only scheme with an increase in BL height. This results in the ACM2 having the best q above 400 m, with a -0.6 g kg^{-1} bias.

The best scheme for the BL depends on what feature it is essential to capture. The ACM2 is best at capturing the change in BL height caused by the change in surface, but still does not manage to change as fast as the observations. The MYJ is giving the ‘best’ BL height over the ice, as it has the lowest value, however it is still far too high. The mixed layer and surface values are good for θ with all the schemes over the ice, though as no scheme can properly simulate the warming of the internal BL no scheme is good. The change in the surface caused the surface temperature values to be better, and the surface moisture values to be better. This implies that the surface representation is more important than choice of BL scheme.

6.2.4 CLOUDS

The liquid water mixing ratio Q_{LW} and the ice water mixing ratio Q_{IW} are shown in Figs. 6.12 and 6.13. In the QNSE and ACM2 plots, the impact of increased BL height compared to the OSTIA surface can be seen, with the Q_{LW} and Q_{IW} (i.e the modelled clouds) now higher, extending up to 600 m for the ACM2, at the southern end of the cross section (around 75.7 °N) when compared to Figs. 5.24 and 5.25. The new surface acts to reduce the maximum Q_{LW} for all the schemes by up to 0.11 g kg^{-1} except the QNSE where the maximum value has increased by 0.9 g kg^{-1} which can be seen at 400 m and 75.84 °N . Qualitatively the new surface looks to have provided better clouds for the ACM2 showing the best increase in cloud height and removing some of the sweep of cloud, while the extra Q_{LW} in the QNSE makes it qualitatively the worst.

As for Q_{LW} the Q_{IW} has reduced for the MYJ and YSU by over 1.4 $\times 10^{-4}$ g kg^{-1}, while it has increased for the QNSE by 3.4 $\times 10^{-4}$ g kg^{-1} at 75.7 °N. Unlike the Q_{LW} the ACM2 also shows an increase in Q_{IW} but only by 0.3 $\times 10^{-4}$ g kg^{-1} between 75.8 °N and 75.9 °N. The increasing BL height is evident in both the QNSE and ACM2, with Q_{IW} now extending up to 600 m for the ACM2, and 500 m for the QNSE. Again the ACM2 is qualitatively the best at cloud, having the combination of increasing height and low enough concentrations.

The new surface has impacted the clouds, with increasing cloud heights, but also reducing the amount of frozen and liquid water. This is similar to what was seen in Chapter 3 where the warmer surface caused there to be increased precipitation and thus reduced the Q_{LW} and Q_{IW} . With the improvement to the surface, the ACM2 now gives the best cloud, when considered qualitatively. The QNSE has the highest values of both Q_{LW} and Q_{IW} with the new surface, which it does not have with the

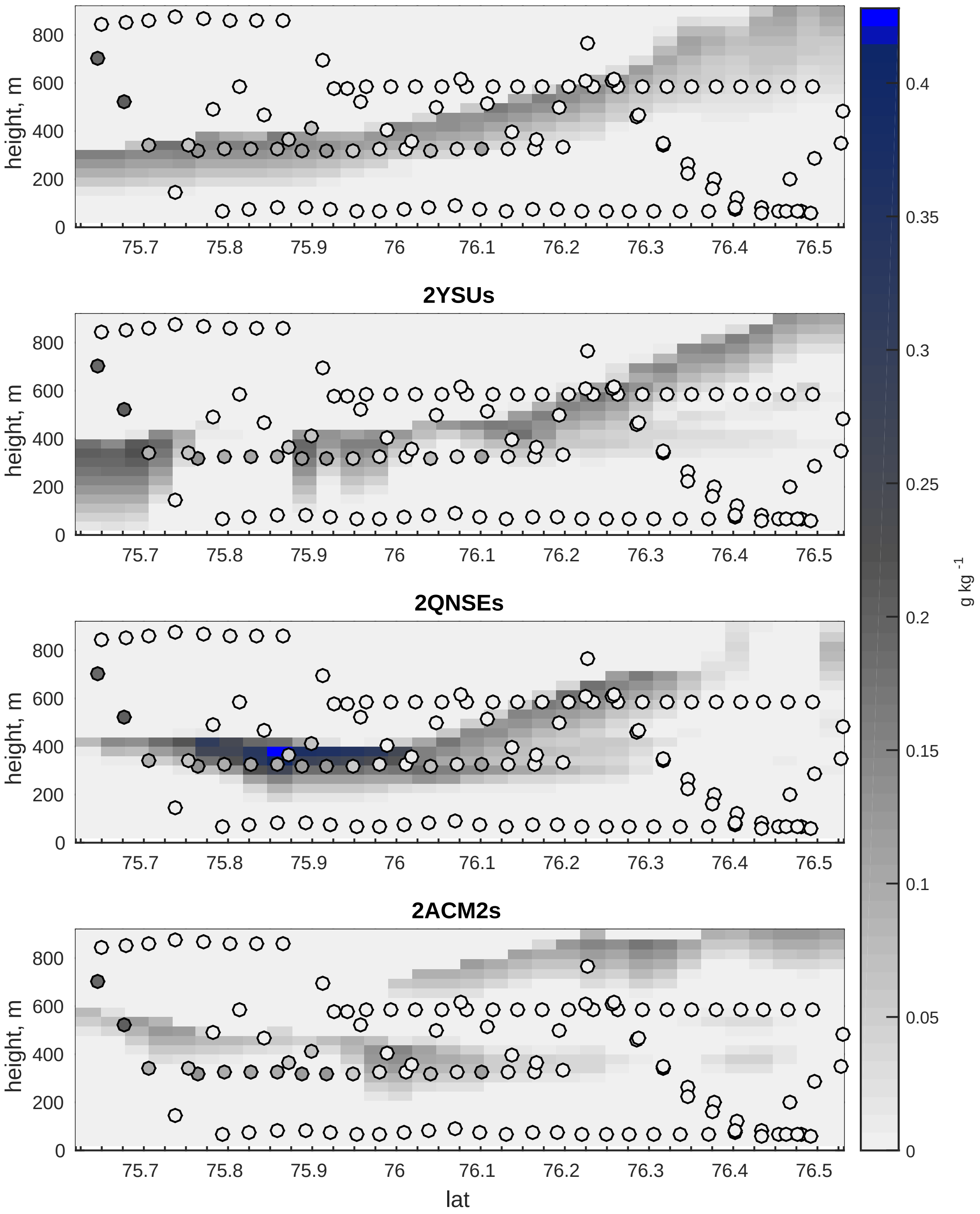

Figure 6.12: Q_{LW} for Case 2 with the new surface, g kg^{-1}, the coloured dots are the aircraft observations, and the surface is the model output. A minimum threshold of 1×10^{-3} g kg^{-1} is applied, with anything below being white. The northern end of the cross section is at the right hand side.

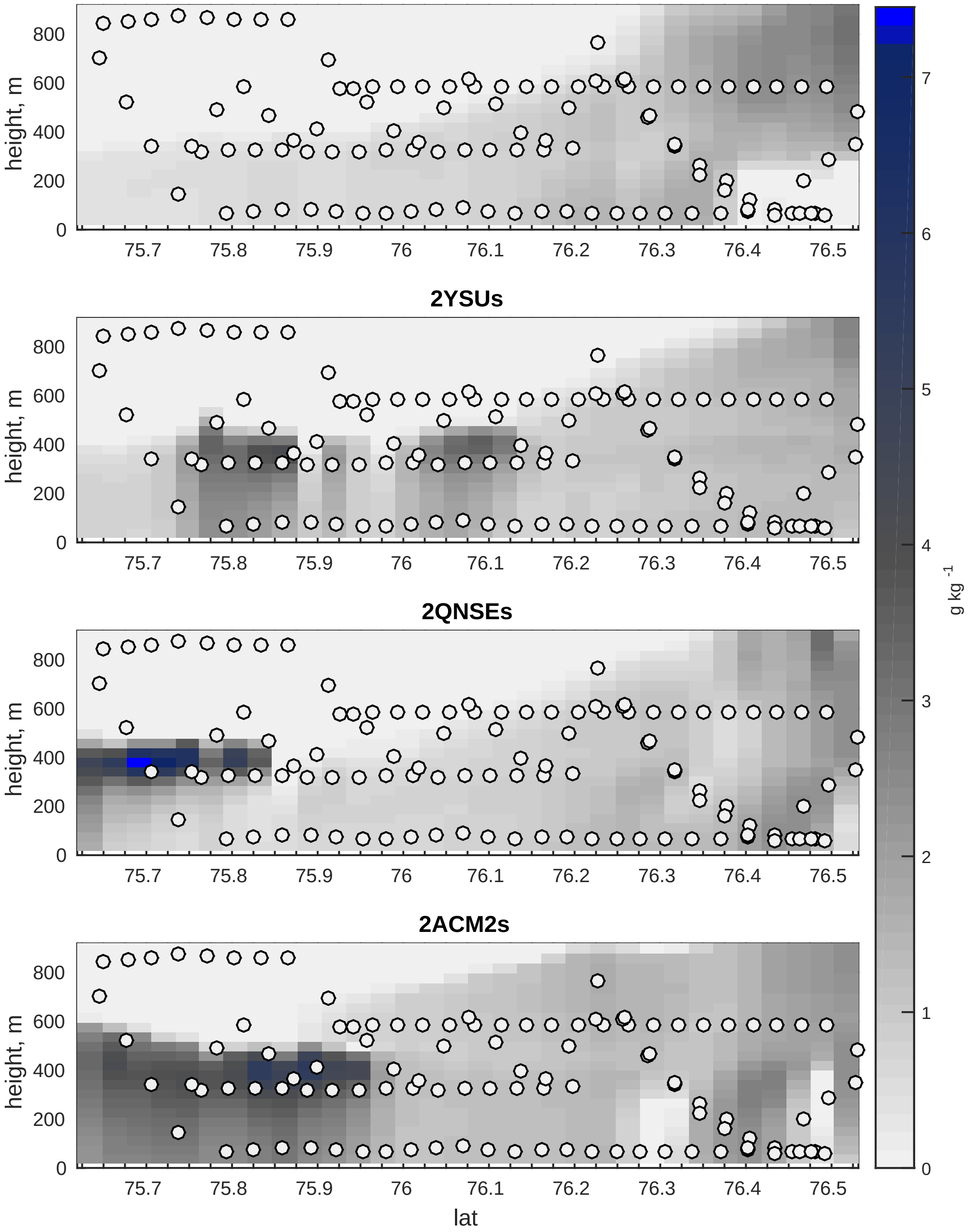

Figure 6.13: Q_{IW} for Case 2 with the new surface, g kg^{-1}, the coloured dots are the aircraft observations, and the surface is the model output. A minimum threshold of 1×10^{-7} g kg^{-1} is applied, with anything below being white. The northern end of the cross section is at the right hand side.

old surface. This is because the new surface is much more moist and the BL more unstable, causing the QNSE to over-do the provision of moisture as it is being applied in a situation it was not designed for.

6.3 DECREASING ICE THICKNESS

It was shown using idealised modelling in Chapter 3 that decreasing the thickness of the ice is important for the representation of the clouds. With thinner ice, the clouds formed further north, and showed an enhanced rate of snow production, resulting in thinner clouds which provide less shading to the surface. It would be instructive to repeat a variable sea ice thickness experiment here in a realistic situation. While the introduction of more realistic ice concentration above has shown changes in surface temperature, fluxes and clouds, further improving the representation of the sea ice could be achieved by using variable ice thickness. Using the same sea ice fraction as in the previous experiments in this chapter, a variable ice thickness was implemented using thresholds based on ice fraction. The ice thickness I_t in meters, chosen based on the ice faction I_f were given by,

$$I_t = \begin{cases} 0 & I_f = 0 \\ 0.5 & 0 < I_f \leq 0.1 \\ 1 & 0 < I_f \leq 0.5 \\ 2 & I_f > 0.5 \end{cases} \tag{6.1}$$

The thresholds were informed by the WMO sea ice nomencalture document (JCOMM, 2014) and Cryosat data (cpo, n.d.). The 0.5 m thick sea ice corresponds to thin first year ice, and 1 m corresponds to typical first year ice, the thickest ice was set at 2 m, which was the average over this area for the duration of the campaign according to cryosat.

The ice thickness is shown in Fig. 6.14, it can be seen that the thicker ice is further from the ice edge, with the cross section (marked in black) taking place over the full range of ice thickness values.

The thinner ice had little impact on the near surface variables. Surface temperature was unchanged apart from a < 1K change where the sea ice fraction is

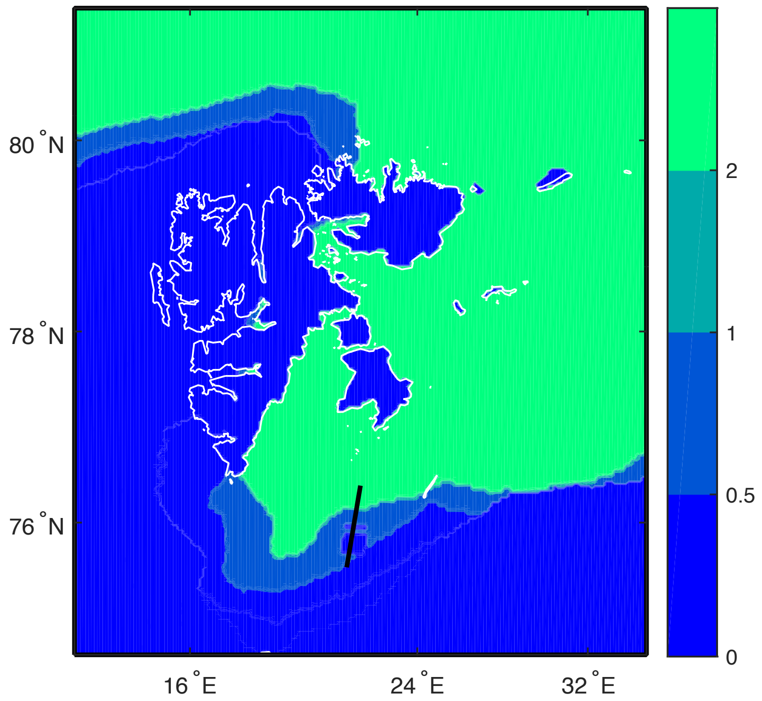

Figure 6.14: The variable ice thickness for case 2 (m), the colours correspond to the four possible thickness values, 0 m for no ice, 0.5 m corresponding to thin new year ice, 1 m (of which there is very little) corresponding to first year ice and 2 m for older ice. The location of the cross section is marked in black.

< 0.5 (not shown). This was expected as the area of the cross section had large areas of open water. The *SHF* shows a maximum increase of 5 Wm^{-2} off the ice edge, while *LHF* shows an increase by up to 1 Wm^{-2} off ice. As there is a large amount of open water in the area of the cross section, the differences in the surface variables were expected to be small. Larger differences were seen in the cloud variables, as there is more scope for upwind changes to ice thickness to affect the clouds. Fig. 6.15 shows the Q_{LW} for the four different BL schemes. Comparing Fig. 6.15 with Fig. 6.12, the most obvious difference is for the QNSE, which shows less area with the maximum concentration (0.44 g kg^{-1}) at 400 m high and 76.95 °N. The amount of Q_{LW} has changed slightly for all the schemes, for the MYJ there has been a slight increase in mean Q_{LW} compared to 2MYJs by 3.6×10^{-3} g kg^{-1}, while for the YSU, QNSE and ACM2 there has been a reduction in Q_{LW} by 6.5×10^{-3} g kg^{-1}, 5.3×10^{-3} g kg^{-1} and 1×10^{-3} g kg^{-1}. The reduction in Q_{LW} was also seen in Chapter 3 and was attributed to the moisture being brought from the surface earlier, and having more time to become frozen and precipitate out.

The Q_{IW} also changes in response to the new surface, comparing Fig. 6.16 and Fig. 6.13 it can be seen there are more areas with darker blue colours. All the schemes show an increase in mean Q_{IW}, with the mean value for the QNSE increasing by 1.9×10^{-5} g kg^{-1}, the mean value for the YSU increasing by 1.6×10^{-5} g kg^{-1}, and for the ACM2 the mean increases by 1.3×10^{-5} g kg^{-1}. The mean value for the MYJ increases by the smallest amount, 2.5×10^{-6} g kg^{-1}. The MYJ having the smallest increase in Q_{IW}, explains why the MYJ has more Q_{LW} compared to the other schemes as less has been converted to ice. The MYJ is a local scheme, so will be less affected by the widespread change in surface temperature. This means the earlier increase in moisture provision to the clouds, which was hypothesised to happen in Chapter 3, does not happen as fast for the MYJ, meaning that after the same amount of time has passed for the air mass, the water has not been in the cloud as long and has not begun being converted into ice. In Chapter 3 the Q_{IW} was found to decrease with thinner ice, though this was dependent on distance from the MIZ, with the more complicated situation here which is three-dimensional the distances from the ice edge are harder to establish.

The experiment with thinner ice was done to see if further changes to make the modelled sea ice more like that observed would improve the representation of the BL and clouds in the model. In Chapter 3 five different idealised experiments were discussed, where the thickness of the sea ice within the MIZ was decreased. It was seen that surface temperature and fluxes increased when the ice was thinner, and this led to an increased mixed layer depth. The thinner experiments had a higher moisture flux, which lead to clouds forming further north. The clouds then lost liquid content as snow formed, and became thinner due to the subsequent sedimentation of the snow. In this experiment, little impact was seen on the surface temperature or fluxes, due to the large amount of open water where the cross section was situated. However the clouds were affected, as they are more dependent on upstream conditions. Like in the idealised experiments, there was a reduction in Q_{LW}, however there was also a reduction in Q_{IW}. This is due to the more complicated situation, where distances from the ice edge are less clear-cut, and with the thickness being variable. Changing the sea ice thickness in the three dimensional model does have an impact on the clouds, which are important for the radiative balance. The inclusion of a variable sea ice thickness should be further investigated.

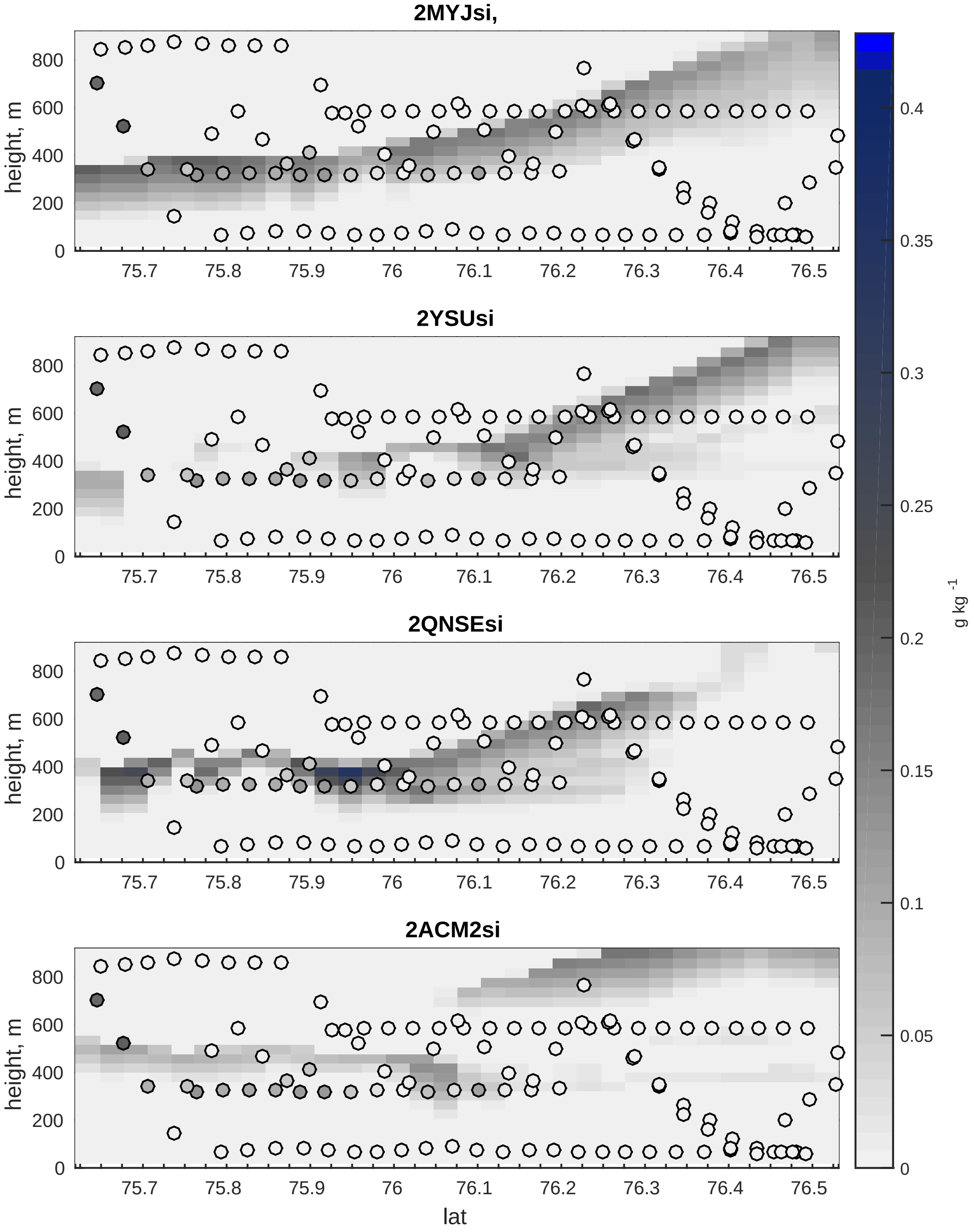

Figure 6.15: *LWC* for Case 2 with variable ice thickness, g kg^{-1}, the aircraft observations are coloured circles, while the model output is in the background. A minimum threshold of 1×10^{-3} g kg^{-1} is applied, with anything below being white. The northernmost end is to the right.

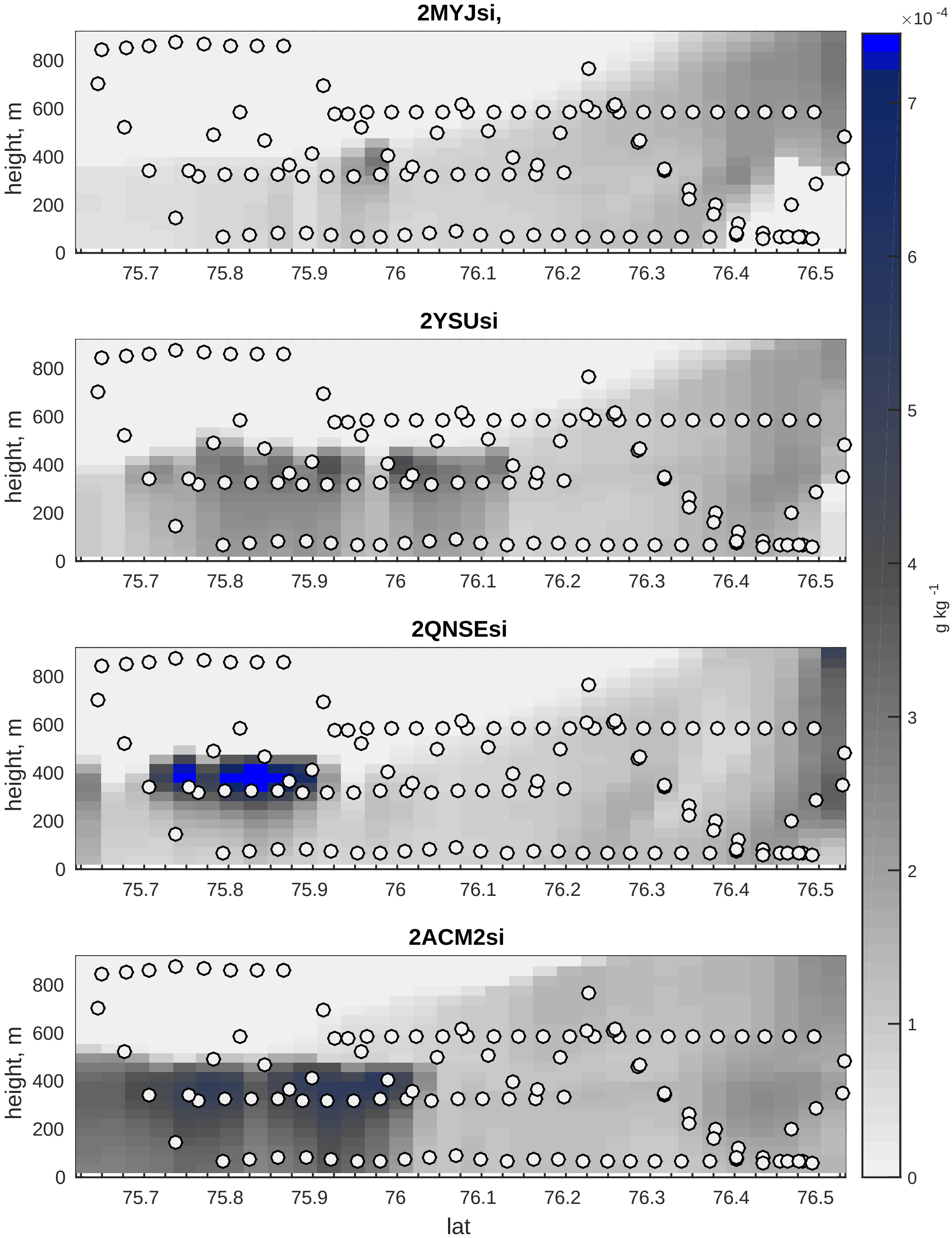

Figure 6.16: *FWC* for Case 2 with variable ice thickness g kg^{-1}, the aircraft observations are coloured circles, while the model output is in the background. A minimum threshold of 1×10^{-7} g kg^{-1} is applied, with anything below being white. The northernmost end is to the right.

6.4 DISCUSSION

The surface representation in the Arctic is important, with other studies showing temperature biases due to albedo problems (Pinto *et al.*, 2003), problems with fluxes (Rinke *et al.*, 2006), changes in cloud fraction (Palm *et al.*, 2010) and convection (Liu *et al.*, 2006). This chapter examined the sensitivity to sea ice cover over the MIZ, using Case 2 which has been discussed in Chapters 4 and 5. The sea ice cover was changed to better match that observed from the aircraft during Case 2. This resulted in a much lower sea ice concentration to the south of the domain, as the OSTIA sea ice estimate was too high.

The surface temperatures were improved, especially as the open water is now in both the observations and the model. However there is now a slight warm bias, as while the surface was dark and warm in the observations, it is not totally ice free as has been specified here. However as the model does not have a capacity for dealing with different regimes of ice such as the close ice seen here, it would be expected that the surface temperature might be too high. The model still does not include the lead seen near 76.25 °N, however the response to the leads it does have are evident as increased T_{sfc} variability across the cross section. The temperature is particularly improved over the transition zone. Again higher ice concentrations have a larger spread between the schemes, with the YSU being warmest. Which BL parametrisation scheme was best seems to be a product of error cancellation, with the scheme with the highest temperature (YSU) having the highest temperature for both the old and new surface, and the opposite being true for the QNSE, though now the QNSE has the lowest rather than the highest bias in T_{sfc}.

As the surface temperature has increased, the surface fluxes of heat are also higher. The biggest spread between the schemes occurs over the water, where the individual surface layer schemes are applied. The MYJ has the lowest flux, while the ACM2 the highest. The QNSE is the highest over ice as it is best at mixing in more stable situations. The fluxes are more varied due to the presence of a more complex surface, which is good. However again the lack of different types of sea ice may be causing them to be too high. As with the fluxes in Chapter 5, there are problems with comparing aircraft to surface fluxes. Indeed as the model fluxes are higher, but unable to produce the warming in the BL seen in the observations, it could be concluded by looking at the ΔT and wind speed, that the observed fluxes are too low over the ice.

The increased fluxes do increase the BL height, whereas with the previous surface the BL height decreased across the cross section. The ACM2, being designed for convective situations is the best at capturing changes in BL height, and the fastest to respond to the surface. The model does have the internal BL being drier than the air above, as this is air being advected from the north. The atmosphere dries out in the model, whereas it is moistening in the observations. The change in surface does improve the moisture in the lowest part of the column for the YSU especially, though the others actually dry out as they are moving this moisture upwards.

The surface has made a change to the clouds, while the śweep' is still visible as in the previous experiments, the effect of the higher BL can be seen in the ACM2 with the cloud being higher up, matching the observations. The cloud liquid water has reduced for all BL schemes, except the QNSE, and the ice has decreased for the MYJ and YSU, while it has increased for the ACM2 and QNSE. Qualitatively the ACM2 looks best as it has the lowest concentrations, and the increase in BL height. The addition of a variable sea ice thickness also made an impact on the clouds, with slight reductions in Q_{LW} for all the BL schemes apart from the MYJ, and with slight increases in Q_{IW} for all the BL schemes. This change in cloud composition does not improve the representation of clouds compared to the observed values, but does change the cloud composition, which is important for the surface energy balance.

Further changes to the surface by decreasing the thickness of the ice, caused few changes in the area of the cross section, due to the low sea ice fraction present. However the Q_{IW} and Q_{LW} were changed between the 3 m thick sea ice and the variable sea ice thickness experiments. All the BL schemes showed an increase in Q_{IW} with the MYJ having the lowest increase, while all schemes except for the MYJ showed a decrease in Q_{LW}. As clouds are an important feature of the surface energy balance it is important to accurately represent them. However as the observations show lower Q_{IW} than in the experiments, this is not an improvement for this case. More work should be done to ascertain the impact of variable ice thickness on the prediction of Arctic clouds.

It can be concluded that a more accurate surface does give better surface temperatures, BL heights and clouds, though whether the fluxes have improved is difficult to ascertain. The representation of the MIZ in WRF as steadily decreasing sea ice fraction is very different to that observed from the aircraft, as seen in Fig. 6.2. The choice of BL scheme is more difficult, as different schemes are better for different things. The ACM2 seems to produce the best clouds here, as it produces the best combination of BL height change and Q_{LW} and Q_{IW}. The ACM2, while best for BL height does give the highest fluxes, while the MYJ is the lowest. The YSU gives the warmest surface temperature over ice, which might be best as the ice here is probably too thick compared to that in our observations, so the provision of a too high surface temperature would cancel that error. The QNSE however provides the lowest surface temperature over ice, which matches best with our observations.

If a better surface does make an impact even on these short time scales, how much more impact might be made on longer climate length simulations? The sea ice edge was wrong by hundreds of kilometres, well within the grid resolution of climate models. Better satellite algorithms for the detection of thinner darker sea ice are needed, as well as the ability to represent this in the model. A fully coupled sea ice and atmosphere model would be ideal, if the sea ice model provides different ice thickness values and types, and if the atmosphere model can interpret this properly.

7

CONCLUSIONS

This thesis has focussed on the boundary layer of the Arctic marginal ice zone, a region of complex interactions between surface, atmosphere and clouds. Studying the Arctic MIZ is of great importance, as the effects of climate change are felt most there. In Chapter 3 the effect of thinner ice on the atmosphere above in the MIZ was examined via idealised modelling. In Chapter 4 the results of the ACCACIA spring 2013 field campaign were examined to provide the context for modelling case studies in Chapters 5 and 6. The first modelling study in Chapter 5 investigated the sensitivity of the simulation of the BL over the MIZ to the choice of BL parametrisation scheme, and compared the results of the simulation to the observations. Following this, in Chapter 6 the sensitivity of the BL simulation to the sea ice surface was tested, by changing the surface in PWRF to better resemble that observed during the campaign. These investigations have resulted in several conclusions, which are presented below.

7.1 THINNER SEA ICE WOULD RESULT IN A REDUCTION OF SEA ICE EXTENT

In Chapter 3 the sea ice thickness of an idealised MIZ was varied, with the thinnest experiment using a 0.1m thickness setting and the thickest 3m corresponding to young ice and multi year ice respectively. The thinner ice caused the surface temperatures to be higher over the MIZ (cf. Fig. 3.4), by up to 2.9 K for the 0.1 m thick ice (IT0.1) when compared to the 3 m thick ice (IT3). This was due to the increased amounts of heat from the warmer water below which were able to diffuse through the thinner ice faster than the thicker ice. This resulted in the ground heat flux GHF being 56.3 W m^{-2} higher over the MIZ for the IT0.1 experiment compared to the IT3 experiment (cf Fig. 3.5). Due to the increased surface temperature the surface fluxes of sensible and latent heat (SHF and LHF) were increased over the MIZ. In Figs.3.6 and 3.7 it is shown that SHF is up to 45.5 W m^{-2} higher and LHF 16 W m^{-2} higher for IT0.1 compared to IT3. Due to the way the model calculates the surface fluxes as a function of the difference between surface and air temperature (cf. eqns. 3.3 and 3.4), the increased heat fluxes over the MIZ cause the air to warm up faster for the thinner experiments. The increased warming results in a decrease in SHF and LHF further downstream, so that over both the MIZ and the open water the differences in SHF and LHF are very small being less than 1.5% different to IT3 as shown in Table 3.3.

As the boundary layer travelled over the MIZ, a warming and destabilisation was seen (Fig. 3.14) with IT0.1 being slightly (1 K) warmer than IT3. The thinnest experiment IT0.1 also has the highest BL height by 38 m and warms the fastest across the MIZ. This increased warming over the MIZ was found to be driven by flux convergence, so the increased fluxes were increasing the air temperature (cf. Fig. 3.18). For specific humidity, q, IT0.1 increases most across the MIZ increasing by 0.02 g kg^{-1} more than IT3 over the 80 km MIZ. As the BL height increased, drier air was seen to be entrained downwards, with the specific humidity, q profiles showing a slight drying at the top of the BL (cf. Fig. 3.16). The increased heat fluxes and entrainment hint at increased Turbulence Kinetic Energy (TKE) for the thinner experiments. This was shown in Fig. 3.17, where the TKE is highest for IT0.1 at 0.21 m^2 s^{-2} compared to 0.14 m^2 s^{-2} for IT3.

The increased moisture, warmer BL and increased TKE were seen to impact the cloud properties. Clouds formed 4 km closer to the ice edge in IT0.1 compared to IT3. However IT3 had the highest liquid water path, LWP, out of all the experiments at 1.83×10^{-2} kg m^{-2} compared to 1.68×10^{-2} kg m^{-2} for IT0.1 Fig. 3.21. This was attributed to IT0.1 forming snow first and losing mass by precipitation. The clouds in the idealised model were found to shade the surface from the down-welling shortwave radiation, and due to the trade off between the earlier formation of cloud in the thinner experiments, with the thicker cloud in the thicker ice experiments. The biggest shading effect was seen in IT0.5 with a reduction of 28.4 W m^{-2} in incoming solar radiation.

One problem with these experiments was the lack of inclusion of CCN in the cloud microphysics. If CCN were included, the increased turbulent mixing in the BL seen in the thinner experiments would bring more upwards from the surface. This would result in longer lived, more reflective clouds, enhancing this negative feedback during summer (Mauritsen *et al.*, 2011; Lloyd *et al.*, 2015). During autumn and spring, the clouds usually act to warm the surface, as the sun is not as high so the reflectivity of clouds is less important, which has also been neglected here. Overall the thinner sea ice would act to enhance the melting and thinning of ice, with the clouds shading the surface in the summer maybe slowing the melting slightly.

The experiments also do not take into account the changing albedo with the thinner sea ice, or the properties of different kinds of sea ice. A reduction in the albedo of thinner sea ice would be expected to increase the surface temperature as more short wave radiation could be absorbed by the surface. This would enhance the results above giving higher SHF and LHF, higher TKE and following the above, thinner clouds. Different sorts of ice do have different properties, as was discussed in the introduction, with some such as nilas giving a very thin but complete covering of sea ice which is matt and dark, having very different properties to 100% sea ice cover as assumed by the model currently. Experiments where the model too has very thin, dark, 100% sea ice cover would be interesting, but the handling of surface fluxes over the ice would have to be changed.

7.2 COMPARISONS OF AIRCRAFT DERIVED FLUXES WITH MODELLED FLUXES ARE DIFFICULT

In Chapters 5 and 6 the modelled fluxes were seen to be consistently overestimated in the model. This could be attributed to problems with the model, the aircraft measurements not being representative or a combination of the two.

This was investigated in Chapter 5, with a combination of idealised modelling and observations. Using the idealised experiments from Chapter 3 an argument for the observed fluxes being not high enough to provide the observed warming in the boundary layer was made. It was found that to produce a BL warming of 4.7 K over the MIZ in the idealised model, a total heat flux of 185 W m^{-2} was required over the MIZ. The warming in the observations was very similar to that seen in the idealised model, implying that the fluxes (if they are the largest source of heating) should be larger in the observations. An argument was made that the aircraft could have been flying too high to capture the fluxes due to the presence of shallow boundary layers and possible multiple inversions as have been seen in the Arctic.

The model parametrisations may not be performing well for these cases where the surface is complicated. To show this the wind speed and the difference between surface and air temperatures were compared between the model and observations. The model is able to produce fluxes which are too high, despite the windspeed being lower and the temperature difference implying a more stable BL. This does show that the parametrisation may be able to over-predict the fluxes. Another argument was made using an eddy covariance flux calculation from the idealised model. As WRF does not output fluxes on model levels, a turbulent flux was calculated for the altitude of the aircraft. The results were smaller than those for the observations, which would be expected as the 1 km resolution of the idealised model can only capture the largest eddies. This could be taken to imply that the aircraft was also only picking up larger eddies and had missed some of the turbulence that the parametrisations were able to provide, or that the parametrisations are providing values which are too high.

It is impossible with the data available to draw a firm conclusion about whether the model or the aircraft is providing fluxes which are not representative of the real fluxes. This causes a problem, as the surface heat fluxes are said to be a very important feature of the Arctic energy balance (Andreas *et al.*, 1979), so if the values are very low in this case then this is interesting, or if the observations were not representative then better strategies need to be employed. More dropsondes could be employed, to establish the structure of the BL, and surface measurements could be used to compare with models. Other studies which have employed aircraft have used other flight patterns, such as Tetzlaff *et al.* (2015) where it was recommended that the aircraft fly parallel to the ice edge when measuring fluxes, as this allows the aircraft to stay within the convective plume being created by a lead. The sensible heat fluxes derived from parallel flight legs was higher than that calculated by perpendicular runs.

As the MIZ is very variable, and can have very thin ice, placing instruments on the ice would be very difficult, unless they could float. A possible approach could be to make use of drones or other remote controlled tools such as the Small Unmanned Meteorological Observer, a remote controlled aeroplane which has been fitted with instruments (Mayer *et al.*, 2012). These tools would have an advantage over aircraft as they can fly very low and make more intensive observations over a smaller area due to their smaller size and slower speed.

7.3 PWRF SKILL IS NOT DEPENDENT ON BL PARAMETRISATION

In Chapter 5 a series of sensitivity tests were carried out using PWRF and comparing against observations from the two cases in Chapter 4. The sensitivity tests aimed to establish if there was an optimal BL parametrisation scheme to use over the MIZ. The schemes tested were the MYJ, YSU, QNSE and ACM2. It was found that all the schemes performed similarly, however they performed better for Case 1 than Case 2. In Chapter 4 the two cases were introduced and discussed, it was shown that while both showed a convective internal boundary layer (CIBL) being formed and a BL transition over the MIZ where the BL becomes warmer, Case 1 was drier, colder and less cloudy than Case 2 which also had a much more dramatic change in the BL over the MIZ.

The sensitivity tests in Chapter 5 showed that for surface temperature the model gave values which were in general too high for Case 1 and too cold for Case 2, with biases of +1.9(± 0.3) K and -1.3(± 0.3) K respectively respectively (cf. Fig. 5.3 and 5.4), with the modelled temperatures being similar between the two cases, due to its dependence on the sea ice cover.

Despite the surface temperatures having biases with opposite signs, the surface fluxes of latent and sensible heat are over estimated for both cases. In Table 5.5 the bias, MAE and RMSE are shown for the SHF and LHF for both Cases 1 and 2. In general the model overestimated the SHF by more than the LHF. The MYJ produced the lowest flux values for SHF for both Cases 1 and 2, resulting in the lowest bias. For LHF the MYJ again had the lowest bias at +15.2 W m^{-2} for Case 1 (which is the lowest bias overall), and the YSU had the lowest for Case 2. The highest bias, and thus the highest flux for SHF, was given by the ACM2 for Case 1 (bias +57.0 W m^{-2}) , and the QNSE for Case 2 (bias +53.5 W m^{-2}). Similarly for LHF the QNSE gave the highest flux for both Case 1, with a bias of +22.7 W m^{-2} and for Case 2 with a bias of 24.6 W m^{-2}. The MYJ was the only local closure scheme tested here, and so as the other schemes can simulate the non-local turbulence as well, it is no surprise it provides the lowest flux. The QNSE has been developed for stably stratified turbulence, so in a more turbulent environment such as over the MIZ, it may well be over predicting the fluxes. The ACM2 was designed for convective boundary layers so it might also be more able to react to the change in surface temperature and provide higher fluxes.

The profiles of θ and q were investigated. They showed that for Case 1, the BL height and mixed layer temperature were well represented, despite the apparent problem with the fluxes. The free atmosphere however had θ 2.7 K lower than the observations for all the runs, as can be seen in Fig. 5.13. For Case 2 the model gave a θ inversion which was too high by up to 200 m for the YSU and ACM2. Over the ice the θ profile showed a good agreement with the mixed layer temperature, though over the open water the model had failed to warm the mixed layer enough (cf. Fig. 5.14). The BL height for Case 2 actually decreases in the model, as opposed to the observations. The q profiles for Case 1 are also better than for Case 2. Over the water the model is too dry by up to 0.54 g kg^{-1} with the MYJ the driest, and the QNSE the wettest. Over the water the mixed layer is well represented again, though the reduction in q is slightly too high in the model, the free atmosphere is too moist, with a +0.4 g kg^{-1} bias, with the MYJ the driest and the QNSE the wettest (cf. Fig. 5.17). In general Case 2 is more moist. Over water the model is unable to capture this and is too dry. The QNSE being the more moist corresponds to it being the most efficient at mixing moisture up from the surface, as it is designed for turbulence in stably stratified situations (cf. Fig. 5.18). Case 1, being drier and with a less dramatic change in BL profiles than Case 2 is better simulated, pointing to there being some situations in which PWRF may have more skill.

For the clouds, Case 1 has little in the observations of Q_{LW} or Q_{IW}, and the model reflects this. This lack of cloud may be what is allowing the model to perform better for Case 1 than Case 2. Case 2 which was observed to form cloud to the south of the cross section, which increased in height with increasing BL height, does have cloud in the model. However the modelled cloud has a larger extent than that seen in the observations and the cloud height decreases with the decreasing BL height. The QNSE, being the most moist has the highest values for Q_{LW} (cf. Fig. 5.24). For Q_{IW} the model overestimates the amount of cloud ice present, with the QNSE giving the lowest values (cf. Fig. 5.25).

The results of Chapter 5 showed that all the parametrisations performed similarly. The surface temperatures were oppositely biased between the two cases, implying a problem with the sea ice cover as the modelled temperatures were similar. Despite the sign for the surface temperature bias being different, all the schemes overestimate the SHF and LHF. It was found that the MYJ being a local scheme, in general provided the lowest bias, while the QNSE provided the highest, as it is more efficient at mixing being designed for turbulence in stable BLs. Despite the fluxes being so overestimated, for Case 1, the BL depth and mixed layer temperature were well simulated, showing that in this situation the model is able to capture a transition from over ice to over water and increase the BL height. However the change in Case 1 was less dramatic than that in Case 2, which the model could not simulate.

These results imply that there may be situations in which PWRF performs better, with the lack of cloud in Case 1 possibly allowing PWRF to better simulate the BL, which also had a slower change across the MIZ. A larger examination of more cases would help point to whether WRF has more skill in cloud free cases than in those with clouds. The similar performance of all the schemes points to these not being the most important factor in the representation of the BL. The other difference between the two cases is that the surface temperatures are underestimated for Case 2. This points to there being a problem with the surface representation.

7.4 SATELLITE OBSERVATIONS OF SEA ICE CAN BE INACCURATE

As the sea ice surface is so important in the Arctic, detection of sea ice cover and the treatment of it in models needs to be accurate. In Chapter 5 problems with simulating the BL over the MIZ were attributed to incorrect sea ice cover. Comparing to our aircraft observations, OSTIA had a high ice fraction where nearly open water was observed as was discussed in Chapter 6. In Figure 6.1 the sea ice from MODIS is compared with the fraction given by OSTIA. The sea ice cover ends further north than that given by OSTIA. Indeed the OSTIA sea ice fraction was too high for 100s of kilometres. In Chapter 6 the sea ice surface was hand edited, which improved surface temperature, increased the fluxes, warmed the BL and made the clouds qualitatively better.

If the sea ice surface is over estimated then following the results from Chapter 3 clouds may be under estimated, or occur at too low a latitude. As the MIZ is implicated in the formation of polar mesoscale convection during cold air outbreaks then if the sea ice extent is too large the model will form these too far south which impacts weather forecasting. As OSTIA is used in the UK Meterological Office's forecasts, it is very important that the sea ice cover is accurate. Improvements in the detection of sea ice therefore need to be made, with better detection of cloud, diagnosis of both ice type and thickness and a small horizontal resolution of less than 1 km.

7.5 PWRF IS MORE SENSITIVE TO SURFACE REPRESENTATION THAN BL PARAMETRISATION.

In Chapter 6 the sea ice cover for Case 2 was edited to better match that which was observed with the aircraft. The new surface can be seen in Fig. 6.2. A second set of sensitivity studies were then carried out, focussing only on Case 2 and once again comparing the performance of the MYJ, YSU, QNSE and ACM2 parametrisation schemes.

This change dramatically affected the surface temperature due to the increased amount of open water. The bias changed from -1.32(±0.3) K to +0.3(±0.3) K, with the surface temperature to the south of the cross section being particularly good, as well as the transition from higher to lower sea ice fractions (cf. Fig 6.4). The QNSE still gave the lowest temperature values while the YSU gave the highest, however as the sign of the bias has flipped, the best performing BL scheme is changed from YSU to QNSE.

The increased surface temperature increased the surface heat fluxes, and showed that some schemes give higher fluxes in different situations. In Figs. 6.6 and 6.7 it can be seen that over the open water, the ACM2 gave the highest fluxes, whereas over medium and high ice fractions, the QNSE was able to give the largest SHF and LHF. This is due to the different applications which were considered when the two schemes were developed. As the ACM2 is designed for unstable, convective situations, it gives higher fluxes in this application, whereas the QNSE which was designed for stable BLs is able to provide higher fluxes in more stable BLs than the other schemes due to its changed stability correction functions. The MYJ always gave the lowest surface heat fluxes, as it is a local scheme.

The increased T_{sfc}, SHF and LHF resulted in a warmer BL which increased in height. The ACM2 showed the biggest change in height (160 m) and was the only scheme able to get close to the sudden change in BL height seen in the observations (cf. Fig. 6.8). The increase in BL height is important for the clouds, as this changes the height of the clouds, and the increased surface fluxes of heat and moisture change the composition of the clouds. The cloud liquid water mixing ratio Q_{LW} is reduced by up to 0.11 g kg^{-1} for all the schemes except the QNSE, which shows an increase of 0.9 g kg^{-1}. The QNSE also shows an increase in cloud ice water mixing ratio Q_{IW} as does the ACM2 (cf. Figs. 6.12 and 6.13). As it is best at mixing in more stable BLs, the QNSE is able to provide liquid for more of the cross section than the other schemes, which explains the increase in Q_{LW} and Q_{IW}. The ACM2 is best at mixing over the open water, and has the highest BL height which explains its increased Q_{IW}. Qualitatively the ACM2 is the best for clouds, as it has the increase in cloud base height as seen in the observations and the closest values of Q_{LW} and Q_{IW}.

Which was the best BL scheme was concluded to be a combination of error cancellation and application. If the sea ice extent is expected to be too high or thick, then the QNSE may be best, as it can provide a higher surface temperature and surface fluxes, thus helping to cancel the error. If increasing BL height is most important, then the ACM2 would be best. New parametrisations need to be developed to cope with the large changes which take place across the MIZ, or a way of diagnosing the stability and choosing a BL parametrisation accordingly could be implemented.

It was concluded therefore that as the atmosphere was better simulated with the inclusion of a better surface, rather than by changing the BL scheme, that the sea ice cover was more important to have simulated correctly.

7.6 SEA ICE IS THE MOST IMPORTANT ASPECT OF THE MIZ.

It can therefore be concluded that as the inclusion of thinner sea ice in PWRF results in both local and non-local changes, and the sensitivity tests show the model is more sensitive to the surface than the choice of BL parametrisation, that the sea ice is the most important aspect of the MIZ. This means that in weather and climate models, where the sea ice is simplistically represented, uncertainty is being introduced into the forecasting of phenomena such as polar mesoscale cyclones and the prediction of future climates. As sea ice continues to reduce and become thinner, the conclusions from this thesis point to there being a positive feedback which will further reduce the sea ice. The enhanced melting could see sea levels rise, and changes in global weather patterns. As the ability to accurately predict the weather in the Arctic becomes more important, with increases in shipping and oil exploration due to the decreased sea ice cover, the accurate simulation of sea ice will become even more important.

7.7 FUTURE

In a world with thinning, reducing sea ice cover then this thesis points to this being a self perpetuating situation. As the sea ice surface is so important more work should be carried out to further assess the impact of the changing sea ice, as well as to better understand the effects it has on the atmosphere. In the idealised experiments in Chapter 3 the thinner sea ice did not have a reduced albedo, as would be the case in real life. The impact of the reduction in albedo needs to be investigated. The modelling experiments point to problems in the way BL parametrisations are able to simulate the BL over the MIZ as it transitions from stable to unstable. More work needs to be done to develop parametrisations which are either very adaptable to different situations, or that different approaches can be used in the areas for which they are most suited.

Sea ice representation in models needs to become more sophisticated. At present the land surface model within WRF can represent one sort of sea ice, while over the land many different land-uses are available (tundra, urban, forest etc). Experiments should be carried out to enable different types of sea ice to be simulated, such as grease ice, which is very thin and less reflective, or areas of close ice, which may appear to be solid from a distance but are made up of small independent chunks. In an ideal world a sea ice model should be coupled to WRF to allow for the best simulation of the sea ice surface. The inclusion of sea ice types in models would require improvements in the detection of sea ice by satellites, along with changes to the assimilation of sea ice data into the models. The coupling of ocean, ice and atmosphere in models would allow more feedbacks between the three areas to be represented, and the ability to form, melt and move sea ice would be very useful for longer time scale studies than those here.

The differences between the simulation of Case 1 and Case 2 were partly attributed to the latter case having cloud, which the model was unable to simulate accurately and which would cause issues with other variables such as the surface temperature and BL height. The BL schemes are very important for the formation of cloud, due to them providing the tendencies of moisture and temperature upwards to the free atmosphere. Other than the QNSE, none have been designed for the Arctic, which may mean that they are behaving in a way which is very different to how the BL in the Arctic in their provision of moisture upwards. Further research into how the BL and clouds interact in the Arctic, along with work on the BL parametrisations and indeed cloud microphysics parametrisations would be beneficial.

If improvements in the simulation of sea ice within models are made, then the BL parametrisation schemes will need to be able to cope with the different surface types. In order to quantify the impacts of the different sorts of sea ice on the atmosphere, through heat fluxes and surface roughness, more observations need to be made. As was discussed, aircraft measurements may not be very reliable, and therefore either surface based experiments need to be carried out, or investigations with facilities such as the Roland von Glasow sea ice chamber. This would allow fully controlled experiments with high resolution measurements to be carried out, quantifying the impact of different sorts of ice on the atmosphere above. Large eddy models, with horizontal scales which are very small could also be used in conjunction with observations and experiments to help develop new parametrisations, and examine the effect of more variable sea ice type in models.

The MIZ is an extremely complex area, which is very important to understand. Improvements in the representation of the MIZ in models will have impacts on both weather and climate simulations, allowing better forecasts and predictions to be made. These are of ever increasing importance in a world which is experiencing warming and the loss of ice due to climate change.

REFERENCES

CryoSat Operational Polar Monitoring. http://www.cpom.ucl.ac.uk/csopr/seaice.html. Accessed: 2015-10-15.

Anderson, P.S., & Neff, W.D. 2008. Boundary layer physics over snow and ice. *Atmospheric Chemistry and Physics*, **8**(July), 3563–3582.

Andreas, E.L., Paulson, C.A., William, R.M., Lindsay, R.W., & Businger, J.A. 1979. The turbulent heat flux from arctic leads. *Boundary-Layer Meteorology*, **17**(1), 57–91.

Atkinson, B.W., & Zhang, J. W. 1996. Mesoscale shallow convection in the atmosphere. *Reviews of Geophysics*, **34**(4), 403–431.

Beljaars, A. 1995. The parametrization of surface fluxes in large-scale models under free convection. *Quarterly Journal of the Royal Meteorological Society*, **121**(522), 255–270.

Birch, C. E., Brooks, I. M., Tjernström, M., Milton, S. F., Earnshaw, P., Söderberg, S., & Persson, P. O. G. 2009. The performance of a global and mesoscale model over the central Arctic Ocean during late summer. *Journal of Geophysical Research: Atmospheres (1984–2012)*, **114**(D13).

Boisvert, L. N., Markus, T., Parkinson, C. L., & Vihma, T. 2012. Moisture fluxes derived from EOS aqua satellite data for the north water polynya over 2003–2009. *Journal of Geophysical Research: Atmospheres*, **117**(D6), n/a–n/a. D06119.

Borys, R. D., Lowenthal, D. H., & Mitchell, D. L. 2000. The relationships among cloud microphysics, chemistry, and precipitation rate in cold mountain clouds. *Atmospheric Environment*, **34**(16), 2593 – 2602.

Bracegirdle, T. J., & Gray, S. L. 2009. The dynamics of a polar low assessed using potential vorticity inversion. *Quarterly Journal of the Royal Meteorological Society*, **135**(641), 880–893.

Bromwich, D. H., Hines, K. M., & Bai, L-S. 2009. Development and Testing of Polar Weather Research and Forecasting Model: 2. Arctic Ocean. *Journal of Geophysical Research: Atmospheres (1984–2012)*, **114**(D8).

Bromwich, D.H, Otieno, F.O, Hines, K.M., Manning, K.W., & Shilo, E. 2013. A comprehensive evaluation of Polar WRF forecast performance in the Antarctic. *J. Geophys. Res.*, **118**, 274–292.

Castro de la Guardia, L., Derocher, A. E., Myers, P. G., Terwisscha van Scheltinga, A. D., & Lunn, N. J. 2013. Future sea ice conditions in Western Hudson Bay and consequences for polar bears in the 21st century. *Global Change Biology*, **19**(9), 2675–2687.

Chechin, D. G., Lüpkes, C., Repina, I. A., & Gryanik, V. M. 2013. Idealized dry quasi 2-D mesoscale simulations of cold-air outbreaks over the marginal sea ice zone with fine and coarse resolution. *Journal of Geophysical Research: Atmospheres*, **118**(16), 8787–8813.

Chen, F., & Dudhia, J. 2001. Coupling an Advanced Land Surface–Hydrology Model with the Penn State–NCAR MM5 Modeling System. Part I: Model Implementation and Sensitivity. *Monthly Weather Review*, **129**(4), 569–585.

Chen, F., Mitchell, K., Schaake, J., Xue, Y., Pan, H., Koren, V., Duan, Q. Y., Ek, M., & Betts, A. 1996. Modeling of land surface evaporation by four schemes and comparison with FIFE observations. *Journal of Geophysical Research: Atmospheres*, **101**(D3), 7251–7268.

Chen, F., Janjić, Z., & Mitchell, K. 1997. Impact of Atmospheric Surface-layer Parameterizations in the new Land-surface Scheme of the NCEP Mesoscale Eta Model. *Boundary-Layer Meteorology*, **85**(3), 391–421.

Cherry, S. G., Derocher, A. E., Stirling, I., & Richardson, E. S. 2008. Fasting physiology of polar bears in relation to environmental change and breeding behavior in the Beaufort Sea. *Polar Biology*, **32**(3), 383–391.

Comiso, J. C. 2012. Large decadal decline of the Arctic multiyear ice cover. *Journal of Climate*, **25**(4), 1176–1193.

Cook, P. A., & Renfrew, I. A. 2015. Aircraft-based observations of air–sea turbulent fluxes around the British Isles. *Quarterly Journal of the Royal Meteorological Society*, **141**(686), 139–152.

CPOM. 2015. CryoSat Operational Polar Monitoring - Arctic Sea Ice Thickness. *Website*. Accessed April 2015.

Curry, J. A., Ebert, E. E., & Herman, G. F. 1988. Mean and turbulence structure of the summertime Arctic cloudy boundary layer. *Q. J. R. Meteorol. Soc.*, **114**, 715–746.

Curry, J. A., Rossow, W. B., Randall, D., & Schramm, J. L. 1996. Overview of Arctic cloud and radiation characteristics. *J. Climate*, **9**, 1731–1764.

Dare, R. A., & Atkinson, B. W. 1999. Numerical modeling of atmospheric response to polynyas in the Southern Ocean sea ice zone. *Journal of Geophysical Research: Atmospheres*, **104**(D14), 16691–16708.

de Boer, G., Morrison, H., Shupe, M. D., & Hildner, R. 2011. Evidence of liquid dependent ice nucleation in high-latitude stratiform clouds from surface remote sensors. *Geophysical Research Letters*, **38**(1), n/a–n/a. L01803.

Dee, D. P., Uppala, S. M., Simmons, A. J., Berrisford, P., Poli, P., Kobayashi, S., Andrae, U., Balmaseda, M. A., Balsamo, G., Bauer, P., Bechtold, P., Beljaars, A. C. M., van de Berg, L., Bidlot, J., Bormann, N., Delsol, C., Dragani, R., Fuentes, M., Geer, A. J., Haimberger, L., Healy, S. B., Hersbach, H., Hólm, E. V., Isaksen, L., Kållberg, P., Köhler, M., Matricardi, M., McNally, A. P., Monge-Sanz, B. M., Morcrette, J.-J., Park, B.-K., Peubey, C., de Rosnay, P., Tavolato, C., Thépaut, J.-N., & Vitart, F. 2011. The ERA-Interim reanalysis: configuration and performance of the data assimilation system. *Quarterly Journal of the Royal Meteorological Society*, **137**(656), 553–597.

Dyer, A. J., & Hicks, B. B. 1970. Flux-gradient relationships in the constant flux layer. *Quarterly Journal of the Royal Meteorological Society*, **96**(410), 715–721.

Ek, M. B., Mitchell, K. E., Lin, Y., Rogers, E., Grunmann, P., Koren, V., Gayno, G., & Tarpley, J. D. 2003. Implementation of Noah land surface model advances in the National Centers for Environmental Prediction operational mesoscale Eta model. *Journal of Geophysical Research: Atmospheres*, **108**(D22), n/a–n/a. 8851.

Elvidge, A. D., Renfrew, I. A., Weiss, A. I., Brooks, I. M., Lachlan-Cope, T. A., & King, J. C. 2016. Observations of surface momentum exchange over the marginal ice zone and recommendations for its parametrisation. *Atmospheric Chemistry and Physics*, **16**(3), 1545–1563.

Fairall, C. W., & Markson, R. 1987. Mesoscale variations in surface stress, heat fluxes, and drag coefficient in the marginal ice zone during the 1983 Marginal Ice Zone Experiment. *J. Geophys. Res*, **92**(C7), 6921–6932.

García-Díez, M., Fernández, J., Fita, L., & Yagüe, C. 2013. Seasonal dependence of WRF model biases and sensitivity to PBL schemes over Europe. *Quarterly Journal of the Royal Meteorological Society*, **139**(671), 501–514.

Garrat, J. R. 1992. *The Atmospheric Boundary Layer*. Cambridge University Press.

Garratt, J.R. 1990. The internal boundary layer—a review. *Boundary-Layer*

Meteorology, **50**(1-4), 171–203.

Gryschka, M., Drüe, C., Etling, D., & Raasch, S. 2008. On the influence of sea-ice inhomogeneities onto roll convection in cold-air outbreaks. *Geophysical Research Letters*, **35**(23).

Gultepe, I., Isaac, G.A., Williams, A., Marcotte, D., & Strawbridge, K.B. 2003. Turbulent heat fluxes over leads and polynyas, and their effects on Arctic clouds during FIRE. ACE: Aircraft observations for April 1998. *Atmosphere-Ocean*, **41**(1), 15–34.

H., Jerry Y., Reisin, T., Cotton, W. R., & Kreidenweis, S. M. 1999. Cloud resolving simulations of Arctic stratus: Part II: Transition-season clouds. *Atmospheric Research*, **51**(1), 45 – 75.

Hines, K. M., & Bromwich, D.H. 2008. Development and Testing of Polar Weather Research and Forecasting (WRF) Model. Part I: Greenland Ice Sheet Meteorology. *Monthly Weather Review*, **136**(6), 1971–1989.

Hines, K. M., Bromwich, D. H., Bai, L., Bitz, C. M., Powers, J. G., & Manning, K. W. 2015. Sea Ice Enhancements to Polar WRF. *Monthly Weather Review*.

Holtslag, A. A. M., & Bruin, H. A. R. De. 1988. Applied Modeling of the Nighttime Surface Energy Balance over Land. *Journal of Applied Meteorology*, **27**(6), 689–704.

Hong, S., & Kim, S. 2008. Stable boundary layer mixing in a vertical diffusion scheme. *In: 18th Symposium on Boundary Layers and Turbulence B*, vol. 16.

Hong, S., Noh, Y., & Dudhia, J. 2006. A new vertical diffusion package with an explicit treatment of entrainment processes. *Monthly Weather Review*, **134**(9).

Hu, X., Nielsen-Gammon, J. W., & Zhang, F. 2010. Evaluation of three planetary boundary layer schemes in the WRF model. *Journal of Applied Meteorology and Climatology*, **49**(9), 1831–1844.

Huang, H., Hall, A., & Teixeira, J. 2013. Evaluation of the WRF PBL Parameterizations for Marine Boundary Layer Clouds: Cumulus and Stratocumulus. *Monthly Weather Review*, **141**(7).

Intrieri, J. M., Fairall, C.W, Shupe, M.D., Persson, P.O.G, Andreas, E.L., Guest, P.S., & Moritz, R.E. 2002. An annual cycle of Arctic surface cloud forcing at SHEBA. *J.G.R.*, **107**(C10).

J., Zaviša I. 1990. The Step-Mountain Coordinate: Physical Package. *Monthly Weather Review*, **118**(7), 1429–1443.

Janjic, Z. I. 1994. The step-mountain eta coordinate model: Further developments of the convection, viscous sublayer, and turbulence closure schemes. *Monthly Weather Review*, **122**(5), 927–945.

JCOMM, WMO-IOC. 2014. *WMO Sea Ice Nomenclature*.

Kay, J. E., & Gettelman, A. 2009. Cloud influence on and response to seasonal Arctic sea ice loss. *J. Geophysical Res.*, **114**(D18204).

Kay, J. E., Raeder, K., Gettleman, A., & Anderson, J. 2010. The Boundary Layer Response to Recent Arctic Sea Ice Loss and Implications for High-Latitude Climate Feedbacks. *J. Climate*, **24**, 428–447.

Kilpeläinen, T., Vihma, T., Manninen, M., Sjöblom, A., Jakobson, E., Palo, T., & Maturilli, M. 2012. Modelling the vertical structure of the atmospheric boundary layer over Arctic fjords in Svalbard. *Quarterly Journal of the Royal Meteorological Society*, **138**(668), 1867–1883.

Kleczek, M. A., Steeneveld, Gert-Jan, & Holtslag, Albert A. M. 2014. Evaluation of the Weather Research and Forecasting Mesoscale Model for GABLS3: Impact of Boundary-Layer Schemes, Boundary Conditions and Spin-Up. *Boundary-Layer Meteorology*, **152**(2), 213–243.

Kwok, R., & Rothrock, D. A. 2009. Decline in Arctic sea ice thickness from submarine and ICESat records: 1958–2008. *Geophysical Research Letters*, **36**(15).

Lance, S., Brock, C. A., Rogers, D., & Gordon, J. A. 2010. Water droplet calibration of the Cloud Droplet Probe (CDP) and in-flight performance in liquid, ice and mixed-phase clouds during ARCPAC. *Atmospheric Measurement Techniques*, **3**(6), 1683–1706.

Lance, S., Shupe, M. D., Feingold, G., Brock, C. A., Cozic, J., Holloway, J. S., Moore, R. H., Nenes, A., Schwarz, J. P., Spackman, J. R., Froyd, K. D., Murphy, D. M., Brioude, J., Cooper, O. R., Stohl, A., & Burkhart, J. F. 2011. Cloud condensation nuclei as a modulator of ice processes in Arctic mixed-phase clouds. *Atmospheric Chemistry and Physics*, **11**(15), 8003–8015.

Larsen, J. N., Anisimov, O. A., Constable, A., Hollowed, A.B., Maynard, N., Prestrud, P., Prowse, T. D., & Stone, J. M. R. 2014. Polar regions. *Pages 1567–1612 of:* Barros, V.R., Field, C.B., Dokken, D.J., Mastrandrea, M.D., Mach, K.J., Bilir, T.E., Chatterjee, M., Ebi, K.L., Estrada, Y.O., Genova, R.C., Girma, B., Kissel, E.S., Levy, A.N., MacCracken, S., Mastrandrea, P.R., & White, L.L. (eds), *Climate Change 2014: Impacts, Adaptation, and Vulnerability. Part B: Regional Aspects. Contribution of*

Working Group II to the Fifth Assessment Report of the Intergovernmental Panel on Climate Change. Cambridge University Press.

Lawson, R. P., O'Connor, D., Zmarzly, P., Weaver, K., Baker, B., Mo, Q., & Jonsson, H. 2006. The 2D-S (Stereo) Probe: Design and Preliminary Tests of a New Airborne, High-Speed, High-Resolution Particle Imaging Probe. *Journal of Atmospheric and Oceanic Technology*, **23**(11), 1462–1477.

Liu, A.Q., Moore, G.W.K., Tsuboki, K., & Renfrew, I.A. 2006. The effect of the sea-ice zone on the development of boundary-layer roll clouds during cold air outbreaks. *Boundary-layer meteorology*, **118**(3), 557–581.

Lloyd, G., Choularton, T. W., Bower, K. N., Crosier, J., Jones, H., Dorsey, J. R., Gallagher, M. W., Connolly, P., Kirchgaessner, A. C. R., & Lachlan-Cope, T. 2015. Observations and comparisons of cloud microphysical properties in spring and summertime Arctic stratocumulus clouds during the ACCACIA campaign. *Atmospheric Chemistry and Physics*, **15**(7), 3719–3737.

Maslanik, J., Stroeve, J., Fowler, C., & Emery, W. 2011. Distribution and trends in Arctic sea ice age through spring 2011. *Geophysical Research Letters*, **38**(13).

Mauritsen, T., Sedlar, J., Tjernström, M., Leck, C., Martin, M., Shupe, M., Sjogren, S., Sierau, B., Persson, P.O.G., Brooks, I.M., *et al.* 2011. An Arctic CCN-limited cloud-aerosol regime. *Atmospheric Chemistry and Physics*, **11**(1), 165–173.

Mayer, S., Jonassen, M. O., Sandvik, A., & Reuder, J. 2012. Profiling the Arctic Stable Boundary Layer in Advent Valley, Svalbard: Measurements and Simulations. *Boundary-layer meteorology*, **143**(3), 507–526.

Mellor, G. L., & Yamada, T. 1982. Development of a turbulence closure model for geophysical fluid problems. *Reviews of Geophysics*, **20**(4), 851–875.

Moore, G. W. K., Reader, M. C., York, J, & Sathiyamoorthy, S. 1996. Polar lows in the Labrador Sea. *Tellus A*, **48**(1), 17–40.

Morrison, H., & Pinto, J. O. 2005. Mesoscale Modeling of Springtime Arctic Mixed-Phase Stratiform Clouds Using a New Two-Moment Bulk Microphysics Scheme. *Journal of the Atmospheric Sciences*, **62**(10), 3683–3704.

Morrison, H., & Pinto, J. O. 2006. Intercomparison of Bulk Cloud Microphysics Schemes in Mesoscale Simulations of Springtime Arctic Mixed-Phase Stratiform Clouds. *Monthly Weather Review*, **134**(7), 1880–1900.

Morrison, H., Curry, J. A., & Khvorostyanov, V. I. 2005. A New Double-Moment

Microphysics Parameterization for Application in Cloud and Climate Models. Part I: Description. *Journal of the Atmospheric Sciences*, **62**(6), 1665–1677.

Morrison, H., Pinto, J. O., Curry, J. A., & McFarquhar, G. M. 2008. Sensitivity of modeled arctic mixed-phase stratocumulus to cloud condensation and ice nuclei over regionally varying surface conditions. *Journal of Geophysical Research: Atmospheres*, **113**(D5), n/a–n/a. D05203.

Morrison, H., Thompson, G., & Tatarskii, V. 2009. Impact of cloud microphysics on the development of trailing stratiform precipitation in a simulated squall line: Comparison of one-and two-moment schemes. *Monthly Weather Review*, **137**(3), 991–1007.

Morrison, H., de Boer, G., Feingold, G., Harrington, J., Shupe, M. D., & Sulia, K. 2012. Resilience of persistent Arctic mixed-phase clouds. *Nature Geoscience*, **5**(January), 11–17.

Nghiem, S.V., Rigor, I.G., Perovich, D.K., Clemente-Colón, P., Weatherly, J.W., & Neumann, G. 2007. Rapid reduction of Arctic perennial sea ice. *Geophysical Research Letters*, **34**(19).

Pachauri, R. K., Allen, M. R., Barros, V. R., Broome, J., Cramer, W., Christ, R., Church, J. A., Clarke, L., Dahe, Q., Dasgupta, P., *et al.* 2014. Climate Change 2014: Synthesis Report. Contribution of Working Groups I, II and III to the Fifth Assessment Report of the Intergovernmental Panel on Climate Change.

Palm, S. P., Strey, S. T., Spinhirne, J., & Markus, T. 2010. Influence of Arctic sea ice extent on polar cloud fraction and vertical structure and implications for regional climate. *J. Geophys. Res.*, **115**, D21209.

Paluch, I.R., Lenschow, D.H., & Wang, Q. 1997. Arctic boundary layer in the fall season over open and frozen sea. *Journal of Geophysical Research: Atmospheres (1984–2012)*, **102**(D22), 25955–25971.

Papritz, L., Pfahl, S., Sodemann, H., & Wernli, H. 2015. A Climatology of Cold Air Outbreaks and Their Impact on Air–Sea Heat Fluxes in the High-Latitude South Pacific. *Journal of Climate*, **28**(1), 342–364.

Paulson, C. A. 1970. The mathematical representation of wind speed and temperature profiles in the unstable atmospheric surface layer. *Journal of Applied Meteorology*, **9**(6), 857–861.

Perovich, D. K., & Polashenski, C. 2012. Albedo evolution of seasonal Arctic sea ice.

Geophysical Research Letters, **39**(8).

Perovich, D. K., Andreas, E. L., Curry, J. A., Eiken, H., Fairall, C. W., Grenfell, T. C., Guest, P.S., Intrieri, J., Kadko, D., Lindsay, R. W., McPhee, M. G., Morison, J., Moritz, R. E., Paulson, C. A., Pegau, W. S., Persson, P.O.G., Pinkel, R., Richter-Menge, J. A., Stanton, T., Stern, H., Sturm, M., Tucker, W.B., & Uttal, T. 1999. Year on ice gives climate insights. *Eos, Transactions American Geophysical Union*, **80**(41), 481–486.

Persson, P. O. G. 2012. Onset and end of the summer melt season over sea ice: thermal structure and surface energy perspective from SHEBA. *Climate Dynamics*, **39**(6), 1349–1371.

Persson, P. O. G., Ruffieux, D., & Fairall, C. W. 1997. Recalculations of pack ice and lead surface energy budgets during the Arctic Leads Experiment (LEADEX) 1992. *Journal of Geophysical Research: Oceans*, **102**(C11), 25085–25089.

Pinto, J. O., Alam, A., Maslanik, J.A., Curry, J.A., & Stone, R. S. 2003. Surface characteristics and atmospheric footprint of springtime Arctic leads at SHEBA. *Journal of Geophysical Research: Oceans (1978–2012)*, **108**(C4).

Pinto, J.O. 1998. Autumnal Mixed-Phase Cloudy Boundary Layers in the Arctic. *Journal of the atmospheric sciences*, **55**(11), 2016–2038.

Pleim, J. E. 2007. A combined local and nonlocal closure model for the atmospheric boundary layer. Part I: Model description and testing. *Journal of Applied Meteorology & Climatology*, **46**(9).

Rasmussen, Erik A., & Turner, J. 2003. *Polar lows*. Springer.

Renfrew, I. A., & Moore, G.W.K. 1999. An extreme cold-air outbreak over the Labrador Sea: Roll vortices and air-sea interaction. *Monthly weather review*, **127**(10), 2379–2394.

Rinke, A., Maslowski, W., Dethloff, K., & Clement, J. 2006. Influence of sea ice on the atmosphere: A study with an Arctic atmospheric regional climate model. *Journal of Geophysical Research: Atmospheres (1984–2012)*, **111**(D16).

Ruffieux, D., Persson, P. O. G., Fairall, C. W., & Wolfe, D. E. 1995. Ice pack and lead surface energy budgets during LEADEX 1992. *Journal of Geophysical Research: Oceans*, **100**(C3), 4593–4612.

Screen, J. A., Deser, C., Simmonds, I., & Tomas, R. 2014. Atmospheric impacts of Arctic sea-ice loss, 1979–2009: separating forced change from atmospheric internal variability. *Climate dynamics*, **43**(1-2), 333–344.

Sedlar, J., Tjernström, M., Mauritsen, T., Shupe, M. D., Brooks, I. M., Persson, P. O. G., Birch, C. E., Leck, C., Sirevaag, A., & Nicolaus, M. 2011. A transitioning Arctic surface energy budget: the impacts of solar zenith angle, surface albedo and cloud radiative forcing. *Climate dynamics*, **37**(7-8), 1643–1660.

Seo, H., & Yang, J. 2013. Dynamical response of the Arctic atmospheric boundary layer process to uncertainties in sea ice concentration. *Journal of Geophysical Research: Atmospheres*, **118**(22), 12,383–12,402.

Serreze, M. C., & Francis, J. A. 2006. The Arctic amplification debate. *Climatic Change*, **76**(3-4), 241–264.

Shin, H. H., & Hong, S. 2011. Intercomparison of Planetary Boundary-Layer Parametrizations in the WRF Model for a Single Day from CASES-99. *Boundary-Layer Meteorology*, **139**(2), 261–281.

Shupe, M. D., & Intriei, J. M. 2003. Cloud Radiative Forcing of the Arctic Surface: The Influence of Cloud Properties, Surface Albedo, and Solar Zenith Angle. *J. Climate*, **17**, 616–628.

Shupe, M. D, Kollias, P., Persson, P. O. G., & McFarquhar, G. M. 2008. Vertical motions in Arctic mixed-phase stratiform clouds. *Journal of the Atmospheric Sciences*, **65**(4), 1304–1322.

Shupe, M.D., Persson, P.O.G., Brooks, I.M., Tjernstrom, M., Sedlar, J., Mauritsen, T., Sjogren, S., & Leck, C. 2013. Cloud and boundary layer interactions over the Arctic sea-ice in late summer. *Atmospheric Chemistry and Physics Discussions*, **13**(5), 13191–13244.

Skamarock, W.C., & Klemp, J.B. 2008. A time-split nonhydrostatic atmospheric model for weather researching and forecasting applications. *Journal of computational physics*, **227**, 3465 – 3485.

Solomon, A., Shupe, M. D., Persson, P. O. G., & Morrison, H. 2011. Moisture and dynamical interactions maintaining decoupled Arctic mixed-phase stratocumulus in the presence of a humidity inversion. *Atmospheric Chemistry and Physics*, **11**(19), 10127–10148.

Stensrud, David J. 2007. *Parameterization schemes: keys to understanding numerical weather prediction models*. Cambridge University Press.

Stocker, T. F, Qin, D., Plattner, G-K., Tignor, M., Allen, S. K., Boschung, J., Nauels, A., Xia, Y., Bex, V., & Midgley, P. M. 2013. Climate change 2013: The physical science basis. *Intergovernmental Panel on Climate Change, Working Group I Contribution to the IPCC Fifth Assessment Report (AR5)(Cambridge Univ Press, New York).*

Stull, R. B. 2012. *An introduction to boundary layer meteorology.* Vol. 13. Springer Science & Business Media.

Sukoriansky, S., Galperin, B., & Staroselsky, I. 2003. Cross-term and ϵ-expansion in RNG theory of turbulence. *Fluid Dynamics Research*, **33**(4), 319 – 331.

Sukoriansky, S., Galperin, B., & Perov, V. 2005. Application of a new spectral theory of stably stratified turbulence to the atmospheric boundary layer over sea ice. *Boundary-layer meteorology*, **117**(2), 231–257.

Tastula, E., Vihma, T., & Andreas, E. L. 2012. Evaluation of Polar WRF from Modeling the Atmospheric Boundary Layer over Antarctic Sea Ice in Autumn and Winter. *Monthly Weather Review*, **140**(12).

Tetzlaff, A., Lüpkes, C., Birnbaum, G., Hartmann, J., Nygard, T., & Vihma, T. 2014. Brief Communication: Trends in sea ice extent north of Svalbard and its impact on cold air outbreaks as observed in spring 2013. *The Cryosphere*, **8**(5), 1757–1762.

Tetzlaff, A., Lüpkes, C., & Hartmann, J. 2015. Aircraft-based observations of atmospheric boundary layer modification over arctic leads. *Quarterly Journal of the Royal Meteorological Society.*

Tjernström, M. 2012. The Arctic ocean boundary layer. *Pages 171–185 of: ECMWF GABLS Workshop on Dirunal cycles and the stable boundary layer.*

Tjernström, M., Žagar, M., Svensson, G., Cassano, J. J., Pfeifer, S., Rinke, A., Wyser, K, Dethloff, K, Jones, C., Semmler, T., *et al.* 2005. Modelling the Arctic boundary layer: an evaluation of six ARCMIP regional-scale models using data from the SHEBA project. *Boundary-Layer Meteorology*, **117**(2), 337–381.

Valkonen, T., Vihma, T., & Doble, M. 2008. Mesoscale modeling of the atmosphere over Antarctic sea ice: A late-autumn case study. *Monthly Weather Review*, **136**(4), 1457–1474.

Valkonen, T., Vihma, T., Johansson, M. M., & Launiainen, J. 2014. Atmosphere–sea ice interaction in early summer in the Antarctic: evaluation and challenges of a regional atmospheric model. *Quarterly Journal of the Royal Meteorological Society*, **140**(682), 1536–1551.

Vihma, T. 1995. Subgrid parameterization of surface heat and momentum fluxes over polar oceans. *Journal of Geophysical Research: Oceans*, **100**(C11), 22625–22646.

Vihma, T., & Brümmer, B. 2002. Observations And Modelling Of The On-Ice And Off-Ice Air Flow Over The Northern Baltic Sea. *Boundary-Layer Meteorology*, **103**(1), 1–27.

Vihma, T., Lüpkes, C., Hartmann, J., & Savijärvi, H. 2005. Observations and modelling of cold-air advection over Arctic sea ice. *Boundary-layer meteorology*, **117**(2), 275–300.

Vihma, T., Pirazzini, R., Fer, I., Renfrew, I.A., Sedlar, J., Tjernström, M., Lüpkes, C., Nygard, T., Notz, D., Weiss, J., *et al.* 2014. Advances in understanding and parameterization of small-scale physical processes in the marine Arctic climate system: a review. *Atmospheric Chemistry and Physics (ACP)*, **14**(17), 9403–9450.

Wallace, J. M, & Hobbs, P. V. 2005a. *Atmospheric Science: An Introductory Survey*. 2 edn. Academic Press. Chap. The Atmospheric Boundary Layer.

Wallace, J. M., & Hobbs, P. V. 2005b. *Atmospheric Science: An Introductory Survey*. 2 edn. Academic Press. Chap. Cloud Microphysics.

Wang, S., Wang, Q., Jordan, R. E., & Persson, P. O. G. 2001. Interactions among longwave radiation of clouds, turbulence, and snow surface temperature in the Arctic: A model sensitivity study. *Journal of Geophysical Research: Atmospheres*, **106**(D14), 15323–15333.

Webb, E. K. 1970. Profile relationships: The log-linear range, and extension to strong stability. *Quarterly Journal of the Royal Meteorological Society*, **96**(407), 67–90.

Zeng, X-M., Wang, B., Zhang, Y., Song, S., Huang, X., Zheng, Y., Chen, C., & Wang, G. 2014. Sensitivity of high-temperature weather to initial soil moisture: a case study using the WRF model. *Atmospheric Chemistry and Physics*, **14**(18), 9623–9639.

Zeng, X-M., Wang, N., Wang, Y., Zheng, Y., Zhou, Z., Wang, G., Chen, C., & Liu, H. 2015. WRF-simulated sensitivity to land surface schemes in short and medium ranges for a high-temperature event in East China: A comparative study. *Journal of Advances in Modeling Earth Systems*, **7**(3), 1305–1325.

Zhang, D., & Anthes, R. A. 1982. A High-Resolution Model of the Planetary Boundary Layer—Sensitivity Tests and Comparisons with SESAME-79 Data. *Journal of Applied Meteorology*, **21**(11), 1594–1609.

Zilitinkevich, S. 1995. Non-local turbulent transport pollution dispersion aspects of coherent structure of convective flows. *Air Pollution III, Air pollution theory and simulation (H Power, N Moussiopoulos, CA Brebbia, eds) Computational Mechanics*

Publl, Southampton, Boston, **1**, 53–60.

Zuidema, P, Baker, B, Han, Y, Intrieri, J, Key, J, Lawson, P, Matrosov, S, Shupe, M, Stone, R, & Uttal, T. 2005. An Arctic springtime mixed-phase cloudy boundary layer observed during SHEBA. *Journal of the atmospheric sciences*, **62**(1), 160–176.